Photoionization spectroscopy of radicals of astrophysical interest in the vacuum ultraviolet

Ning Chen

université PARIS-SACLAY

Photoionization spectroscopy of radicals of astrophysical interest in the vacuum ultraviolet

Spectroscopie de photoionisation de radicaux d'intérêt astrophysique dans l'ultraviolet du vide

Thèse de doctorat de l'Université Paris-Saclay

École doctorale n°572, ondes et matière (EDOM)
Spécialité de doctorat : Physique
Graduate School : Physique. Référent : Faculté des sciences d'Orsay

Thèse préparée dans l'unité de recherche **Institut des Sciences Moléculaires d'Orsay** (Université Paris-Saclay, CNRS), sous la direction de **Séverine BOYE-PERONNE**, Professeure, et le co-encadrement de **Bérenger GANS**, Chargé de recherche CNRS

Thèse soutenue à Paris-Saclay, le 24 Novembre2023, par

Ning CHEN

Composition du Jury

Membres du jury avec voix délibérative

Kevin HICKSON Directeur de recherche au CNRS, Université de Bordeaux/ISM	Président
Héloïse DOSSMANN Maîtresse de conférences (HDR), Sorbonne Université/IPCM	Rapporteur& Examinatrice
Clément LAUZIN Professeur, Université Catholique de Louvain la Neuve/IMCN	Rapporteur & Examinateur
Christian ALCARAZ Directeur de recherche au CNRS, Université Paris-Saclay/ICP	Examinateur
Géraldine FERAUD Maîtresse de conférences, Sorbonne Université/LERMA	Examinatrice
Jennifer NOBLE Chargée de recherche au CNRS, Université d'Aix-Marseille/PIIM	Examinatrice

THESE DE DOCTORAT
NNT : 2023UPASP154

université PARIS-SACLAY | ÉCOLE DOCTORALE Ondes et matière (EDOM)

Titre : Spectroscopie de photoionisation de radicaux d'intérêt astrophysique dans l'ultraviolet du vide

Mots clés : radical, VUV, laser, synchrotron, photoionisation, spectroscopie

Résumé : L'évolution de la matière dans les environnements astrophysiques, tels que le milieu interstellaire, est gouvernée par des processus chimiques complexes impliquant de nombreuses espèces stables et radicalaires en phase gazeuse. L'identification et l'étude des molécules interstellaires constituent des étapes fondamentales pour comprendre les processus chimiques dans l'espace, offrant des perspectives sur la compréhension de l'origine de la vie dans l'univers, les processus de formation des étoiles et la caractérisation des environnements interstellaires. La quête d'identification des espèces interstellaires et la construction de modèles chimiques reposent largement sur des études expérimentales en laboratoire.

Ce travail de doctorat est dédié à la génération de nouvelles données spectroscopiques de haute qualité en laboratoire pour des espèces en phase gazeuse d'intérêt astrophysique, en mettant particulièrement l'accent sur les espèces radicalaires, en utilisant des techniques de spectroscopie de photoionisation. Mes travaux peuvent être divisés en deux composantes principales :

- le premier aspect implique l'exploration d'un dispositif de source de radicaux stable et efficace pour produire des radicaux *in situ* ;

- le deuxième aspect consiste à développer et utiliser des techniques de spectroscopie de photoionisation à haute résolution permettant l'investigation de la structure (ro)vibronique des cations de radicaux.

Cette thèse documente des expériences sur le montage VULCAIM à haute résolution spectrale à l'ISMO et sur le montage SAPHIRS à moyenne résolution sur la ligne DESIRS du synchrotron SOLEIL.

L'installation VULCAIM, unique en France et l'une des trois seules au monde, possède la capacité de fournir un rayonnement laser VUV accordable à haute résolution entre 6 et 17 eV. Cette thèse met l'accent sur des développements effectués sur cet appareil unique, y compris l'introduction d'un laser OPO largement accordable pour étendre la gamme du laser VUV, l'exploration de sources de radicaux par pyrolyse et décharge électrique, et la mise en place d'un réflectron. Le couplage de la source de radicaux par pyrolyse avec le montage VULCAIM a permis d'obtenir un résultat de premier plan : la production de radicaux CH_3 excités vibrationnellement, fournissant des données de laboratoire à haute résolution *via* la spectroscopie photoélectronique PFI-ZEKE pour confirmer pour la première fois expérimentalement la détection de CH_3^+ dans l'espace. De plus, une nouvelle méthode de spectroscopie photoélectronique appelée PRFI-ZEKE à haute résolution et à rapport signal/bruit élevé a été proposée et appliquée dans le domaine de la recherche.

SAPHIRS, le deuxième montage utilisé au cours de cette thèse au synchrotron, associe une source de radicaux basée sur un réacteur au fluor à écoulement avec un spectromètre de photoélectrons/photoions en coïncidence à double imagerie (i^2PEPICO) et le rayonnement synchrotron. Cette configuration a permis l'enregistrement simultané du rendement d'ion et des spectres photoélectroniques résolus vibrationnellement pour divers radicaux SixCyHz, offrant des informations inédites sur la structure vibronique de leurs cations. Dans ce manuscrit, je présente des résultats expérimentaux sur SiH, Si_2, SiC et SiCH. Ces études ont permis de déterminer des valeurs fiables d'énergie d'ionisation et d'obtenir des informations sur les structures vibroniques des cations et des états de Rydberg du composé neutre observés par autoionisation. Ce travail constitue un premier pas vers la compréhension de la chimie du silicium au sein des nuages interstellaires.

université PARIS-SACLAY | ÉCOLE DOCTORALE Ondes et matière (EDOM)

Title : Photoionization spectroscopy of radicals of astrophysical interest in the vacuum ultraviolet

Keywords : radical, VUV, laser, synchrotron, photoionization, spectroscopy

Abstract : The evolution of matter in astrophysical environments, such as the interstellar medium, is governed by complex chemical processes involving numerous stable and radical species in the gas phase. Identifying and studying interstellar molecules constitute fundamental steps toward understanding the chemical processes in space, offering insights into the origin of life in the universe, star formation processes, and interstellar environments' characterization. The quest for identifying interstellar species and constructing chemical models relies heavily on laboratory-based experimental studies.

This doctoral work is dedicated to generate new, high-quality spectroscopic laboratory data for gas-phase compounds of astrophysical interest, with a particular focus on radical species, using photoionization spectroscopic techniques. My work can be broadly divided into two main components:

- the first aspect involves the exploration of a stable and efficient radical source device to produce radicals *in situ*;

- the second aspect entails the development and application of high-resolution photoionization spectroscopic techniques that enable the investigation of the (ro)vibrational structure of cations of radicals.

This thesis documents experiments conducted using the high-resolution VULCAIM setup at ISMO and the medium-resolution SAPHIRS setup at the DESIRS beamline of the SOLEIL synchrotron.

The VULCAIM setup, unique in France and one of the only three worldwide, boasts the capability to provide high-resolution tunable VUV laser radiation from 6 to 17 eV. This thesis highlights developments performed on this unique apparatus, including the introduction of a broadly tunable OPO laser to extend the range of the VUV laser, the exploration of radical sources through pyrolysis and electric discharge, and the implementation of a reflectron. The coupling of the pyrolysis radical source to the VULCAIM setup achieved a significant result: the production of vibrationally excited CH_3 radicals, providing high-resolution laboratory data *via* PFI-ZEKE photoelectron spectrosocpy that support experimentally the detection of CH_3^+ in space for the first time. Additionally, a novel high-resolution and high signal-to-noise ratio PRFI-ZEKE PES method has been proposed and applied within the research domain.

SAPHIRS, the second setup used in this thesis at the synchrotron, couples a fluorine flow-tube reactor-based radical source with a double-imaging photoelectron/photoion coincidence (i^2PEPICO) spectrometer and the synchrotron radiation. This configuration allowed for the simultaneous recording of ion yield and mass-selective photoelectron spectra at vibrational resolution for various SixCyHz radicals, offering essential insights into the vibronic structure of their cations. In this manuscript, I present experimental results encompassing SiH, Si_2, SiC, and SiCH. These studies have provided reliable photoionization energy values and information on the vibronic structures of cations and Rydberg states of the neutral species observed *via* autoionization. This work represents a first step toward understanding the chemistry of silicon within interstellar clouds.

To all those who dare to explore the unknown,

And to my family, whose unwavering support has been my guiding star on this journey of exploration.

Résumé

L'évolution de la matière dans les environnements astrophysiques, tels que le milieu interstellaire, est gouvernée par des processus chimiques complexes impliquant de nombreuses espèces stables et radicalaires en phase gazeuse. L'identification et l'étude des molécules interstellaires constituent des étapes fondamentales pour comprendre les processus chimiques dans l'espace, offrant des perspectives sur la compréhension de l'origine de la vie dans l'univers, les processus de formation des étoiles et la caractérisation des environnements interstellaires. La quête d'identification des espèces interstellaires et la construction de modèles chimiques reposent largement sur des études expérimentales en laboratoire.

Ce travail de doctorat est dédié à la génération de nouvelles données spectroscopiques de haute qualité en laboratoire pour des espèces en phase gazeuse d'intérêt astrophysique, en mettant particulièrement l'accent sur les espèces radicalaires, en utilisant des techniques de spectroscopie de photoionisation. Mes travaux peuvent être divisés en deux composantes principales :

- le premier aspect implique l'exploration d'un dispositif de source de radicaux stable et efficace pour produire des radicaux *in situ* ;

- le deuxième aspect consiste à développer et utiliser des techniques de spectroscopie de photoionisation à haute résolution permettant l'investigation de la structure (ro)vibronique des cations de radicaux.

Cette thèse documente des expériences sur le montage VULCAIM à haute résolution spectrale à l'ISMO et sur le montage SAPHIRS à moyenne résolution sur la ligne DESIRS du synchrotron SOLEIL.

L'installation VULCAIM, unique en France et l'une des trois seules au monde, possède la capacité de fournir un rayonnement laser VUV accordable à haute résolution entre 6 et 17 eV. Cette thèse met l'accent sur des développements effectués sur cet appareil unique, y compris l'introduction d'un laser OPO largement accordable pour étendre la gamme du laser VUV, l'exploration de sources de radicaux par pyrolyse et décharge électrique, et la mise en place d'un réflectron. En particulier la complémentarité d'une ligne large bande et facile d'utilisation et d'une ligne à haute résolution est unique au monde. Le couplage de la source de radicaux par pyrolyse avec le montage VULCAIM a permis d'obtenir un résultat de premier plan : la production de radicaux CH_3 excités vibrationnellement, fournissant des données de laboratoire à haute résolution *via* la spectroscopie photoélectronique PFI-ZEKE pour confirmer pour la première fois expérimentalement la détection de CH_3^+ dans l'espace. Il s'agit également de la première utilisation di-

recte d'un résultat expérimental obtenu par la spectroscopie d'ionisation pour interpréter le spectre astronomique. De plus, basé sur la technique PFI-ZEKE PES, une nouvelle méthode de spectroscopie photoélectronique appelée PRFI-ZEKE à haute résolution et à rapport signal/bruit élevé a été proposée et appliquée dans le domaine de la recherche. Une autre technique, où les ions sont détectés, appelée MATI, est également mise en œuvre sur VULCAIM. Les développements significatifs réalisés sur l'installation VULCAIM ouvrent des perspectives prometteuses pour l'avenir de la spectroscopie d'ionisation à haute résolution sur les radicaux réactifs.

SAPHIRS, le deuxième montage utilisé au cours de cette thèse au synchrotron, associe une source de radicaux basée sur un réacteur au fluor à écoulement avec un spectromètre de photoélectrons/photoions en coïncidence à double imagerie (i^{2}PEPICO) et le rayonnement synchrotron. Cette configuration a permis l'enregistrement simultané du rendement d'ion et des spectres photoélectroniques résolus vibrationnellement pour divers radicaux $Si_xC_yH_z$, offrant des informations inédites sur la structure vibronique de leurs cations. Dans ce manuscrit, je présente des résultats expérimentaux sur SiH, Si_2, SiC et SiCH. Ces études ont permis de déterminer des valeurs fiables d'énergie d'ionisation et d'obtenir des informations sur les structures vibroniques des cations et des états de Rydberg du composé neutre observés par autoionisation. Ce travail constitue un premier pas vers la compréhension de la chimie du silicium au sein des nuages interstellaires.

Acknowledgements

I would like to express my deepest gratitude to the numerous individuals who have contributed to the completion of this thesis.

The majority of the work undertaken during this PhD was at the Institut des Sciences Moléculaires d'Orsay. I extend my sincere thanks to the director of the Institut des Sciences Moléculaires d'Orsay, **Thomas PINO**, for hosting me at the institute.

I am immensely grateful to my thesis referees, **Héloïse DOSSMANN** and **Clément LAUZIN**, for their willingness to review and assess this manuscript. I also extend my appreciation to my thesis jury members, **Christian ALCARAZ**, **Géraldine FERAUD**, **Kevin HICKSON**, and **Jennifer NOBLE**, for accepting the responsibility of evaluating my work. This manuscript represents the culmination of three years of doctoral research and over four months of writing, and I am truly thankful for your time and expertise.

My deepest and most heartfelt acknowledgments go to my thesis director, **Séverine BOYE-PERONNE**, and co-director, **Bérenger GANS**. Their unwavering support and guidance have been instrumental in my academic journey. I consider myself fortunate to have had them as my supervisors. Through their mentorship, I not only learned valuable research skills but also gained insights on becoming a better individual.

Séverine has been a pillar of patience and kindness, always willing to offer her support and valuable insights, not only in research but also in life. Her warm smile has been a source of comfort for me. Her meticulous corrections and suggestions for the final version of this thesis manuscript have greatly enhanced its quality, and I am profoundly grateful for her dedication.

Bérenger's boundless energy, positivity, and passion for research have had a profound impact on my development as an experimentalist. His mentorship and guidance have been invaluable, and I cannot express my gratitude adequately. His unwavering optimism during times of experimental setbacks, his guidance during moments of confusion, and his encouragement have been truly motivating. Thank you for your immeasurable support and mentorship.

I would also like to acknowledge all the collaborators who made significant contributions to my doctoral work, with a special mention to **Jean-Christophe LOISON**, who guided several projects related to flow-tube reactions at SOLEIL and conducted theoretical calculations for most of the molecules I studied. I also want to express my

gratitude to **Gustavo GARCIA** and **Sebastian HARTWEG** for their assistance during our experiments on the DESIRS beamline at SOLEIL. I also appreciate the theoretical contributions of **Laurent COUDERT** regarding SiH_2, those of **Changala P.BRYAN** on CH_3^+, as well as those of **Jacques LIEVIN** and **Philippe HALVICK** on SiC and SiN.

During my time at ISMO, the members of the SYSTEAME team provided invaluable assistance. I extend my thanks to **Ugo Jacovella**, who often played the role of a third supervisor, for his guidance and discussions on experimental setups and proposals for new experiments involving aromatic radicals. My appreciation also goes to **Marie-Aline MARTIN** for providing experimental materials and the work on CH_3^+. The team's warm and welcoming atmosphere has made my journey all the more enjoyable, and I am grateful for their camaraderie.

I would like to acknowledge the fellow PhD students in the group, especially **Hai Linh LE**, who has been like a sister to me. We faced many challenges together during my second and third years, and I will always cherish the happy times we spent in the experimental room during long scans and our outings in Paris. I also want to express my appreciation for the companionship of **Daniel CRUZ** and **Anam FATIMA**, our "queens". I must mention **Ozan LACINBALA** and **Joffrey FREREUX** for their warm welcome during my first year.

Outside of the research group, I extend my gratitude to **Satchin SOORKIA** and **Michel BROQUIER**. My M2 internship in their group was a happy experience and Satchin's recommendation ultimately led me to my current PhD position. I also want to thank Michel for providing the chemical compound CH_3NO_2 for my experiments with CH_3, as well as lending us the voltage box for the spectrometer.

I appreciate the invaluable support from the technical service groups, particularly **Catherine LEBRIS** and **Christophe LEFUMEUX** for their assistance with lasers, including solving laser issues and installing the new OPO laser. Special thanks to **Jean-Philippe DUGAL**, **Jérome GUIGAND**, and **Hugo BAUDUIN** for their exceptional mechanical work, including the fabrication and optimization of devices for radical sources. I extend my appreciation to **Christophe CHARRIERE**, **Julien VINCENT**, **Marc ALBARET**, and **David CHARALAMPOUS** for their contributions to electronic equipment, including pulsers, grating controllers, and software programming.

Last but certainly not least, I wish to express my deepest gratitude to my family, especially my parents, who have selflessly supported all my decisions and never imposed their opinions on me. My sister has been a pillar of strength and responsibility, particularly during difficult times when our mother underwent surgery. Her dedication to accompanying our parents, as well as her understanding and support for my decisions, is truly priceless.

Thank you to each and every individual who has played a part in my academic journey and contributed to the completion of this thesis. Your support, guidance, and friendship have been invaluable.

Contents

List of Figures

List of Tables

List of Abbreviations

IE Ionization Energy. 101

AGB Asymptotic Giant Branch. 124

ALMA Atacama Large Millimeter/submillimeter Array. 20

AS Active Space. 124

ASE Amplified Spontaneous Emission. 42

BBO BaB_2O_4. 43

CASSCF Complete Active Space Self-Consistent Field. 101

CBS Complete Basis Set. 102

CW Continuous-Wave. 42

DCM 4-(Dicyanomethylene)-2-methyl-6-(4-dimethylaminostyryl)-4H-pyran. 42

DELICIOUS Dichroism and ELectron/Ion Coincidence in IOnization Using Synchrotron. 97

DESIRS Dichroïsme Et Spectroscopie par Interaction avec le Rayonnement Synchrotron. 95

FC Franck-Condon. 102

FT Fourier-Transform. 49

FWHM Full Width at Half Maximum. 106

i^{2}PEPICO double Imaging PhotoElectron PhotoIon COincidence. 97

ISM InterStellar Medium. 19

JWST James Webb Space Telescope. 19

MATI Mass-Analyzed Threshold Ionization. 25

MCP Micro-Channel Plate. 60

MRCI + Q MultiReference Configuration Interaction method with Davidson correction. 101

OPO Optical Parametric Oscillator. 38

PES PhotoElectron Spectroscopy. 26

PFI-ZEKE PES Pulsed Field Ionization-ZEro-Kinetic-Energy PhotoElectron Spectroscopy. 25

PIY PhotoIon Yield. 26

PRFI-ZEKE PES Pulsed-Ramped-Field-Ionization ZEro-Kinetic Energy PhotoElectron Spectroscopy. 34

PSD Position Sensitive Detector. 99

SAPHIRS Spectroscopie d'Agrégats PHotoIonisés par le Rayonnement Synchrotron. 96

SO Spin-Orbit. 106

SOLEIL Source Optimisée de Lumière d'Energie Intermédiaire du Laboratoire pour l'utilisation du rayonnement électromagnétique. 95

SPES Slow PhotoElectron Spectroscopy. 25

SR Scalar Relativity. 124

TOF Time-Of-Flight. 34

TPES Threshold PhotoElectron Spectroscopy. 25

UV UltraViolet. 39

VMI Velocity Map Imaging. 99

VULCAIM VUv Laser for Considering Astrophysical and Isolated Molecules. 37

VUV Vacuum UltraViolet. 25

WM Wiley-McLaren. 99

List of publications

1. O. J. Harper, **N.L. Chen**, S. Boyé-Péronne, and B. Gans, "Pulsed-ramped-field-ionization zero-kinetic-energy photoelectron spectroscopy: a methodological advance," Phys. Chem. Chem. Phys., vol. 24, no. 5, pp. 2777–2784, 2022, doi: 10.1039/D1CP04569E.

Article selected as 2021 PCCP HOT Articles, and chosen for the front cover of this PCCP issue.

2. **N.L. Chen**, B. Gans, S. Hartweg, G. A. Garcia, S. Boyé-Péronne, and J.-C. Loison, "Photoionization spectroscopy of the SiH free radical in the vacuum-ultraviolet range," J. Chem. Phys., vol. 157, no. 1, p. 14303, 2022, doi: 10.1063/5.0094863.

3. **N.L. Chen**, B. Gans, S. Hartweg, G. A. Garcia, S. Boyé-Péronne, and J.-C. Loison, "Unravelling the electronic structure of the silicon dimer using threshold photoelectron spectroscopy," Mol. Phys., Nov. 2022, doi: 10.1080/00268976.2022

4. B. Gans, J. Liévin, P. Halvick, **N.L. Chen**, S. Boyé-Péronne, S. Hartweg, G.A. Garcia, and J.-C. Loison, "Single-photon ionization of SiC in the gas phase: experimental and ab initio characterizations of SiC^+," Phys. Chem. Chem. Phys., vol. 25, no. 35, pp. 23568–23578, 2023, doi: 10.1039/D3CP02775A.

5. U. Jacovella, B. Ruscic, **N.L. Chen**, H.-L. Le, S. Boyé-Péronne, S. Hartweg, M.R. Chowdhury, G.A. Garcia, J.-C. Loison, and B. Gans, "Refining the thermochemical properties of CF, SiF, and their cations by combining photoelectron spectroscopy, quantum chemical calculations, and the Active Thermochemical Tables approach," Phys. Chem. Chem. Phys., vol. 25, no. 45, pp. 30838–30847, 2023, doi: 10.1039/D3CP04244H.

Article selected as 2023 PCCP HOT Articles, and chosen for the front cover of this PCCP issue.

6. P.B. Changala, **N.L. Chen**, H.L. Le, B. Gans, K. Steenbakkers, T. Salomon, L. Bonah, I. Schroetter, A. Canin, M.-A. Martin-Drumel, U. Jacovella, E. Dartois, S. Boyé-Péronne, C. Alcaraz, O. Asvany, S. Brünken, S. Thorwirth, S. Schlemmer, J.R. Goicoechea, G. Rouillé, A. Sidhu, R. Chown, D. Van De Putte, B. Trahin, F. Alarcón, O. Berné, E. Habart, and E. Peeters, "Astronomical CH_3^+ rovibrational assignments.A combined theoretical and experimental study validating observational findings in the d203-506 UV-irradiated protoplanetary disk," Astron. & Astrophys., vol. 680, p. A19, Dec. 2023, doi: 10.1051/0004-6361/202347765.

7. **N.L. Chen**, B. Gans, S. Boyé-Péronne, S. Hartweg, G. A. Garcia, and J.-C. Loison, "First experimental characterization of $SiCH^+$ via single-photon ionization of gas-phase SiCH," J. Chem. Phys., vol. to be submitted, 2024.

Chapter 1

Introduction

1.1 Context: spectroscopic study on interstellar molecules

In June 2023, a significant discovery in the field of astronomy captured widespread attention across both scientific circles and mainstream media. Scientists announced the groundbreaking observation of the methyl cation (CH_3^+) within a protoplanetary disk in the Orion star forming region, through the meticulous analysis of data obtained by NASA's James Webb Space Telescope (JWST).[12] The CH_3^+ molecule, simple in structure, is believed to play a pivotal role in the carbon chemistry within the InterStellar Medium (ISM), initiating the formation of more complex carbon-based molecules.[76,153,173] Thus, the observation of this species is of great importance, a significant breakthrough towards the understanding of carbon chemistry and possibly unveiling the origin of carbon-based life forms in space.

The observations of molecular species within the ISM, the region between stars in galaxies, trace its origins back to nearly a century ago. The emergence and rapid development of quantum mechanics, marked by Max Planck's revolutionary quantum hypothesis in 1900, allowed astronomers to begin their quest to identify elements within the ISM. The method employed involved a comparison of absorption lines present in stellar spectra with the laboratory spectra of known elements. In the 30s, the interpretation of new spectroscopic lines observed through telescopes led to the conclusion that the interstellar medium was not solely populated by atoms but also housed molecular species.[113,119,160]. Since then, the search for interstellar molecules and their study became a very active field of research. This not only offers exciting possibilities for exploring compounds as potential building blocks of life and gaining insights into the origins of life in the universe,[21,170] but also enables the tracing of star formation processes and characterization of interstellar environments.[21,23,36,112,142]

The systematic and comprehensive detection and study of interstellar molecules rely on collaborative efforts among astronomers, laboratory experimentalists, and modelers:

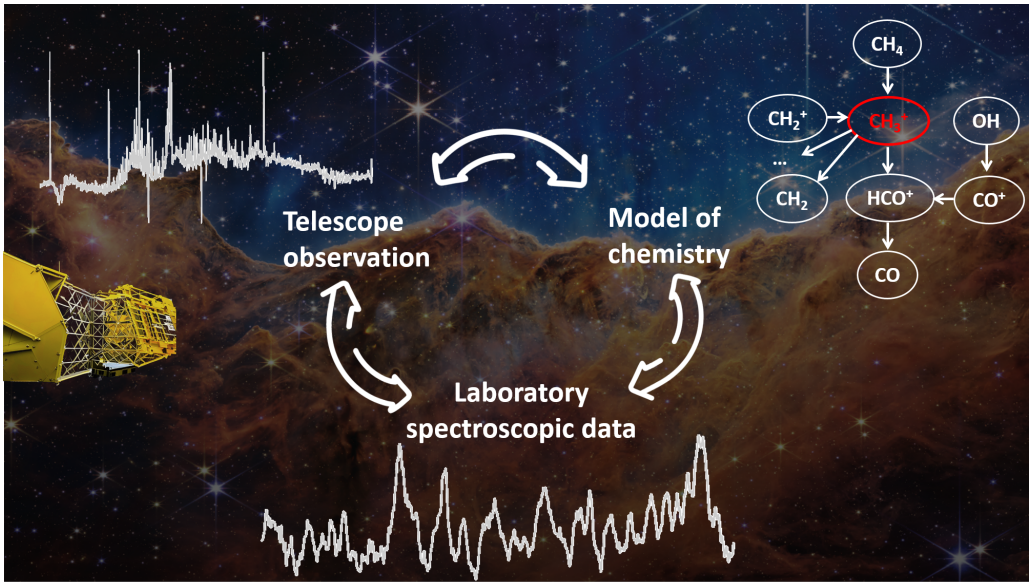

Figure 1.1: Three steps required to observe interstellar molecules and to understand the chemistry in the ISM. Laboratory spectroscopic data is indispensable for identifying interstellar species and for validating theoretical models. The example of telescope observation and that of chemistry model are extracted and adapted from Ref. 12. Credits for the background pictures: "Cosmic Cliffs" in the Carina Nebula.[5]

- Astronomers employ telescopes to capture spectral data from space;
- Laboratory researchers provide essential experimental data to substantiate the analysis of these spectra, enabling the identification of various molecular species;
- Modelers contribute by constructing intricate theoretical models, serving as frameworks to assimilate the amassed information. Additionally, these models serve to predict the presence of hitherto unobserved species in a given medium, thus providing back instructive information for astronomers and experimentalists.

The intricate interplay of these roles is illustrated in Fig. 1.1, with the observation and study of CH_3^+ serving as a tangible example.

In recent years, propelled by rapid advancements in observational techniques, astronomers have amassed an extensive amount of highly resolved spectra on interstellar molecules. The trend of this growth becomes evident in Fig. 1.2, illustrating the cumulative number of known interstellar molecules over time in tandem with the evolution of observational techniques. Since the historic detection of the first interstellar molecule, the cyano radical (CN), within the ISM in 1937[160], the study of interstellar molecules has undergone several pivotal phases of development. Landmark milestones include the inception of radio astronomy in the early 60s and the deployment of advanced telescopes like the Green Bank Telescope (GBT), the Yebes Observatory RT40m, and the Atacama Large Millimeter/submillimeter Array (ALMA) in the present century.[23,112] The trajectory of new molecule detection has experienced acceleration, escalating from an average of approximately 3.9 new molecules annually prior to 2005 to an approximate rate of 6 new molecules per year.[112] This trend is projected to gain further momentum with the

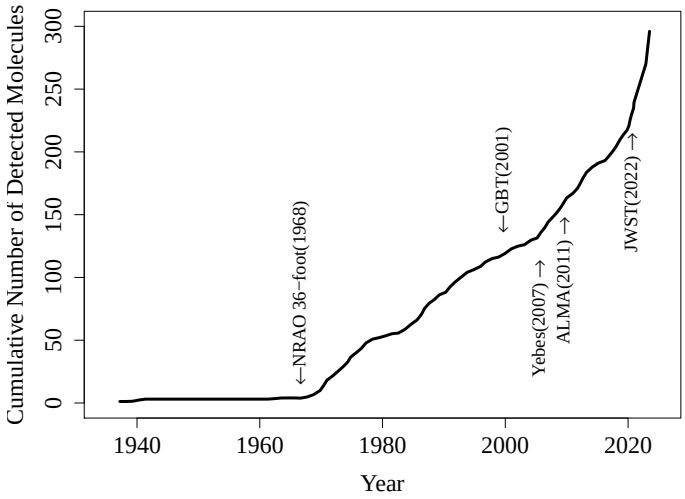

Figure 1.2: Cumulative number of known interstellar molecules over time. Figure extracted from Ref. 112 and updated with data obtained from https://cdms.astro.uni-koeln.de/classic/molecules.

recent deployment of the James Webb Space Telescope in 2022.[12,112]

Following the detection of these species, modelers started to build models to delve into the complex chemistry of compounds abundant in interstellar clouds, such as carbon,[153] sulfur,[25] and silicon.[77,120,167,179] It is important to note, however, that these models have mainly relied on thermodynamic information and analogies with other well-studied reactions, due to the limited support derived from astronomical observations and, more critically, laboratory spectroscopic data.

The large amount of high-resolution spectra furnished by astronomers and the theoretical predictions, yet to be substantiated, necessitate high-resolution laboratory spectroscopic data. A salient example illustrating this demand stems from a recent broad and high-resolution submillimeter observation of IRC+10216 using ALMA. In this observation, astronomers discovered hundreds of narrow spectral lines that could not be assigned to any known species.[23] This underscores the pressing need for rigorous and precise laboratory spectroscopic data.

In addition to the demand for high-resolution measurements, another crucial aspect concerns the laboratory production of target species. As seen in Table 1.1 which lists all the approximately 300 molecular species observed within interstellar and circumstellar media in June 2023, a significant proportion—30%—of these species are radicals or their ions. The intrinsic instability of radicals (or their ions) positions them as pivotal entities within chemical networks, often assuming the role of key intermediates in reactions.[172] This is especially relevant in the context of interstellar environments, characterized by temperatures ranging from 50 to 100 K in diffuse clouds, or at 10 K or even below in cold, dense clouds.[76] Furthermore, gas densities range between approximately 10 cm^{-3} in diffuse clouds and more than 10^5 cm^{-3} in dense regions.[76] In such conditions, the presence of radicals (or their ions) becomes even more significant. Their high reactivity, despite minimal collisions and thermal energy, may contribute in amplifying reaction efficiency. However, due to their inherently transient nature, the experimental production

and measurement of radical species are very challenging. Up to now, high-quality laboratory spectroscopic measurements of radical molecules and their ions remain scarce, in particular their high-resolution measurements. This underscores the pressing need for intensive research in this domain. Some high-resolution measurements related to radicals have been achieved using various techniques. For instance, a high-resolution (0.0045 cm^{-1}) spectroscopic measurement for the ν_2 fundamental band of NH_2 radical was performed using a Fourier transform infrared spectrometer and a fast-flow multiple-path absorption cell.[18] Two carbon-chain radicals, HC_5O and HC_7O, have been observed in the ISM based on the laboratory work using Fourier transform microwave spectroscopy of a supersonic molecular beam.[121] Additionally, high-resolution vacuum ultraviolet (VUV) photoabsorption spectra (FWHM = 0.27 cm^{-1}) were recorded for the OH radical, generated in a plasma-discharge source.[75]

Throughout my doctoral studies, I focused my work on conducting medium- and high-resolution photoionization spectroscopic measurements on radical molecules in the gas phase — particularly those holding astrophysical relevance. This endeavor can be roughly delineated into two primary facets:

1) The exploration of a stable and efficient radical source device coupled to a photoionization spectrometer.

2) The realization of high-resolution spectral measurements on targeted molecules.

The former, elucidated in Chapters 2 and 4, delves into practical considerations. As for the latter, since the photoionization spectroscopic technique forms the bedrock of this endeavor, the following section presents a general review of this method, highlighting its current state-of-the-art in high-resolution techniques.

Table 1.1: List of detected interstellar molecules sorted with increasing number of atoms. Most of them are ordered by detection year following Ref. 112. The list has been updated in June 2023 according to https://cdms.astro.uni-koeln.de/classic/molecules. Neutral radicals and their ions are highlighted in purple and orange, respectively.

2 Atoms		3 Atoms		4 Atoms		5 Atoms		6 Atoms	7 Atoms
CH	NH	H_2O	MgCN	NH_3	SiC_3	HC_3N	C_4H^-	CH_3OH	CH_3CHO
CN	SiN	HCO^+	H_3^+	H_2CO	CH_3	HCOOH	CNCHO	CH_3CN	CH_3CCH
CH^+	SO^+	HCN	SiCN	HNCO	C_3N^-	CH_2NH	HNCNH	NH_2CHO	CH_3NH_2
OH	CO^+	OCS	AlNC	H_2CS	PH_3	NH_2CN	CH_3O	CH_3SH	CH_2CHCN
CO	HF	HNC	SiNC	C_2H_2	HCNO	H_2CCO	NH_3D^+	C_2H_4	HC_5N
H_2	N_2	H_2S	HCP	C_3N	HOCN	C_4H	H_2NCO^+	C_5H	C_6H
SiO	CF^+	N_2H^+	CCP	HNCS	HSCN	SiH_4	$NCCNH^+$	CH_3NC	c-C_2H_4O
CS	PO	C_2H	AlOH	$HOCO^+$	HOOH	c-C_3H_2	CH_3Cl	HC_2CHO	CH_2CHOH
SO	O_2	SO_2	H_2O^+	C_3O	l-C_3H^+	CH_2CN	MgC_3N	H_2C_4	C_6H^-
SiS	AlO	HCO	H_2Cl^+	l-C_3H	HMgNC	C_5	HC_3O^+	C_5S	CH_3NCO
NS	CN^-	HNO	KCN	$HCNH^+$	HCCO	SiC_4	NH_2OH	HC_3NH^+	HC_5O
C_2	OH^+	HCS^+	FeCN	H_3O^+	CNCN	H_2CCC	HC_3S^+	C_5N	$HOCH_2CN$
NO	SH^+	HOC^+	HO_2	C_3S	HONO	CH_4	H_2CCS	HC_4H	HC_4NC
HCl	HCl^+	SiC_2	TiO_2	c-C_3H	MgCCH	HCCNC	C_4S	HC_4N	HC_3HNH
NaCl	SH	C_2S	CCN	HC_2N	HCCS	HNCCC	CHOSH	c-H_2C_3O	c-C_3HCCH
AlCl	TiO	C_3	SiCSi	H_2CN	HNCN	H_2COH^+	CHSCN	CH_2CNH	CH_2CHCN
KCl	ArH^+	CO_2	S_2H		H_2NC		HCCCO	C_5N^-	l-H_2C_5
AlF	NS^+	CH_2	HCS		$HCCS^+$		NaCCCN	HNCHCN	MgC_5N
PN	HeH^+	C_2O	HSC				MgC_3N^+	SiH_3CN	CH_2C_3N
SiC	PO^+	MgNC	NCO					MgC_4H	NC_4NH^+
CP		NH_2	CaNC					CH_3CO^+	MgC_5N^+
		NaCN	NCS					H_2CCCS	
		N_2O	MgC_2					CH_2CCH	
			HSO					HCCCHS	
								C_5H^+	
								$HCCNCH^+$	
								c-C_3C_2H	
								HC_4S	
								$HMgC_3N$	
								MgC_4H^+	

8 Atoms	9 Atoms	10 Atoms	11 Atoms	12 Atoms	13 Atoms	> 13 Atoms
$HCOOCH_3$	CH_3OCH_3	CH_3COCH_3	HC_9N	C_6H_6	C_6H_5CN	1-$C_{10}H_7CN$
CH_3C_3N	CH_3CH_2OH	$HOCH_2CH_2OH$	CH_3C_6H	n-C_3H_7CN	$HC_{11}N$	2-$C_{10}H_7CN$
C_7H	CH_3CH_2CN	CH_3CH_2CHO	C_2H_5OCHO	i-C_3H_7CN	1-c-C_5H_5CCH	C_9H_8
CH_3COOH	HC_7N	CH_3C_5N	CH_3COOCH_3	1-C_5H_5CN	2-c-C_5H_5CCH	C_{60}
H_2C_6	CH_3C_4H	CH_3CHCH_2O	CH_3COCH_2OH	2-C_5H_5CN	c-$C_5H_4CCH_2$	C_{60}^+
CH_2OHCHO	C_8H	CH_3CH_2OH	C_5H_6	$C_2H_5OCH_3$		C_{70}
HC_6H	CH_3CONH_2	c-C_6H_4	$HOCH_2CH_2NH_2$	1-c-C_5H_5CN		2-C_9H_7CN
CH_2CHCHO	C_8H^-	H_2CCCHC_3N	H_2CCCHC_4H	n-C_3H_7OH		
CH_2CCHCN	CH_2CHCH_3	C_2H_5NCO	$C_{10}H^-$	i-C_3H_7OH		
NH_2CH_2CN	CH_3CH_2SH	HC_7NH^+				
CH_3CHNH	HC_7O	$CH_3CHCHCN$				
CH_3SiH_3	CH_3NHCHO	$CH_3C(CN)CH_2$				
NH_2CONH_2	$H_2CCCHCCH$	CH_2CHCH_2CN				
$HCCCH_2CN$	HCCCHCHCN					
CH_2CHCCH	H_2CCHC_3N					
HC_5NH^+						
MgC_6H						
$C_2H_3NH_2$						
$(CHOH)_2$						
$HC_2(H)C_4$						
C_7N^-						
CH_3CHCO						
MgC_6H^+						

1.2 Review of photoionization spectroscopy: principles and state of art

Photoionization spectroscopy, the main activity of my doctoral project, serves as a powerful experimental tool for investigating the cationic structures of isolated molecules by probing their photoionization processes upon irradiation. This spectroscopy stands distinct from absorption and emission (optical) spectroscopies conducted on cations, presenting various notable advantages:

1. Spectroscopic measurements of cationic structures are performed using neutral parent molecules. This eliminates the potential concentration losses arising from the electrostatic repulsion among cations. Unlike the approach involving optical measurements on cations, which often necessitates an ion trap to address this issue, the use of neutral molecules avoids such concerns.

2. Neutral molecules can be cooled *via* supersonic expansion before ionization measurements. This cooling process reduces spectral congestion that arises from the thermal population of initial neutral states. In contrast, the optical spectroscopic approach generates ions within a hot plasma, typically necessitating the use of a cold (cryogenic) ion trap to efficiently manage the cooling process.

3. Photoionization transitions obey different selection rules compared to optical spectroscopy, granting access to many rovibronic states of the cation with different spin multiplicities for instance. Thus it offers an alternative for studying states that are inaccessible *via* absorption or emission spectroscopy.

4. Beyond providing insight into quantum aspects such as rovibronic structures and molecular parameters, photoionization spectroscopy yields valuable thermodynamical data, including ionization energies. These attributes stem from the inherent nature of the ionization process.

This section aims to develop the principles and applications of various photoionization spectroscopic techniques. It will describe Threshold PhotoElectron Spectroscopy (TPES), along with the Slow PhotoElectron Spectroscopy (SPES) technique, as well as more spectrally resolved methodologies, notably the Pulsed Field Ionization-ZEro-Kinetic-Energy PhotoElectron Spectroscopy (PFI-ZEKE PES) technique and its derivative technique Mass-Analyzed Threshold Ionization (MATI). All these advanced techniques have been used during the thesis to explore cationic structures of isolated molecules. In addition, a technique is further developed based on the PFI-ZEKE PES method, showing an excellent improvement of both the spectral resolution and the signal-to noise ratio, which will be described in Chapter 3.

1.2.1 PES at a fixed photon energy

Photoionization spectroscopy involves neutral molecules in the gas phase irradiated by Vacuum UltraViolet (VUV) radiation. With the photon energy exceeding the threshold ionization energy of the molecular species, the ionization occurs. The energy carried by one photon is transformed into the resonant transition energy between the cationic state (X^+) and the neutral state (X, usually the ground state in cooled molecules), as well as the kinetic energy associated with the cation-electron system. Given the ion's significantly greater mass and negligible kinetic energy,

the kinetic energy is approximated to that of the emitted photoelectron. This leads to the following equation, which plays a crucial role in photoionization spectroscopy:

$$h\nu = E_{\mathrm{ion}}(\mathrm{X}^+, \mathrm{X}) + E_{\mathrm{k,tot}} \approx E_{\mathrm{ion}}(\mathrm{X}^+, \mathrm{X}) + E_{\mathrm{k,e^-}}.$$

Hence, at a fixed photon energy ($h\nu$), by monitoring the kinetic energy distribution of the photoelectron ($E_{\mathrm{k,e^-}}$), we can extract insights into the cationic energy levels relative to those of the neutral state X ($E_{\mathrm{ion}}(\mathrm{X}^+, \mathrm{X})$). This is the principle of PhotoElectron Spectroscopy (PES) at a fixed photon energy, as illustrated in Fig.1.3.

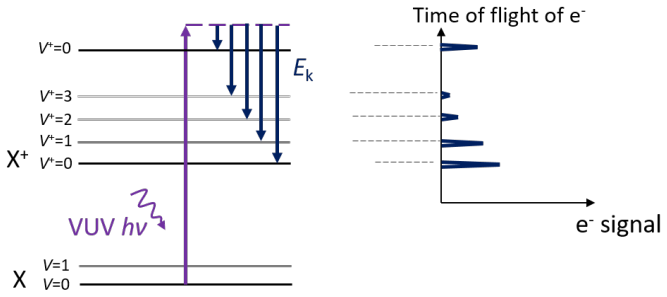

Figure 1.3: Scheme of the photoelectron spectroscopy at a fixed radiation energy

PES at a fixed radiation energy was popular in the early decades of the technical development, starting from the 50s, using radiation sources such as the He I lamp. This method has undergone improvements over time, but the spectral resolution remains limited to a few meV.[7] The main obstacle to achieving higher resolution in this approach is the challenge of precisely discriminating the kinetic energy of photoelectrons. The spectral resolution determines the accessible structure of cations. Although the resolution of a few meV proved sufficient for investigating vibrational structures, it fells short in resolving the rotational structure of polyatomic molecules. Notably, this technique can serve as a valuable detection tool for real-time monitoring of chemical reaction systems. In such cases, the high resolution is less necessary for species identification and it can satisfy shorter acquisition times without the need of scans. A notable instance involves the Southampton group's[49] successful use of PES at a fixed HeI photon energy (21.22 eV) to detect a chemically significant reaction (Cl_2 + CH_3S CH_3). Through calculations, they identified the intermediate $(CH_3)_2SCl_2$ for the first time.[49]

1.2.2 PIY spectroscopy

With the advent of tunable radiation sources like synchrotron radiation, the PhotoIon Yield (PIY) spectroscopy emerged as a significant development. This technique focuses on quantifying ionization yields in relation to photon energy, see left panel of Fig. 1.4. The signal in PIY represents the accumulation of ion/e^- quantities produced by all accessible ionization channels under irradiation at a specific photon energy. As photon energy is tuned from low to high values, the opening of new ionization channels at resonant energies provides access to higher cationic states. This

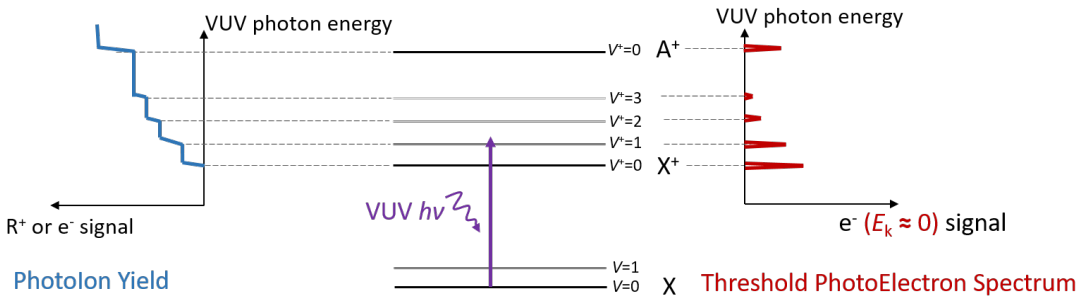

Figure 1.4: Scheme of two types of photoionization spectroscopy with tunable radiation: photoion yield (PIY) and threshold photoelectron spectroscopy (TPES)

results in a distinct 'step-like' increase in the ion/electron quantity signal. The position of these step features provide information about cationic energy levels, and their intensities about ionization cross-sections.

A notable advantage of measuring ion signals lies in the inherent mass-selectivity of the spectrum. This mass-selectivity proves particularly beneficial when dealing with experimental mixtures of compounds. Besides, the spectral resolution is solely determined by the bandwidth of the radiation. However, the step features in PIY are not always distinct due to the inherent molecular structures (multiple vibrational modes, rotational structures, etc.) or the presence of autoionization resonances. Consequently, PIY was used as a supplementary tool during my thesis, offering preliminary insights into energy levels and autoionization processes.

1.2.3 TPES

Threshold PhotoElectron Spectroscopy (TPES) involves scanning the photon energy while selectively detecting photoelectrons possessing zero kinetic energy, commonly referred to as threshold photoelectrons. In this technique, ionization energies associated with cationic states relative to the neutral ground state are directly extracted through photoelectron signals, as illustrated in the right panel of Fig. 1.4.

TPES effectively addresses the resolution limitations tied to the measurement of PES at a fixed photon energy (see Section 1.2.1). The primary challenge in TPES lies in accurately differentiating threshold photoelectrons from fast electrons. The initial accomplishment of this distinction was achieved through a steradiancy analyzer.[8,131] However, the precision in determining zero kinetic energy electrons is still constrained by factors including geometric design and time-of-flight resolution.[53,118,123] Subsequent advancements in design have led to an enhancement in the spectral resolution of TPES to approximately 2-3 meV (equivalent to several tens of wavenumbers), thereby enabling the investigation of molecular vibronic structures. Nonetheless, at this resolution, the rotational structure of most molecules, except simple diatomic ones like H_2 or D_2, remains unresolved.

Despite this limitation, the fundamental notion of TPES, which revolves around detecting threshold photoelectrons, remains profound in the field. This idea has paved the way for subsequent innovations in PES techniques, such as Slow PhotoElectron Spectroscopy (SPES) as well as ZEro-Kinetic-Energy PES (ZEKE-PES) and related methodologies.

1.2.4 SPES

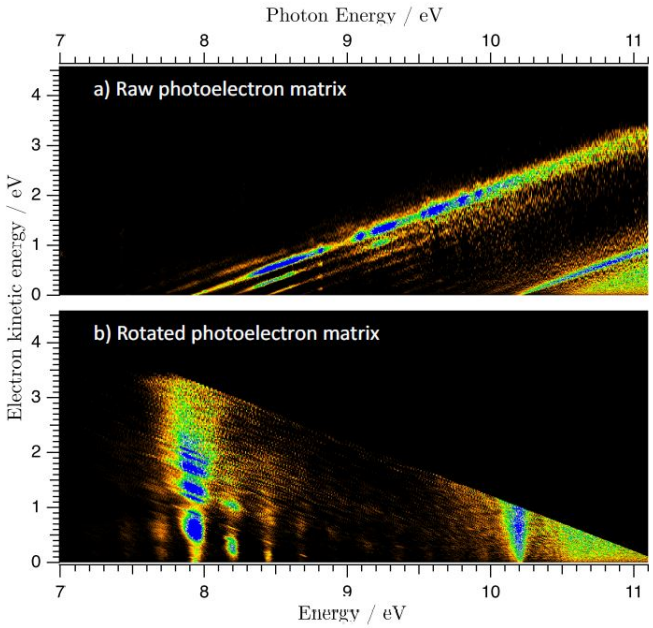

Figure 1.5: Raw photoelectron matrix (panel a)) and rotated matrix (panel b)) of the SiH radical from Ref. 26.

Slow PhotoElectron Spectroscopy (SPES), a technique derived from TPES, aims to increase the signal-to-noise ratio within the spectrum by not only counting threshold electrons but also a portion of slow electrons possessing exceedingly low kinetic energy. This increase necessitates data acquisition encompassing both photoelectron signals registered under tunable radiation and the corresponding kinetic energies of the photoelectrons.

The acquired data is then represented in the form of a "photoelectron matrix." This matrix represents the intensity of the signal (aligned along the z axis) as a function of both the electron's kinetic energy (aligned along the y axis) and the photon energy (aligned along the x axis). Each photoelectron originating from the same ionization channel appears as a distinct diagonal line within the matrix. In Fig. 1.5, an illustrative photoelectron matrix for the SiH radical ($m/z = 29$) is depicted in panel a). To enhance the signal-to-noise ratio in the ultimate photoelectron spectrum while retaining a satisfactory spectral resolution, a data treatment technique is applied to the two-dimensional matrix. Firstly, the matrix is rotated at the zero-kinetic-energy point to orient the diagonal line vertically. Following this, a specific kinetic energy interval near the zero-kinetic-energy point is chosen. Integration across this selected range yields the desired photoelectron spectrum, which exhibits an improved signal-to-noise ratio when contrasted with traditional TPES. This enhancement proves particularly advantageous when examining samples characterized by low photoionization cross-sections or when working within constraints of limited measurement time. However, it is important to acknowledge that the incorporation of slow electrons may slightly compromise the overall spectral resolution, a trade-off that should be carefully balanced with the signal-to-noise ratio considerations.

In the course of my thesis, SPES is employed extensively for experimental investigations at SOLEIL. The acquired

experimental spectra and analysis will be comprehensively introduced in Chapter 5 of this work.

1.2.5 ZEKE PES

The technique of ZEro-Kinetic-Energy (ZEKE) photoelectron spectroscopy was introduced by Muller-Dethlefs and colleagues in 1984.[122,123] This technique significantly enhanced the discrimination between zero-kinetic-energy electrons and slow electrons by using pulsed radiation and a delayed pulsed-electric-field extraction. By introducing a time delay in the extraction field, fast electrons can be effectively eliminated and the time-of-flight (TOF) of slow electrons and threshold electrons are more clearly discerned.

In subsequent studies, researchers uncovered the existence of long-lived Rydberg state molecules that could survive extraction times of several tens of microseconds. These Rydberg state molecules could be ionized by the extraction field through the Stark effect and directed towards the detector. Consequently, their associated ejected electrons became indistinguishable from photoionized threshold electrons. Notably, in experiments with stray fields, the stray field could sweep away the photon-ionized threshold electrons, leaving only the electrons from Rydberg molecules ionized by the pulsed electric field. This phenomenon led to spectral inaccuracy following the Stark shift relation, as observed in the ZEKE-PES measurement of NO, conducted by Muller-Dethlefs *et al.*[122,138]

The discovery of these phenomena paved the way for the development of new methods based on the ionization of high Rydberg state molecules using electric fields. Two notable examples of such methods are Pulsed Field Ionization-ZEKE PES (PFI-ZEKE PES), proposed by Muller-Dethlefs and Schlag[122] at the end of the last century, and Mass-Analyzed Threshold Ionization (MATI) spectroscopy.[186] Further insights into these methods will be provided in the subsequent sections.

1.2.6 PFI-ZEKE PES

One distinguishing characteristic of Pulsed-Ramped-Field-Ionization ZEro-Kinetic Energy PhotoElectron Spectroscopy (PFI-ZEKE PES) compared to the previously mentioned methods, which investigate cationic states through direct photoionization processes, is its approach to obtaining the threshold photoelectron. In PFI-ZEKE PES, the threshold photoelectron is not acquired through direct photoionization; instead, it is generated by a pulsed electric field that is introduced with a delay time after the photoexcitation to a high-n (principal quantum number) Rydberg state. This process is depicted in Fig. 1.6.

Consequently, even though the photoelectron signal is still monitored as a function of the wavenumber of the tunable radiation, it is important to bear in mind that the energy of the spectral signals obtained corresponds to the detected high Rydberg states. The high Rydberg states with typically $n \geq 200$ are usually only a few wavenumbers below the corresponding cationic states. To obtain the true cationic energy levels, a minor correction for the ionization energy shift (ΔIP) induced by the electric field is necessary, which is described by the formula for the Stark

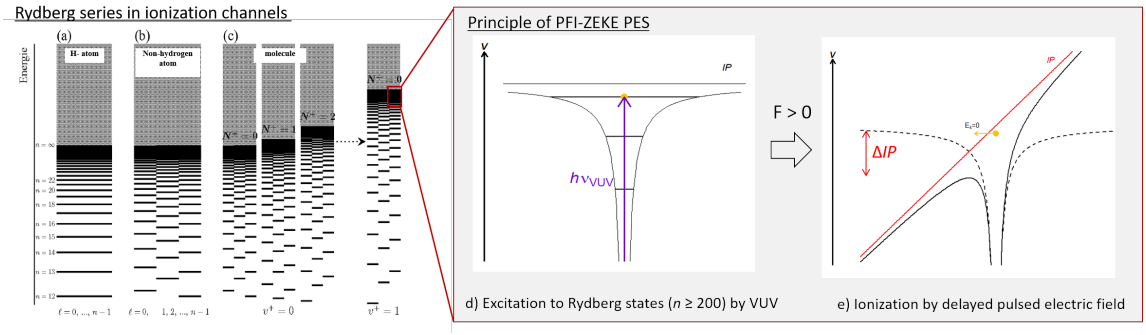

Figure 1.6: Left extracted from Ref. 116: Rydberg series in (a) the H-atom, (b) a nonhydrogenic atom, and (c) a molecule. Each horizontal line in (c) represents an l state as in (b); right: simplified scheme to depict the process of the field ionization of high molecular Rydberg states. The potential well is drawn to represent the binding energy of the excited electron in the molecule to show its variance under electric field. More details shown in text.

effect:

$$\Delta IP = -A\sqrt{|F|} \tag{1.1}$$

Here, A represents a constant, and F denotes the electric field strength.

One key advantage of the PFI-ZEKE PES technique is its remarkable spectral resolution. In contrast to TPES, where the spectral resolution is constrained by the challenges associated with the determination of zero-kinetic-energy electrons, PFI-ZEKE PES introduces an improved energetic selectivity through its delayed pulsed-field ionization process. The spectral resolution is thereby typically improved by at least one order of magnitude (a few wavenumbers). Moreover, PFI-ZEKE PES minimizes the influence of stray fields in the experimental setting. Stray fields can disrupt measurements in TPES by potentially causing the premature escape of zero-kinetic-energy electrons before the extraction pulse. Although stray fields can still introduce some imperfections in spectral measurements within PFI-ZEKE PES, such as spectral distortions or the broadening of spectral lines, their impact is comparatively reduced with respect to TPES.

The formula 1.1 showing the Stark effect on the ionization potential results from the complex quantum mechanism describing the interaction between electric fields and Rydberg states. To gain a more comprehensive understanding of the underlying principle of PFI-ZEKE PES and to be able to design electric field sequences that can further improve the spectral resolution, a profound quantum understanding of this mechanism is imperative. As demonstrated in Fig. 1.7, the interaction between an electric field and a n Rydberg state causes it to split into n Stark

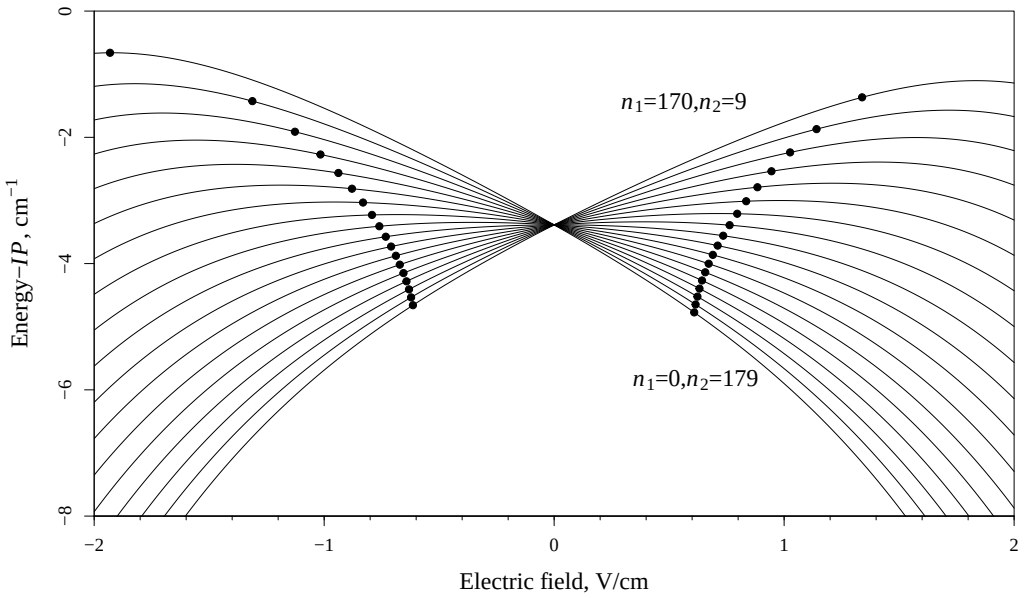

Figure 1.7: Simulated lifting of degeneracy in a Rydberg state due to the Stark effect. Illustrated using an instance where the principal and magnetic quantum numbers of the Rydberg state, n and m, are 180 and 0, respectively. The black dots highlight the field thresholds that correspond to Stark states exhibiting sufficiently high ionization rates for detection.

manifolds. The formula for fourth-order Stark energies is given by:[83]

$$
\begin{aligned}
E(n,m,n_1,n_2,F) = &-\frac{1}{2n_2} \\
&+\frac{3}{2}n(n_1-n_2)\boldsymbol{F} \\
&-\frac{1}{16}n^4\left[17n^2-3(n_1-n_2)^2-9m^2+19\right]\boldsymbol{F}^2 \\
&+\frac{3}{32}n^7(n_1-n_2)\left[23n^2-(n_1-n_2)^2-11m^2+39\right]\boldsymbol{F}^3 \\
&-\frac{1}{1024}n^{10}\left[5487n^4+35182n^2-1134m^2(n_1-n_2)^2+1806n^2(n_1-n_2)^2-3402n^2m^2\right. \\
&\left.+147(n_1-n_2)^4-549m^4+5754(n_1-n_2)^2-8622m^2+16211)\right]\boldsymbol{F}^4
\end{aligned}
$$

Here, n_1 and n_2 represent the parabolic quantum numbers, n and m denote the principal and magnetic quantum numbers, respectively, and F is the electric field strength. The calculated Stark energy is given in atomic units. Those Stark states are classified as red- and blue-shifted, based on whether their energy is lower or higher compared to the field-free state. Red-shifted states are situated closer to the left side of the potential well illustrated in e) of Fig. 1.6 and exhibit a higher probability of ionization, while blue-shifted states exhibit the opposite behavior. This ionization probability can be quantitatively described by the ionization rate Γ, which represents the number of ionization events

per unit time. It can be estimated using the fourth-order calculated energies and is given by:[83]

$$\Gamma = \frac{(4R^{'})^{2n_2+m+1}}{n^3 n_2!(n_2+m)!}\exp\{-\frac{2}{3}R^{'} + \frac{1}{4}n^3F(34n_2^2 + 34n_2m + 46n_2 + 7m^2 + 23m + \frac{53}{3})\}$$

where

$$R^{'} = (-2E)^{3/2}/F$$

Only those Stark states with sufficiently high ionization rates, ensuring that ionization occurs rapidly compared to the experimental time scale, can be detected. The black dots highlighted in Fig. 1.7 indicate the field strengths at which the Stark states exhibit an ionization rate of 10^{-7} s^{-1}, which is a common rate limit required in these types of experiments.[83]

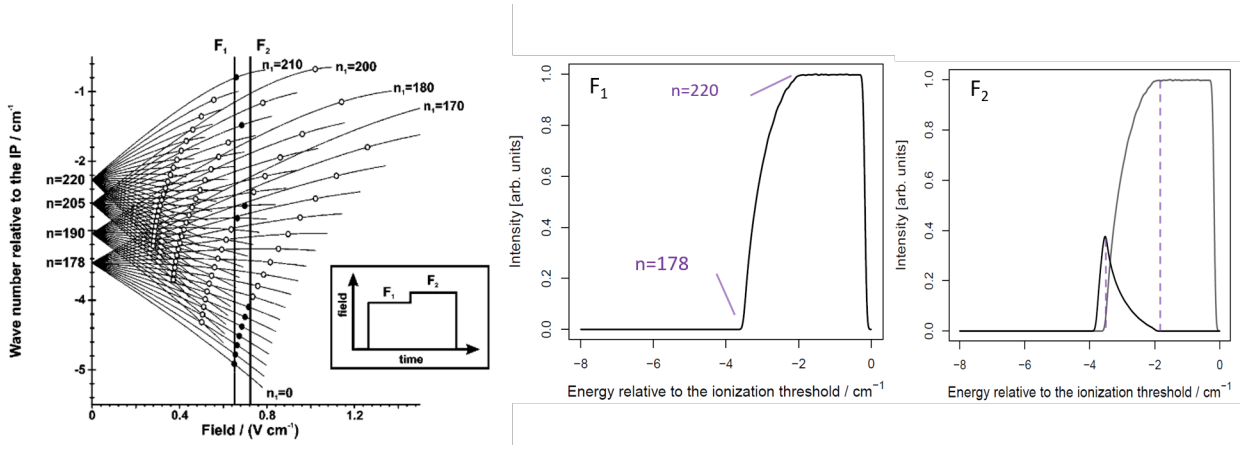

Figure 1.8: Demonstration of the field ionization of high Rydberg states with the sequence of two successive pulses of the same polarity (F_1 and F_2), extracted from Ref. 83, and the simulated spectra obtained respectively by these two pulses.

For a given value of n, red-shifted Stark states ionize at lower field strengths compared to blue-shifted ones. This different (asymmetric) threshold field behavior for red- and blue-shifted Stark states implies that a single field strength cannot fully ionize a specific n Rydberg state to obtain zero-kinetic energy photoelectrons. In other words, a specific field strength will always ionize a mixture of different n Rydberg states. To selectively ionize a subset of Rydberg states with a limited range of n values, a sequence of electric field pulses is applied in practice. Fig. 1.8 provides a simple example of PFI-ZEKE PES conducted with a sequence of two electric field strengths, F_1 and F_2. At $F_1 =$ 650 mV/cm, the Stark manifolds stemming from the Rydberg states with $n \geq 220$ are purely ionized; those from lower Rydberg states until $n = 178$ are partially ionized. The simulated spectra obtained by F_1 and $F_2 =$ 760 mV/cm are depicted. Notably, the spectral resolution obtained with the second field strength, F_2, is significantly higher than that acquired with a single field strength, F_1. The amplitude difference between F_1 and F_2 acts as a pivotal factor in the selectivity of ionized Rydberg components, consequently determining the spectral resolution of the technique.

However, even the infinitesimal amplitude pulse ionizes a mixture of Rydberg states with different n values, lead-

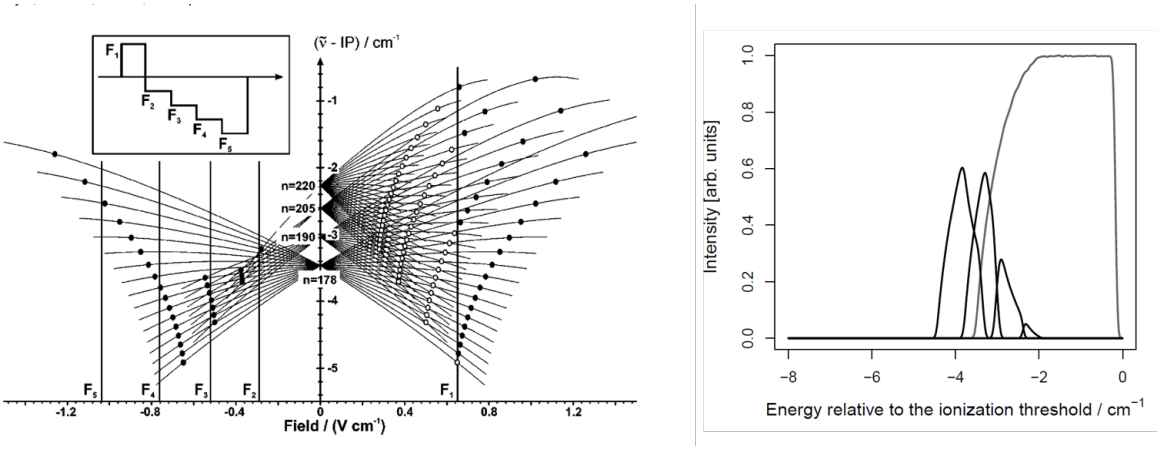

Figure 1.9: Demonstration of the field ionization of high Rydberg states with the sequence of five pulses with inversion of polarity after the first pulse, figure extracted from Ref. 83, and the simulated spectra corresponding to each pulse.

ing to a resolution estimated to $2.3\sqrt{F}$ by Hollenstein.[83] This establishes the ultimate resolution limitation achievable through PFI-ZEKE photoelectron spectroscopy when employing electric sequences of this nature (*i.e.*, a series of electric fields with the same polarity).

To overcome this resolution constraint and further enhance spectral accuracy, the use of electric pulses with reversed polarity has been proposed.[83] This concept is rooted in the phenomenon known as Stark inversion, which involves the permutation of the parabolic quantum numbers n_1 and n_2 when the polarity of the electric field is quickly reversed. An example of PFI-ZEKE PES using electric fields with opposite polarity from Ref. 83 is illustrated in Fig. 1.9, alongside the corresponding simulated spectra. The electric field sequence consists of a positive prepulse ($F_1 = 0.65$ mV/cm) followed by four negative electric field strengths, F_2 to F_5, set at -0.3, -0.5, -0.76, and -1.04 mV/cm.

As above, the first field F_1 partially ionizes the Stark series of a given n Rydberg state, spanning n values from 220 to 178. Subsequently, under the effect of F_2 with an opposite polarity, the remaining Stark states characterized by higher n_1 values, which remain un-ionized, can be transformed into states characterized by smaller n_1 values. Here it is imperative to underscore the importance of avoiding the randomization of parabolic quantum numbers near zero field, ensuring a distinct inversion of the parameter k ($k = n_1 - n_2$). Through the application of successive pulses with opposite polarities to F_1 and with smaller magnitudes than F_1, it becomes possible to further selectively ionize all non-ionized Stark states originating from the Rydberg state that was partially ionized by F_1. This precise selective ionization leads to a higher spectral resolution.

Employing the above mentioned principles, Hollenstein *et al.* achieved exceptional spectral resolutions of 0.06 and 0.055 cm^{-1} in recording PFI-ZEKE photoelectron spectra of argon and nitrogen, respectively, using a sequence composed of a prepulse of +166 mV/cm, followed by successive negative pulses ranging from -75 mV/cm to -161 mV/cm with steps of -8.5 mV/cm.[83] This impressive accomplishment underscores the promising potential of this technique in probing the rovibronic structure of molecules. Nevertheless, while this approach does enhance resolution, it is

important to acknowledge its trade-off with sensitivity. In this thesis, we will introduce a further advancement of this technique, known as Pulsed-Ramped-Field-Ionization ZEro-Kinetic Energy PhotoElectron Spectroscopy (PRFI-ZEKE PES), which allows for both high resolution and a high signal-to-noise ratio, as discussed in Chapter 3.

1.2.7 MATI spectroscopy

Mass-Analyzed Threshold Ionization (MATI) spectroscopy, introduced as a variant of PFI-ZEKE spectroscopy, was initially proposed by Zhu and Johnson[186] in 1991 and further developed by Dessent *et al.*[43] in 1999. Analogous to PFI-ZEKE spectroscopy, MATI spectroscopy involves the field ionization of Rydberg states subsequent to their excitation through irradiation. This approach capitalizes on the unique ability to discriminate between field-ionization at the threshold level and photon-ionization above threshold by the ionization process. This stands in contrast to conventional TPES techniques, which rely on selectively measuring photoelectrons after the ionization. Thus, the field-ionization process can select not only threshold photoelectrons but also the corresponding ions. In essence, PFI-ZEKE PES detects Rydberg electrons, whereas MATI spectroscopy focuses on the corresponding Rydberg ionic cores. This fundamental principle underscores the basis of MATI spectroscopy.

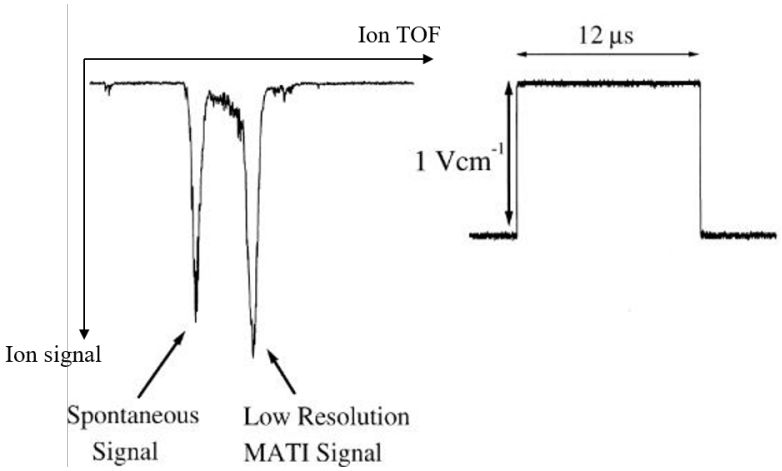

Figure 1.10: Typical pulse detection scheme and resulting ion TOF spectrum in MATI, figure extracted and adapted from Ref. 43. The pulse scheme displays only the small-voltage prepulse; the high voltage pulse of 290 V/cm, applied 3 ms after, is not shown in the scheme.

In a typical MATI experiment, a two-step voltage pulse sequence is commonly employed. The purpose of the small-voltage prepulse is to select ions resulting from direct photoionization (prompt ions) or field-ionization of very high Rydberg states, known as spontaneous ions, from the excited Rydberg neutrals. Following this, a high-voltage pulse is applied to initiate the field-ionization process of the Rydberg molecules, generating MATI ions. Simultaneously, this high-voltage pulse serves to extract all ions, including both MATI ions and spontaneous ions, towards the detector. Consequently, two Time-Of-Flight (TOF) ion signals are simultaneously detected, allowing the recording of both a photoion yield spectrum and a MATI spectrum. Fig. 1.10 displays a typical pulse scheme and resulting ion

TOF spectrum. The dispersion of the two TOF ion signals is governed by a variety of parameters such as the amplitudes and time durations of the applied pulses. It is important to note that due to the significantly larger mass of ions compared to electrons, MATI necessitates the application of larger and longer separation fields. These factors, while essential for the ionization process, can lead to a a compromise between separation and spectral resolution. Consequently, MATI spectroscopy generally exhibits a reduced spectral resolution in comparison to PFI-ZEKE spectroscopy. Notably, an evident advantage of MATI over PFI-ZEKE PES is its mass-selectivity, similar to PhotoIon Yield (PIY) spectroscopy. This attribute enhances the capability of MATI in analyzing a complex molecular system.

During the course of my thesis work, we successfully implemented MATI spectroscopy using our VULCAIM setup. We incorporated an advanced approach developed by Dessent *et al.*[43] to achieve higher spectral resolution, which will be detailed in Chapter 3.

Chapter 2

Experimental setup VULCAIM based on VUV laser

Radiation sources in the VUV range, at wavelengths between 200 and 60 nm (6-20 eV), are fundamental tools to study molecular photoionization, photodissociation and dissociative ionization,[143] as the VUV domain covers the spectral region of the bond energies of all molecules and the ionization energies of most materials.[34] However, the lack of bright, efficient and tunable VUV radiation sources has been a limit for a long time in this field. The development of modern synchrotron radiation facilities brought a huge success in the production of high-quality VUV radiation that is simultaneously intense, widely tunable, spectrally narrow and of high duty cycle.[129] Nevertheless, the synchrotron radiation source is still limited by its rarity and the high cost. In addition, along with the call for higher spectral resolution radiation to study rotational structure of small molecules and vibrational structure of large molecules, the synchrotron VUV light with a typical bandwidth of several meV is insufficient. The production of a VUV laser source based on two-photon resonance-enhanced four-wave mixing in rare gases as nonlinear medium is able to compensate the inconvenience of synchrotron sources and to offer higher spectral resolution. At ISMO, a laser system capable of generating high-resolution tunable VUV radiation was built in 2018. Its coupling to the photoionization experiment was completed in 2019, as a part of Oliver Harper's PhD project.[69] The setup is named "VULCAIM", which stands for VUv Laser for Considering Astrophysical and Isolated Molecules (VULCAIM), designed to perform high-resolution VUV spectroscopic experiments on gas-phase molecules with astrophysical interests.

During my own PhD research, I continued to develop the setup in several ways to extend its versatility. In this chapter, I will provide a general overview of the setup (see Fig. 2.1), and then delve into the detail of the laser setup system (Section 2.2), the gas-phase molecular chamber (Section 2.3) and the photoionization spectrometer (Section 2.4). While the general plan of the setup has remained substantially unchanged and most schemes of it have been already detailed in Oliver Harper's thesis, I will specifically highlight the recent advances. These include the introduc-

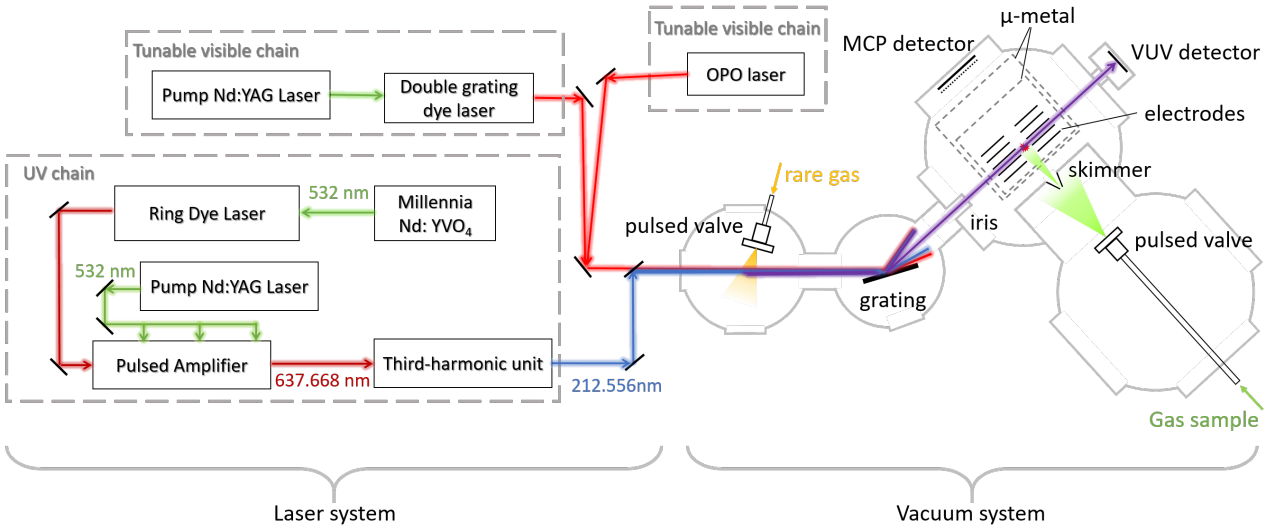

Figure 2.1: Overview of VULCAIM setup, which is constituted by the laser system and the vacuum system. The laser system consists of a high-resolution UV laser chain and two tunable visible laser chains. By selectively choosing one of the visible laser chains to couple with the UV line, it enables to generate VUV laser with either high resolution or a broad tunable range, catering to different experimental requirements. The vacuum system is composed of a VUV generation stage followed by a purification stage, a molecular chamber and a photoionization spectrometer chamber. The wavelength values marked after the ring dye laser correspond to the required ones for the Kr(I) resonance. See more details in the text.

tion of a new broadly-tunable Optical Parametric Oscillator (OPO) laser coupled to the VUV laser generation system, discussed in Section 2.2, the development of radical sources, discussed in section 2.3, as well as the implementation of the new Reflectron mass spectrometer, discussed in Section 2.4.

2.1 Overview of the VULCAIM setup

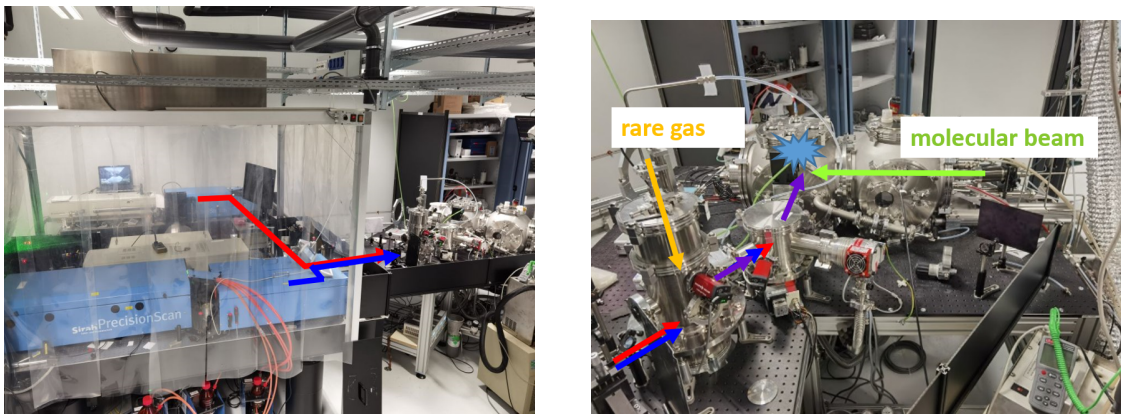

(a) UV and high-resolution visible laser chains

(b) vacuum chambers

Figure 2.2: Photos of the VULCAIM setup.

Figure 2.1 presents an overview of the VULCAIM setup, which is composed of three parts: a VUV generation

source, a molecular source as well as a photoionization spectrometer. The laser system and the vacuum chambers are depicted in the two pictures of Figure 2.2. The laser system encompasses various nanosecond-pulsed lasers operating at 20 Hz, including a high-resolution UV laser chain and two tunable visible laser chains. The laser system coupled with the first two stages (four-wave mixing stage and monochromator stage) in the vacuum system allows to generate the VUV laser and to perform its spectral purification. The two tunable visible lines enable the generation of VUV laser with either a high resolution and limited tunability range (achieved with the double-grating dye laser), or a broad tunable range with medium spectral resolution (achieved with the OPO laser). In the remaining two vacuum chambers, a molecular beam is generated, skimmed and then intersects the VUV laser. The produced charged particles (ions or electrons) are detected with a MCP detector as a function of VUV wavelength to record photoionization spectrum.

The whole vacuum system is evacuated by two-stage pumping systems constituted by multistage root and turbo-molecular pumps. For each chamber the pressure is monitored by a pressure gauge without permanent magnetic moment, avoiding the source of external magnetic field from the environment that could affect our measurements.

2.2 VUV laser source

2.2.1 General principle for VUV generation

According to our experimental requirements, a VUV laser radiation should satisfy at the same time high brightness, narrow bandwidth as well as tunability over broad spectral regions. To do so, we employ a non-linear optical process called four-wave mixing in rare gases. The basic idea of the four-wave mixing process is that three incident wavelengths are involved to interact with the non-linear medium, resulting into the generation of a fourth wavelength. As shown in Fig. 2.3, two incident radiations are required: one is a UltraViolet (UV) radiation at fixed frequency f_{UV} to match the two-photon resonance with a specific atomic transition in rare gas (usually Kr or Xe), the other is a tunable radiation with frequency f_{vis} to generate a tunable VUV laser by either resonance-enhanced sum-frequency mixing ($f_{\mathrm{sum}} = 2f_{\mathrm{UV}} + f_{\mathrm{vis}}$) or difference-frequency mixing ($f_{\mathrm{diff}} = 2f_{\mathrm{UV}} - f_{\mathrm{vis}}$) (see middle and right panels of Fig. 2.3). The third harmonic generation is a special case of the sum-frequency mixing process with three UV photons summing up into one fixed output photon ($f_{3\mathrm{UV}} = 3f_{\mathrm{UV}}$)(see left panel of Fig. 2.3). Compared to the non-resonant VUV generation, which does not require a resonance between photon energy and an atomic transition, with a production efficiency typically of the order of 10^{-6}, the efficiency of the resonant process can be improved to 10^{-4}.[80] Thanks to the improved conversion efficiency, higher VUV intensity could be reached without using high pulse energies in the fundamental lasers, which limits the risk of the ionization and optical gas breakdown due to high brightness of incident light.[38,50,80] Another advantage of the resonant process is that the VUV frequency can be scanned over wide frequency intervals without significant intensity fluctuation.[82]

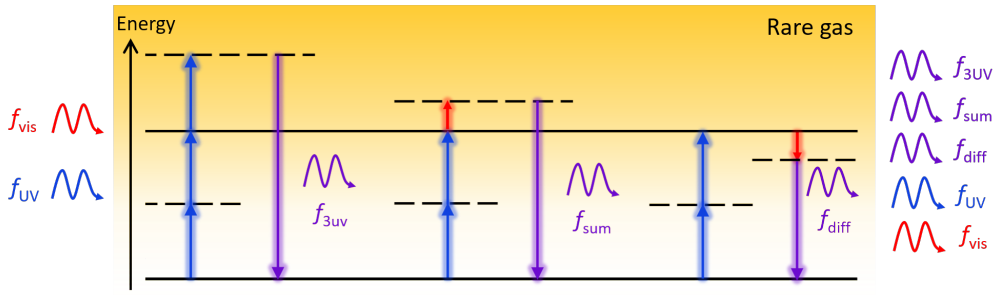

Figure 2.3: Four-wave mixing resonant scheme used on VULCAIM setup, combining fixed UV and tunable visible radiation in rare gas (Kr or Xe). Dashed lines represent virtual states and full lines represent actual states exploited for atomic resonances. From left to right: third harmonic generation, sum-frequency mixing and difference-frequency mixing.

The two-photon resonant transitions usually used in Kr or Xe as well as the required UV wavelength are listed in Table 2.1; these transitions are forbidden for single-photon absorption according to the selection rule (total angular momentum J=0 $\not\leftrightarrow$ 0), preventing the relaxation of the excited state. During my study the Kr(1) and Xe(1) resonances were used to reach different VUV energy ranges.

In the four-wave mixing stage, depicted in Fig. 2.1, the UV and visible radiations focus and intersect in a rare gas pulsed jet to generate efficiently the VUV radiation. As the VUV radiation is unable to pass through air mainly due to its absorption by O_2, from this stage until the ionization region the laser path has to be under vacuum. The rare gas pulsed jet is produced and expanded by an Amsterdam Piezo Valve, with 1 bar backing pressure of the rare gas. The pulse duration of the Amsterdam Piezo Valve used to generate the rare gas beam is set to be 40 μs to limit the rare gas consumption. The position of the gas nozzle is adjustable in three dimensions, allowing to optimize the local pressure (density) of rare gas where the beams are focused to get the best energy conversion efficiency.

At the exit of the VUV generation chamber, the radiations of the fundamental frequencies and various frequencies produced by nonlinear optical processes (harmonic generation and sum/difference-frequency mixing process) overlap. We use a toroidal TGM300 VUV reflective diffraction grating to disperse the light and to select a specific beam using an iris and by rotating the grating. The grating has 275 grooves per mm and its toroidal geometry ensures that the selected beam is refocused at the 1 mm diameter exit iris of the monochromator chamber. The small size of the hole simultaneously warrants a clean selection of the selected beam and efficient differential pumping.[82] During the experiment, the third harmonic radiation $f_{3\mathrm{UV}}$ is typically at first selected to optimize the alignment of

Rare gas	Resonance	Two-photon transition	Transition energy / cm^{-1}	UV wavelength / nm
Kr	Kr(1)	$4p^6\,{}^1S_0 \rightarrow 4p^5(^2P^0_{3/2})5p[1/2](J=0)$	94092.86[159]	212.5560
	Kr(2)	$4p^6\,{}^1S_0 \rightarrow 4p^5(^2P^0_{1/2})5p[1/2](J=0)$	98855.06[159]	202.3164
Xe	Xe(1)	$5p^6\,{}^1S_0 \rightarrow 5p^5(^2P^0_{3/2})6p[3/2](J=0)$	80118.96[86]*	249.6288
	Xe(2)	$5p^6\,{}^1S_0 \rightarrow 5p^5(^2P^0_{1/2})6p[1/2](J=0)$	89860.02[86]*	222.5684

Table 2.1: Two-photon resonant transitions used in VUV laser generation. *The values in Ref. 86 are adjusted according to the database https://physics.nist.gov/PhysRefData/Handbook/Tables/xenontable5.htm

the UV light, and then the expected sum-frequency or difference-frequency radiation is selected after careful spatial and temporal overlaps of the two fundamental lasers.

The reflection efficiency of the grating on incident light depends on the polarization and wavelength of the light. In Fig. 2.4, the efficiencies of the grating for incident light with s and p polarizations are depicted in red and blue, respectively. It is clear that s polarization has to be chosen to minimize the losses upon reflection. As the polarization of VUV radiation is determined by the tunable laser, it is therefore requested to keep the polarization of the Cobra laser or OPO laser to be perpendicular to the incident plane (s polarization), thus in the vertical direction.

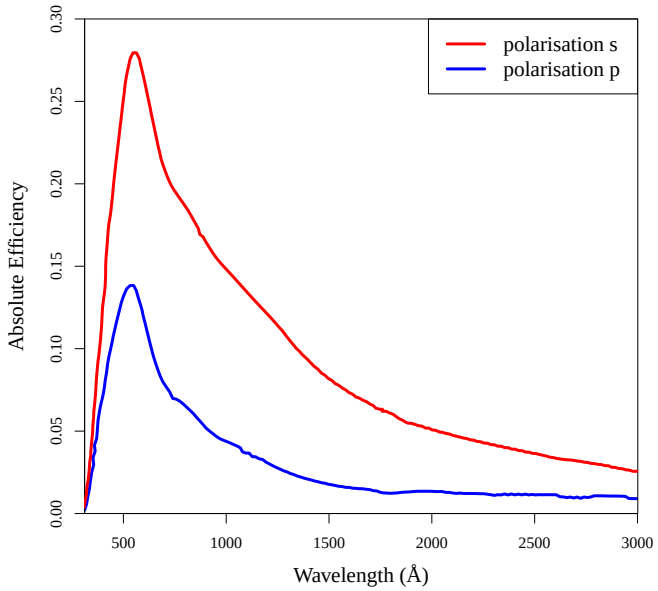

Figure 2.4: Comparison of the reflection efficiency for radiation with polarization s (in red) or p (in blue) by the grating (275 gr/mm) coated with Pt as a function of the wavelength. The figure is adapted from reference offered by the HORIBA supplier of the grating product.

The intensity of VUV radiation is monitored by a R5150-10 electron multiplier installed in front of the VUV laser after the spectrometer (see Fig. 2.1). This detector has a good sensitivity for VUV radiations and soft X-rays. The monitoring of the VUV intensity is used to optimize the VUV production and to correct signals from variations of VUV intensity during a scan. Note that the detection efficiency of the VUV detector is dependent on photon energy, which should be considered when the scanned photon energy varies over a wide range.

2.2.2 Laser system

Above we have explained the mechanism of the VUV laser generation in our setup, now let us take a close look into the laser system which provides the required UV and visible radiations for the VUV generation, as shown in Fig. 2.1. The Cobra dye laser chain was used in the beginning of the setup construction in 2018, providing a visible laser

radiation with a bandwidth of less than 0.1 cm^{-1}. Its coupling with the UV line, which produces the UV laser with a bandwidth of a few 10^{-3} cm^{-1}, generates VUV laser with a relatively high resolution under 0.1 cm^{-1}. Nevertheless, despite the high resolution of the visible light offered by the dye laser chain, its limitation is evident with the inconvenience of dye selection and change, especially when energy information of studied molecules is unknown or when we want to study at once a mixture of various molecules over wide spectral ranges. The relatively narrow wavelength range of the output of the visible laser corresponding to the dye solution range leads to the VUV tunability range limited to about 1000 cm^{-1}. That is why the second complementary tunable visible laser line equipped with an OPO (NT342 series) tunable laser has been coupled to our laser system very recently in 2023. During my PhD, we have tested this new laser line capable to generate a VUV laser radiation with a tunability of more than 24000 cm^{-1}. By selectively choosing one of the two laser systems to couple with the UV line, we are able to easily generate a VUV laser with either high resolution or a broad tunable range, catering to different experimental requirements.

2.2.2.1 High-resolution UV laser chain

The UV laser chain aims to produce a pulsed UV laser at a fixed wavelength, which is determined by the two-photon transition in the rare gas used to generate the VUV (see Table 2.1). A narrow bandwidth, good temporal profile as well as high stability are requested for the UV output which determines directly the quality of the VUV output.

The chain starts with a Continuous-Wave (CW) diode-pumped solid-state (DPSS) frequency-doubled Nd: YVO_4 laser Millennia that produces a beam at 532 nm with power levels up to 5 W. This laser is used to pump a ring dye laser (Sirah Matisse 2 DR series laser), with which the output laser can be tuned from 550 to 750 nm with various dyes. In our case we circulate the 4-(Dicyanomethylene)-2-methyl-6-(4-dimethylaminostyryl)-4H-pyran (DCM) dye in 2-pheoxy-ethanol and ethylene glycol (1:1) solvent. In Fig. 2.1, the wavelength values marked after the ring dye laser correspond to the required ones for the Kr(I) resonance. The output laser has a narrow bandwidth of typically 7.10^{-4} cm^{-1}.[69] The power of resulting radiation is maintained to about 400 mW.

Then the cw laser is pulsed amplified in the Pulsed Dye Amplifier (Sirah), which consists of four amplification stages in three circulating dye solutions. In this amplifier, the cw seed laser passes through the cuvettes with dye solution, which are pumped by an injection seeded pulsed Nd: YAG laser (Spectra-Physics Quanta-Ray Lab-190) at a 20 Hz repetition rate and typically 300 mJ per pulse (6 W). The resulting radiation is at almost the same wavelength as the incident cw light (see below) but has a pulsed temporal profile determined by the pump laser (pulse duration is 6-7 ns). During the experiment, the optimization of the amplification efficiency of each stage is necessary and it is realized by a step-to-step optimization. The power of the resulting pulsed laser is typically 20-30 mJ/pulse after the fourth amplification, using DCM dye in ethanol solvent as dye solution at around 636 nm. The Amplified Spontaneous Emission (ASE) is normally inevitable although in the two amplification stages of the first dye circulation ASE is minimized. A unique performance of this Pulsed Amplifier is that a phase conjugated mirror based on Stimulated Brillouin Scattering (SBS) is integrated before the last amplification stage to suppress dramatically the ASE and the

cw seed beam. But this mirror cell causes also a small but constant wavelength shift (≈3.2 pm) , which requires us to place a high precision wavemeter afterwards to measure the real wavelength of the output pulsed amplified laser.

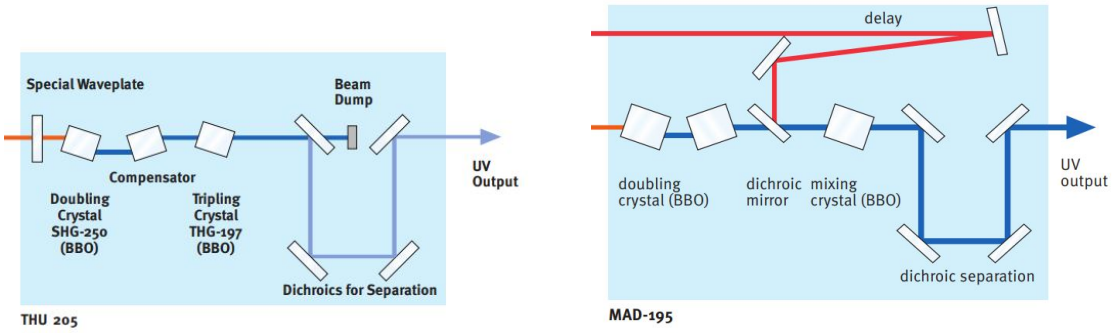

(a) third harmonic

(b) mixing after doubling

Figure 2.5: Figures extracted from the Sirah THG unit manual. Optical layout for UV generation by a) the third harmonic of the fundamental radiation ($f_{\mathrm{UV}} = 3f_{\mathrm{fun}}$) and by b) the mixing of the doubled fundamental radiation with a YAG laser at 1064 nm, required for four-wave mixing in Kr(I) and Xe(I), respectively.

Following the pulsed amplification-stage, the UV radiation is finally generated by mixing the pulsed visible laser in two BaB_2O_4 (BBO) crystals in a Sirah THU-205 third harmonic unit (see Fig.2.5(a)). The BBO nonlinear crystal is particularly used thanks to its extended transparency toward the UV wavelength down to 200 nm. To accomplish the third harmonic generation, the first crystal acts as a doubler and the second mixes the doubled radiation and the fundamental radiation. In addition, this unit can also be modified to realize a mixing-after-doubling process to reach the UV wavelength requested for the Xe(1) transition, as shown in Fig.2.5(b). In this case, the doubled radiation is mixed with a residual radiation at 1064 nm of the YAG laser used in the Pulsed Dye Amplifier.

The final UV radiation generated by the UV laser chain has a wavelength between 200 and 250 nm, a spectral resolution of a few 10^{-3} cm^{-1}, a repetition rate of 20 Hz, a temporal pulse length of ≈5 ns, and an energy per pulse up to 3 mJ.

2.2.2.2 Cobra tunable dye laser dedicated to high-resolution configuration

The tunability of generated VUV radiation is set by the tunable visible laser, as explained in Section 2.2.1. Two tunable laser lines can now be chosen. The first one is a Sirah Cobra-Stretch dye laser pumped by a pulsed Nd: YAG laser at 355 or 532 nm and equipped with a double grating. Various dye solutions can be used, combined or not with a doubling unit, to cover a spectral range from around 300 to 900 nm (near-UV to near-IR). Lower wavelengths in UV range can be attained by adding a BBO crystal as frequency doubler of visible light. Table 2.2 lists several representative dye solutions alongside their corresponding tunability ranges achieved with the pulsed Nd: YAG laser at 532 nm. While the tunability range may vary across different dye solutions, it generally remains confined to approximately 1000 cm^{-1}. As such, this limitation defines the achievable tunability range for the VUV laser generated

with the Cobra dye laser. The tuning of the wavelength is realized with a double grating (1800 & 1800 or 1800 & 3000 gr/mm). The whole scanning process is electronically controlled and the output wavelength is measured in real time by a High Finesse WS6-600 series wavemeter to provide an absolute calibration during the scan. **The bandwidth of the visible light is about 0.1 cm^{-1}. As this bandwidth is larger than that of the UV laser, it is the limiting bandwidth for the final generated VUV laser. So ideally we can easily have a VUV radiation with a bandwidth of about 0.1 cm^{-1} using the Cobra tunable laser chain.**

Dye solution	peak maximum/ nm	spectral range / nm	tunability range / cm^{-1}
Fluorescein 27 (Ethanol + H_2O)	550	541 - 571	971
Rhodamine B (Ethanol)	596	588 - 614	720
DCM (Ethanol)	627	602 - 660	1460
Pyridine 1 (Ethanol)	692	667 - 720	1104
LDS 867	863	832 - 900	908

Table 2.2: Tunability range of the Cobra dye laser obtained with various typical dye solutions, with the pulsed Nd:YAG laser at 532 nm. The solute and solvent used in each dye solution are listed in the first column. The peak wavelength and spectral range information are provided by the Sirah manufacturer.

2.2.2.3 Tunable OPO laser dedicated to broadly tunable configuration

Since the second tunable visible line I am about to introduce is a new system installed during the third year of my PhD, I would like to provide a more detailed description of its components and characteristics.

This visible line (NT342 series laser from EKSPLA company) is composed of a nanosecond optical parametric oscillator (OPO) and a Nd:YAG Q-switched nanosecond laser, allowing to electronically control the wavelength tuning from UV to IR with high conversion efficiency. The unit starts with a fundamental pulsed Nd:YAG radiation (1064 nm), which is converted into the second (532 nm) and third (355 nm) harmonics. The third harmonic f_{pump} is directed into the OPO cavity which contains two nonlinear crystals, generating the signal wave f_{signal} and the idler wave f_{idler} based on the nondegenerate parametric amplification phenomenon with $f_{\mathrm{pump}} = f_{\mathrm{signal}} + f_{\mathrm{idler}}$. Wavelength tuning is achieved by rotation of the two nonlinear crystals. Based on type II BBO nonlinear crystal, the wavelength tunable range of the OPO laser covers 410 - 2600 nm, including the signal radiation range (410 - 709 nm) and the idler radiation range (710 - 2600 nm). In addition, there are some more tuning range extensions like the range of 210 - 409 nm, which is realized by the second harmonic from the OPO signal radiation, or the range of 296 - 409 nm with high pulse energy, which is generated by the sum-frequency of the OPO signal radiation and the fundamental YAG radiation, etc. In practice, as the OPO laser has to go through a dichroic mirror for its spatial superposition with the UV line, we can only use the wavelength range from 300 to 1100 nm, which allows already a large tunable VUV range over more than 24000 cm^{-1}.

The conversion efficiency of the VUV radiation with this OPO laser has been investigated during my PhD. In Fig.2.6, the typical output energy of the OPO laser is presented across the wavelength range of 400 - 2600 nm. It is evident from the graph that the maximal pulse energy of 35 mJ is achieved at approximately 475 nm, with a

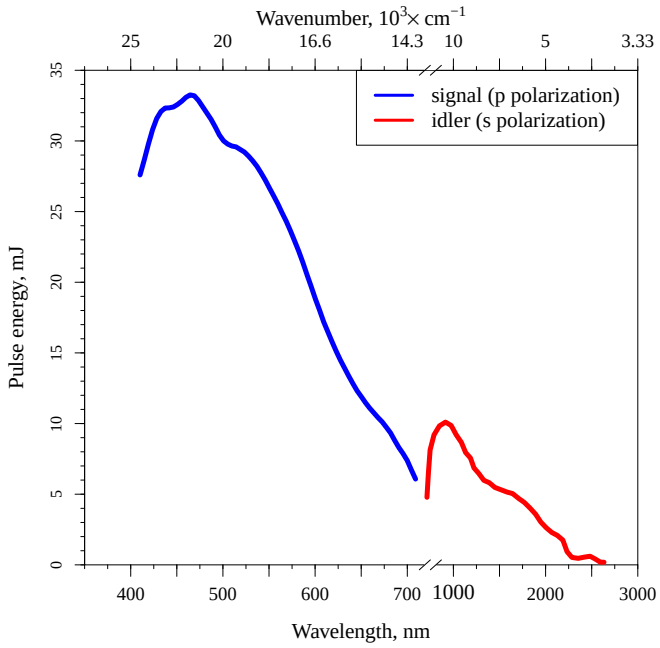

Figure 2.6: Typical shapes of tuning curves for NT342B-SH/SF series laser, extracted from the user's manual.

conversion efficiency up to 30% according to the user's manual. Notably, the pulse energy of the signal radiation (below 709 nm) is generally higher than that of the idler radiation (above 710 nm). Additionally, around 709 nm, there is a noticeable discontinuity due to the mode change between the two radiations. Besides, it should be mentioned that the two radiations have different polarization directions: it is horizontal (p) for the signal radiation and vertical (s) for the idler radiation. Consequently, it is necessary to rotate the polarization of the OPO signal radiation to get a s polarized radiation, taking into account the reflection efficiency for radiation with different polarizations by the grating, as previously discussed (see section 2.2.1).

Based on these discussions, we measured the intensity for both the $\mathrm{VUV_{diff}}$ and the $\mathrm{VUV_{sum}}$ radiations obtained with the OPO laser within the range of 400 - 1100 nm, using 4-wave mixing process in Kr(I) transition, as depicted in Fig.2.7. The generated $\mathrm{VUV_{diff}}$ radiation covers the photon energy range approximately from 8.5 to 10.5 eV; the $\mathrm{VUV_{sum}}$ radiation covers 12.8 to 15.4 eV. Note that, due to the wide range of measured wavelengths, the grating in the monochromator chamber needs to be rotated. With respect to the non-dispersed 0 order, the rotation angle (θ) for selecting a radiation with a specific wavelength λ exhibits a linear relationship. Very recently, an electronically controlled system has been installed to automate the grating rotation according to the VUV wavelength. This facilitates the experimental recording and is crucial for a constant adjustment of the VUV laser trajectory in the ionization chamber. As shown in Fig. 2.7, the general intensity of $\mathrm{VUV_{diff}}$ laser is lower that that of the $\mathrm{VUV_{sum}}$ laser. However, the $\mathrm{VUV_{sum}}$ exhibits numerous holes in the energy range, which are caused by the absorption lines of Kr. These gaps hinder the wide-range spectroscopic measurement in this region. To address this issue, alternative 2-photon resonant transitions for 4-wave mixing VUV production can be used, as shown in Table 2.1 (but they are not presented

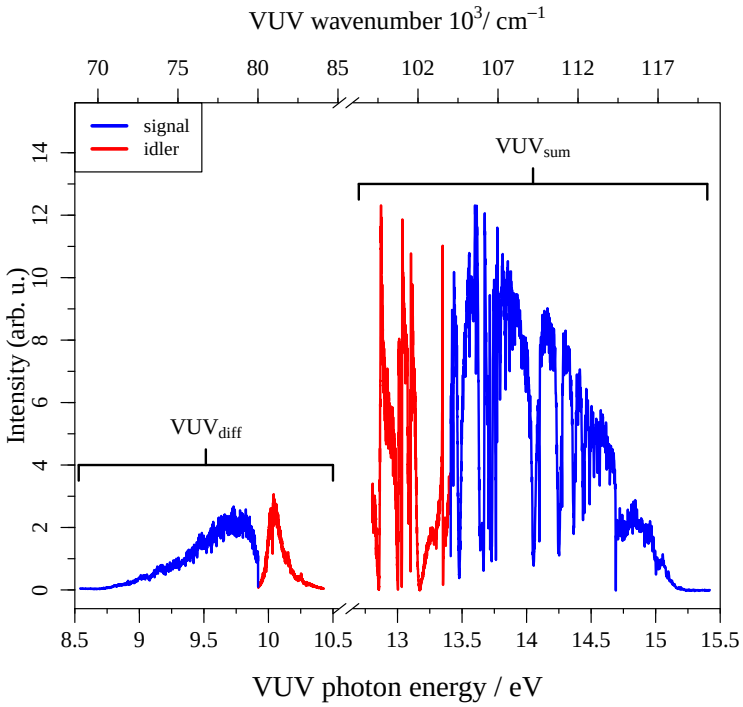

Figure 2.7: VUV intensity as a function of the photon energy obtained with the OPO laser in the range of 400 to 1100 nm using 4-wave mixing processes (both sum- and difference frequency mixing) with Kr(I) transition. The VUV radiation with photon energy below 11 eV is obtained with difference frequency mixing, and above 12 eV with sum frequency mixing. The polarization is rotated by 90° when the signal radiation of OPO laser is used.

here). Notably, despite the higher output power of the signal radiation shown in Fig.2.6, the VUV intensity produced using the idler radiation (see Fig. 2.7) is likely not lower than that obtained with the signal radiation, indicating a lower VUV conversion efficiency with the signal radiation. The decreasing trend in VUV intensity below 9 eV and above 14.5 eV can be attributed to the low transparency efficiency of the dichroic mirror at shorter wavelengths.

Although the $\mathrm{VUV_{diff}}$ radiation shows relatively low intensity, possibly due to the weak sensitivity of the VUV detector in this low-energy range, it provides sufficient and stable VUV intensity within a specific photon energy around 9.3 to 10.4 eV. This is more clearly presented in Fig.2.8. Using this VUV laser, we succeeded to record a MATI spectrum of the $\mathrm{X}^+\,^1\Sigma^+ \leftarrow \mathrm{X}\,^2\Pi_{1/2}$ transition of NO (see Chapter3). Fig.2.8 presents the measured $\mathrm{VUV_{diff}}$ intensity as a function of the wavenumber during the MATI measurement. This measurement enables higher precision with smaller scan steps and higher statistics. During this measurement, the grating in the monochromator chamber was rotated manually to optimize the VUV radiation. The corresponding wavelength of the OPO laser is also depicted on the upper axis. It can be observed that despite the mode change of the OPO radiation and some noticeable sharp gaps in the high wavenumber range attributed to the absorption lines of Kr, the generated $\mathrm{VUV_{diff}}$ radiation allowed for broad-range spectral measurement. Furthermore, in this spectrum, the VUV conversion efficiency with the idler OPO laser above 710 nm is generally higher than that with the OPO laser below 709 nm. Comparing with measure-

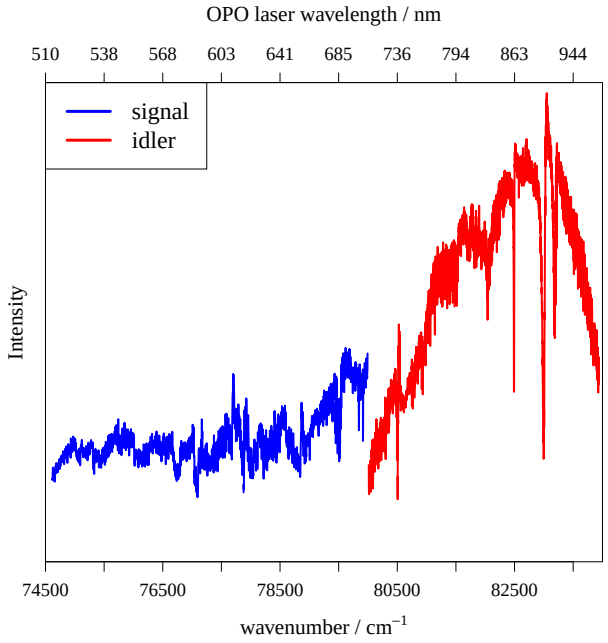

Figure 2.8: $\mathrm{VUV_{diff}}$ intensity as a function of the wavenumber measured when carrying out a MATI spectral measurement on the $\mathrm{X}^{+\,1}\Sigma^{+} \leftarrow \mathrm{X}\,^{2}\Pi_{1/2}$ transition of NO. The discontinuity of the intensity signal is due to the mode change of OPO laser between the signal radiation (below 709 nm) and the idler radiation (above 710 nm).

ments depicted in Fig.2.7, it was found that the VUV laser intensity with the idler radiation was much higher in this measurement, while that with the signal radiation was quite similar. This discrepancy may be due to optimization of the OPO laser or the VUV generation, or it might be attributed to a different pulse duration for the signal and idler beams. This point requires further verification. Overall, due to considerable intensity fluctuations of the VUV, it is necessary to correct the measured photoionization spectra with VUV intensity (by dividing the photoionization signal by the VUV detector signal.).

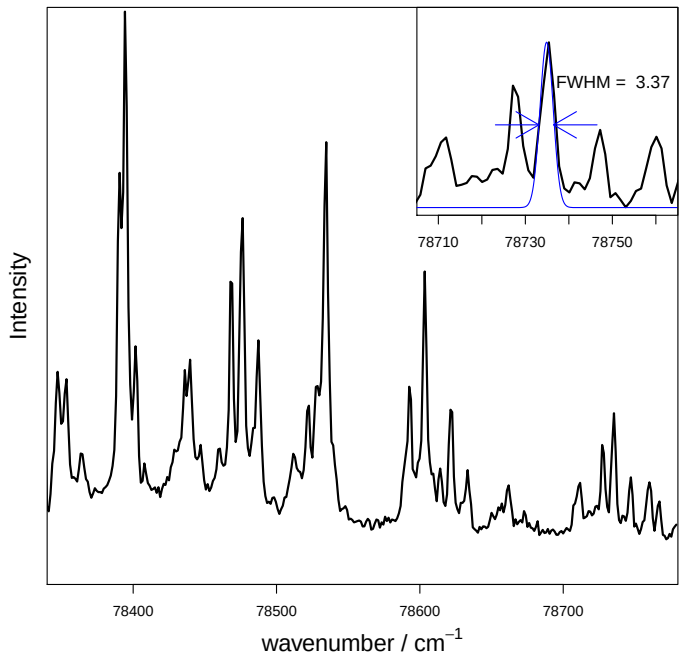

Figure 2.9: Ion yield spectrum obtained using low-resolution MATI sequence and the VUV laser coupled with the OPO laser, on the $\mathrm{X}^{+\,1}\Sigma^{+}(v^{+}=1) \leftarrow \mathrm{X}\,^{2}\Pi_{1/2}(v=0)$ transition of NO.

The laser bandwidth of the VUV radiation is also assessed through the ion yield spectrum recorded by the MATI experiment on NO. Fig. 2.9 depicts the ion yield of the $\mathrm{X}^{+\,1}\Sigma^{+}(v^{+}=1) \leftarrow \mathrm{X}\,^{2}\Pi_{1/2}(v=0)$ transition of NO. The photon energy was scanned with a step size of approximately 2 cm^{-1}. The bandwidth of the autoionization peak signals is primarily reliant on the laser resolution. **A typical bandwidth is found to be around 3 cm^{-1}. This is considered as the photon resolution of the OPO laser, and thus also the photon resolution of the VUV radiation produced with the OPO laser.**

2.2.3 Summary of laser characteristics

	VUV laser radiation of VULCAIM	
	with dye laser	with OPO laser
Pulse duration	≈7 ns pulses at 20 Hz	
Photon flux	10^9-10^{10} ph/pulse	
Spectral range	6-17 eV, by range of ≈1000 cm^{-1}	6-17 eV, by range of ≈24000 cm^{-1}
Spectral bandwidth	< 0.1 cm^{-1}	≈3 cm^{-1}
Polarization	s polarization	

Table 2.3: Characteristics of the VUV laser radiation of VULCAIM setup for the 2 different configurations.

In summary, the VULCAIM VUV laser source, equipped with two tunable laser lines, demonstrates its remarkable capacity to generate VUV laser beams with distinct characteristics. These include high resolution within a limited tunability range, or a broader tunable range with medium spectral resolution. The comprehensive characteristics of the VUV laser produced by coupling the UV laser with the Cobra dye laser or with the OPO laser in the VULCAIM system are systematically summarized in Table 2.3.

The estimated photon flux of the VUV laser spans between 10^9 and 10^{10} ph/pulse. Experimental evaluation of the VUV laser intensity is performed by a VUV detector. The VUV intensity can be influenced by various factors. These factors encompass the pulse power of the UV and visible lasers, their precise temporal and spatial overlap with the rare gas pulse, and other parameters. Achieving optimal laser performance necessitates meticulous laser optimization and precise pathway alignment on a daily basis.

In conjunction with a meticulously controlled UV laser boasting high resolution of the order of a few 10^{-3} cm^{-1}, the spectral resolution of the VUV laser predominantly hinges on the tunable visible laser. This resolution can be tailored to 0.1 cm^{-1} when using the Cobra dye laser, or set to 3 cm^{-1} when employing the OPO laser. The pulse duration, spanning a few nanoseconds, engenders a Fourier-Transform (FT)-limited spectral bandwidth of 10^{-3} cm^{-1}, ensuring that the laser bandwidth remains unconstrained by the short pulse. The high resolution attainable with the Cobra dye laser aptly caters to exploring the rotational structures of small molecules. In contrast, the OPO laser provides a medium-high resolution that suits the study of vibrational structures.

The tunability range of the VUV laser mirrors that of the tunable visible laser. With the Cobra dye laser, wavelength tuning is achieved through the rotation of a double-grating equipped within the dye laser setup. The attainable tunability range is confined to approximately 1000 cm^{-1}, primarily due to limitations imposed by the dye solution. Conversely, the OPO laser facilitates wider tunability of the output visible laser through the manipulation of two nonlinear crystals, enabling a continuous tunability range of up to 24000 cm^{-1}, restricted primarily by the spectral characteristics of the dichroic mirror.

The VUV laser radiation is s-polarized, optimally aligning with the direction of the high reflection efficiency of the monochromator chamber's grating. Notably, when utilizing the OPO signal radiation, a polarization rotation (p-polarization) is necessary to effectively realize this alignment.

2.3 Coupling of radical sources with VULCAIM

As illustrated in Fig.2.1, the gas-phase molecular sample is introduced through a nozzle into the vacuum chamber. If the sample is gaseous, it can be pre-mixed with a carrier gas such as Helium or Argon. In the case of a liquid sample, according to its vapor pressure, it can be vaporized by passing the carrier gas through or over the liquid. In accordance to the pulsed nature of our experiments, a pulsed molecular source is employed. Compared to a continuous jet, a pulsed jet is advantageous for higher molecular densities or lower gas consumption. In our experiments, a pulsed molecular jet is generated using either the General Valves Series 9 pulsed solenoid valve or the Amsterdam piezo valve.[1] The former produces a pulsed jet with a duration larger than 100 μs (typically 150-250 μs), while the latter is capable of achieving durations in the range of a few tens of microseconds (typically 30 μs), resulting in significantly higher molecular densities. The pulsed gas jet, with an upstream stagnation pressure of several bars, undergoes supersonic expansion through the valve nozzle into the vacuum chamber. During this expansion, the molecules undergo cooling. The cooled gas-phase molecular beam then passes through a skimmer and intersects with VUV radiation in the interaction region. The valve is mounted on a rod which is mechanically movable in three directions, allowing to adjust the position of gas beam relative to the skimmer.

During my PhD studies, one important project involved to couple unstable radical molecular sources with the VULCAIM setup, enabling photoionization experiments on free radicals. The basic idea was to incorporate a device connected to the pulsed valve, which would dissociate the gas-phase precursor molecules and generate the target radical species. These strategies involve different mechanisms to dissociate the molecular bonds of precursor molecules, including high thermal energy, high-voltage electrical discharge, laser irradiation, and chemical reactivity. Each strategy has its own set of advantages and disadvantages. For instance, the strategy using chemical reactions, typically using the H-abstraction reactions by fluorine atoms from H-bearing precursor molecules, is technically mature and efficient. However, this strategy is more suitable for continuous experiments. At the DESIRS beamline of SOLEIL synchrotron we carried out a series of experiments on radical molecules based on this type of radical source, which are presented in Chapter 5 in which the flow-tube reactor will be briefly described.

Within the scope of my PhD project, I primarily focused on testing the pyrolysis and electric discharge strategies using our VULCAIM setup. Both strategies involved evaluating their efficiency in generating radicals and optimizing the parameters to achieve high radical yields at low temperatures (except for the hot CH_3^+ experiment which will be introduced in Chapter4).

2.3.1 Pyrolysis source

The technique using pyrolytic dissociation to produce a pulsed radical source was firstly demonstrated in 1986,[29] and it has since undergone further developments in the following decades. This method offers significant advantages. For instance, it allows for the clean and specific production of radical species with a stable and high conversion

efficiency, by carefully selecting an appropriately designed organic precursor and controlling the experimental conditions. However, this method does have limitations. It is primarily suitable for precursors with weak bond energies, and radicals produced through pyrolysis typically have high internal energy. In our experiments with pyrolysis radical source, we used the device illustrated in Fig. 2.10, which is based on the design proposed by Kohn *et al.*[95] Note that, in the experiments involving the pyrolysis radical source, careful considerations were made due to the high temperatures up to around 1500 K.[55] This level of heat posed a potential risk of damage to the fragile and expensive piezo valve. As a precaution, only the general valve was used for these tests.

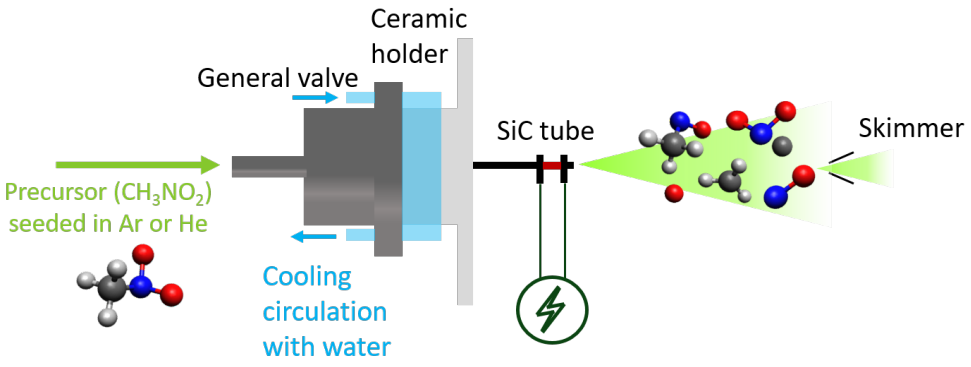

Figure 2.10: Illustration of the pyrolysis radical source. A SiC tube mounted on the general valve is heated by the intense current applied by the electrodes. As an example, the CH_3NO_2 precursor seeded in carrier gas can be thermally dissociated to various fragments or ions (CH_3, NO, NO_2^+, CH_3NO^+, etc.). By controlling the experimental conditions, the production yield of a target radical (e.g. CH_3) can be selectively improved.

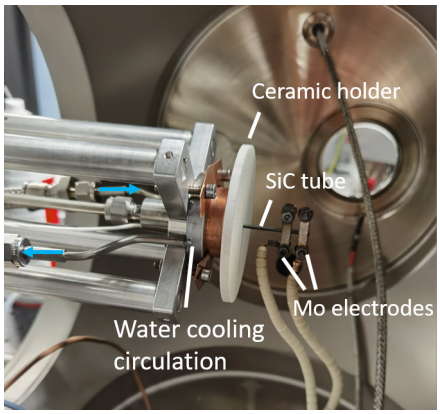

Figure 2.11: Photo of the pyrolysis device.

As illustrated in Fig. 2.10, precursor molecules are seeded in a carrier gas (He or Ar) at a stagnation pressure of several bars. The mixture is expanded at high speed into a SiC tube with a diameter of 1 mm. At the heated end of the tube, achieved through the application of current (typically at 1 to 2 A) *via* attached electrodes separated by typically 1 cm, the precursor molecules undergo rapid pyrolysis. The electrodes are made of molybdenum with a high current transfer coefficient but a low heat transfer coefficient. To ensure uniform contact, thin and soft tantalum layers are interposed between the electrodes and the SiC tube. To protect the general valve from the

high temperature, a ceramic holder at low heat transfer coefficient is inserted between the valve and the SiC tube. Meanwhile, the holder is designed with a larger diameter on one side in order to cut off the radiation heat transfer. In addition, a water cooling system is implemented to further reduce the valve's temperature. Fig. 2.11 displays a photo of the pyrolysis device.

In pyrolytic radical production experiments, numerous parameters require consideration and optimization. These parameters include heating power (current and voltage), heating length, polarity of current, length of SiC tube, distance between the tube exit and the skimmer, stagnation pressure of sample gas, carrier gas, etc. The objective is to simultaneously increase the production yield of target radicals at relatively low temperatures while minimizing direct ionization of the radicals or recombination of radicals downstream. Typically, when dealing with a precursor aimed at generating a specific radical, the heating power plays a crucial role in adjusting the neutral-to-ion ratio. Furthermore, the internal energy of the radicals is more effectively controlled by adjusting parameters associated with the supersonic expansion, such as the distance between the tube exit and the skimmer.

Using this method, we succeeded to produce CH_3 radicals from CH_3NO_2 precursor. Specifically, we explored this technique to an inverse direction, aiming to generate vibrationally hot CH_3 radicals with a thermal population up to the $\nu_2 = 1$ vibrational state in the electronic ground state $\tilde{\mathrm{X}}\,^2\mathrm{A}_2''$. The resulting experimental data for the vibrational mode ν_2^+ of CH_3^+ provided valuable support for validating the presence of the methyl cation in a Protoplanetary Disk, as very recently observed by the James Webb Space Telescope (JWST).[12] The results will be presented in Chapter 4.

2.3.2 High-voltage electric discharge source

Because of the low cost and wide range of applications, high-voltage electric discharges are very interesting for the generation of atoms, radicals or ions. In particular, high-voltage discharges are well-suited for experiments requiring pulsed particle beams rather than continuous beams. This makes it an appealing option for our pulsed experiments when compared with other discharge techniques such as microwave discharge. However, the high instability of the discharge poses challenges in controlling the dissociation environment and ensuring relatively high efficiency.

Fig. 2.12 illustrates the basic design of the high-voltage discharge source in the upper panel. A pulsed gas mixture of precursor molecules, seeded in the carrier gas (Ar or He), is introduced *via* a pulsed valve and passes through a tube before undergoing supersonic expansion. The tube is constituted by two metallic ring electrodes held by three insulating Teflon pieces. The distance between the electrodes is typically between 1 and 2 mm. The outer electrode is polarized to a high voltage exceeding the striking voltage (breakdown voltage) of the carrier gas, while the inner electrode is grounded, avoiding the possible electric discharge with the valve. The high electric potential difference (typically 1 to 3 kV) leads to self-sustaining ionization of the carrier gas, generating a plasma. Within this plasma, abundant ions and highly energetic electrons, driven by the intense electric field, rapidly transfer their energy to the precursor molecules through collisions. Consequently, the precursor molecules undergo fragmentation, giving

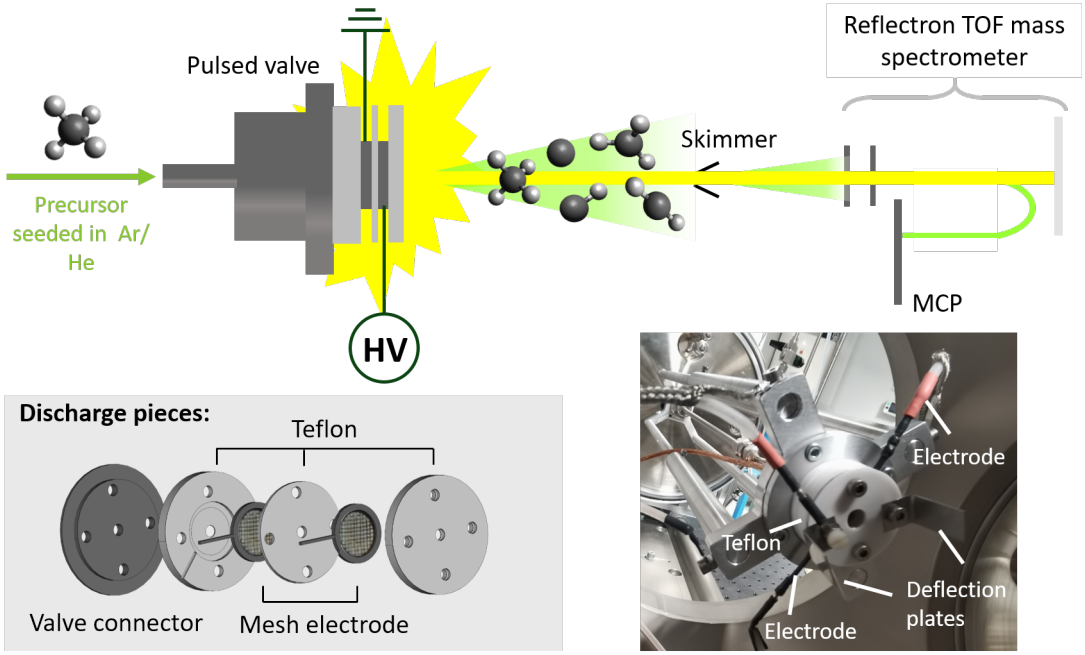

Figure 2.12: Illustration of high-voltage electric discharge radical source.

rise to the formation of radicals. These radicals subsequently cross the downstream skimmer and are analyzed *via* photoionization spectroscopy under VUV irradiation.

However, during the test experiments, we encountered several challenges. The first issue was the intense brightness emitted by the discharge, which caused saturation of the on-axis MCP detector (described in Section 2.4). This saturation, in turn, hindered the detection of ionization signals. To address this problem, we replaced the spectrometer configuration illustrated in Fig. 2.1 by a Reflectron TOF mass spectrometer, as shown in Fig. 2.12. This newly coupled spectrometer allowed us to position the MCP detector away from the direct light pathway. More details regarding the Reflectron TOF mass spectrometer are discussed in Section 2.4. However, it is important to note that the implementation of the Reflectron TOF spectrometer prevented high-resolution PFI-ZEKE photoelectron spectroscopic measurements on the radicals generated by the discharge method. To overcome this limitation, we propose two potential solutions. Firstly, we can explore the use of the MATI spectroscopic method in conjunction with the Reflectron TOF mass spectrometer. Alternatively, we can modify the initial spectrometer to a vertical configuration, thereby avoiding the interference from intense light since the MCP detector will be perpendicular to the beam axis. Both of these potential solutions require further experimentation and development.

The second challenge we encountered with the electric discharge source was the direct ionization or even fragment-ionization of abundant precursor molecules during the intense electric discharge. This was attributed to the excessively high energy transferred to the precursor molecules, either due to numerous collisions or a high amount of energy transferred per collision. To mitigate the issue of the too violent discharge, we made several design improvements and ultimately adopted an up-scaled electric discharge device, which is displayed in details in the lower panel

of Fig.2.12. In this device, the ring electrodes are embedded in the grooves of the insulating Teflon holders, ensuring that they do not directly contact with the gas pulses. Two fine grids made of stainless steel wire mesh are held in contact with the electrodes, forming what we refer to as the "mesh electrodes". This design modification aims to prevent charge accumulation on the main body of the electrodes. Additionally, to our intuitive perception, the mesh would promote a more stable and uniform release of the electrons, which is supposed to provide more stable operation with lower voltage pulses.[58]

The third issue we had was that, despite the more stable operation with the "mesh electrodes", there were still ions generated directly from the discharge during measurements. To exclude them, a pair of aluminum deflection plates were placed either at the exit of the discharge device or in front of the skimmer entrance leading to the interaction room. However, we observed that these deflection plates were only effective with a relatively low amount of ions. The photo in Fig.2.12 depicts the device with the deflection plates mounted at the exit of the discharge device. An additional metal piece connected to the ground, serving to avoid the interrupted fields between the high-voltage discharge and the deflection plates, and a Teflon slice, serving to isolate the metal piece from the deflection plates, were inserted between the discharge pieces and the deflection plates.

For the benchmark tests of the electric discharge device, we selected two simple precursor molecules, namely methane (CH_4) and ammonia (NH_3), aiming to generate CH_x (x = 1-3) radicals and NH_y (y = 1, 2) radicals, respectively. These derivative radicals have been observed in the Interstellar Medium (ISM) (refer to Table 1.1) and are believed to play significant roles in astrochemistry. Notably for CH_3[40] radical as well as NH_2[72] radical, the photoionization spectroscopy in the vicinity of the threshold *IP* has been well measured. They serve as references for evaluating the performance of our device and provide insights into the temperature of the generated radicals, thereby enabling the evaluation of experimental conditions. Other radicals such as CH_2, CH, and NH have been relatively under-studied, especially in terms of high-resolution measurements, due to the challenges associated with their production. Consequently, this motivated us to improve the device to achieve high yields of these radicals for spectroscopic measurements.

During the test experiments, various parameters, such as the species of the carrier gas, ignition pressure, concentration of the seed precursor, voltage pulse amplitude and pulse width, were tested to improve the radical yield. For example, it was generally observed that collisions in an argon (Ar) plasma were milder compared to a helium (He) plasma due to the significant difference in atomic mass and size between the two gases. In the case of dissociating CH_4, we found that using He as the carrier gas resulted in a higher signal compared to using Ar. Conversely, for NH_3, Ar appeared to be a more favorable choice. Besides , the concentration of precursor molecules could also influence significantly the radical yield. For instance, the yield of CH_3 radicals produced from CH_4 increased as the concentration of CH_4 in the carrier gas increased from 0.5% to 15%. However, as the concentration increased beyond 15% up to 40%, we noticed only a negligible difference in the CH_3^+ signal. This observation could be attributed to an increased probability of recombination of radicals at higher concentrations, leading to a plateau in the radical

yield.

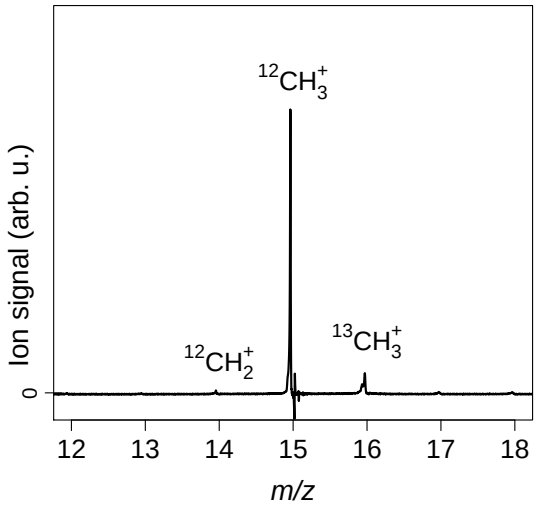

Figure 2.13: Experimental mass spectrum obtained with the high-voltage electric discharge radical source and 15% CH_4 in He, at the photon energy of 9.85 eV

The implementation of the up-scaled "mesh electrodes" device resulted in a significantly milder and more stable discharge. During the experiment using CH_4 precursor in He, we observed a much higher signal of CH_3^+ ions resulting from the ionization of CH_3 radicals, rather than that from the direct fragment-ionization of CH_4 induced by the electric discharge. However, few signals corresponding to smaller CH_x radicals were found. This suggests two possible reasons: either the collisions between precursor molecules and carrier atoms were too gentle, or these smaller radicals recombined at a later stage under the experimental conditions.

Fig.2.13 displays the mass spectrum obtained with 15% CH_4 in He at the photon energy of 9.85 eV. At this energy, only CH_3 radicals with an *IP* = 9.84 eV[40] can be ionized. The signal at *m/q* = 16 corresponds to the $^{13}CH_3^+$ and that at *m/q* = 14 is attributed to CH_2^+ ions directly generated by electric discharge, since the photon energy in this case is not sufficient to ionize neutral CH_4 and CH_2, as their *IP* is 12.61 [105] and 10.39 eV, [35] respectively. The signal at *m/q* = 16 is roughly 10% of that at *m/q* = 15, exceeding the ratio expected from the presence of the ^{13}C isotope, which is approximately 1%. Therefore, we cannot rule out other possibilities, such as the presence of CH_4^+ ions directly generated by electric discharge. More information about the ionization spectra of CH_3 will be discussed in Chapter 4.

Similarly, experiments were conducted using NH_3 as the precursor. Fig. 2.14 depicts the experimental mass spectrum using 1.5% NH_3 in Ar at the photon energy of 13.518 eV, with which the weak signals corresponding to NH_2^+ and NH^+ are displayed. The signal at *m/q* = 18 is due to the residual water in the vacuum chamber.

NH radicals are of great interest for high-resolution studies. In an attempt to compensate for the low NH yield, a signal amplifier was intended to be employed. However, it was discovered that the VUV generation process based on

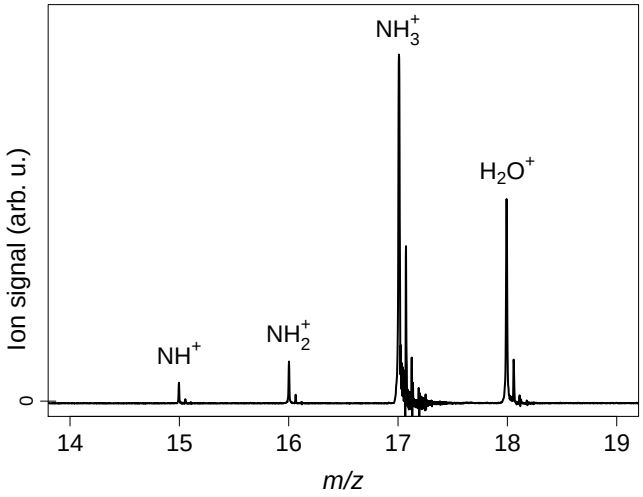

Figure 2.14: Experimental mass spectrum obtained from the high-voltage electric discharge source with 1.5% NH_3 in Ar, at the photon energy of 13.518 eV. The rebound noise signal appeared alongside the primary signal is attributed to experimental artifacts, such as issues with cable connections or detector saturation.

4-wave mixing in krypton (Kr) resulted in a spectral hole precisely at the ionization potential (*IP*) position of NH (13.480 $\pm$ 0.002 eV[62]) due to Kr absorption. This compelled us to switch the VUV generation line from Kr(I) to xenon (Xe(I)). Consequently, the UV laser was adjusted to 249.63 nm. However, another unforeseen obstacle arose. To reach the *IP* of NH, the required wavelength for the visible laser was approximately 350 nm in the near-UV region, which coincided closely with the limitation range covered by the dichroic mirror responsible for superimposing the UV and visible lasers. As a result, the transparency for the visible line was low, leading to reduced VUV intensity. Despite attempts to optimize the optical setup and the local pressure of the rare gas, the VUV intensity remained several times lower than normal, rendering efficient ionization measurements for NH radicals unachievable. Consequently, the study on NH radicals was temporarily halted. NH studies could be realized in the future by improving the NH radical concentration through the development of the source device or by finding a way to achieve higher VUV intensity at the *IP* of NH.

2.3.3 Radical source coupling electric discharge and chemical reaction

The use of metastable atoms to react with precursor molecules, followed by successive hydrogen abstraction, has proven to be a powerful and widely adopted method for radical production[64] Halogen atoms, particularly fluorine, have often been preferred due to their high reactivity[35,93] On the DESIRS beamline at the synchrotron SOLEIL, we employed the chemical reaction between silane precursor and fluorine atoms generated by microwave-discharge to produce a series of silane-derivative radicals, which will be discussed in Chapter 5. However, the corrosive nature of halogen elements poses safety risks and is not suitable for pulsed experiments as it can damage the pulsed valve. Therefore, it is necessary to explore alternative atoms that can be easily produced in a metastable state to enable

efficient reactions with precursors. Additionally, cost is also a significant factor to consider. Oxygen and nitrogen are considered as potential alternatives. Several references [108,114,126] have investigated the reactivity of the metastable oxygen atom, O(^{1}D), with various organic molecules, showcasing the production of radical species. Similarly, the reactivity of the metastable nitrogen atom, N(^{2}D), has been studied in the context of radical generation from organic molecules. [52,127] Note that these studies were mainly continuous experiments and the metastable atoms were produced by either laser photolyis [114,126,127] or microwave discharge. [52] Experiments applying electric discharge to produce metastable O or N atoms are still relatively scarce, not to mention those aiming to produce radicals. Lu *et al.* succeeded in doing this by generating metastable O atoms and conducting reactions with silane (SiH_4) and ethene (C_2H_4) under cross-beam conditions. [108]

Based on the electric discharge device we had, we proposed a new strategy combining a high-voltage discharge source for generating metastable atoms (O/N), along with chemical reactions for radical production. This pulsed experiment will offer an exciting and novel approach to radical source development in our setup.

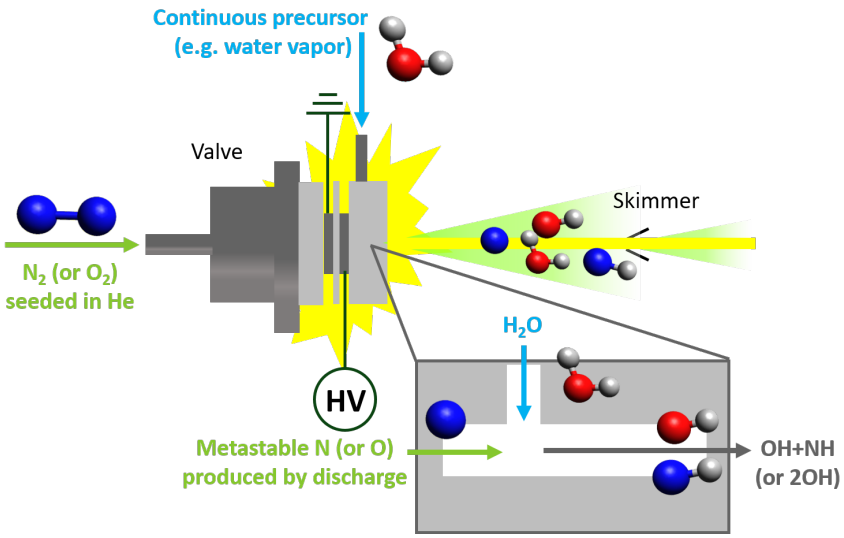

Figure 2.15: Illustration of the radical source coupling electric discharge and chemical reaction

As illustrated in Fig. 2.15, the new device is similar to the discharge device but includes an additional molecular entrance carved into the third Teflon piece after the discharge electrodes. In this device, O_2 or N_2 molecules seeded in the carrier gas are introduced *via* the pulsed valve, and are subsequently broken within the plasma generated by the pulsed high-voltage electric field applied to the two mesh electrodes. The resulting metastable atoms then encounter a continuous flow of precursor molecules fed from above, where they interact by abstracting hydrogen atoms from the precursor molecules, leading to the production of radicals. For test experiments, we used water as precursor molecules. Ideally, this device should generate pure OH radicals through the reaction with O(^{1}D) atoms or produce OH and NH radicals through the reaction with N(^{2}D) atoms.

In our experimental conditions, we observed that metastable nitrogen is more readily produced than metastable

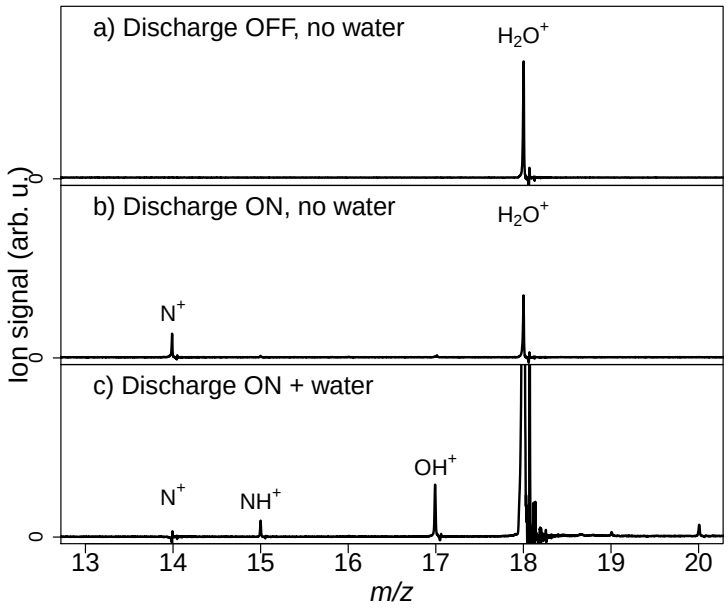

Figure 2.16: Mass spectra recorded for reaction of H_2O with N produced by discharge from 6% N_2 in He, at the photon energy of 13.519 eV. a) No discharge voltage is applied, and no water is injected. b) High discharge voltage is applied, without the injection of water. c) High discharge voltage and continuous water vapor are supplied.

oxygen, resulting in the generation of OH and NH radicals. Fig. 2.16 illustrates the mass spectra recorded at photon energy of 13.519 eV using 6% N_2 in He and H_2O precursor. The radical production through the two-step process is clearly demonstrated by the observed signals:

- When the discharge voltage is not supplied and no water is injected, only a weak signal corresponding to the ionized residual water is detected (see panel a) of Fig. 2.16).
- Under high-voltage discharge conditions, a signal at *m/q* = 14 appears, attributed to the photoionization of metastable N(^{2}D) atoms (see Panel b). Indeed, the *IP* of ground state N is 14.53 eV, indicating that the photon energy is not sufficient for ionizing N atom in its ground state.
- With both the discharge voltage and continuous water vapor supplied, NH^+ and OH^+ ions at *m/q* = 15 and *m/q* = 17, respectively, are observed (see panel c). This suggests that these radicals are produced by the reaction between the metastable N(^{2}D) atoms and the water molecules.

With the new strategy for radical generation, we successfully produced NH radicals, with a higher yield compared to the method of electric discharge. However, as mentioned earlier, the ionization potential value of NH falls within a small range that our VUV generation setup based on the 4-wave mixing process cannot reach. This limitation has resulted in a stalemate for the spectroscopic work on this radical. On a different note, for the generated OH radical, the spectroscopic studies of the neutral and cationic states have been extensively conducted at medium to high resolution.[66,70,75,115] This makes the OH radical a benchmark molecule to evaluate the production efficiency of our radical source, rather than a target for spectroscopic measurements. In short, the combination of the electric

discharge and the reaction with metastable atoms in this new device offers potential for generating a broader range of radicals, which could be further explored in future studies.

2.4 Photoionization spectrometers

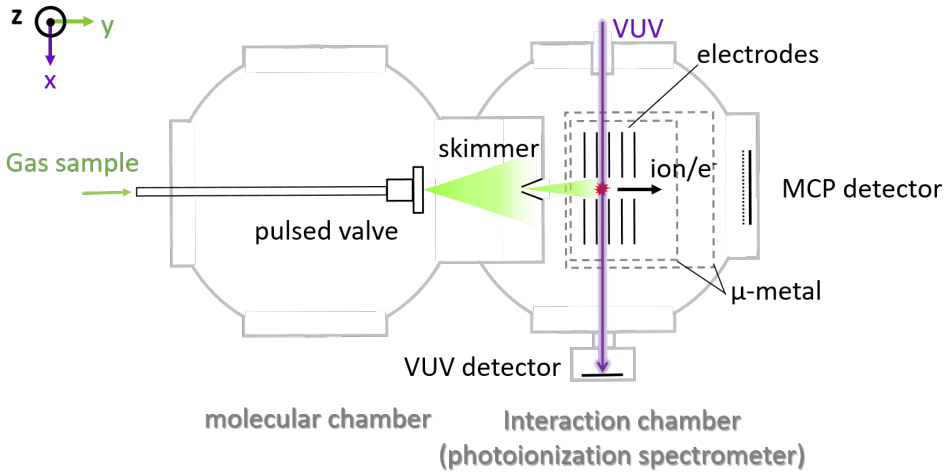

Figure 2.17: Layout of the photoionization spectrometer in the interaction chamber of the VULCAIM setup. The directions of the VUV laser and the molecular beam are indicated on the diagram, aligned along the *x* and *y* axes, respectively. The *z*-axis represents the direction perpendicular to the plane. In this spectrometer configuration, the TOF direction is parallel to the molecular beam, and the MCP detector is positioned along this axis for measurements.

As illustrated in Fig.2.17, the photoionization spectrometer of the VULCAIM setup consists of a compact 5-ring-electrode stack and a Micro-Channel Plate (MCP) detector located at the end of the interaction chamber, parallel to the *y* direction of the pulsed molecular beam. Two holes aligned along the *x*-axis allows the VUV laser radiation to enter the electrode stack and interact with the molecules within the spectrometer. The design of this spectrometer structure allows us to perform various photoionization spectroscopic methods, such as PFI-ZEKE PES, MATI and mass spectrometry, making it suitable for fulfilling most of the spectral measurement requirements in the context of my PhD project. However, during the test of the radical source using electric discharge, we encountered a difficulty (see section 2.3.2). The pulsed discharge process emitted a bright light that inevitably saturated the on-axis MCP ion detector before the arrival of ions. Since the microchannel plate detector required more time to recover than the arrival time of ions, the ion detection was dramatically reduced by the light.

To address this issue, two solutions have been investigated. In the first one, we replaced the previous configuration by a Reflectron TOF mass spectrometer (aligned in the *y* direction), with which the detector is laterally shifted from the molecular beam axis. In the second solution, a new spectrometer, very similar to the original one, has been designed to be used vertically (TOF direction along the *z*-axis). In this section, I will provide a detailed description of the structure of the two photoionization spectrometers I used during my PhD work, with a particular focus on the newly coupled Reflectron TOF setup integrated into the VULCAIM configuration.

2.4.1 Photoion/photoelectron spectrometer

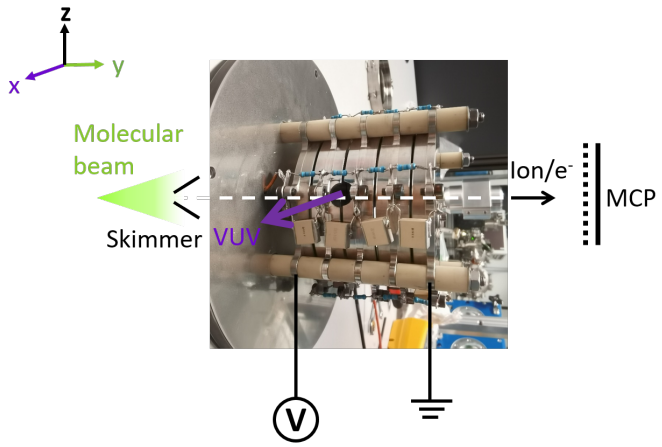

(a) electrode stack

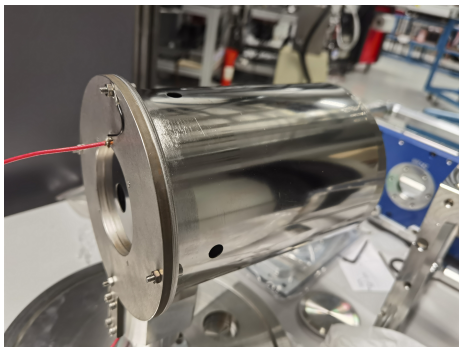

(b) double μ-metal covers serving as magnetic shielding

Figure 2.18: Photo of the components of the VULCAIM photoion/photoelectron spectrometer. a) Electrode stack composed of five ring electrodes. Two holes aligned along the *x*-axis allows the VUV laser radiation to enter the electrode stack and interact with the molecules on the *y*-axis within the spectrometer. b) Electrode stack equipped with the double μ-metal covers serving to cancel out the background magnetic field.

Fig. 2.18 (a) displays a photo of the electrode stack, originally built by Christian Alcaraz and Barbara Cunha de Miranda for the laser center of the Paris-Sud University (CLUPS)[39,99] following the design of the Merkt's group.[117] The main structure is composed of five ring electrodes in stainless steel, each isolated from the others by ceramic cylinders. Additionally, these electrodes are connected in series with four parallel resistors and four parallel capacitors that have fixed parameters. This design enables the application of synchronized gradient voltages to the series of electrodes, characterized by a sharp temporal slope. Within the central region of the circle electrodes lies the interaction region where the VUV laser intersects with the cold molecular beam, which enters the interaction chamber through the skimmer hole. Once molecules are irradiated, after a delay time of typically 1-2 μs, pulsed voltages are applied to the electrodes. Either positive ions or negative electrons are then accelerated and directed towards the MCP detector. The MCP detector is composed by regular arrays of channels, with each channel serving as a continuous-dynode electron multiplier. This means that a single charged particle or photon can initiate a cascade of electrons, amplifying the original signal by several orders of magnitude. The voltage signal is ultimately transmitted to the oscilloscope and the data-acquisition interface.

The photoionization spectroscopic experiments are highly sensitive to stray electric and magnetic fields, particularly in photoelectron spectroscopy. On the one hand, stray fields induce shifts in molecular energy levels through the Zeeman or Stark effect, leading to spectral distortions or broadening of spectral lines. On the other hand, stray fields may also induce additional pathways or alter the ionization dynamics, impacting the observed intensities and shapes of the ionization signals. To mitigate the effects from stray fields, all components in the setup, including

pumps and pressure gauges, are chosen with minimal magnetic effects. Besides, the interaction area is enclosed within double covers made of μ-metal (a nickel-iron ferromagnetic alloy) with high magnetic permeability, as displayed in Fig.2.18 (b). These covers serve as magnetic shields, protecting the interaction area from static magnetic fields such as Earth's magnetic field.

Recently, a new compact set of electrodes made from molybdenum metal has been bought to replace the original one, aiming to further decrease the presence of potential parasitic magnetic field issued from the electrodes themselves. This new stack has been designed such that it allows two perpendicular beams to enter the spectrometer and be orthogonal to the TOF axis. It can thus be used either with the TOF aligned along the *y*-axis of the molecular beam, or with the TOF aligned along the *z*-axis. With this later configuration, it allows to extract charged particles in a direction perpendicular to the radiation and molecule axes. This serves the purpose of mitigating the Doppler broadening effect on linewidths and can address the challenge of MCP saturation resulting from discharge light when investigating radical sources *via* electrical discharge. Another potential of the updated electrode stack is to induce an additional radiation pathway. This opens avenues for studying radical sources using photolysis, as well as facilitating applications in action spectroscopy. Both development directions for the experimental configuration with the new stack are interesting and promising.

2.4.2 Reflectron ion-mass spectrometer

As previously mentioned, the Reflectron ion mass spectrometer was installed to address the issue of MCP saturation when using electric discharge as a radical source, as seen in Fig. 2.19 showing the layout of the equipment and its photo. To ensure a background pressure of <10^{-6} mbar, the TOF tube is equipped with a turbomolecular pump. A more detailed illustration of the equipment setup, which includes the electrode stack and the Angular Reflectron D-850 TOF tube used in the Reflectron TOF ion mass spectrometer, is given in Fig.2.20 (a). Fig.2.20 (b) shows the photo of the electrode stack (without the Reflectron part). This spectrometer configuration is based on a classic Wiley-McLaren time of flight (TOF) momentum imaging analyzer,[176] which is featured by the double-acceleration region for ion extraction. Under irradiation, positive ions are created between the first plate (A1, Repeller plate) and the second plate (A2, Extraction grid). They are initially accelerated by the voltage applied to the repeller plates. Subsequently, ions are successively accelerated in a second electric field between A2 and the grounded third plate before entering the field-free tube. Compared to a single-acceleration system, this double-acceleration system offers advantages in terms of space resolution, which can be adjusted by controlling the ratio between the two electric fields.[176] As illustrated in the scheme, the axis of the extraction electrodes compact set is not aligned with that of the tube, therefore a pair of deflection plates (XY1 and XY2) are equipped to be able to deflect ions on transversal direction according to the target location. Typically, the XY1 plate is grounded, and the voltage of XY2 is adjusted to optimize the signal. If the MCP detector is installed at the end of the tube, linear TOF mass spectroscopic measurements

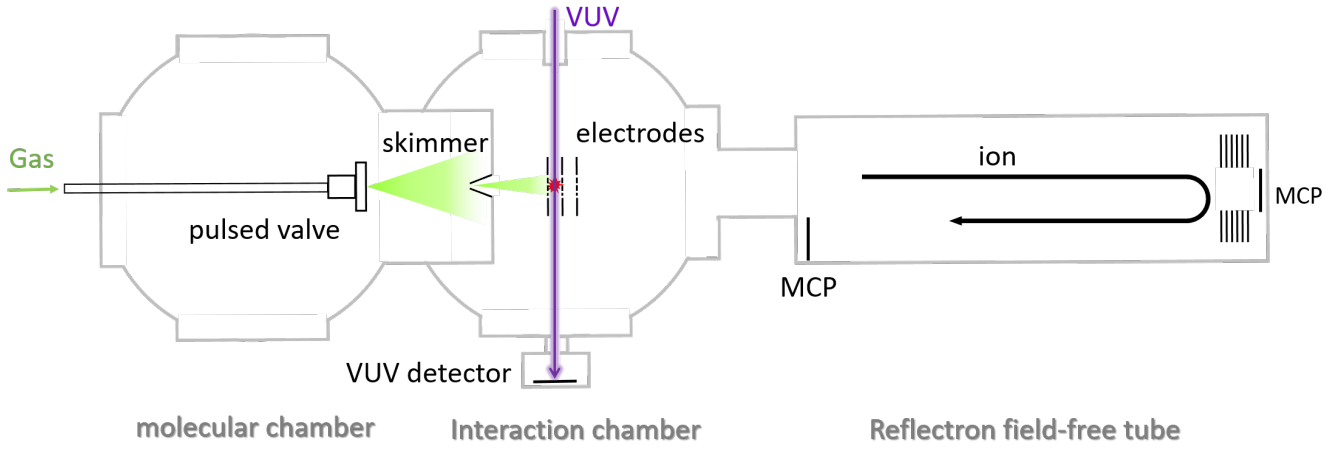

(a)

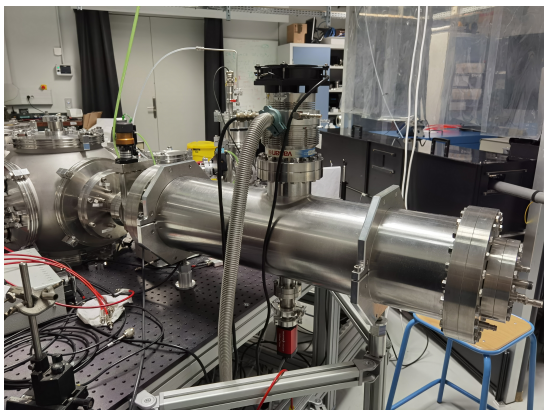

(b)

Figure 2.19: Layout of the Reflectron ion-mass spectrometer coupled to the VULCAIM setup in (a) and its photo in (b).

can be performed. Alternatively, at the end of the tube, there are the grids (R1, Retarding grid) for decelerating the charged particles, followed by another one (R2, reflector grid) for reflecting them back. In this case, the MCP detector is positioned backward to the ion source. All voltages are supplied by the D-803 Positive Ion Power Supply. Initially, in the test experiments, the extraction voltages on A1 and A2 were pulsed separately using two pulsers. Later, a box containing resistances and capacitors,similar to the electronic structure in the previous electrodes compact set design, was added to supply simultaneously the voltages on A1 and A2 with the appropriate ratio.

In Fig. 2.13,Fig. 2.14 and Fig. 2.16 recorded using the Reflectron TOF configuration, a mass resolution of approximately 1200 is demonstrated, which is close to the standard resolution of 1500 offered by the manufacturer.[3] Here the mass resolution is defined as $m/\Delta m$. To further improve the resolution for both configurations (linear and Reflectron TOF), additional tests need to be conducted. One possible approach is to explore the use of focus voltages. By optimizing and adjusting the focus voltages, it is possible to achieve higher resolution in both the linear and Reflectron TOF configurations.

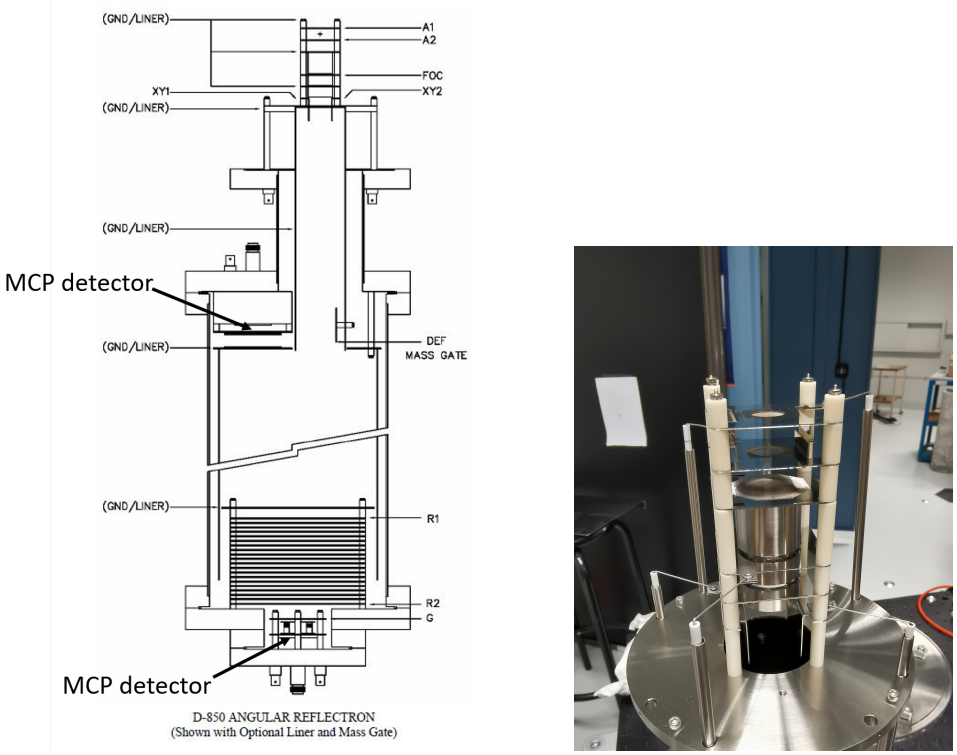

Figure 2.20: Scheme of the reflectron TOF (Jordan TOF Products) mass spectrometer in (a), extracted from the user's manual. Photo of the electrode stack shown in (b).

2.5 Temporal synchronization of the setup

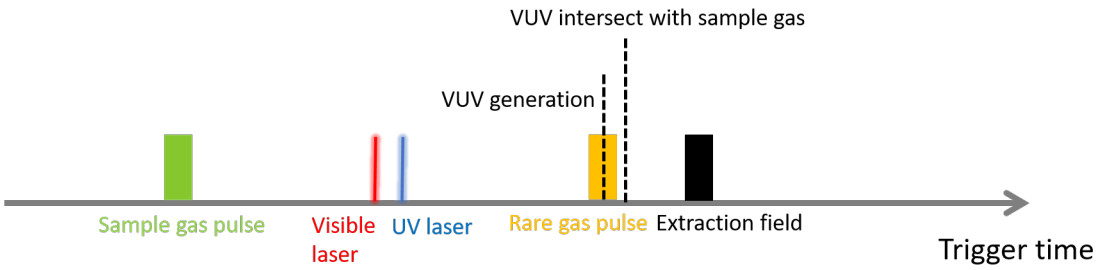

Figure 2.21: Temporal synchronization system of VULCAIM by controlling the trigger timing of laser pulses, gas pulses, and extraction field pulses.

The entire VULCAIM setup operates in synchronization, with all components pulsed at a frequency of 20 Hz. Fig. 2.21 illustrates the temporal synchronization system, which is achieved through an electronic interface. This interface allows for precise control over the timing of laser pulses, gas pulses, and extraction field pulses. By optimizing the trigger timings, we ensure a temporal superposition of the nanosecond laser pulses with the rare gas pulse, a critical factor for the efficient generation of VUV radiation. Additionally, it is essential to achieve temporal superposition of the generated VUV pulse with the sample gas pulse. This synchronization ensures an efficient inter-

action between them, facilitating the photoionization spectroscopic measurement process. To avoid any undesired influence of electric fields such as the Stark effect, the extraction field is triggered after the laser irradiation.

Chapter 3

Photoionization spectroscopic methods on VULCAIM: development of PRFI-ZEKE PES and implementation of MATI spectroscopy

In the realm of this thesis, photoionization spectroscopy is used as a powerful tool for investigating the (ro)vibronic structure of cations of isolated molecules. As discussed in Chapter 1, this technique has been developed over several decades, with a particular focus on achieving measurements at high spectral resolution. However, the pursuit of high resolution often comes at the cost of reduced signal-to-noise ratio in the measured spectra. This compromise presents a significant challenge, especially in our work with free radicals, where the spectroscopic signal is limited by the low production yield due to their inherent instability. To address this issue, we have proposed an advanced technique called Pulsed-Ramped-Field-Ionization ZEro-Kinetic Energy PhotoElectron Spectroscopy (PRFI-ZEKE PES), which will be presented in detail in Section 3.1.

Furthermore, given that our experiments on radical species may involve diverse molecules during the production of a specific radical, we have also explored the Mass-Analyzed Threshold Ionization (MATI) spectroscopy. The advantage of this technique lies in its capacity to acquire photoionization spectra with an inherent mass selectivity. Additionally, this approach serves the dual purpose of monitoring the presence of the target molecule while identifying its transition energies, a particularly valuable asset when working with unstable radical sources. More comprehensive details on this method will be given in Section 3.2.

Both of these spectroscopic techniques are implemented using our VULCAIM setup, which is thoroughly described in Chapter 2. This experimental setup provides a versatile and reliable platform for conducting precise and insightful spectroscopic investigations in our research on free radicals.

3.1 PRFI-ZEKE

3.1.1 Introduction

The Pulsed-Field-Ionization ZEro-Kinetic Energy PhotoElectron Spectroscopy (PFI-ZEKE PES) is a well-established technique for high-resolution photoelectron spectroscopy and its principles have been illustrated in Chapter 1. In this section, I will present a recent development of this technique, baptized Pulsed-Ramped-Field-Ionization (PRFI) ZEKE PES, which was proposed during the PhD of Oliver Harper[69] (previous PhD student in the group) and finalized during my PhD first year. It introduces a new scheme for data acquisition and treatment, aiming at recording PFI-ZEKE PE spectra with "artificially" increased statistics. The inspiration for the development came from the procedures described by Hollenstein *et al.*[83] along with the technique proposed by Reiser *et al.*[138], as well as the data treatment procedure used in Slow PhotoElectron Spectroscopy (SPES, see Section 1.2.4 of Chapter 1).[134] The experiments to test this new method were carried out using our VULCAIM setup. The detailed description and results of these experiments have been published in 2022.[73] Very recently, our method has been used by Professor Merkt's research group to investigate the photoionization thresholds of metastable rare gases.[78] A new record for spectral resolution of photoelectron spectroscopy was established, reaching an impressive 0.05 cm^{-1}, for photoionizing transitions of metastable Argon.

3.1.2 Method principle

As a reminder, the high spectral resolution of PFI-ZEKE PES can be achieved by applying a sequence of pulsed electric fields with steps of small amplitudes, which allows for high selectivity in pulsed-field-ionization of high Rydberg states. This resolution can be further improved by employing a prepulse followed by a series of pulses with opposite polarity with respect to the prepulse and with smaller amplitude, as depicted in Fig.1.9 of Chapter 1. With this procedure, Hollenstein *et al.*[83] successfully recorded the PFI-ZEKE spectra with the highest spectral resolution ever obtained, below 0.1 cm^{-1} (0.06 and 0.055 cm^{-1} for argon and molecular nitrogen, respectively), using a sequence composed of a prepulse of +167 mV/cm followed by successive negative pulses from -75 mV/cm down to -161 mV/cm with -8.5 mV/cm steps.

Theoretically, the best spectral resolution could be reached by using a sequence with infinitesimal step amplitudes. In this case, the spectral resolution would no longer be limited by the electric field but by other factors such as the laser bandwidth, Doppler broadening, etc.[73] However, achieving PFI-ZEKE PES with such a sequence is challenging as the resolution improvement comes at the expense of the signal intensity. To address this issue, our solution consists in 'artificially' increasing the statistics to improve the signal-to-noise ratio (S/N ratio) by adding the signals obtained through a ramp of electric fields after a suitable Stark-shift correction.

To do so, we use an electric field sequence composed by a prepulse, like in the work of Hollenstein *et al.*,[83]

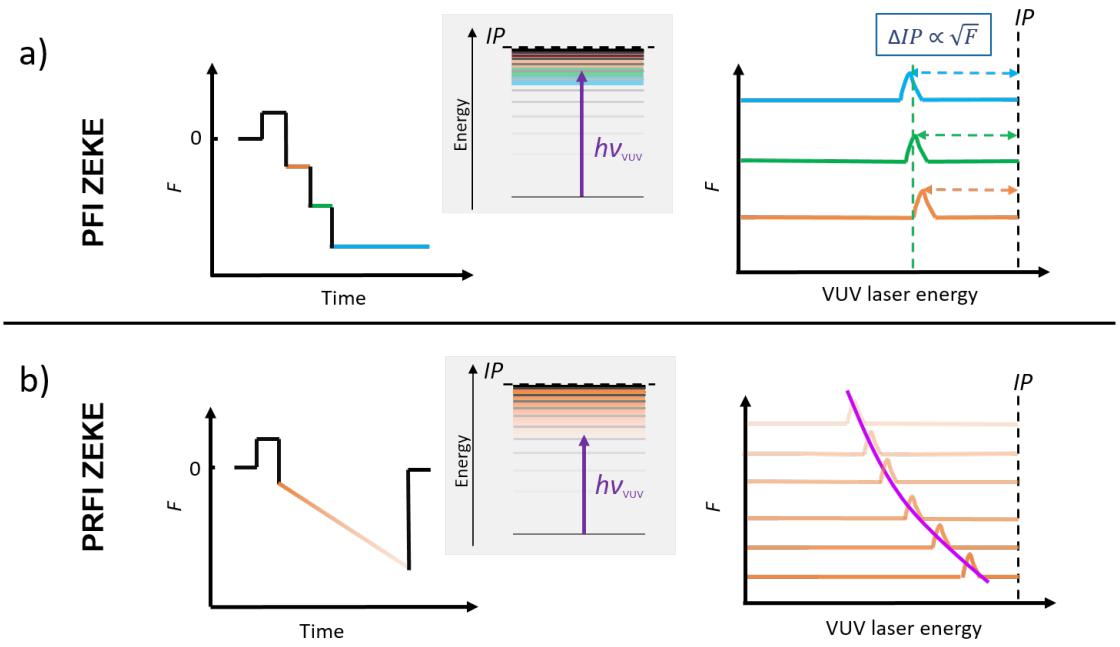

Figure 3.1: Comparison of the PFI-ZEKE (panel a)) and PRFI-ZEKE (panel b)) PES methods. A pulsed step sequence and a pulsed ramp sequence are respectively displayed in the left part of the panels. Their selectivity of the field-induced ionization of Rydberg states is illustrated in a simplified way in the middle. The photoelectron signal recorded as a photoelectron spectrum and a 'ZEKE' matrix corresponding to the two methods is illustrated to the right of the panels. The field-free ionization potential (*IP*) is represented by a black dashed line. The colors are used to explain the correspondence among the electric field pulse, the field-ionized Rydberg states and the resulting photoelectron signal with a certain Stark shift.

followed by a linear ramp of negative electric field, similar to the one used in the work of Reiser *et al.*[138] Fig. 3.1 illustrates the comparison between the field sequence used in conventional PFI-ZEKE PES (panel a)) and the proposed sequence with infinitesimal step amplitudes, forming a linear ramp of field sequence (panel b)). In the conventional PFI-ZEKE technique, the ionization of Rydberg states occurs in a specific order, with each pulse in the sequence targeting a particular "bunch" of Rydberg states. In Fig. 3.1 the corresponding pulses and ionized Rydberg states are represented with the same color. The resulting photoelectron spectra are recorded by integrating the time-of-flight (TOF) signal of the electron over the corresponding time windows as a function of the laser wavenumber. In Fig. 3.1 a), three photoelectron spectra are recorded with a sequence of three pulses, where the amplitude of the pulse determines the magnitude of the Stark shift from the field-free *IP*. This is obvious from the difference in the signals shown in orange and blue. On the other hand, in PRFI-ZEKE (see panel b)), each point along the linear ramp sequence corresponds to an extremely narrow Rydberg 'bunch'. There is no longer a distinct splitting between field-ionized Rydberg 'bunches' or TOF of the produced photoelectron. As a result, the entire TOF is recorded, leading to a 2D matrix representation. The shape of the signal in the matrix appears as a curved line, which indicates the Stark shift evolution of the ionization potential (ΔIP) as a function of the square-root of the electric field.[83] The width of the "bunch" could be estimated to be approximately $2.3\sqrt{F}$,[83] the limited resolution of PFI-ZEKE technique (see Chapter1). However, it is important to note that, at the very beginning of the negative sequence, where the

magnitude is smaller or equal to that of the prepulse, the obtained resolution can be even smaller than the expected limitation.

The left scheme in Fig. 3.2 illustrates a more realistic matrix generated by modeling, with a photon resolution of 0.1 cm^{-1}.[73] In this matrix, the photoelectron TOF is turned into electric-field, taking into account the applied pulsed sequence and precise calibration of the electron TOF. An asymmetric profile of the curve signal could be observed with this more realistic modeling, which reflects the different field-ionization dynamics of the "red-" and "blue-shifted" Stark states,[83] as explained in Section 1.2.6.

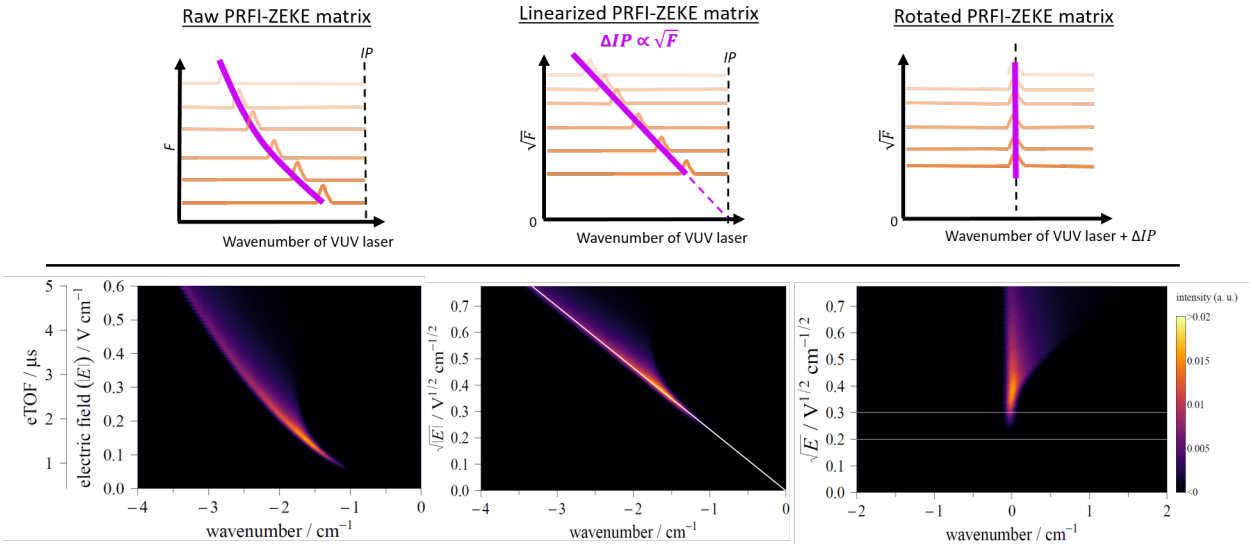

Figure 3.2: Illustration of the data treatment procedure from the raw PRFI-ZEKE matrix (left) to the linearized matrix (middle) and to the rotated matrix (right). In the lower panel, simulated matrix extracted from Ref. 73 are depicted to show more realistic matrix signal. See text for details.

After recording the "ZEKE matrix" in the PRFI-ZEKE technique, the next step is to perform the data treatment to obtain a photoelectron spectrum with higher S/N ratio, as explained before. In this case, we adopt a treatment procedure inspired by Slow PhotoElectron Spectroscopy,[134] which has been introduced in Chapter1. As a reminder, in SPES the “photoelectron matrix” represents the signal intensity (z axis) as a function of electron kinetic energy (y axis) and photon energy (x axis). To extract a photoelectron spectrum with a higher S/N ratio, the matrix is rotated in order to integrate the photoelectron signals over a specific kinetic energy range. In PRFI-ZEKE, the ZEKE matrix differs in the y axis, which represents the time-of-flight of the electron. To linearize this matrix, a square-root function is applied to the electric field (y-axis). Since the field-induced Stark shift is proportional to the square root of the electric field,[83] this transformation results in the linearized matrix shown in the middle panel of Figure 3.2. Subsequently, the straight diagonal line is fitted, shown as the straight white line in the linearized matrix. Once the line is fitted, it serves as a reference for "rotating" the matrix by the cross-point at zero field, producing the rotated matrix. The ionization threshold appears now as a vertical line, aligned with the y-axis.

The final step to extract a photoelectron spectrum from the rotated matrix consists in integrating the matrix

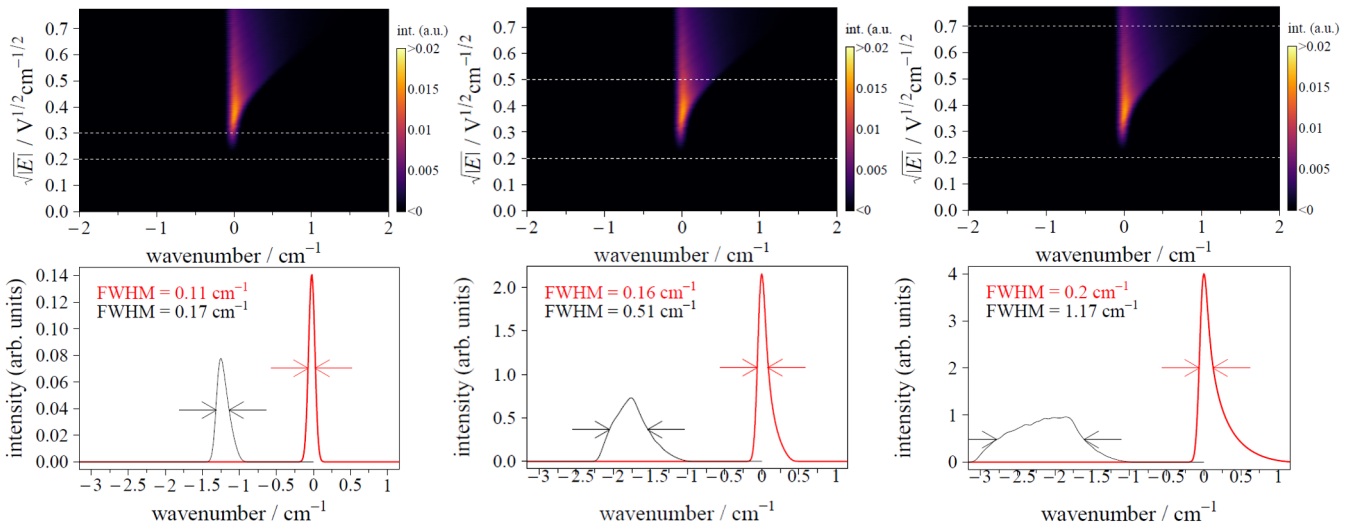

Figure 3.3: Illustration extracted from Ref. 73, showing a comparison of the modeled photoelectron spectra obtained by PRFI-ZEKE and PFI-ZEKE techniques. The photoelectron spectra in red in the lower panels are obtained by integrating the rotated matrix (upper panels) over the ranges delimited by the horizontal white dashed lines. The spectra in black are obtained by the standard PFI-ZEKE technique with a pulsed electric field covering the equivalent electric field range.

over a given range along the y axis. This step corresponds to the basic idea of the signal accumulation in the PRFI-ZEKE method. In Fig.5 of our article[73] (see Fig. 3.3), a comparison of spectra obtained by PRFI-ZEKE and PFI-ZEKE techniques with electric field covering the same range is demonstrated by modeling. It shows that the spectral resolution that PRFI-ZEKE could reach at the beginning of the ramp (small electric field range below the amplitude of the prepulse) is estimated to 0.11 cm^{-1}, which is very close to the laser bandwidth (0.10 cm^{-1}). In addition, with PRFI-ZEKE, by increasing the integrating region of the matrix, the signal can significantly increase without degrading the spectral resolution. In contrast, the conventional PFI-ZEKE method exhibits a lower increase in signal intensity and a more significant deterioration of the spectral resolution.

3.1.3 Experimental results and analysis

During Oliver Harper's PhD and my own, we conducted measurements using the PRFI-ZEKE method to investigate the rovibronic structure of two benchmark molecules, CO_2 and NO. We have recorded the PRFI-ZEKE PES of the $X^+\,^2\Pi_{g,1/2}(v^+ = 0) \leftarrow X\,^1\Sigma_g^+(v = 0)$ ionizing transition of CO_2. The corresponding results are reported in Ref. 73. This study also pointed out that the data treatment procedures such as the electron time-of-flight calibration and the matrix rotation could introduce uncertainties on the final field-free energy values.

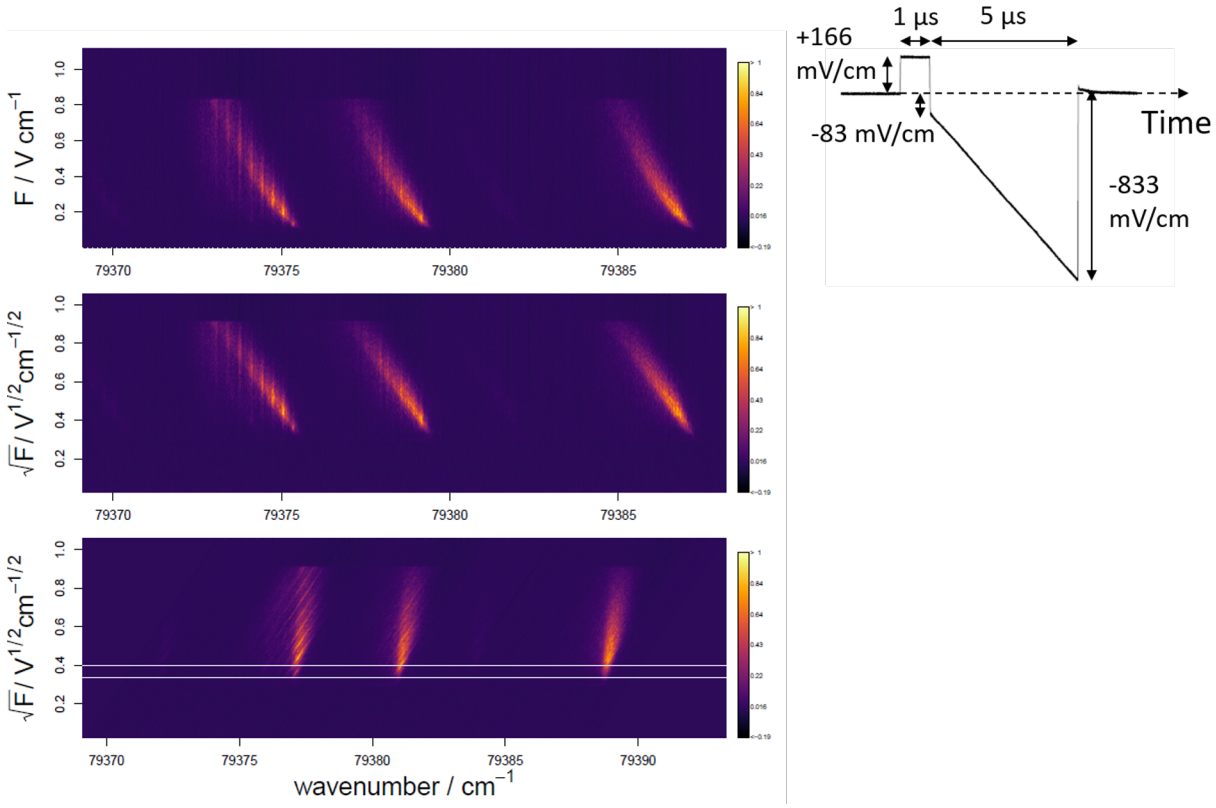

Figure 3.4: Experimental measurement of the $\mathrm{X}^+\,{}^1\Sigma^+(v^+=2) \leftarrow \mathrm{X}\,{}^2\Pi_{1/2}(v=0)$ transition of NO recorded with the PRFI-ZEKE method. The raw matrix, the linearized matrix and the rotated matrix are depicted in the upper, middle, and lower panels respectively. The color scales are arbitrary. The pulse sequence used for this measurement is shown on the right.

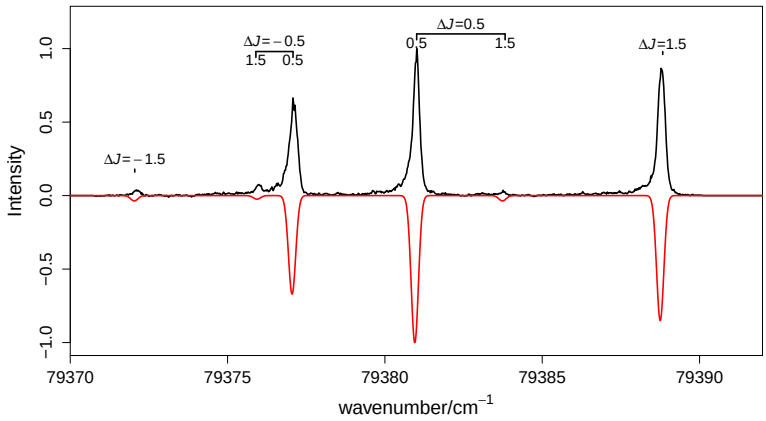

Figure 3.5: Final photoelectron spectrum of the $\mathrm{X}^+\,{}^1\Sigma^+(v^+=2) \leftarrow \mathrm{X}\,{}^2\Pi_{1/2}(v=0)$ transition of NO, obtained by integrating signal in the range delimited by the two white lines in the rotated matrix of Fig. 3.4. The simulation is shown in red, performed at T_{rot} = 1.8 K with a FWHM of 0.25 cm^{-1}.

At the beginning of my PhD, I performed PRFI-ZEKE experiments with NO in the vicinity of the $\mathrm{X}^+\,{}^1\Sigma^+(v^+=2) \leftarrow \mathrm{X}\,{}^2\Pi_{1/2}(v=0)$ photoionization transition. The PRFI-ZEKE matrix recorded and treated with the procedure

described above are illustrated in Fig. 3.4. The ramp sequence used to record the matrix is composed of a pre-pulse of 167 mV/cm for 1 μs, followed by a ramp from -83 mV/cm to -833 mV/cm during 5 μs. The photoelectron spectrum depicted in Fig. 3.5 is obtained by integrating the signal in the range delimited by the two white lines in the rotated matrix of Fig. 3.4, with the electric field strength smaller than the amplitude of the prepulse. The simulated spectrum in red shows excellent agreement with the experimental one. To simulate this band, I used the rotational constants obtained by Ref. 90 and Ref. 91 for the vibronic ground states of NO and the $v^+ = 2$ vibrational state of the electronic ground state of NO^+, respectively. The relative line-intensities of the simulations account mainly for the rotational temperature of NO in its ground state, which governs the population of the various rotational levels according to Boltzmann's law.

The obtained ionization energy for $\mathrm{X}^+\,^1\Sigma^+(v^+ = 2, J = 0) \leftarrow \mathrm{X}\,^2\Pi_{1/2}(v = 0, J = 0.5)$ transition is determined to be 79377.01±0.60 cm^{-1}, which is very close to the previously measured value of 79377.20±0.50 cm^{-1}.[91] The rotational temperature is estimated at 1.8 K with the simulation. The low rotational temperature indicates a good cooling of NO by the supersonic expansion through the Amsterdam Piezo Valve. The spectral resolution of the spectrum is approximately 0.25 cm^{-1}, which is a bit higher than the bandwidth of our VUV laser. There is an apparent increase of the bandwidth at the base of each peak, which makes the experimental spectrum look broader than the simulated one. We speculate that this phenomenon arises from the data treatment procedure, although further investigation is needed to provide a definitive explanation.

Fig. 3.6 addresses an interesting feature observed in the PRFI-ZEKE matrix during experiments on NO. Panel a) displays the raw PRFI-ZEKE matrix before the linearization treatment. The ramp sequence used to record the matrix is composed of a 1 μs prepulse of 167 mV/cm, followed by a 4 μs ramp from -83 mV/cm to -1.33 V/cm. To visualize the curved signals corresponding to rotationally resolved structure of NO^+, the color panel of the matrix is manually adjusted, leading to the saturation of the vertical lines appearing at higher energy and marked by an asterisk. These vertical signals are attributed to autoionization processes.[128] This assumption is confirmed by comparing the matrix with the NO^+ photoion yield spectrum recorded using our setup (panel b) and an absorption spectrum of NO obtained with the VUV FT spectrometer at the DESIRS beamline of the SOLEIL synchrotron (panel c)[42,74] in Figure 3.6. The vertical lines in the matrix precisely coincide with the positions of structures marked with asterisks in the photoion yield and absorption spectra, indicating their dependence on resonance with photon energy. Three of the vertical lines in the matrix appear as soon as the negative electric field is applied. In this case, the electric field serves only to extract electrons to the detector. The length of the vertical lines may provide information about the lifetime of the autoionizing states.

It is important to note that not all peaks of the photoion yield spectrum representing autoionization signals are present in the matrix. This can be attributed to either autoionization processes with fast dynamics or the low extraction electric field strength. Fast autoionization involves the ejection of photoelectrons during the delay time of electric pulse or by the prepulse. In the photoion yield spectrum, where ions are slower to leave the extraction region,

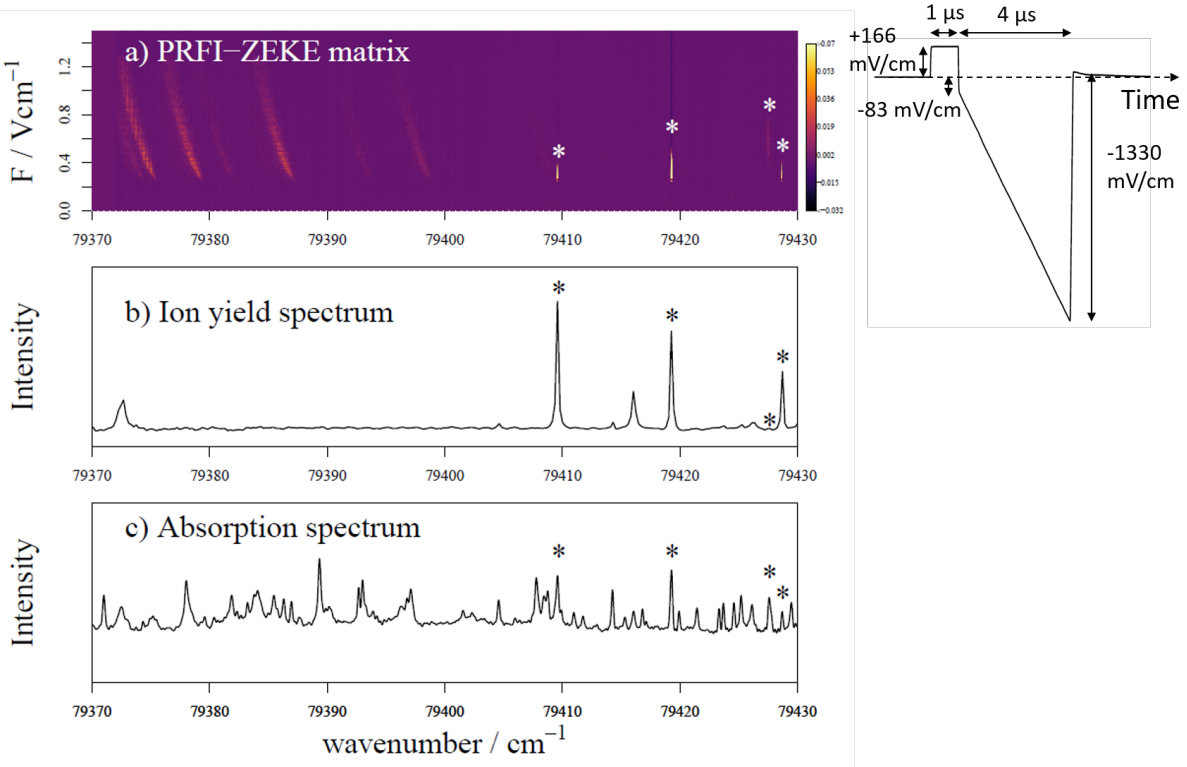

Figure 3.6: Comparison of a) the raw matrix obtained with a PRFI-ZEKE method, b) the photoion yield spectrum and c) the absorption spectrum[74] of NO in the vicinity of the $X^+\,^1\Sigma^+(v^+=2) \leftarrow X\,^2\Pi_{1/2}(v=0)$ photoionizing transition. The color scale in a) is manually modified to be saturated in order to see both the standard ZEKE signals in curved lines and the signals in vertical straight shape due to the autoionization process. The signals marked by an asterisk are common in the three measurements. Modified version of Fig.7 of Ref. 73. The pulse sequence used for the PRFI-ZEKE measurement is shown on the right.

the detection of signals from fast autoionization process is less selective compared to the matrix measurements. The absence of matrix signals due to the forced autoionization process can be understood as this type of signal only appears when the electric field is strong enough, as observed in the ion yield measurements (typically around 200 V/cm) but not in photoelectron measurements. This indicates a resonance between Stark states under a certain electric field and a cationic state. Furthermore, the vertical line observed at 79427.5 cm^{-1}, which appears after the electric field surpasses a certain value, can also be attributed to the forced autoionization process. In this case, the effect of the electric field does not lead to direct ionization, resulting in a vertical structure without a shift due to the electric field strength. The length of this vertical line provides insight into the possibility of coupling between Stark states and a specific cationic state.

3.1.4 Conclusion and perspectives

The PRFI-ZEKE technique shows several advantages compared to conventional PFI-ZEKE technique. Firstly, it allows to obtain meaningful spectrum with lower statistics, which reduces the measurement time. This point is particularly important when studying radical species produced in sources for which the temporal stability is limited. Secondly,

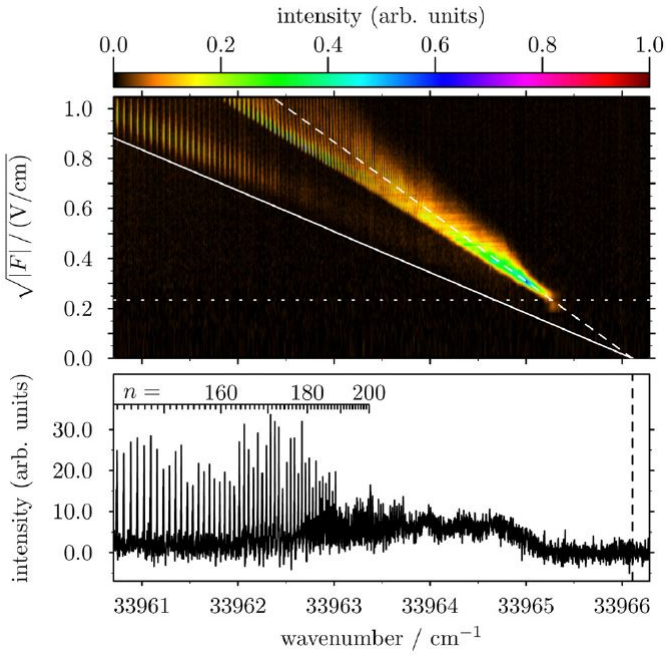

Figure 3.7: PRFI-ZEKE photoelectron spectrum of the $(3p)^5\,^2P_{3/2} \leftarrow (3p)^5(4s)^1\,^3P_2$ photoionization transition of Ar, extracted from Ref. 78. The one-dimensional spectrum below the 2D-matrix is obtained by integrating the latter over the complete vertical $\sqrt{F}$ range

the PRFI-ZEKE method provides a significantly improved signal-to-noise ratio, at a minimal cost of spectral resolution. In addition, the transition energies obtained in the final photoelectron spectrum are already field-free *IP*s, without the need to perform Stark-shift correction. Besides, the PRFI-ZEKE method shows great promise as a tool for studying autoionization processes. The presence of distinct autoionization signatures in the matrix may help to gain deeper insights into the dynamics and mechanisms of autoionization processes. However, further research is required to fully understand the nature and characteristics of these autoionization signatures in the matrix. The PRFI-ZEKE method, with its unique capabilities for high-resolution spectroscopy and matrix analysis, holds great potential for advancing our knowledge in this field.

Very recently, the group of F. Merkt[78] has adopted the PRFI-ZEKE technique, following our publication, to investigate the Rg^+ [...]$(ns)^2(np)^5\,^2P_{3/2} \leftarrow$ Rg[...]$(ns)^2(np)^5((n+1)s)^1\,^3P_2$ transitions of metastable rare-gas atoms Ar, Kr and Xe, with n = 3, 4, 5, respectively. Using a home-made tunable UV laser with a narrow bandwidth of 0.001 cm^{-1}, they studied the resolution limit and uncertainties in determining the field-free ionization energies of the PRFI-ZEKE PES method. As seen in Fig. 3.7, in a PRFI-ZEKE photoelectron spectra of Ar recorded with a pulse sequence consisting of a prepulse of 0.05 V/cm followed by negative-field ramp from -0.03 to -1.10 V/cm, the Rydberg states up to n = 190 are resolved. Their findings revealed that to achieve the resolution limit of this technique, a clear Stark inversion is only possible for Rydberg states with a limited range of n values. If n is too small, for example, n below 180 for Ar, the field ionization becomes adiabatic, leading to the failure of Stark inversion. On the other hand, if n is too high, the Stark states are randomized due to stray fields. By carefully selecting an appropriate n range (around 200 to 250)

and minimizing the effects of stray fields (using a minimal field of 3.3 mV/cm), they achieved a spectral resolution of 0.05 cm^{-1} for metastable Ar, which is now the new record in photoelectron spectroscopy. These studies offer valuable insights into the resolution limit and uncertainties associated with the PRFI-ZEKE technique. In the future, we aim to improve this technique on our VULCAIM setup and to use it to conduct photoionization spectroscopy for radicals produced by various radical sources.

3.2 MATI

3.2.1 Introduction

MATI (Mass-Analyzed Threshold Ionization) spectroscopy is a variant of PFI-ZEKE spectroscopy based on ion detection with the advantage of mass-selectivity. This spectroscopy involves also the field ionization of Rydberg states following their excitation under irradiation. However, due to the heavy mass of ions compared with that of electrons, relatively large electric fields are required to extract them from the ionization region, which leads to a reduced spectral resolution compared to PFI-ZEKE spectroscopy. More details have been discussed in Chapter1. In this section, I will present the first application of the MATI technique using our VULCAIM setup. This pioneering work serves as a foundation for further developments, particularly through the future coupling of MATI spectroscopy with a reflectron time-of-flight spectrometer. This combination would enable enhanced mass resolution and improved detection capabilities, opening up new avenues for investigating molecular states of ions.

3.2.2 Principle and first experimental tests

The first test experiments of MATI spectroscopy were carried out by investigating the $\mathrm{X}^{+\,1}\Sigma^{+} \leftarrow \mathrm{X}\,^{2}\Pi_{1/2}$ ionization transition of NO. Our design of pulsed electric field sequence for the MATI experiments is based on the work of Dessent *et al.*[43] Fig. 3.8 depicts our pulsed electric field sequences dedicated to low-resolution MATI spectroscopy (panel a)) and high-resolution MATI spectroscopy (panel b)), along with the illustration of the corresponding field-ionized Rydberg structures.

In the low-resolution MATI scheme, after the pulsed laser firing, we applied a 8 μs prepulse of 833 mV/cm, followed by a 10 μs high voltage pulse of 167 V/cm (see Fig. 3.8). The purpose of the prepulse was to spatially separate the spontaneous ions, which are produced by direct photonionization and field-ionization of very high-n Rydberg states (in orange), from the ions generated by field-ionization under the high voltage pulse (in red). This separation results in two corresponding TOF ion signals, as displayed in Fig. 3.8 panel a). The TOF positions of the two types of signal were confirmed by turning the prepulse OFF and ON, as demonstrated in panel a) and b) of Fig. 3.9, respectively. When the prepulse was OFF, only a single ion signal consisting in the direct photoionized molecules and high-voltage field-ionized molecules was observed, with its TOF determined by the high voltage extraction pulse. Conversely, when the prepulse was ON, the MATI signal produced by the high voltage pulse exhibited the same TOF as in the case of the prepulse OFF, while only the TOF of the spontaneous ions was shifted due to the presence of the prepulse.

However, it was counter-intuitive to observe that the MATI ions arrived at the detector earlier than the spontaneous ions, as depicted in the experimental TOF spectrum in panel b) of Fig. 3.9. The distance between the extraction electrodes is defined as "d_{ext}". This observation contradicted our initial expectation that the positive prepulse would

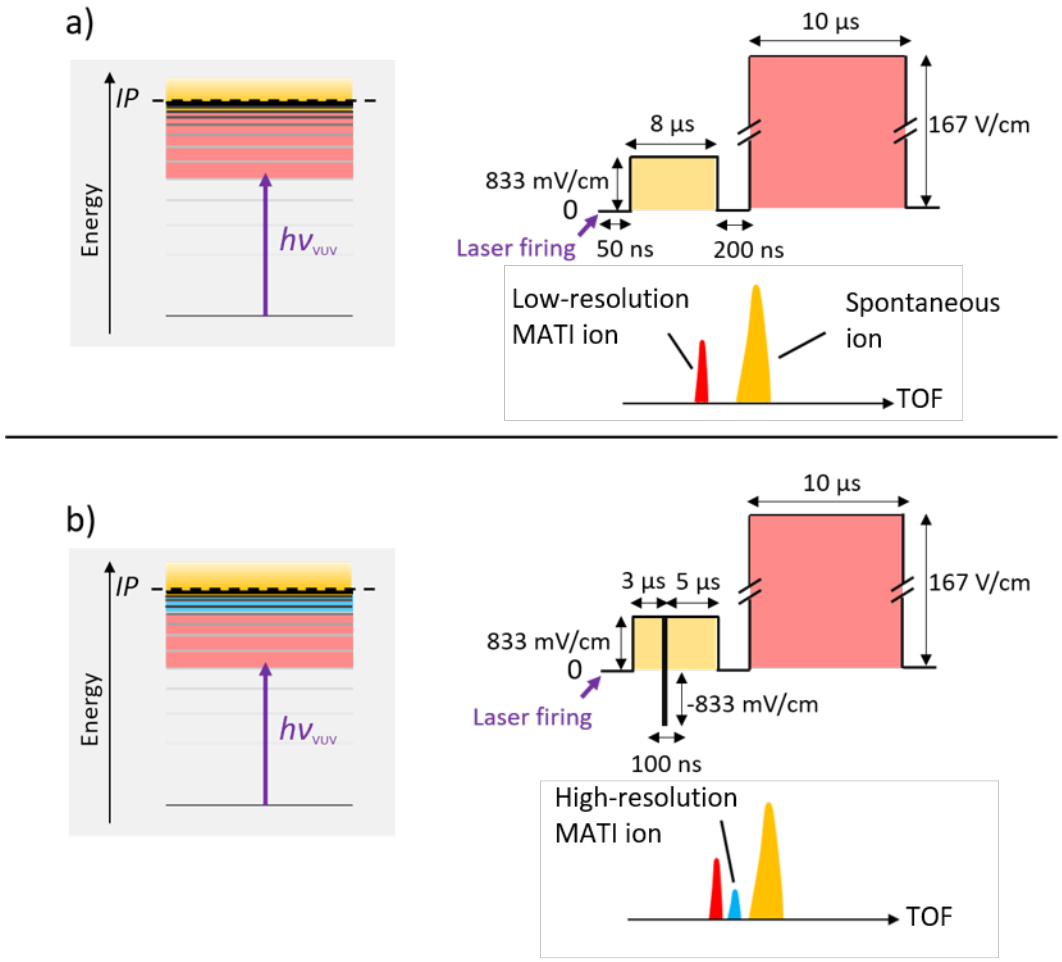

Figure 3.8: Scheme of the typical pulsed electric field sequences dedicated to low-resolution MATI spectroscopy (panel a)) and high-resolution MATI spectroscopy (panel b)). The selectivity of ionization by the electric field pulses is depicted in a simplified manner to the left of the panels. The TOF spectra are shown below the sequences. The colors are used to illustrate the correspondence among the electric field pulses, the ionized states, and the TOF signals of ions.

accelerate the spontaneous ions, resulting in earlier arrival times, as demonstrated in the paper of Dessent *et al.*[43] To explain this discrepancy, we propose a mechanism illustrated in Figure 3.10. Specifically, the spontaneous ions are accelerated by the prepulse towards the detector direction, traveling a distance denoted as "*x*". However, during the high voltage pulse, the MATI ions are produced and acquire more electric potential energy upon leaving the extraction region compared to the spontaneous ions, especially considering the almost 200 times difference of the V_1 and V_2 values (V_1=0.833 V/cm, V_2=167 V/cm). Consequently, the MATI ions overtake the spontaneous ions in the free-field region along the path towards the detector.

We also explored high-resolution MATI method by introducing an additional negative pulse of -833 mV/cm for 100 ns in the prepulse, after 3 μs of the trigger of the prepulse, as illustrated in panel b) of Fig 3.8. This small pulse with opposite polarity served to selectively field-ionize the remaining Stark states of high-n Rydberg states which are partially ionized by the prepulse, leading to a high spectral resolution. The principle behind this process has been

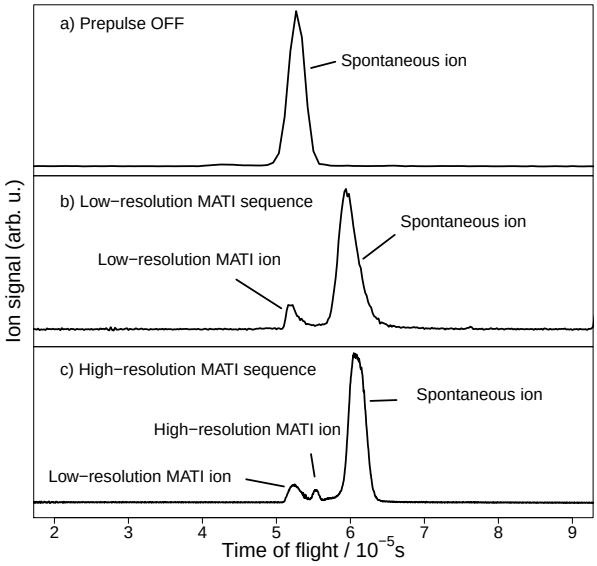

Figure 3.9: Comparison of TOF ion signals produced a) without the trigger of the prepulse, b) by field sequence dedicated to low-resolution MATI spectroscopy and c) by field sequence dedicated to high-resolution MATI spectroscopy. Note that the TOF spectrum displayed in c) panel was recorded under different conditions compared to panel a) and b), resulting in differences in spectral characteristics such as the bandwidth. The time scale of the TOF spectrum in c) is provided.

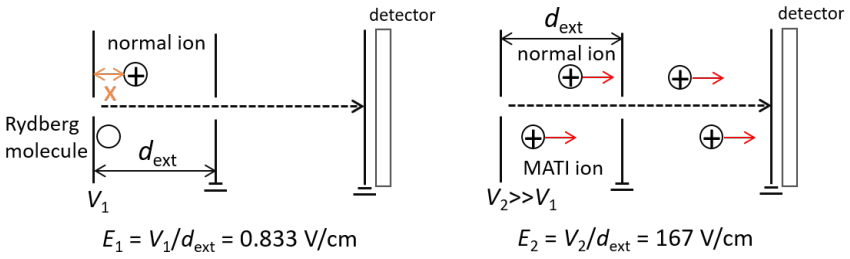

Figure 3.10: Scheme illustrating the dynamics of the MATI ions and the spontaneous ions in our experiments.

explained in Chapter1 and is also employed in PRFI-ZEKE PES, as demonstrated in the previous section. The short duration of this negative pulse is necessary to ensure the spatial separation of the three obtained ion signals. The recorded TOF spectrum is depicted in panel c) of Fig. 3.9.

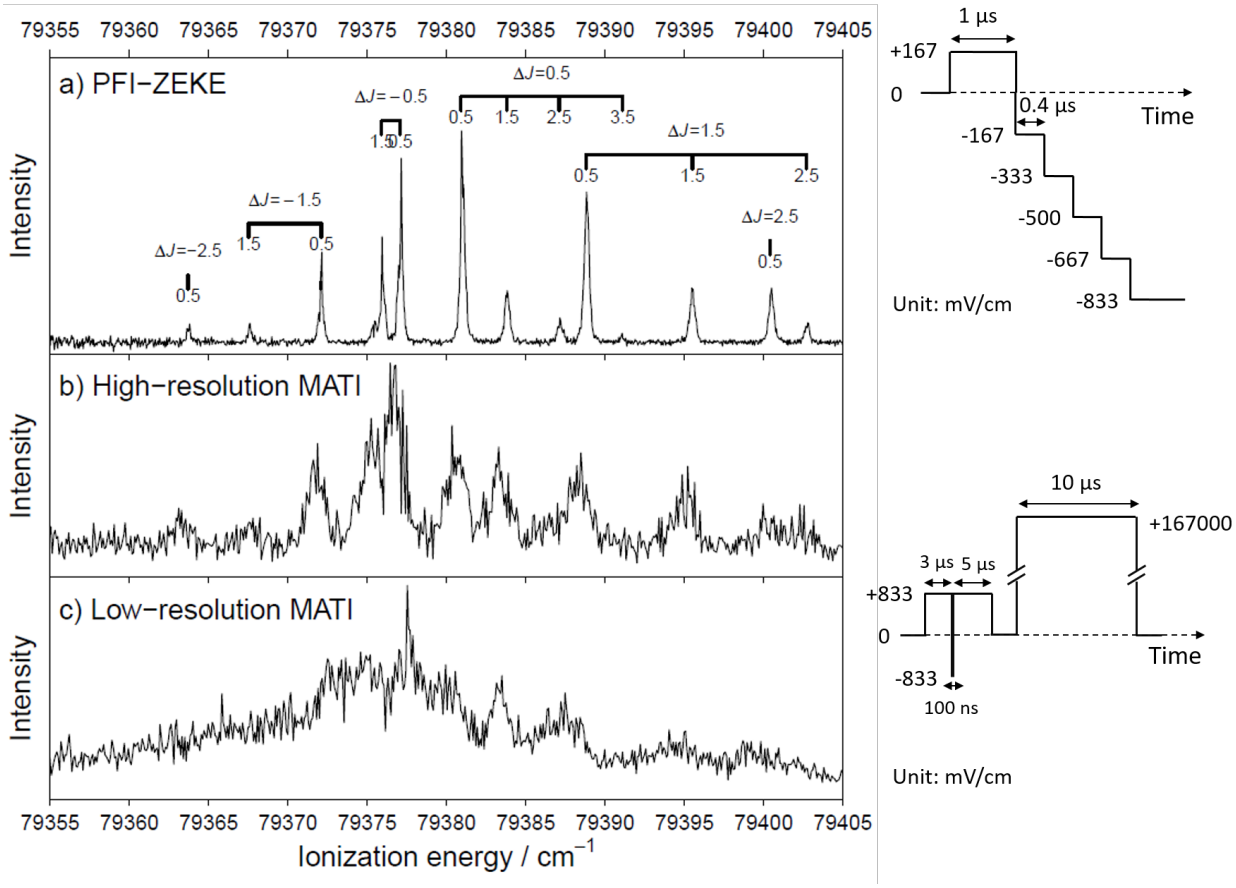

Figure 3.11: Comparison of NO spectra recorded by PFI-ZEKE spectroscopy (a) and MATI spectroscopy at high resolution (b) and low resolution (c). The Stark shift has been corrected to compare the spectra. The pulsed electric field sequence employed for the PFI-ZEKE measurement is composed by a prepulse of 167 mV/cm followed by successive negative pulses from -167 mV/cm down to -833 mV/cm with -167 mV/cm steps. The spectrum depicted in panel a) corresponds to the first negative pulse (-167 mV/cm), which performs the best resolution obtained by this sequence at 0.3 cm^{-1}. The sequence for the MATI is composed by a 8 µs prepulse of 833 mV/cm, inserted with a 100 ns negative pulse of -833 mV/cm at 3 µs, and a 10 µs high voltage pulse of 167 V/cm after a delay of 200 ns. The spectral resolution of the recorded high-resolution and low-resolution MATI spectrum is 1.8 and 2.9 cm^{-1} respectively. The statistics and scan step for PFI-ZEKE and MATI measurements are 40 sweeps, 0.002 nm and 40 sweeps, 0.004 nm, respectively.

Fig.3.11 b) and c) illustrate the MATI spectra obtained by the high- and low-resolution MATI sequence, compared with the one recorded by PFI-ZEKE method, in the vicinity of the $X^+\,^1\Sigma^+(v^+=2) \leftarrow X\,^2\Pi_{1/2}(v=0)$ photoionization transition of NO. In panel a), the PFI-ZEKE spectrum was obtained using a negative pulse (-167 mV/cm) following a positive prepulse of the same amplitude, leading to a good resolution of 0.3 cm^{-1}. This magnitude of pulsed field strength is not feasible in MATI considering the requirement of the spatial separation from the ions produced by high-voltage pulse. The spectral resolution of the recorded high-resolution and low-resolution MATI spectra are 1.8 and 2.9 cm^{-1}, respectively. Note that these MATI measurements are currently in a preliminary stage. A better signal-to-noise ratio should be obtained with increased statistics. Although not as good as PFI-ZEKE, these MATI measurements still reach the rotational resolution. Even though the resolution achieved by Dessent *et al.*[44] (3 and

6 cm^{-1} for the high- and low-resolution MATI spectra of phenol·Ar) is similar to what we obtained, we should be able to improve further the resolution.

3.2.3 Conclusion and perspective

Despite the relatively lower spectral resolution reached by MATI compared to the PFI-ZEKE method, MATI spectroscopy offers several advantages. Firstly, it is capable of mass selectivity, which is very useful when dealing with a molecular source that contains multiple species with similar ionization energies. Secondly, as the photoion yield spectrum is at the same time recorded with MATI sequence (an example is given in Fig. 3.12), this provides supplementary information, such as the autoionization structures, which can be convenient for our understanding of the ionization process. Thirdly, the presence of the spontaneous ion signal in MATI can also serve as a tool for monitoring the existence of target species. This becomes particularly advantageous when studying cationic structures without prior knowledge of their energy levels.

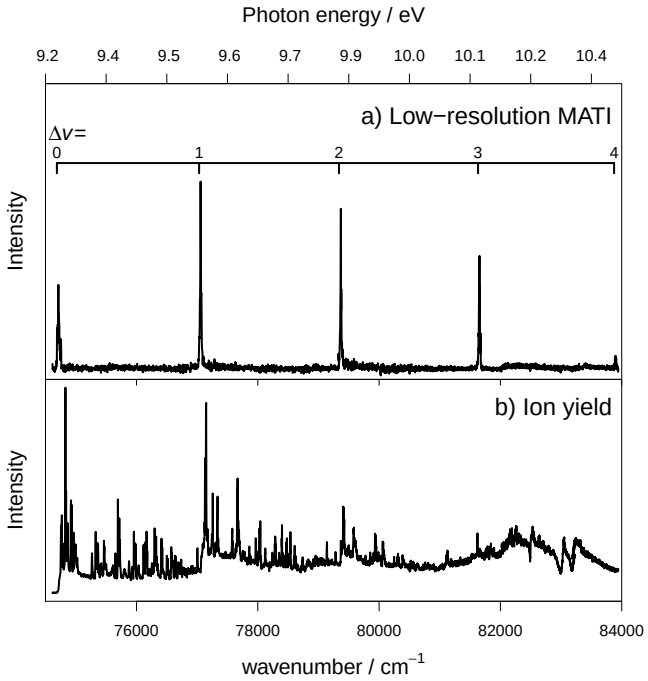

Figure 3.12: The low-resolution MATI (panel a)) and photoion yield (panel b)) spectra obtained using low-resolution MATI sequence and the VUV laser coupled with the OPO laser, on the $X^+\,^1\Sigma^+ \leftarrow X\,^2\Pi_{1/2}$ transition of NO.

Combined with the recently installed OPO laser, which has been described in Section 2.2.1.3, we have unlocked the capability to investigate the photoionization energies of molecules across a wide energy range. As a supportive proof, Fig. 3.12 illustrates the spectrum obtained by low-resolution MATI method with the OPO laser, on the $X^+\,^1\Sigma^+ \leftarrow X\,^2\Pi_{1/2}$ transition of NO. Notably, the vibrational structure of NO^+ with $v^+ = 0 - 3$ is clearly observed in the spectrum in an energy range covering 10000 cm^{-1} (i.e. 1.2 eV). This serves as a demonstration of the potential of our approach. Let us imagine that we are investigating a particular species (or several species) without prior knowl-

edge of the photoionization energies. By simultaneously recording the photoion yield spectrum and MATI spectrum, we can easily acquire relevant information.

Further testing of the MATI spectroscopy is required to investigate its applicability to measure unstable radicals. Due to the need for a stable beam shape in the MATI method, the radical source utilizing high-voltage electric discharge presented in Chapter2 is considered more viable compared to the pyrolysis-based source. Additionally, the combination of the MATI method with Reflectron TOF mass spectroscopy holds significant potential, offering improvements in both the mass selectivity and spectral resolution of MATI. Using the linear TOF mode as an example, by increasing the free-flight distance, the TOF dispersion of ions generated from different pulses becomes larger, which allows for smaller step amplitudes in the sequences, similar to the step sequence used in PFI-ZEKE PES. However, further tests are required to optimize various parameters, such as the delay time of the extraction field and the design of the MATI sequence. A compromise may be necessary to achieve a balance between mass selectivity and MATI spectral resolution.

Chapter 4

Rovibronic structure of CH_3^+ by rotationally resolved photoelectron spectroscopy

4.1 Astrophysical context and spectroscopic background

In June 2023, Berné *et al.* have announced the first observation of the methyl cation (CH_3^+) in space through the analysis of the astronomical spectrum recorded by JWST.[12] This discovery represents a significant advance in our understanding of the origin of carbon-based life in space as CH_3^+ is considered as a key intermediate in the carbon chemistry of the interstellar medium (ISM).[76,153,173] The high-resolution infrared emission spectrum, obtained from the d203-506 protoplanetary disk, revealed distinct red-shifted emission features around 7 μm that were attributed solely to the ν_2^+ (out-of-plane bending, "umbrella" motion) and ν_4^+ (in-plane bending) vibrational bands of CH_3^+, as no other molecules were identified as contributors to these features.[12] Extensive supporting evidence, such as laboratory vibrational spectroscopy of CH_3^+, satisfactory rovibronic simulation, and the intensity pattern suggesting the spin statistics of a system with three equivalent hydrogen atoms, reinforced this attribution.[12] However, despite this evidence, a direct validation through high-resolution laboratory measurements was not accessible at that time, leaving a desire for further confirmation.

The vibrational structure of the $\tilde{\mathrm{X}}^+\,{}^1\mathrm{A}_1'$ electronic ground state of CH_3^+ has been probed through the vibrationally resolved photoelectron spectrum of CH_3 by Dyke *et al.*[48] at a 15-20 meV resolution, and by Cunha de Miranda *et al.* at a 7-11 meV resolution.[40] In terms of rotational analysis, investigations have yielded resolved measurements for the ν^+ = 0 vibrationless level of the $\widetilde{\mathrm{X}}^+\,{}^1\mathrm{A}_1'$ electronic state, stemming from the experiments of photoelectron spectra obtained by Blush *et al.*,[13] Wiedmann *et al.*[175] and Schulenburg *et al.*[149] Additionally, the rotational features of the ν_3^+ band (asymmetric stretching) of the $\widetilde{\mathrm{X}}^+\,{}^1\mathrm{A}_1'$ state have been elucidated through infrared spectroscopy, as documented by Crofton *et al.*[37] To our knowledge, no experiments concerning the rotational structure of the ν_2^+

(and ν_4^+) of the $\tilde{\mathrm{X}}^{+\,1}\mathrm{A}_1'$ electronic state of CH_3^+ have been achieved. Note that, in Cunha de Miranda's work,[40] the rotational structure was discussed in the rovibrational spectral simulation to explain the shape of the vibrationally resolved bands.

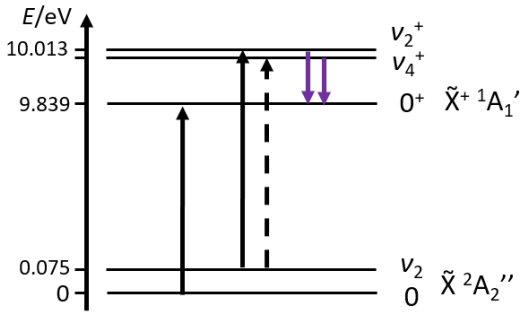

Figure 4.1: Energy diagram of the involved vibrational states of CH_3 and its cation. The origin band ($\tilde{\mathrm{X}}^{+\,1}\mathrm{A}_1'(\nu^+ = 0) \leftarrow \tilde{\mathrm{X}}\,^2\mathrm{A}_2''(\nu = 0)$) and the sequence band ($\tilde{\mathrm{X}}^{+\,1}\mathrm{A}_1'(\nu_2^+ = 1) \leftarrow \tilde{\mathrm{X}}\,^2\mathrm{A}_2''(\nu_2 = 1)$) are shown with plain arrows. The $\tilde{\mathrm{X}}^{+\,1}\mathrm{A}_1'(\nu_4^+ = 1) \leftarrow \tilde{\mathrm{X}}\,^2\mathrm{A}_2''(\nu_2 = 1)$ transition is indicated by a dashed arrow. The emission features around 7 μm in the astronomical spectrum were attributed to the ν_2^+ and ν_4^+ vibrational bands of CH_3^+, indicated by solid purple arrows.

In recent experiments focusing on CH_3 radicals, we successfully generated vibrationally hot CH_3 radicals with a thermal population up to the ν_2 = 1 vibrational state of the electronic ground state $\tilde{\mathrm{X}}\,^2\mathrm{A}_2''$ using the pyrolysis method. The significant difference in vibrational frequency between ν_2^+ and ν_2 modes resulted in distinct transition energies for the origin band ($\tilde{\mathrm{X}}^{+\,1}\mathrm{A}_1'(\nu^+ = 0) \leftarrow \tilde{\mathrm{X}}\,^2\mathrm{A}_2''(\nu = 0)$) and the sequence band ($\tilde{\mathrm{X}}^{+\,1}\mathrm{A}_1'(\nu_2^+ = 1) \leftarrow \tilde{\mathrm{X}}\,^2\mathrm{A}_2''(\nu_2 = 1)$) (see the simplified energy diagram of Fig. 4.1). This unique feature, combined with known vibrational parameters of the ν_2 mode of CH_3,[182] allowed us to investigate for the first time the rotational structure of the ν_2^+ mode of CH_3^+ through the high-resolution PFI-ZEKE photoelectron spectroscopy. The recorded spectrum was explained with the help of theoretical calculations, with which we elucidated in addition the observed transitions from $\tilde{\mathrm{X}}\,^2\mathrm{A}_2''(\nu_2 = 1)$ to the $\tilde{\mathrm{X}}^{+\,1}\mathrm{A}_1'(\nu_4^+ = 1)$ state due to Coriolis interactions. Further details on these findings will be provided in Section 4.3. The achievement of this work marks the first high-resolution laboratory data supporting the detection of CH_3^+ in space.

CH_3 (or its cation) is a planar molecule of D_{3h} point group symmetry. The rotational levels of CH_3 can be labeled by the good quantum number *N* (*N*$^+$ for the ion), which represents the total angular momentum excluding electronic spin, and *K* (*K*$^+$ for the ion), which represents the projection of the angular momentum *N* on the principal axis. Using molecular constants listed in Tab. 4.1, the energy of the rotational states of the ground states of CH_3 and CH_3^+ can be calculated, following the formula:[182]

$$E_{\mathrm{r}}(N^{(+)}, K^{(+)}) = B_{\mathrm{v}} N^{(+)}(N^{(+)} + 1) + (C_{\mathrm{v}} - B_{\mathrm{v}}) K^{(+)2} \tag{4.1}$$

where B_{v} and C_{v} are the rotational constants considering the vibrational-rotational interaction. It is worth noting

that this calculation does not consider centrifugal distortion or spin interactions.

Vibronic state		ω (cm^{-1})	$B_{\rm v}$ (cm^{-1})	$C_{\rm v}$ (cm^{-1})
$\tilde{\rm X}\,^2{\rm A}_2''$	0	0	9.577926(91)[149]	4.73831[149]
	ν_2	606.4531[182]	9.25814(16)[182]	4.811 643(71)[182]
$\tilde{\rm X}^+\,^1{\rm A}_1'$	0^+	0	9.362232(51)[149]	4.6072(44)[149]
	ν_2^+	1406.65950	9.36212(9)	4.63705(12)
	ν_4^+	1396.24321	9.46436(7)	4.56942(9)

Table 4.1: Molecular constants of the CH_3 radical and its cation used for the simulation in this chapter (see section 4.2).

For the intensities, we can calculate the Boltzmann weighting factor of the initial rovibronic level of the neutral state using the expression:[149]

$$\rho = \chi \exp\{-E_{\rm r}/k_{\rm B}T\}(2N+1) \tag{4.2}$$

where $E_{\rm r}$ stands for the rotational energy with respect to the ground state, and χ is the spin-statistical weight which takes values of (0, 0, 4, 4, 2, 2) for states of rovibronic symmetries (A_1', A_1'', A_2', A_2'', E', E'') respectively.[149]

The selection rules for the single-photon photoionization transition of CH_3 have been previously discussed in Ref. 149, and they require:

$$\Delta N = N^+ - N = 0, \pm 1 \text{ and } \Delta K = K^+ - K = 0. \tag{4.3}$$

In this chapter, I will begin with a characterization of CH_3 radicals produced by the two radical sources (electric discharge and pyrolysis) tried in this work and described in Section 2.3, followed by a discussion on the origin band. Then, I will emphasize on the experimental results related to the sequence bands of vibrationally hot CH_3 radicals.

4.2 The $\tilde{\rm X}^+\,^1{\rm A}_1'(\nu^+ = 0) \leftarrow \tilde{\rm X}\,^2{\rm A}_2''(\nu = 0)$ origin transition

As depicted in Fig. 2.13 of Chapter 2, we succeeded to use the high-voltage electric discharge to produce CH_3 radicals. Figure 4.2 a) illustrates the photoion yield spectrum of CH_3 produced by electric discharge in the vicinity of the origin band transition ($\tilde{\rm X}^+\,^1{\rm A}_1' \leftarrow \tilde{\rm X}\,^2{\rm A}_2''$). The vertical line in the figure marks the adiabatic ionization threshold energy (*IP*a) of the transition measured at 79357.3 cm^{-1}. To characterize the spectral features, a relevant study by Schulenburg *et al.*[149] is also depicted in the figure (panel b)). In their research, they produced CH_3 radicals through the photolysis of the CH_3NO_2 precursor, which were characterized by a rotational temperature of 40 K. Notably, both photoionization spectra exhibit several steps outlined by the dotted lines, the main step corresponding to the origin ionization channel exhibiting good Franck-Condon factors.[40,149] However, in panel b), because of the low rotational temperature leading to a significant population only in the lowest rotational levels with $N'' \leq 2$, the step at around 79317 cm^{-1} attributed to $N^+ = 1 \leftarrow N'' = 2$ ($\Delta K = 0$) is distinct, unlike in panel a). Additionally, at

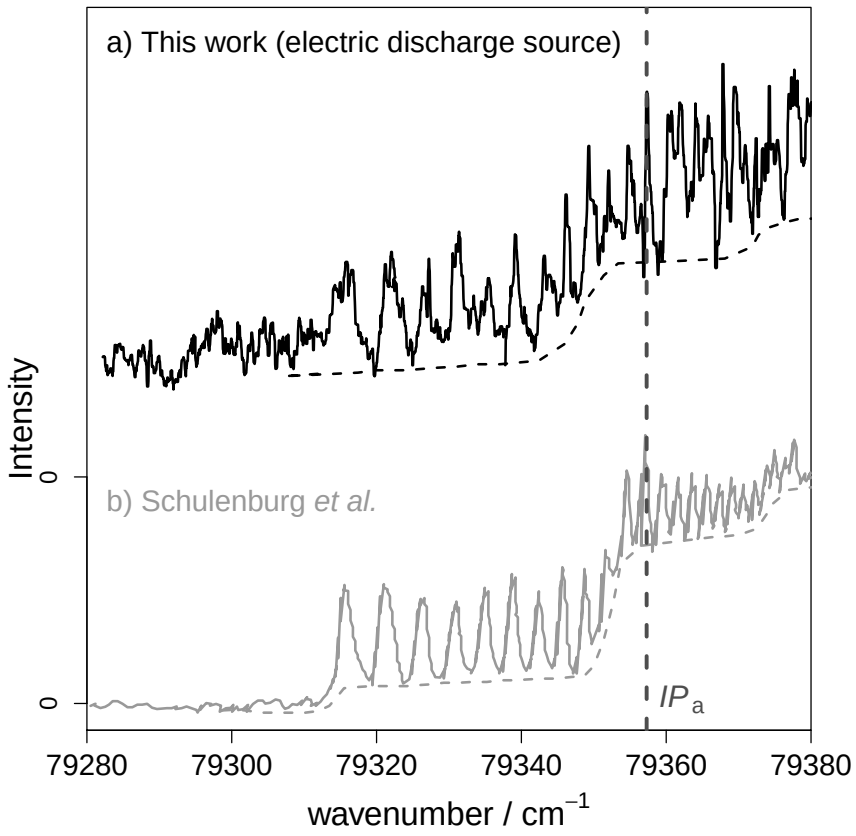

Figure 4.2: a) Photoion yield spectrum of CH_3 obtained by high-voltage electric discharge of 15% CH_4 in He. To validate the spectral structure of CH_3, the photoion yield spectrum obtained by Schulenburg *et al.*[149] is displayed in gray in panel b). They produced CH_3 by photolysis and the spectrum exhibits a rotational temperature of 40 K.

lower photon energy, the photoion yield of Schulenburg *et al.*[149] is nearly zero. In contrast, in our spectrum, the unobserved step at around 79317 cm^{-1}, along with the non-zero signal observed at lower photon energy, suggest a higher rotational temperature of the radicals produced in our discharge plasma. Besides, the lower signal-to-noise ratio of our spectrum is a proof of the instability of the radical generation by electric discharge.

As explained in Sections 2.3.2 and 2.4.2, our spectrum was recorded with the Reflectron ion mass spectrometer when using the electric-discharge radical source, to avoid the MCP saturation caused by the discharge light. This implementation prevented us to perform high-resolution PFI-ZEKE photoelectron spectroscopic measurements. To overcome this limitation, two possible approaches were considered: performing MATI spectroscopy or modifying the spectrometer's configuration. Both options required additional work for improvement and testing. Therefore, we decided to switch to a radical source using pyrolysis.

Fig. 4.3 (panels a) and b)) presents the photoion yield spectra of CH_3 obtained by pyrolysis of CH_3NO_2 seeded in He within two different operating conditions, one favoring a higher internal energy of the produced radicals. Typically, various experimental parameters were adjusted, such as a higher heating power (current and voltage) and a shorter distance between the tube exit and the skimmer, to achieve the production of CH_3 radicals with higher

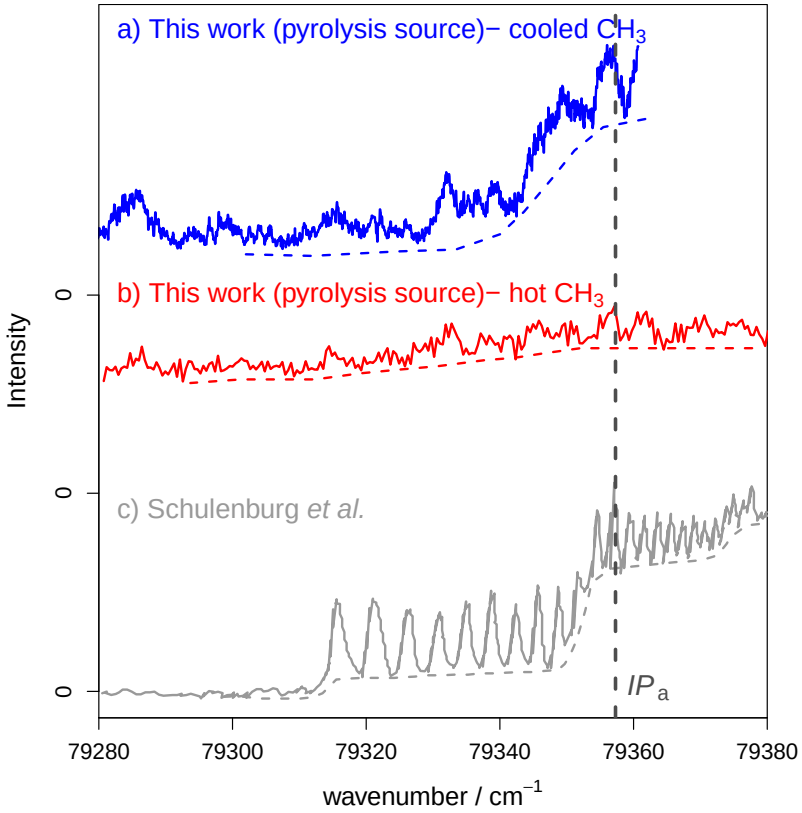

Figure 4.3: Panels a) and b): comparison of two photoion yield spectra for CH_3 obtained by pyrolysis of CH_3NO_2 in He in two different conditions. The red one corresponds to CH_3 radicals with high internal energy. The blue one represents the radicals that have been efficiently cooled. The photoion yield spectrum obtained by Schulenburg *et al.*[149] is displayed in gray in panel c). The dashed line indicates the ionization threshold energy.

internal energy. The spectrum in blue represents the CH_3 radicals that have been efficiently cooled, leading to the observation of a distinct steplike appearance, similar to the one observed in the discharge-produced spectrum in Fig. 4.2. However, compared to Schulenburg's spectrum in gray (panel c)), it is observed that the peak features are much less distinct in the pyrolysis spectrum, which may be explained by the higher rotational temperature.

We measured the PFI-ZEKE photoelectron spectrum for the cooled CH_3 radicals in the vicinity of the origin transition $\tilde{\mathrm{X}}^+\,{}^1\mathrm{A}_1'(\nu^+ = 0) \leftarrow \tilde{\mathrm{X}}\,{}^2\mathrm{A}_2''(\nu = 0)$, using a pulsed sequence composed by +83 mV/cm prepulse followed by -1.16 V/cm electric field, leading to a resolution of 1 cm^{-1}. The recorded spectrum is displayed in Fig. 4.4 as the black curve. To assign the PFI-ZEKE spectrum, I performed a spectral simulation, depicted in blue in Fig. 4.4. The rotational transitions with $\Delta N = -1, 0, 1$ correspond to the P, Q, and R branches, and the N'' numbers of the neutral electronic ground state are noted on the comb. The relative positions of the rotational lines are well reproduced in the simulation. To fit the intensities, a manually adjusted ratio of 1:0.8:0.5 was applied to the Q, P and R branches, respectively. The discrepancy in intensities between the experimental and simulated spectra can be attributed to rotational channel interactions, as discussed by Schulenburg *et al.*[149]. Based on the simulation, the rotational temperature of the cooled CH_3 radicals is estimated to be approximately 250 K.

From the spectral simulation, the ionization potential (*IP*a) of the origin band transition was extracted to be

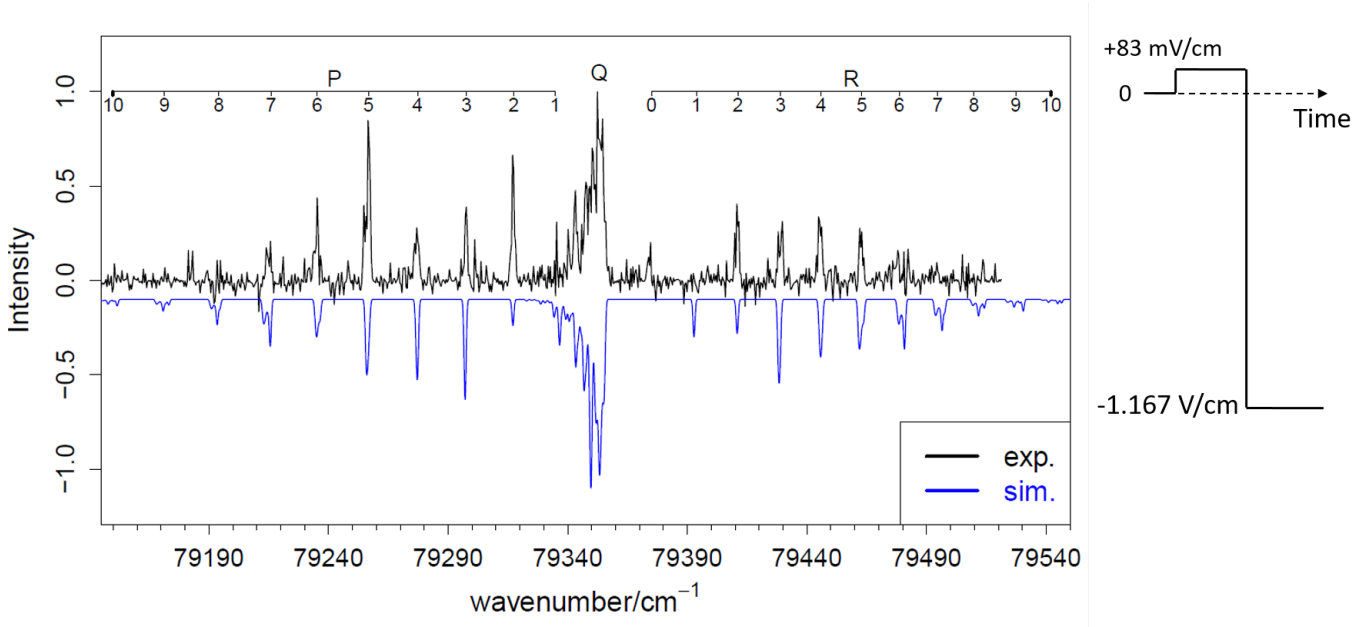

Figure 4.4: PFI-ZEKE photoelectron spectrum of CH_3 in the vicinity of the origin transition $\tilde{X}^+\,^1A_1'(\nu^+ = 0) \leftarrow \tilde{X}\,^2A_2''(\nu = 0)$, produced by pyrolysis of CH_3NO_2 in He, using a pulsed sequence composed by +83 mV/cm prepulse followed by -1.16 V/cm electric field (see scheme to the right). The simulated spectrum displayed in blue was performed at T_{rot} = 250 K with a FWHM of 1 cm^{-1}.

79355.7(2) cm^{-1}. However, when considering the correction for the Stark shift to obtain the final *IP*a value, an intriguing phenomenon was observed. As depicted in Fig. 4.5, two different electric field sequences were applied to measure the PFI-ZEKE photoelectron spectrum for the same experimental conditions of the pyrolysis source. In sequence (a), a +167mV/cm prepulse (F_0) was followed by a -1.33 V/cm electric pulse. In sequence (b), the prepulse was followed by a series of pulses with electric fields F_i equal to -0.33, -0.66, -0.99, -1.33, and -1.67 V/cm for i = 1 to 5, respectively. Initially, we expected to see a shift of spectrum obtained with sequence (b) from right to left with increasing $|F_i|$, indicating an increasing Stark shift. Additionally, it was also expected that the spectrum obtained with the sequence (a) would exhibit a larger spectral bandwidth with a cumulative Stark shift ranging from F_1 to F_4. However, the observed results were completely different (see left part of Fig. 4.5). The spectral positions of the spectra obtained with sequence (a) and with sequence (b) were almost superimposed, and the intensities obtained with F_2 to F_4 of sequence (b) were significantly decreased, indicating the rapid relaxation of Rydberg states corresponding to electric fields larger than -0.33 V/cm during the experiments. A similar phenomenon had been also observed in the PFI-ZEKE experiments of propargyl radicals by Jacovella *et al.*[88] As a result, we chose to use the equations described in Ref. 83 to estimate the Stark shift for the spectrum in Fig. 4.4. Since the spectral resolution (FWHM = 1 cm^{-1}) is quite close to the resolution estimated for the spectrum obtained by the sequence composed by +83 mV/cm prepulse followed by -0.33 V/cm electric field, the Stark shift was determined to be about 1.4 cm^{-1} using this sequence. After the Stark shift correction, the final *IP*a was determined to be 79357.1(12) cm^{-1}, which is very close to the value (79356.2(15) cm^{-1}) measured by Schulenburg *et al.*[149] The ultimate error bar encompasses

the potential overestimation of the Stark shift correction, which is determined to be 1 cm^{-1}.

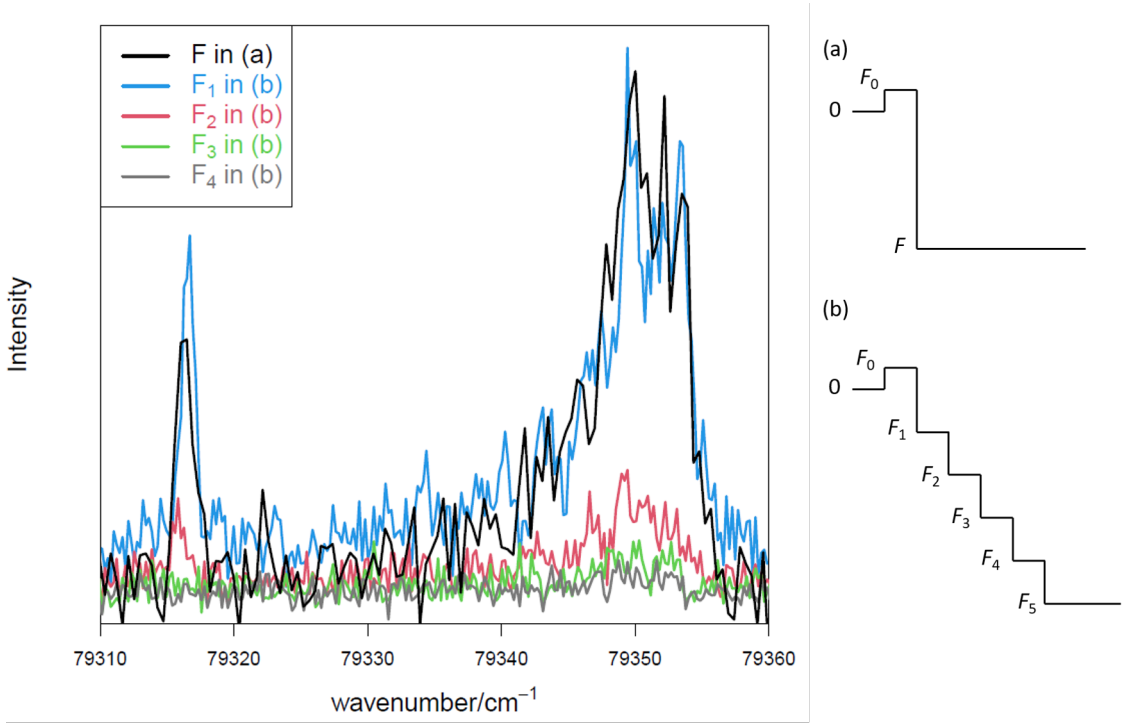

Figure 4.5: Comparison of PFI-ZEKE photoelectron spectrum of CH_3 using two electric field sequences composed of a +167 mV/cm prepulse (F_0) and negative pulses (see schemes to the right): in (a) sequence F =-1.33 V/cm; in (b) sequence F_i = -0.33, -0.66, -0.99, -1.33, -1.67 V/cm for i = 1 to 5 .

4.3 Sequence band transitions $\tilde{\mathrm{X}}^{+\,1}\mathrm{A}_1'(\nu_2^+ = 1) \leftarrow \tilde{\mathrm{X}}\,^2\mathrm{A}_2''(\nu_2 = 1)$

In the experiments using pyrolysis as a radical source, it was observed that the temperature of the produced radicals could be varied over a wide range by adjusting the experimental parameters of pyrolytic dissociation and supersonic expansion. The red curve in Fig. 4.3 exhibits the case where the produced CH_3 radicals were poorly cooled and consequently possessed high internal energy. The thermal distribution of the neutral states of CH_3 led to an ambiguous steplike structure and a high residual ion signal at low photon energy. In most cases, the operating mode of the radical source is focused on producing cold molecules to simplify spectral structures. However, in the present work, the observation that the temperature of the produced radicals can be potentially increased inspired us to explore the production of hot CH_3 radicals with a thermal population up to the $\nu_2 = 1$ vibrational state of the electronic ground state $\tilde{\mathrm{X}}\,^2\mathrm{A}_2''$. This endeavor aimed to study the ν_2^+ mode of CH_3^+, as explained in section 4.1.

Fig.4.6 shows the final PFI-ZEKE photoelectron spectrum measured for the sequence band transition $\tilde{\mathrm{X}}^{+\,1}\mathrm{A}_1'(\nu_2^+ = 1) \leftarrow \tilde{\mathrm{X}}\,^2\mathrm{A}_2''(\nu_2 = 1)$. The wavenumber range of this transition was guided by the findings of Ref. 40 where vibrationally resolved TPES measurements of CH_3 have been performed. Due to the low production yield of hot radicals and the resulting low signal-to-noise ratio of the spectra, we summed up to 10 measured spectra and averaged them

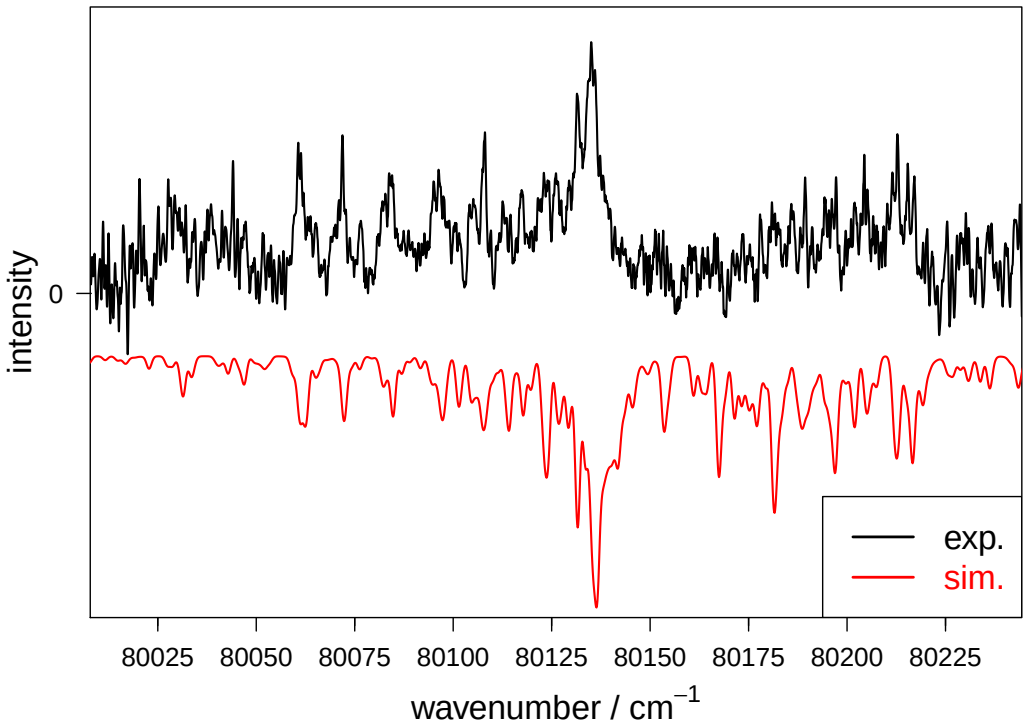

Figure 4.6: PFI-ZEKE photoelectron spectrum of CH_3 in the vicinity of the sequence transition $\tilde{X}^{+\,1}A_1'(\nu_2^+ = 1) \leftarrow \tilde{X}\,^2A_2''(\nu_2 = 1)$, produced by pyrolysis of CH_3NO_2 in He, using a pulsed sequence composed by +167 mV/cm prepulse followed by -1.33 V/cm electric field. The simulated spectrum illustrated in red was performed at T_{rot} = 250 K with a FWHM of 1.5 cm^{-1}. Figure adapted from Ref. 24

to acquire the final spectrum shown in the figure. This process led to a minor degradation in the spectral resolution, from 1 cm^{-1} to 1.5 cm^{-1}. To explain this experimental spectrum, simple simulations were tried and revealed unsuccessful. Consequently, we collaborated with a theoretician from Harvard (Cambridge), P. Bryan Changala, who calculated the spectroscopic constants of CH_3^+ listed in Tab.4.1 including the consideration of centrifugal distortion and Coriolis interactions. More details about these calculations are given in a recent shared publication.[24]

Besides, in the photoionization transition from the $\tilde{X}\,^2A_2''$ state of CH_3 to the $\tilde{X}^{+\,1}A_1'$ state of CH_3^+, the photoelectron is ejected from a $2p_z$ orbital, which leads to l (the orbital angular momentum quantum number of the photoelectron partial wave) being even (l = 0 or 2), following the selection rule $\Delta l = \pm 1$ for an electric dipole transition. Consequently, the selection rules for a single-photon photoionization transition can be seen as the rules for a single-photon electric dipole transition, as demonstrated in Ref. 152. This allowed us to use the PGOPHER program[171] to simulate the rotationally-resolved photoelectron spectrum of CH_3.

Surprisingly, for the sequence band transition, it was found that, to explain the obtained spectrum in Fig. 4.7, besides the $\tilde{X}^{+\,1}A_1'(\nu_2^+ = 1) \leftarrow \tilde{X}\,^2A_2''(\nu_2 = 1)$ transition, there is another transition involved, namely: $\tilde{X}^{+\,1}A_1'(\nu_4^+ = 1) \leftarrow \tilde{X}\,^2A_2''(\nu_2 = 1)$. The occurrence of this transition can be explained by Coriolis interactions between rotational states of the ν_2^+ and ν_4^+ modes, which are located very close to each other with an energy difference of approximately

10 cm^{-1} (see Fig. 4.1). The $\nu_2^+ = 1$ and $\nu_4^+ = 1$ states are so strongly mixed that their rotational levels exhibit characteristics of both (ν_2^+ and ν_4^+), providing an explanation for the observation of the $\tilde{\mathrm{X}}^+\,^1\mathrm{A}_1'(\nu_4^+ = 1) \leftarrow \tilde{\mathrm{X}}\,^2\mathrm{A}_2''(\nu_2 = 1)$ transition. Essentially, it remains the $\tilde{\mathrm{X}}^+\,^1\mathrm{A}_1'(\nu_2^+ = 1) \leftarrow \tilde{\mathrm{X}}\,^2\mathrm{A}_2''(\nu_2 = 1)$ transition at its core. Based on this information and using the spectroscopic constants calculated by P. Bryan Changala, we performed the spectral simulation which is reported in red in Fig. 4.6. Most of the lines in the experimental spectrum can be reproduced by the simulation. In the simulation, a ratio of 1:0.4 for the ν_2^+ and the ν_4^+ transitions, respectively, was manually adjusted to fit the experimental spectrum. The separated simulations of these two ionization transitions are in addition shown in Fig. 4.7 (panel b) and c)). The remaining discrepancies in intensities are attributed to the rotational channel interactions and autoionizations, as discussed for the origin band by Schulenburg *et al.*,[149] which were not considered in our work.

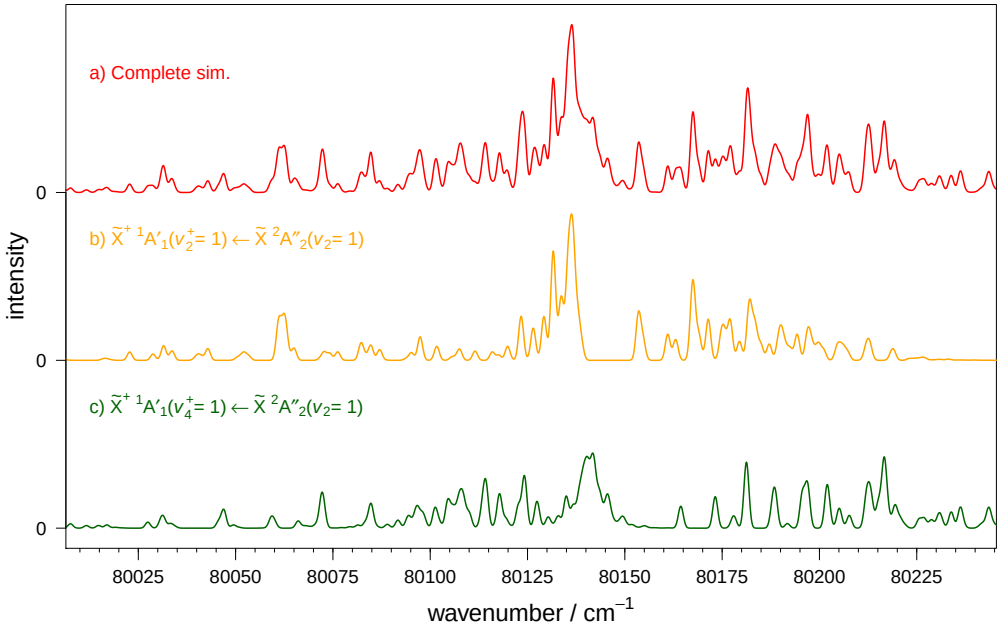

Figure 4.7: Panel a): the complete simulated spectrum (in red), composed by the separated simulations of the two ionization transitions $\tilde{\mathrm{X}}^+\,^1\mathrm{A}_1'(\nu_2^+ = 1) \leftarrow \tilde{\mathrm{X}}\,^2\mathrm{A}_2''(\nu_2 = 1)$ (Panel b) in orange) and $\tilde{\mathrm{X}}^+\,^1\mathrm{A}_1'(\nu_4^+ = 1) \leftarrow \tilde{\mathrm{X}}\,^2\mathrm{A}_2''(\nu_2 = 1)$ (Panel c) in green). Figure adapted from Ref. 24

4.4 Conclusion

In this chapter, we discussed CH_3 radicals produced by electric discharge and pyrolysis, and presented the high-resolution PFI-ZEKE photoelectron spectra for the origin transition $\tilde{\mathrm{X}}^+\,^1\mathrm{A}_1'(\nu^+ = 0) \leftarrow \tilde{\mathrm{X}}\,^2\mathrm{A}_2''(\nu = 0)$ and the sequence band transition $\tilde{\mathrm{X}}^+\,^1\mathrm{A}_1'(\nu_2^+ = 1) \leftarrow \tilde{\mathrm{X}}\,^2\mathrm{A}_2''(\nu_2 = 1)$. In the latter work, we observed an additional transition involving the ν_4^+ mode authorized by Coriolis interactions. The good agreement between the experimental and sim-

ulated spectra validates the calculations for the ν_2^+ and ν_4^+ modes of CH_3^+ performed by Changala.[24] This marks the first high-resolution laboratory data confirming the detection of CH_3^+ in space, which is based on the emission from these ν_2^+ and ν_4^+ states.[12] These findings contribute significantly to our understanding of the chemical evolution of carbon-bearing species in space and pave the way for further research on the complex molecular interactions in astrophysical environments.

Chapter 5

Spectroscopy of cationic silicon-bearing radicals studied with synchrotron radiation

Chemically similar to carbon, silicon is believed to be an element that exists abundantly in interstellar space.[107] Even though most silicon is in the form of silicate grains, the chemistry of the remaining silicon (estimated at around 1% of total silicon[92,145]) is very poorly known. All species containing silicon are, therefore, potentially very interesting to better understand its chemistry. Back in the 70's and 80's, based on limited thermodynamic information or analogy with other studied reactions, some theoretical models have been built to discuss the chemistry of silicon-bearing compounds in interstellar clouds.[77,120,167,179] A simple scheme of the model proposed by Herbst[77] is depicted in Fig. 5.1. In this model, 51 silicon-bearing species were predicted, including 21 neutral and 30 ionic species. The silicon chemistry was believed to start with the proton transfer reaction between Si and H_3^+ to produce SiH^+, which then reacts with various atoms (O, C, N, or metal), generating species composed by Si and other non-hydrogen atoms. Besides, for silicon- and carbon-bearing species, especially relatively large organo-silicon compounds, another pathway triggered by the insertion reaction of Si^+ with hydrocarbons was also believed to occur, in analogy with the source of organo-sulphur compounds from C^+ and S^+ ions. However, despite the large number of predicted species in theoretical models, only around 13 silicon-bearing species have been confirmed to exist in interstellar media in the last decades (see Table 1.1). Some of these confirmed species are boxed in white in Fig. 5.1. Notably, while various species such as SiS, SiO, SiN, and SiC that are predicted in the model have been detected, the existence of the key intermediate SiH^+ is still not confirmed. Therefore, there is a pressing need for laboratory spectroscopic data on silicon-bearing species, which would not only help in identifying unknown species but also in validating theoretical models.

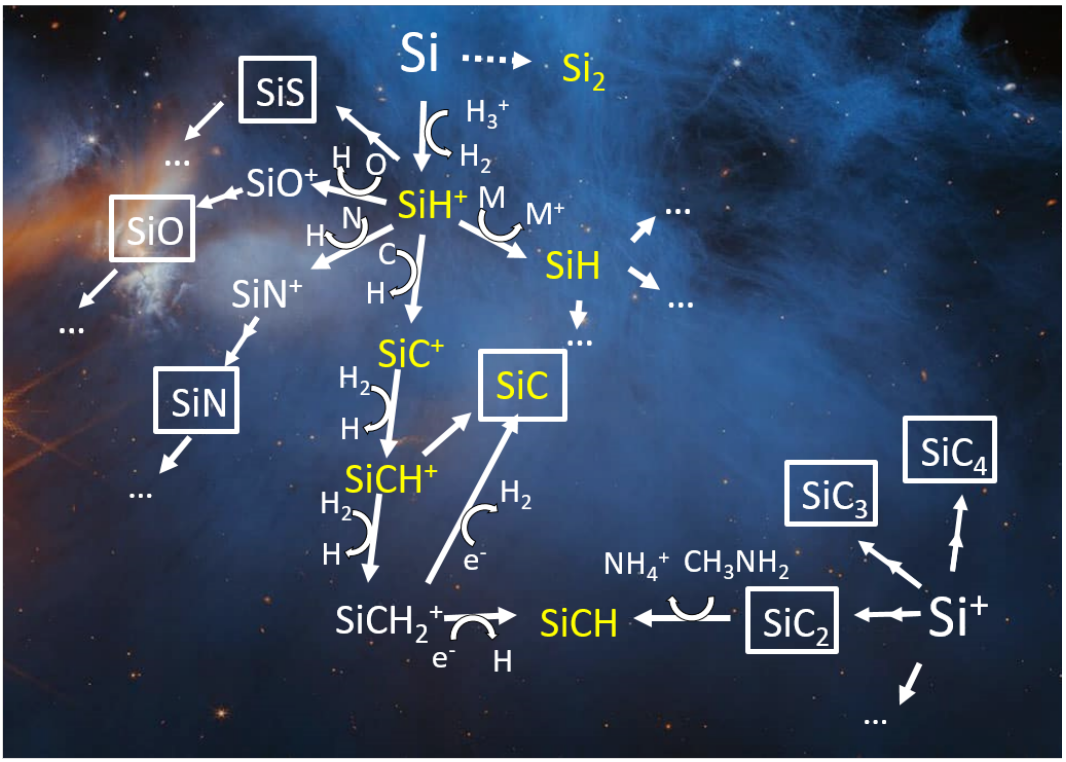

Figure 5.1: Illustration of chemical evolution of silicon-bearing species in the interstellar medium, based mainly on the model proposed by Herbst in Ref. 77. All species in this picture have been discussed in the model except Si_2. Species having been detected in the ISM are boxed in white. Species studied in this thesis are highlighted in yellow. Credits for the background pictures: Webb's view of the molecular cloud Chameleon I.[6]

In this chapter, I will present our recent experimental results concerning the photoionization spectroscopy of a variety of silicon-bearing radicals (Si_xH_y) and silicon- and carbon-bearing radicals ($Si_xC_yH_z$) which had been scarcely studied up to now because of their instability. The experiments were performed at the SOLEIL French synchrotron facility, on the DESIRS beamline,[124] in collaboration with Jean-Christophe Loison from the Institute of Molecular Sciences (ISM) of Bordeaux. The production of these radicals is achieved by using a flow-tube reactor coupled with a microwave discharge that generates fluorine atoms in the molecular beam end-station SAPHIRS.[139] The SiH_4 precursor or SiH_4/CH_4 mixture undergoes H-abstraction reaction with F atoms (and potentially other chemical reactions) to obtain silicon- and carbon-bearing radicals $Si_xC_yH_z$. The coupling of this radical source with a double-imaging photoelectron/photoion coincidence (i^2PEPICO) spectrometer[60] and the DESIRS beamline allowed us to acquire the ion yield and mass-selected photoelectron spectra for a series of radicals. Photoionization energies have been derived from the spectra. In addition, using *ab initio* calculations and Franck-Condon simulations, several photoionization transitions have been assigned and interesting phenomena like the observation of spin-forbidden transitions or rich autoionization structures have been described.

In Section 5.1, I will give the main details of the experimental setup used at SOLEIL. In Sections 5.2, 5.3, 5.4 and 5.5, results obtained on the photoionization of SiH, Si_2, SiC and SiCH, respectively, will be presented.

5.1 Experiments at SOLEIL Synchrotron Facility

5.1.1 VUV synchrotron radiation of the DESIRS beamline

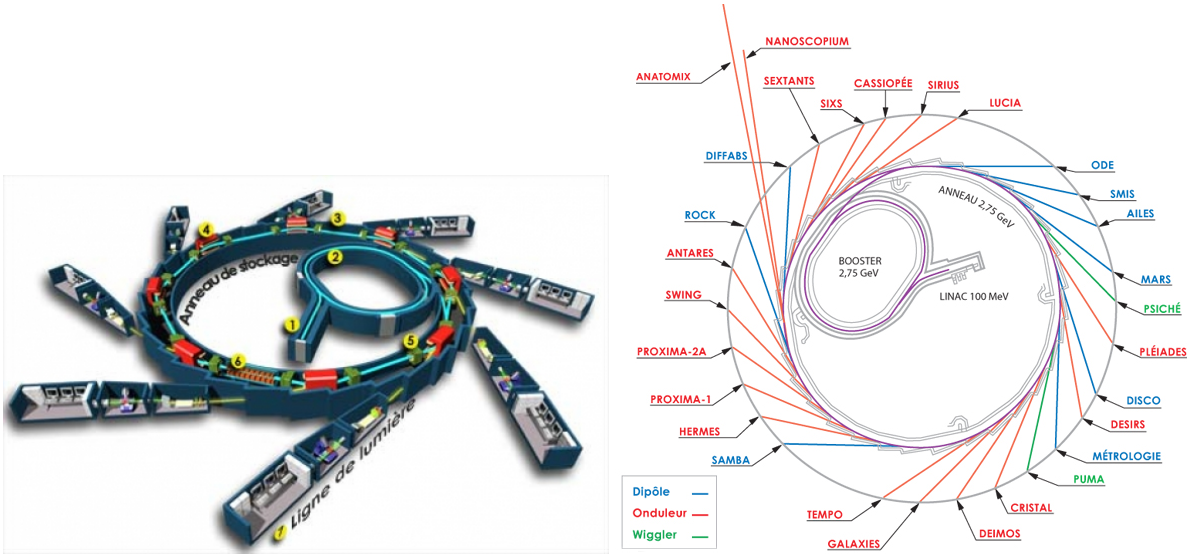

(a) 1: Electron accelerator 2: Booster 3: Storage ring 4: Undulator 5: Radiofrequency cavity 6: Storage ring 7: Beamline

(b)

Figure 5.2: Layout of the Synchrotron SOLEIL (a) and its beamlines (b) from Ref. 4

Fig. 5.2 (a) depicts the layout of the Synchrotron Source Optimisée de Lumière d'Energie Intermédiaire du Laboratoire pour l'utilisation du rayonnement électromagnétique (SOLEIL), the third-generation French national synchrotron facility that has been providing scientific works since its first operation for external users in early 2008. In the facility, the electron beam emitted from an electron gun is firstly accelerated in a 16-meter-long linear accelerator to a first energy level of 100 MeV, and then further accelerated in a circular accelerator called Booster, to reach an operating energy of 2.75 GeV. Then the relativistic electrons are injected into the storage ring, where bending magnets and insertion devices are installed to deviate the trajectory of electrons to generate synchrotron radiation optimized for various experimental requirements.

The distribution of beamlines around the storage ring is depicted in Fig. 5.2 (b). Following the need of VUV radiation for photoionization measurements, we work on the Dichroïsme Et Spectroscopie par Interaction avec le Rayonnement Synchrotron (DESIRS) beamline [124] where synchrotron radiation covers the 5-40 eV photon energy range. The synchrotron radiation is offered by a specific undulator HU 640, which imposes an oscillatory movement with small deflection to electrons, leading to higher flux, brightness, and spectral range of light. [177] The emitted radiation from undulator is discrete and multi-harmonic due to interference. By controlling parameters such as electric currents fed through the undulator, the magnetic field can be finely tuned to vary the wavelengths of radiations with constructive interferences. This is the preliminary step to get the suitable energy range of radiation for experiments.

Then, filled with rare gas, a gas filter is set to eliminate those high-harmonic radiation whose photon energies are above the ionization potential of the rare gas. Meanwhile, the absorption lines of the rare gas below the *IP* can also be used to calibrate the photon energy scale of measurement, with a certainty within around 2 meV.

After the gas filter, the harmonic-free radiation goes to the monochromator where dispersive gratings (with groove densities of 200, 400, 2400 and 4300 lines mm^{-1}) allow the selection of wavelength of radiation covering the whole energy range of 5-40 eV to pass through a very tiny exit slit (whose size is also vertically adjustable up to 300 μm[60]). Choosing a higher dispersion grating leads to improved spectral resolution of radiation. When employing two low-dispersion gratings, the spectral resolution is limited by the slit to a moderate extent.[124] The monochromatised radiation is then sent to the end-station where we carried out our VUV photoionization experiments on gas-phase molecules.

Tab. 5.1 compares several characteristics of the VUV laser produced in the VULCAIM setup described in Chapter 2 with those of the VUV synchrotron radiation of the DESIRS beamline. One notable advantage of synchrotron radiation is its tunability over a wide spectral range. Although we can enhance the tunability range of the VUV laser by incorporating a tunable OPO laser, the stable intensity of radiation across the wide spectral range makes synchrotron radiation an excellent tool for medium-resolution measurements. The ultimate photon resolution of synchrotron radiation, approximately 1 cm^{-1}, is roughly estimated based on fine radiation characterization *via* the autoionization spectrum of Ne and Xe (approximately 174 μeV at around 21 eV and 54 μeV at around 13 eV, respectively) in Ref. 124. In the experiments on silicon-bearing species discussed in this chapter, the photon energy was scanned in the 7-10.5 eV energy range, with a photon resolution about $\delta\lambda$ = 2.16 Å corresponding to δE from 9 to 19 meV.

Table 5.1: Characteristics of VUV radiation sources at ISMO (VULCAIM) and at SOLEIL (DESIRS beamline)

	VUV laser radiation of VULCAIM		synchrotron radiation of DESIRS
	dye laser	OPO laser	
Temporal mode	≈7 ns pulses at 20 Hz		quasicontinuous
Photon flux	10^9-10^{10} ph/pulse		10^{10}-10^{14} ph/s
Spectral range	6-17 eV, by range of ≈1000 cm^{-1}	6-17 eV, by range of ≈24000 cm^{-1}	6-40 eV, continuous
Spectral resolution	< 0.1 cm^{-1}	≈3 cm^{-1}	80 cm^{-1} *
Typical acquisition time	1 h/0.001 eV	1 min/0.001 eV	1 h/1 eV

* Typical resolution used during my PhD.

5.1.2 SAPHIRS equipped with the radical source and the DELICIOUS 3 spectrometer

Using the VUV synchrotron radiation, we performed the photoionization measurements on radicals at the molecular beam end-station Spectroscopie d'Agrégats PHotoIonisés par le Rayonnement Synchrotron (SAPHIRS).[139] The exper-

imental setup was equipped with the flow-tube reactor[63] as the radical source (built by Jean-Christophe Loison in the frame of the SYNCHROKIN ANR project) and a double Imaging PhotoElectron PhotoIon COincidence (i^{2}PEPICO) spectrometer called Dichroism and ELectron/Ion Coincidence in IOnization Using Synchrotron (DELICIOUS) 3.[60] Fig. 5.3 (a) provides an illustration of the entire experimental system, followed by a photo of the setup in (b).

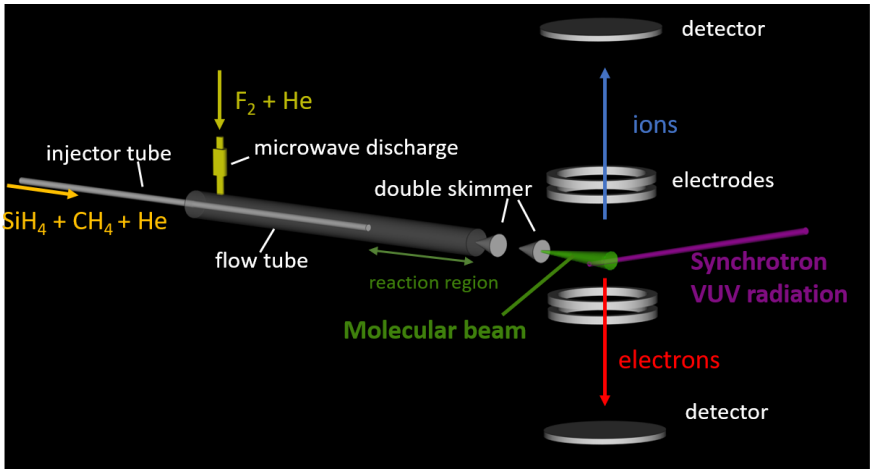

(a)

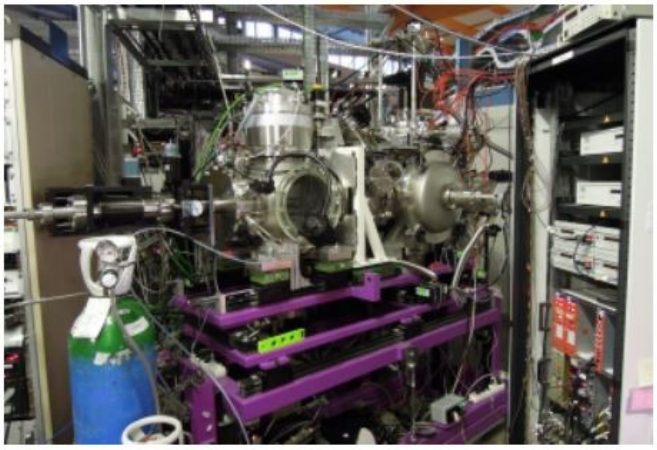

(b)

Figure 5.3: (a) Illustration of the SAPHIRS setup including the flow-tube reactor and the DELICIOUS 3 spectrometer. (b) Photo of the setup extracted from Ref. 69.

5.1.2.1 Flow-tube reactor as the radical source

As depicted in Fig. 5.3 (a), the flow tube reactor,[63] consists in a main quartz tube with a 24 mm internal diameter/65 cm length, along with a collinear quartz injector tube with a 6 mm internal diameter and a 190 cm length. A perpendicular microwave discharge of a mixture of F_2 diluted in He introduces fluorine atoms (around 1×10^{13} atom·cm^{-3}) into the flow tube (total pressure of 4×10^{-1} mbar), which then react with the diluted precursor gas from the injector tube. This reaction leads to the formation of various radicals through H-abstraction reactions. In

our project focusing on silicon-bearing species, we used SiH_4 (1×10^{13} molecules·cm^{-3}) seeded in He (1:1000) as the precursor gas, resulting in the formation of a series of SiH_x (x=1-3) radicals by successive reactions:

$$\mathrm{SiH_4 + F \rightarrow SiH_3 + HF}$$

$$\mathrm{SiH_3 + F \rightarrow SiH_2 + HF}$$

$$\mathrm{SiH_2 + F \rightarrow SiH + HF}$$

Apart from these radicals produced through H-abstraction, other products arose from radical-radical reactions, including F-bearing species from F-addition.

In the experiment, several parameters can be adjusted in order to favor the yield efficiency of targeted radicals. Firstly, the injector tube is able to slide inside the flow tube, varying consequently the reaction time between the F atoms and precursor molecules in the reaction region. Typically, a longer distance of the reaction region allows for a more extended reaction time, favoring the multi-H abstraction and radical-radical reactions. Secondly, the gas concentrations and their ratio play a crucial role in the radical formation process. A higher F_2 flow rate promotes H-abstraction reactions, but it may also increase the rates of F-addition reactions. Therefore, finding the appropriate F_2 flow rate is essential to strike a balance between maximizing H-abstraction and minimizing unwanted F-addition reactions. Additionally, proper adjustment of the precursor gas concentration is necessary to improve radical yield while limiting radical-radical reactions, which can occur at high precursor concentrations.

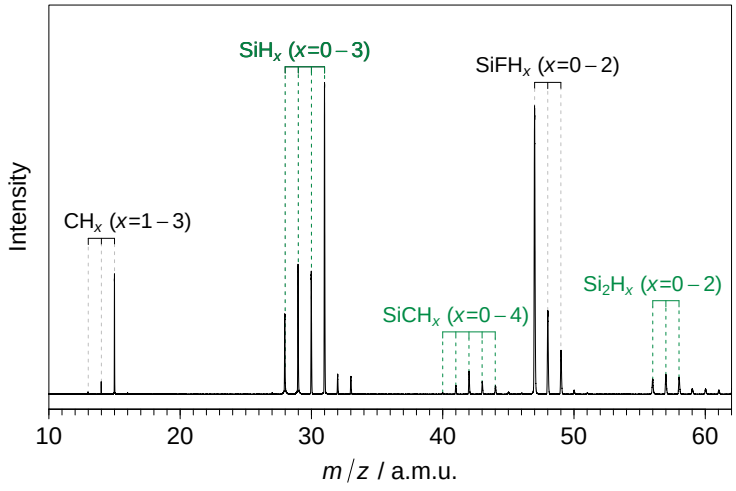

Figure 5.4: Integrated mass spectrum over the 8-11 eV energy range using SiH_4/CH_4 mixture as the precursor. In our project focusing on silicon-bearing species, the interesting $Si_xC_yH_z$ species are highlighted in green.

To further explore the variety of radical products, we also used the SiH_4 (1×10^{13} molecules·cm^{-3}) /CH_4 (1×10^{13} molecules·cm^{-3}) mixture seeded in He (2:1000) as the precursor to undergo chemical reactions with F atoms (2×10^{13} atom·cm^{-3}). The corresponding mass spectra of the obtained products are shown in Fig. 5.4. Notably, in addition to the CH_x and SiH_x radicals, we also observe a small quantity of silicon- and carbon-bearing radicals, $Si_xC_yH_z$,

presumably formed through radical-radical reactions. The production of these radicals was challenging due to their high instability, making it difficult to measure them accurately in a laboratory setup. The capability of the flow-tube reactor to generate them is a significant achievement.

Upon leaving the reaction region, the continuous flow beam of the molecular mixture is doubly skimmed before entering the ionization chamber (pressure of 2×10^{-7} mbar). This double-skimming configuration is used for differential pumping and allows a slight expansion which slightly reduces the translational temperature of the sample. By using double skimmers, the molecular beam profile becomes smaller, leading to a noticeably reduced level of room temperature background gas in the ionization chamber. Moreover, the smaller beam size improves the ion mass sensitivity as well as electron kinetic energy resolution of the i^{2}PEPICO spectrometer.[161]

5.1.2.2 Double imaging spectrometer

As depicted in Fig. 5.3, in the ionization chamber, the molecular beam intersects at right angle with the monochromatized synchrotron radiation between the repeller and the extraction electrodes. The small sizes of the gas beam and the radiation (typically 300 (horizontal) $\times$ 100 (vertical) μm at focal position[60]) define a small region of photoionization.[139] Under photoionization, ions and electrons are vertically extracted in coincidence by typically a 88.7 V/cm DC electric field in opposite directions to a modified Wiley-McLaren (WM) TOF momentum imaging analyzer[176] and a Velocity Map Imaging (VMI)[51] device, respectively. The arrival of lighter electrons at the Position Sensitive Detector (PSD) starts a clock of a multistop time-to-digital converter which would be closed when ions formed from the same neutral molecule reach the detector in opposite direction, leading to a statistically mass-selective photoelectron spectroscopy.

On the ion side, the basic principle of the WM spectrometer has been described in Section 2.4.2 of Chapter2. To recall, the double-acceleration region characterizes the WM spectrometer, a design choice aimed at achieving superior mass resolution compared to a single-acceleration configuration.[176] By adjusting the electric field ratio, the blurring effect on TOF signals resulting from the initial spatial distribution can be eliminated for any voltage applied to the extraction plate.[60,176] Additionally, the energy resolution, which is linked to the temporal dispersion introduced by the initial kinetic energy distribution, is contingent solely upon the ions' turn-around time — an inversely proportional relationship to the strength of the extraction field.[60] Consequently, the extraction voltage could be appropriately increased to improve the mass resolution of the WM-TOF spectra. Based on this conventional WM arrangement, an enhancement is introduced through the incorporation of two grid electrostatic lenses within the second acceleration region,[61] serving to further refine spatial focusing capabilities. With the ion optic configuration as well as the double-skimmer molecular source, the mass resolution $m/\Delta m$ can be 1700.[161] Combined to TOF information with the position records on the 2D position sensitive detector, the full 3D ion momentum distribution of ions is acquired. Although the transverse image devoted to record the kinetic energy of ions is particularly beneficial for examining photodynamics of dissociation,[161] in our context encompassing radical production source, it also

proves useful to focus on ions with low translational temperature (*i.e.* cold part of the beam).

On the electron side, a three-plate electrostatic lens with open electrodes rather than grid ones is placed, designed to focus the trajectory of the particles and deblur the imaging.[51,59] As light electrons have short times of flight, the approach recording the 3D momentum of ions is no longer suitable due to constraints on time resolution. Consequently, the reconstruction of the 3D image (more specifically, the central 2D slice of the sphere) for electrons is achieved through the process of inverse Abel transformation, which requires that whole electrons should be recorded.[59] After the treatment of the raw electron image, we get a photoelectron image at the fixed photon energy, with the kinetic energy of photoelectrons defined by the radius of concentric circles. By scanning the photon energy, we acquire a two-dimensional photoelectron matrix that depicts electron signal intensity (*z*-axis) as a function of electron kinetic energy (*y*-axis) and photon energy (*x*-axis). As illustrated in Fig. 5.5 a), an example of photoelectron matrix for the SiH radical ($m/z = 29$) is presented. To extract a photoelectron spectrum with a higher signal-to-noise ratio, the matrix is subjected to rotation (see panel b)), enabling the integration of photoelectron signals within a specific kinetic energy range (0-10 meV in the case of SiH). This is the SPES (Slow Photoelectron Spectroscopy) described in Chapter1. By employing this approach, we ultimately derive a mass-selective photoelectron spectrum of the target molecules (see later), striking a good compromise between signal-to-noise ratio and spectral resolution.

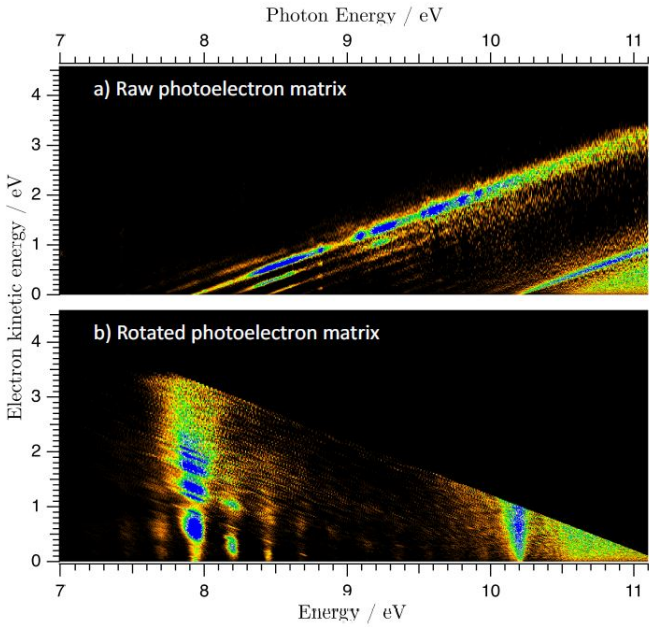

Figure 5.5: Raw photoelectron matrix (panel a)) and rotated matrix (panel b)) of the SiH radical from Ref. 26.

5.2 First threshold photoelectron spectrum of SiH

5.2.1 Astrophysical context and spectroscopic background

As indicated by Fig. 5.1, SiH and its cation SiH^+ are predicted to be pivotal intermediates in the realm of gas-phase silicon chemistry.[77] It accentuates specifically the potential significance of SiH^+ in contributing to the formation of silicon-bearing compounds involving non-hydrogen elements. Moreover, SiH and SiH^+ might play a crucial role in processes occurring on interstellar grains, stemming from the hydrogenation of atomic silicon that adheres to these grains. Notably, hydrogen addition reactions are ubiquitous on these grains.[162] However, despite the successful detection of various silicon compounds predicted in the downstream consequences in the model, such as SiC,[22] SiO,[109,166,188] SiN,[148,187] and SiS[132], the existence of SiH^+ has yet to be substantiated. Similarly, the existence of SiH is not ascertained albeit for a tentative detection in Orion-KL,[147] several decades after the prediction of its existence in 1978.[41] The ambiguous identification of SiH arises from the blending of certain characteristic hyperfine transitions with lines from other known species, such as CH_3CN, CH_3OCH_3, and CH_3OH, coupled with its relatively weak spectral signature.[147]

The first experimental determination of the adiabatic ionization energy of SiH was documented by Berkowitz *et al*.[11] in 1987, employing photoionization mass spectrometry with a wavelength resolution of approximately 0.8 Å. By pinpointing the half-rise of the abrupt step signal in the ion yield spectrum, they extracted a threshold ionization energy (*IE*) value of 7.91 ± 0.01 eV. Furthermore, theoretical investigations have also explored the threshold *IE* value of SiH, yielding results of 7.86 eV[133] and 7.93 eV.[141] Berkowitz's[11] study also delved into the discussion of autoionization processes, which significantly influence the ion yield spectrum. A partial assignment of autoionization features to neutral Rydberg series converging to the first excited electronic state of the cation ($a^+\,^3\Pi$) was outlined. From this analysis, an ionization energy for the $a^+\,^3\Pi$ state was extrapolated to be 10.21eV.

Building upon these foundations, our present work presents the first measurement of the threshold photoelectron spectrum of SiH, culminating in refined Ionization Energy (*IE*) values with an improved accuracy. In addition to this, our experimental photoionization spectrum takes a step further in advancing the assignments of autoionization features. The detailed description and results have been published in 2022.[26]

5.2.2 *Ab initio* calculations

The *ab initio* calculations on the electronic states of SiH and its cation, SiH^+, were provided by Jean-Christophe Loison (Institute of Molecular Sciences of Bordeaux), using the internally contracted MultiReference Configuration Interaction method with Davidson correction (MRCI + Q) with Complete Active Space Self-Consistent Field (CASSCF) wave-functions. The detailed description of the calculations is available in Ref. 26. Here only the main results of the calculations are reported.

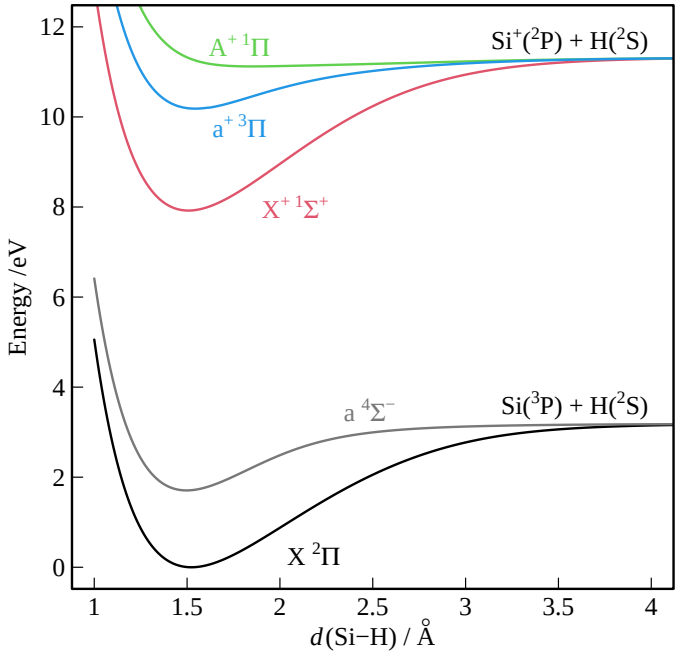

Figure 5.6: Calculated potential energy curves (MRCI/AVQZ method) of SiH and SiH^+ from Ref. 26.

The potential energy curves of five states (2 for neutral SiH and 3 for cationic SiH^+) were computed as a function of the Si–H bond length, $d(\mathrm{Si}-\mathrm{H})$, using the AVQZ basis set. The resulting plots are depicted in Fig. 5.6. Single-point calculations were executed employing the AVnZ basis sets (with n = T, Q, 5, and 6) for equilibrium geometries. Anharmonic frequencies were determined employing the same basis sets. The potential curves corresponding to the SiH($\mathrm{X}\ ^2\Pi$), SiH($\mathrm{a}\ ^4\Sigma^-$), SiH^+($\mathrm{X}^+\ ^1\Sigma^+$), and SiH^+($\mathrm{a}^+\ ^3\Pi$) states were fitted with an eighth-order polynomial, enabling the calculation of anharmonic frequencies.

To achieve higher accuracy, Complete Basis Set (CBS) extrapolations were conducted using the AVnZ (n = T, Q, 5, and 6) basis set series. Extrapolations of CASSCF (E_{CASSCF}) and dynamical correlation ($E_{\mathrm{MRCI+Q}}-E_{\mathrm{CASSCF}}$) energies were performed using functions $E_{\mathrm{CASSCF}}(\mathrm{CBS}) + A \times \exp(-Bn)$ and $E_{\mathrm{Corr}}(\mathrm{CBS}) + C \times n^{-3}$, respectively. The vibrational frequencies (ω_e) and equilibrium geometries (R_e) were extrapolated using the same function as for the dynamical correlation extrapolation. The calculated energies reported in this work correspond to $E_{\mathrm{CASSCF}}(\mathrm{CBS}) + E_{\mathrm{Corr}}(\mathrm{CBS})$, adjusted by the Zero-Point Energy (ZPE) when explicitly indicated. The calculated results of the harmonic vibrational wavenumbers and transition energies are listed in Tab. 5.2.

The Franck-Condon (FC) calculations shown in the following paragraph were performed with the PGOPHER software[171] using the *ab initio* output files (Molden output files calculated with the AVQZ basis set for all states) and neglecting spin. The adiabatic transition energies obtained by the CBS extrapolations corrected from the ZPE were used to fix the energy of the origin bands ($v^+ = 0 \leftarrow v = 0$) of the calculated spectra.

Table 5.2: Calculated molecular properties of the electronic states of SiH and SiH^+,

State	Main configuration[a]	R_e /Å	ω_e /cm^{-1}	$\omega_e x_e$ /cm^{-1}	$\omega_e y_e$ /cm^{-1}	E /eV	$E(\mathrm{corr\,ZPE})$ /eV
$X\ ^2\Pi$	$[\ldots](4\sigma)^2(5\sigma)^2(2\pi)^1$	1.521	2043.87	35.88	0.07	0	0
		(1.5169)[185]	(2041.5346)[185]	(32.9505)[185]			
$a\ ^4\Sigma^-$	$[\ldots](4\sigma)^2(5\sigma)^1(2\pi)^2$	1.493	2059.24	57.80	-1.65	1.715	1.716
		(1.4893)[185]	(2069.6140)[185]	(64.8035)[185]		1.7528[185]	
$X^+\ ^1\Sigma^+$	$[\ldots](4\sigma)^2(5\sigma)^2(2\pi)^0$	1.505	2154.37	33.64	0.05	7.927	7.934
		(1.510)[141]	(2153.5)[141]	(38.9)[141]			7.93[141]
			(2155.35)[81]	(38.82)[81]			
$a^+\ ^3\Pi$	$[\ldots](4\sigma)^2(5\sigma)^1(2\pi)^1$	1.540	1734.08	76.82	-1.40	10.191	10.171
			(1729.79)[81]	(103.68)[81]			

[a] Inner electronic configuration $(1\sigma)^2(2\sigma)^2(3\sigma)^2(1\pi)^4$ is replaced by $[\ldots]$

5.2.3 Results and discussion

5.2.3.1 Photoelectron spectroscopy

In the SPES spectrum illustrated in Figure 5.7, the most prominent bands, located around 7.93 eV and 10.2 eV, are definitively assigned to the origin bands of the $X^+\ ^1\Sigma^+ \leftarrow X\ ^2\Pi$ and $a^+\ ^3\Pi \leftarrow X\ ^2\Pi$ transitions, respectively. Beyond the energy of 10.3 eV, the photoelectron spectrum exhibits an onset attributed to contributions from the $SiH_3 \rightarrow SiH^+ + H_2$ + e^- dissociative ionization channel. We observe additional weaker bands at each side of the two prominent bands. These bands are associated with vibrational progressions, and their energies with respective $\Delta\nu$ ($= \nu^+ - \nu$) values have been determined using the calculated vibrational parameters presented in Table 5.2. Due to the closely matched vibrational frequencies, ν^+ and ν, of the involved electronic states, each $\Delta\nu$ band emerges as a convolution of transitions originating from the initial electronic state with distinct ν values. A closer examination of the spectrum, particularly the magnified section to the left of Figure 5.7, reveals the presence of the $\Delta\nu = -4$ band at approximately 7 eV. This observation indicates that the vibrational states of the neutral SiH ground state are populated up to, at the very least, $\nu = 4$ within the radical source.

Subsequently, a more detailed analysis was conducted on the bands centered around 8.46 eV. The signal at the energy corresponding to the $\Delta\nu = +2$ band of the $X^+\ ^1\Sigma^+ \leftarrow X\ ^2\Pi$ transition exhibits an unusually intense intensity in relation to the overall vibrational progression. This enhanced intensity indicated a non-Franck-Condon (non-FC) behavior. To provide an explanation for this observation, we suggest two plausible sources for this enhanced intensity:

1. Observation of the photoionization transition involving the $a\ ^4\Sigma^-$ metastable state of neutral SiH: $a^+\ ^3\Pi \leftarrow a\ ^4\Sigma^-$. In the first scenario, this notion gains support from the fact that the calculated energies of the $a^+\ ^3\Pi(\nu^+) \leftarrow a\ ^4\Sigma^-(\nu)$ vibronic transition coincide with the non-FC signals. This alignment is illustrated by the gray comb pattern in Figure 5.7. It is worth noting that when considering the thermodynamics of the process, the successive exothermic

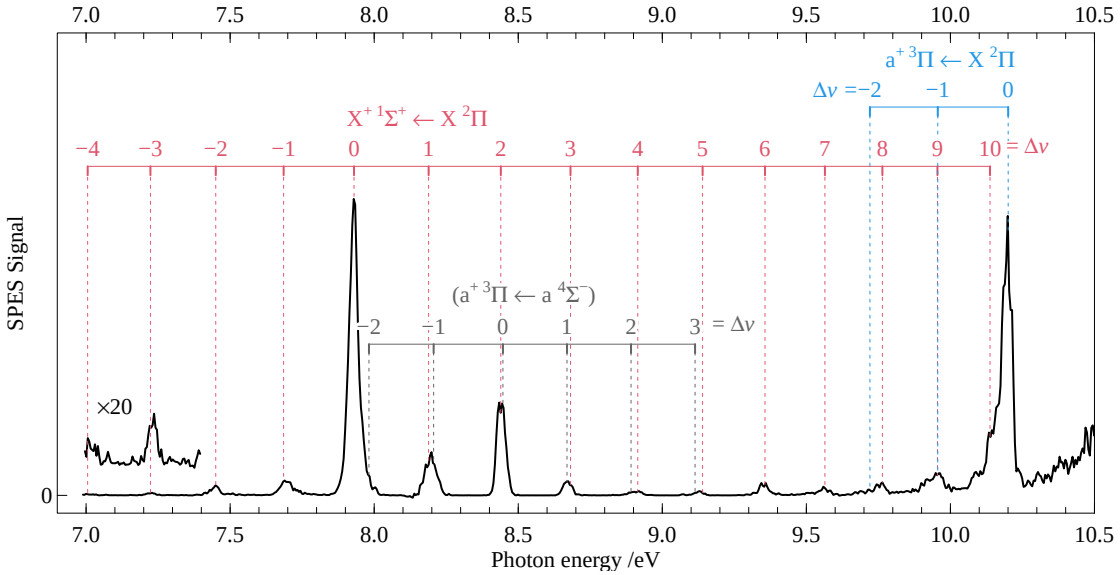

Figure 5.7: Slow photoelectron spectrum of the SiH radical from Ref. 26. The red and blue combs mark the observed $\Delta\nu$ bands for the $\mathrm{X}^+\,^1\Sigma^+ \leftarrow \mathrm{X}\,^2\Pi$ and $\mathrm{a}^+\,^3\Pi \leftarrow \mathrm{X}\,^2\Pi$ photoionization transitions, respectively. The $\mathrm{a}^+\,^3\Pi \leftarrow \mathrm{a}\,^4\Sigma^-$ expected band positions are also located with a gray comb, whose $\Delta\nu$ = 0 band coincides with the $\Delta\nu$ = 2 band of $\mathrm{X}^+\,^1\Sigma^+ \leftarrow \mathrm{X}\,^2\Pi$ (see text for details).

hydrogen-abstraction reactions involved in SiH radical production[11]

$$\mathrm{SiH_4(X\,^1A_1) + F(^2P) \rightarrow SiH_3(X\,^2A_1) + HF(X\,^1\Sigma^+)}\ (\Delta H_\mathrm{r} = -1.9\ \mathrm{eV})$$

$$\mathrm{SiH_3(X\,^2A_1) + F(^2P) \rightarrow SiH_2(X\,^1A_1) + HF(X\,^1\Sigma^+)}\ (\Delta H_\mathrm{r} = -2.1\ \mathrm{eV})$$

$$\mathrm{SiH_2(X\,^1A_1) + F(^2P) \rightarrow SiH(X\,^2\Pi) + HF(X\,^1\Sigma^+)}\ (\Delta H_\mathrm{r} = -2.1\ \mathrm{eV})$$

result in a total excess energy exceeding 6 eV. This energy is distributed as kinetic and internal energies between the HF and SiH_n fragments. While the $\mathrm{a}\,^4\Sigma^-$ state of SiH is situated 1.75 eV above the ground state,[185] the energetic feasibility of populating this state is evident. Nevertheless, an opposing viewpoint arises from similar hydrogen atom abstraction reactions by fluorine,[110,174] where the excess energy was found to be predominantly in the form of vibrational energy in HF. As a result, one would expect relatively minimal internal energy in SiH, despite the significant exothermicity of its production reactions.

2. Intensity enhanced by autoionization processes at threshold energies. In the second scenario, as previously pointed out by Berkowitz *et al.*,[11] the existence of robust autoionizations within the energy range of the $\Delta\nu = +2$ band of the $\mathrm{X}^+\,^1\Sigma^+ \leftarrow \mathrm{X}\,^2\Pi$ photoionizing transition is evident. This assertion is further corroborated by our subsequent discussion on ion yield spectra.

To examine the effect of these two possible processes on the non-FC feature, we conducted two additional analytical approaches. Firstly, we carried out individual FC calculations for all three photoionizing transitions ($\mathrm{X}^+\,^1\Sigma^+ \leftarrow \mathrm{X}\,^2\Pi$, $\mathrm{a}^+\,^3\Pi \leftarrow \mathrm{X}\,^2\Pi$, and $\mathrm{a}^+\,^3\Pi \leftarrow \mathrm{a}\,^4\Sigma^-$), as illustrated in Figure 5.8. For the purpose of comparing the calculated

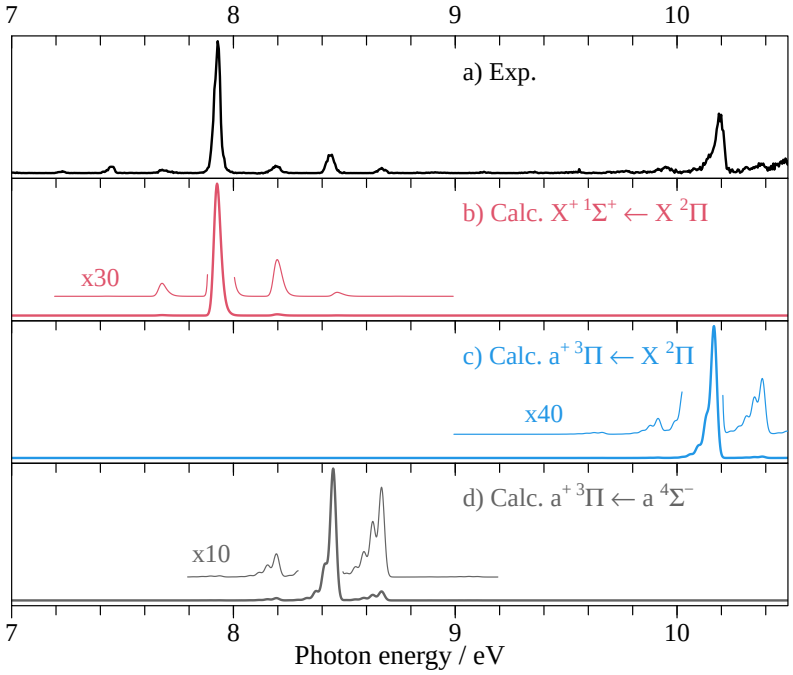

Figure 5.8: Experimental SPES (panel a) compared with the calculated spectra ($T_{\mathrm{vib}} = 2500$ K, $FWHM = 30$ meV) from Ref. 26

spectrum with the experimental one (affected by Stark effect), we applied a downward shift of 7 meV to the energy scale of our calculated spectrum. This correction accounted for the Stark shift caused by the extraction electric field. In these calculations, the vibrational temperature was manually tuned to 2500 K. This adjustment was based on the asymmetrical profile of the origin band of the $\mathrm{a}^{+\,3}\Pi \leftarrow \mathrm{X}\,^{2}\Pi$ photoionizing transition, which arises due to the considerable disparity in vibrational frequencies between the initial and final electronic states (refer to Tab. 5.2). Notably, the elevated vibrational temperature is consistent with the observation of population up to $\nu = 4$ in the neutral electronic ground state, as well as the substantial excess energy within the reaction system. The results of these calculations reveal that the FC factors associated with the $\Delta\nu = 0$ transitions for all three cases are closely approximating 1. Consequently, the spectrum is anticipated to primarily feature the origin bands for each transition (refer to panels b), c), and d) of Fig. 5.8). Upon comparison with our experimental spectrum, it becomes evident that the intensities of the weak bands attributed to the vibrational progression are notably influenced by autoionization processes.

Secondly, we extracted two SPES from the rotated photoelectron matrix (see Fig. 5.5) by integrating over two specific kinetic energy ranges (0-100 meV and 500-600 meV). These integrated spectra are represented in blue and red, respectively, in Fig. 5.9. By examining the dynamic characteristics of the $\Delta\nu = 2$ band presented in the two SPES, we can infer the contribution stemming from two possible sources. When we consider the direct ionization leading to an ionic state, the contribution to the SPES remains relatively stable. This assumption is grounded in the expectation that the partial cross-section in proximity to the threshold energy does not undergo significant fluctuations.

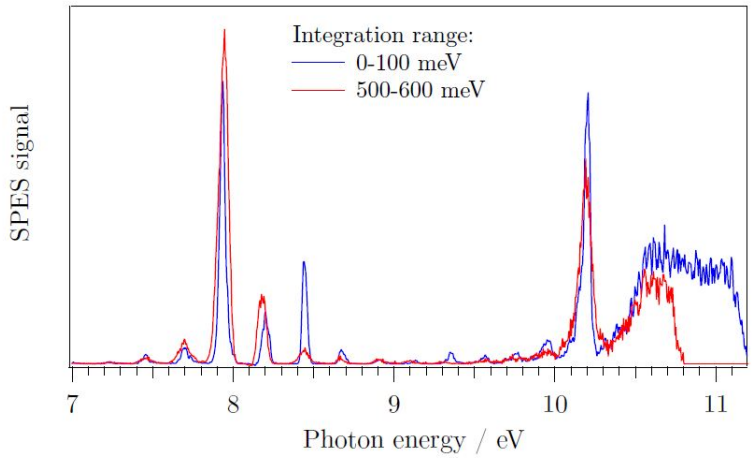

Figure 5.9: SPES spectra extracted from the rotated matrix of Fig. 5.5 for two different electron kinetic energy ranges (0-100 meV in blue, 500-600 meV in red) from Ref. 26.

However, the situation diverges notably in the context of autoionization processes. Autoionizing states manifest at specific photon energies, and their presence is not aligned with the constant ionic state lines. Consequently, the contribution of these autoionizing states to the SPES exhibits significant variation across different integration intervals. Examining Figure 5.9, we observe a marked reduction in the intensity of the $\Delta\nu = 2$ band as kinetic energy increases. This observation leads us to conclude that the contribution arising from the photoionizing transition originating from the neutral $\mathrm{a}\ ^4\Sigma^-$ metastable state appears to be negligible.

To deduce the ionization energies from our experimental spectrum, we carried out a straightforward simulation of the $\mathrm{X}^+\ ^1\Sigma^+ \leftarrow \mathrm{X}\ ^2\Pi$ transition while excluding considerations of spin-orbit coupling and rotational structure. This simulation is depicted in Fig. 5.10. Notably, due to the experimental spectral resolution, we limited our focus to the vibrational features of SiH and SiH^+, utilizing the experimental vibrational wavenumbers as detailed in Refs 85 and 105. For intensity modeling, we maintained a constraint where the FC factors corresponding to a given $\Delta\nu$ band were consistent across the corresponding transitions originating from each vibrational level. Comprehensive details are provided in Ref. 26. Subsequently, the theoretical stick spectrum underwent convolution using a Gaussian line shape characterized by a Full Width at Half Maximum (FWHM) of 30 meV. The vibrational temperature remained at 2500 K as in Fig. 5.8. Through manual adjustment of the ionization energies and FC factors, we successfully reproduced the experimental spectrum, specifically capturing the distinct shapes exhibited by the vibrational bands. For example, the $\Delta\nu = +2$ band, which is noticeably narrower than the $\Delta\nu = -1$ band. This accomplishment permits us to mitigate the impact of autoionization effects on the determination of adiabatic ionization energies.

The adiabatic ionization energies (IE_{ad}) towards the two cationic states ($\mathrm{X}^+\ ^1\Sigma^+$ and $\mathrm{a}^+\ ^3\Pi$) are finally determined by the energy position of the $\mathrm{X}^+\ ^1\Sigma^+$ (ν^+ = 0) $\leftarrow \mathrm{X}\ ^2\Pi$ (ν = 0) and the $\mathrm{a}^+\ ^3\Pi$ (ν^+ = 0) $\leftarrow \mathrm{X}\ ^2\Pi$ (ν = 0) transitions. After field-induced shift corrections, these derived adiabatic ionization energies are presented in Tab. 5.3. The ionization energies are given with 1σ (standard deviation) error bars and have been derived neglecting the Spin-

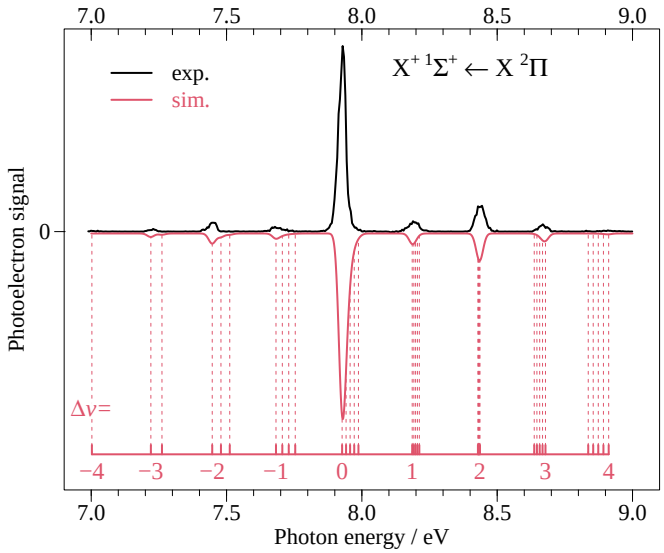

Figure 5.10: Experimental SPES of SiH in the vicinity of the $X^+\,^1\Sigma^+ \leftarrow X\,^2\Pi$ transition (in black) and calculated spectrum (in red), extracted from Ref. 26. The red comb locates the energies of each $\Delta v(= v^+ - v)$ band involving one populated v level of the SiH electronic ground state.

Transition	This work	Ref. 11
$X^+\,^1\Sigma^+ \leftarrow X\,^2\Pi$	7.934(5)	7.91(1)
$a^+\,^3\Pi \leftarrow X\,^2\Pi$	10.205(5)	10.21(1)

Table 5.3: Experimental adiabatic ionization energies (IE_{ad}) of SiH.

Orbit (SO) coupling, which is present in the neutral ground state and characterized by a SO coupling constant[105] $A_{\mathrm{SO}} = 142.83$ cm^{-1}, and possible asymmetric rotational envelopes. In Tab. 5.2 and Tab. 5.3, the experimental and calculated results obtained in this work are compared with calculated and experimental values from the existing literature. The level of agreement is highly satisfactory. Our measured transition energies confirm those determined by Berkowitz *et al.*[11] (7.91(1) eV and 10.21(1) eV) through photoionization mass spectrometry, as well as the calculation by Rosmus and Meyer (7.93 eV).[141] The value from the Active Thermochemical Tables,[2] which is determined to be 7.912 ± 0.014 eV through a rigorous analysis comprising several standard composite calculations, supports also our measured value.

By employing the equation $IE(\mathrm{SiH}) + D_0(\mathrm{SiH}^+) = D_0(\mathrm{SiH}) + IE(\mathrm{Si})$, with the known values of IE(Si) = 8.15166(3) eV[15] and D_0(SiH$^+$) = 3.22(3) eV[20], the derived dissociation energy D_0(SiH) of SiH is found to be 3.00(3) eV according to our $IE(\mathrm{SiH})$ measurement. This value aligns with the value obtained by Berkowitz *et al.* (2.98(3) eV) and the upper limit provided by Huber and Herzberg (D_0(SiH) ≤ 3.060 eV).[85] Moreover, the calculated and experimental energy differences between the two lowest cationic states ($\Delta E_{\mathrm{X^+-a^+}} = T_0(\mathrm{a}^+) - T_0(\mathrm{X}^+)$) are determined to be 2.24 eV and 2.271(5) eV, respectively. These findings closely correspond with the computed ΔE values of Sannigrahi *et al.* (2.31 eV, corrected for Zero-Point Energy)[144]. The experimental ΔE value obtained by Berkowitz *et al.*[11] is 2.30 ± 0.01

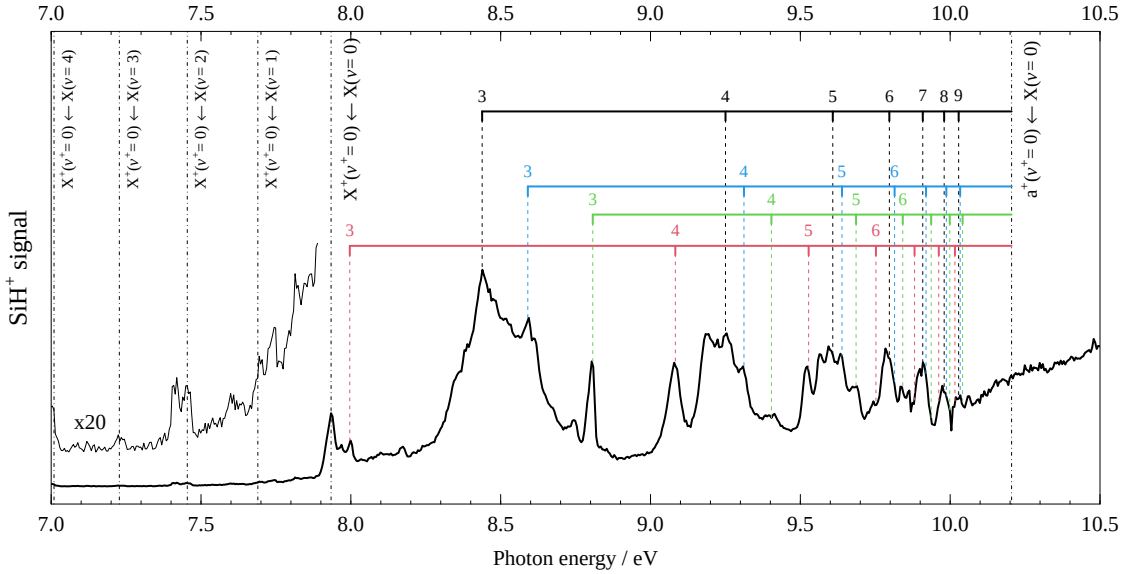

Figure 5.11: Mass-selected ion yield of the SiH radical from Ref. 26. The labels located by combs correspond to the assignments of the Rydberg series of neutral species observed by autoionization. The gray dashed vertical lines locate ionization thresholds from different vibrational levels.

eV, inferred indirectly from the Rydberg series converging to a^+ (as described in section 5.2.3.2).

5.2.3.2 Photoion yield

The SiH^+ photoion yield recorded in this study is depicted in Fig. 5.11. Similar to our previous investigation on CH radical,[56] a series of strong features stemming from autoionization is discernible. Drawing from the distinctive peak characteristics and building upon the prior work by Berkowitz *et al.*[11], a preliminary assignment of Rydberg series is undertaken. This assignment is based on the Rydberg energy formula:

$$E_{\mathrm{Ry}} = IE - \frac{R_{\mathrm{y}}}{(n^*)^2} \tag{5.1}$$

with R_{y} representing the Rydberg constant of SiH (R_{y} = 13.60544 eV) and n^* denoting the effective quantum number such that $n^* = n - \delta$ (with δ the quantum defect).

Within Figure 5.11, four sets of combs are presented, corresponding to calculated Rydberg series converging towards the a^+ cationic state using Eq. 5.1, the adiabatic ionization energy (10.205(5) eV), and four distinct quantum defects (0.225 in black, 0.518 in red, 0.097 in blue, and -0.120 in green). The labeling of the principal quantum number introduces an element of uncertainty and has been arbitrarily initiated at $n = 3$ for each series. It is pertinent to mention that the first two series (in black and red) were previously reported by Berkowitz *et al.*[11], while the blue and green combs represent new preliminary assignments. As the production of SiH occurs across multiple vibrational levels (as discussed earlier), several sequence bands exist for each series. Specifically, these Rydberg states converge toward $\mathrm{a}^+\,{}^3\Pi(\nu^+ = \nu)$, originating from the $\mathrm{X}\,{}^2\Pi(v)$ state with different ν values. For the sake of clarity, only the

Rydberg transitions originating from $\nu = 0$ are presented.

The ground-state electronic configuration of the SiH united-atom system [79] is described as $[\cdots](3s\sigma)^2(3p\sigma)^2(3p\pi)^1$. Consequently, the photoelectron involved in the ionization towards the $X^+\,^1\Sigma^+$ and $a^+\,^3\Pi$ cationic states possesses a "p-like" character, specifically originating from the 3pπ and 3pσ orbitals, respectively. This leads to the anticipation of neutral Rydberg series classified as only "s" and "d," in adherence to the selection rule $\Delta l = \pm 1$, where l represents the orbital angular momentum quantum number of the photoelectron partial wave. In the context of hydrocarbon molecules, quantum defects associated with "s," "p," and "d" series typically exhibit δ values near 1, 0.5, and 0, respectively.[100] However, for molecules containing heavier atoms, these values can significantly deviate from the norm, with quantum defects nearing 2, as exemplified by the "s" series in the case of the S_2 molecule.[84] Despite these trends, our present study (as well as Berkowitz's work[11]) encounters an ambiguity in characterizing the corresponding states as having either "s" or "d" attributes. This ambiguity arises due to the absence of a definitive assignment of the principal quantum number value.

It is noteworthy that the δ =0.225 Rydberg series at n = 3 coincides precisely with the $\nu^+ = 2$ vibrational level of the $X^+\,^1\Sigma^+$ cationic state. This overlap gives rise to a distinct autoionization-at-threshold structure, characterized by the emission of a photoelectron without any accompanying kinetic energy. This phenomenon elucidates the prominent $\Delta\nu = 2$ band of the $X^+\,^1\Sigma^+$ (ν^+) $\leftarrow X\,^2\Pi$ (ν) transition observed in the SPES spectrum.

Through our investigation, nearly all the discernible peak signals have been successfully assigned, with one notable exception—a sharp feature aligning with the ionization energy ($X^+ \leftarrow X$ at 7.934 eV). Intriguingly, this particular feature could account for the presence of subtle "hot band" structures that manifest below the primary ionization energy. These structures are evident in the magnified section of the spectrum presented in Fig. 5.11. It is reasonable to associate the remaining structures within this spectral region with vibrational autoionization processes, drawing parallels to the scenario observed in the case of the CH radical.[56]

5.2.4 Conclusions

In this work, we measured for the first time the threshold photoelectron spectrum of the SiH radical, enabled by the mass-selective capabilities of the double-imaging spectrometer. The adiabatic ionization energies corresponding to the electronic ground state $X^+\,^1\Sigma^+$ and the first excited electronic state $a^+\,^3\Pi$. have been determined, in good agreement with our calculated values, as well as with findings from prior research endeavors, and showing an improved accuracy compared to the previous work of Berkowitz *et al.*[11]

Furthermore, our investigation delves into the pronounced autoionization features detected within the SiH^+ ion yield. These observations were analyzed in light of the earlier work by Berkowitz *et al.*[11], and a preliminary assignment of additional Rydberg series was proposed. Notably, similar strong autoionization processes were previously observed in the study of the CH radical by Gans *el al.*, using the same experimental framework.[56] It is pertinent to

underline that both the CH and SiH systems serve as benchmark models for the exploration of autoionization processes. The outcomes of our experimental ion yield analyses hold the potential to stimulate new theoretical inquiries in this realm, offering an avenue for further exploration and understanding.

Exploring higher spectral resolution through techniques such as PFI-ZEKE PES on VULCAIM setup holds significant promise. Such investigations would offer a valuable avenue to unravel the intricate fine structure inherent in the ionizing transitions discussed earlier. This would encompass not only the rotational and spin-orbit structures but also provide enhanced precision in determining the ionization energies.

5.3 Elucidation of threshold photoelectron spectrum of Si_2

5.3.1 Astrophysical context and spectroscopic background

Similar to C_2 [67] and SiC [22] which have been observed in installer space, Si_2 attracts the interest as it could potentially play a role in the astrophysical reactions like the building block of interstellar silicate dust. Meanwhile, as the smallest Si_n cluster, study on Si_2 is also crucial to explore how chemical bonding in a cluster evolves with the number of atoms. This is extremely interesting in some application areas such as the semiconductor device in the electronics industry. [9,111]

Despite the significant research interest, spectroscopic investigations on Si_2 and its ions remain limited due to challenges in producing sufficient quantities of the molecules and the spectroscopic complexity arising from numerous low-lying electronic states. The ground electronic state of Si_2 is the triplet $\mathrm{X}\ ^3\Sigma_\mathrm{g}^-$, and the lowest excited state $\mathrm{D}\ ^3\Pi_\mathrm{u}$ lies in close proximity above it. The energy separation between these states was experimentally measured to be 0.053±0.015 eV by Nimlos *et al.* [125] and 0.083±0.010 eV by Kitsopoulos *et al.* [94] using photodetachment spectroscopy on the Si_2^- anion. Kitsopoulos *et al.* also determined the energies of excited states of Si_2 $\mathrm{a}\ ^1\Delta_\mathrm{g}$, $\mathrm{b}\ ^1\Pi_u$, and $\mathrm{c}\ ^1\Sigma_g^+$ relative to the $\mathrm{X}\ ^3\Sigma_\mathrm{g}^-$ ground state. These experimental findings are in good agreement with calculated values by Shi *et al.*, who extensively studied the properties of numerous states of Si_2 using the complete active space self-consistent field (CASSCF) method followed by the valence internally contracted multireference configuration interaction (MRCI) approach. [150]

The ionization energy of the Si_2 dimer was the subject of controversy in the past. [14,165,178] Subsequent experimental efforts narrowed down its range to be between 7.9 to 8.1 eV. [178] Computational predictions suggested an ionization energy of 7.913 eV. [45] Technological advancements enabled the determination of the adiabatic ionization potential (*IP*) of Si_2 to be 7.9206(9) eV using laser ablation radical sources in combination with mass-selected photoionization spectroscopy through the intermediate $\mathrm{N}\ ^3\Sigma_u^-$ state. [111] Another study by Kostko *et al.* using VUV single-photon ionization measured the *IP* of Si_2 and extracted a value of 7.92±0.05 eV. [97] In their work, a feature at 8.3 eV was observed and attributed, through calculations, to the photoionization from the $\mathrm{X}\ ^3\Sigma_\mathrm{g}^-$ neutral state of Si_2 to the $\mathrm{a}^+\ ^2\Pi_\mathrm{u}$ excited state of Si_2^+ ($\mathrm{a}^+\ ^2\Pi_\mathrm{u} \leftarrow \mathrm{X}\ ^3\Sigma_\mathrm{g}^-$). Dixon *et al.* [45] calculated an adiabatic ionization energy of 8.44±0.02 eV for this transition, where the excited $\mathrm{a}^+\ ^2\Pi_\mathrm{u}$ state of the cation lies 0.52 eV above the $\mathrm{X}^+\ ^4\Sigma_\mathrm{g}^-$ ground state. The *IP* value from the Active Thermochemical Tables [2] is determined to be 7.902 ± 0.014 eV. Further calculations involving more low-lying excited states of Si_2^+, including $\mathrm{a}^+\ ^2\Pi_\mathrm{u}$, $\mathrm{b}^+\ ^2\Delta_\mathrm{g}$, $\mathrm{c}^+\ ^2\Sigma_\mathrm{g}^-$, $\mathrm{e}^+\ ^2\Pi_\mathrm{u}$, were conducted at the MRCI+ Q/AVQZ level by Liu *et al.*. [106] More recently, photodissociation spectroscopy of ions authorized transitions from the cationic ground state $\mathrm{X}^+\ ^4\Sigma_g^-$ revealed the two lowest quartet excited states of Si_2^+, $^4\Sigma_u^-$(I) and $^4\Sigma_u^-$(II). These states are relatively far from the ground state, with energy intervals of approximately 2.9 and 4.6 eV, respectively. [158]

In our study, we report more experimental energy values for the excited states ($\mathrm{b}^+\ ^2\Delta_\mathrm{g}$, $\mathrm{c}^+\ ^2\Sigma_\mathrm{g}^-$, and $\mathrm{e}^+\ ^2\Pi_\mathrm{u}$) of Si_2^+ by means of photoionization spectroscopy. The description of the geometric and electronic structure of the

Si_2 and Si_2^+ as well as the discussion on the selection rules of photoionization transition should be valuable for theoretical works. The detailed description and results have been published in 2022.[27]

5.3.2 *Ab initio* calculations

Table 5.4: Electronic configurations of Si_2 and Si_2^+ electronic states from Ref. 27.

Species	State	Main Configurations[a]	Weights[b]
Si_2	$X\ ^3\Sigma_g^-$	$(4\sigma_u)^2(5\sigma_g)^2(2\pi_u)^2(2\pi_g)^0$	92%
	$D\ ^3\Pi_u$	$(4\sigma_u)^2(5\sigma_g)^1(2\pi_u)^3(2\pi_g)^0$	176%
		$(4\sigma_u)^2(5\sigma_g)^1(2\pi_u)^1(2\pi_g)^2$	8%
		$(4\sigma_u)^2(5\sigma_g)^1(2\pi_u)^2(2\pi_g)^1$	5%
	$a\ ^1\Delta_g$	$(4\sigma_u)^2(5\sigma_g)^2(2\pi_u)^2(2\pi_g)^0$	181%
		$(4\sigma_u)^2(5\sigma_g)^2(2\pi_u)^0(2\pi_g)^2$	6%
Si_2^+	$X^+\ ,^4\Sigma_g^-$	$(4\sigma_u)^2(5\sigma_g)^1(2\pi_u)^2(2\pi_g)^0$	90%
	$a^+\ ^2\Pi_u$	$(4\sigma_u)^2(5\sigma_g)^2(2\pi_u)^1(2\pi_g)^0$	177%
		$(4\sigma_u)^2(5\sigma_g)^0(2\pi_u)^3(2\pi_g)^0$	7%
	$b^+\ ^2\Delta_g$	$(4\sigma_u)^2(5\sigma_g)^1(2\pi_u)^2(2\pi_g)^0$	174%
		$(4\sigma_u)^2(5\sigma_g)^1(2\pi_u)^0(2\pi_g)^2$	8%
	$c^+\ ^2\Sigma_g^-$	$(4\sigma_u)^2(5\sigma_g)^1(2\pi_u)^2(2\pi_g)^0$	90%
	$d^+\ ^2\Sigma_g^+$	$(4\sigma_u)^2(5\sigma_g)^1(2\pi_u)^2(2\pi_g)^0$	86%
		$(4\sigma_u)^2(5\sigma_g)^1(2\pi_u)^0(2\pi_g)^2$	6%
	$e^+\ ^2\Pi_u$	$(4\sigma_u)^2(5\sigma_g)^0(2\pi_u)^3(2\pi_g)^0$	96%
		$(4\sigma_u)^2(5\sigma_g)^2(2\pi_u)^1(2\pi_g)^0$	72%
		$(4\sigma_u)^0(5\sigma_g)^2(2\pi_u)^3(2\pi_g)^0$	7%
		$(4\sigma_u)^2(5\sigma_g)^0(2\pi_u)^1(2\pi_g)^2$	7%

[a] Inner electronic configuration $(1\sigma_g)^2(1\sigma_u)^2(2\sigma_g)^2(2\sigma_u)^2(3\sigma_g)^2(3\sigma_u)^2(1\pi_u)^4(1\pi_g)^4(4\sigma_g)^2$ is omitted.
[b] Only configurations with a weight higher than 5% are reported.

The *ab initio* calculations on the electronic states of Si_2 and Si_2^+ were conducted by Jean-Christophe Loison, using the MRCI + Q method with CASSCF wave-functions, as outlined in Section 5.2.2. For an in-depth exposition of the calculation specifics, refer to Ref. 27. Below, only the main calculated results are presented.

The main configurations for the three lowest states of Si_2 and the six lowest states of Si_2^+ have been extrapolated and summarized in Table 5.4. Notably, the sum of the coefficients of the multi-configurations for Π and Δ electronic states approaches approximately 200%, accounting for their inherent doublet degeneracy within diatomic molecules, while for Σ states, the total coefficient summation approximates 100% due to an equal degeneracy of 1.

The potential energy curves corresponding to these Si_2 and Si_2^+ states are displayed as a function of the Si–Si bond length, R(Si-Si), in Fig. 5.12. Comprehensive molecular properties calculated for these states are listed in Tab. 5.5. All values in the table are obtained through CBS extrapolations (as detailed in Section 5.2.2), with the exception of

the anharmonicity constants, which are computed at the AV6Z level of theory.

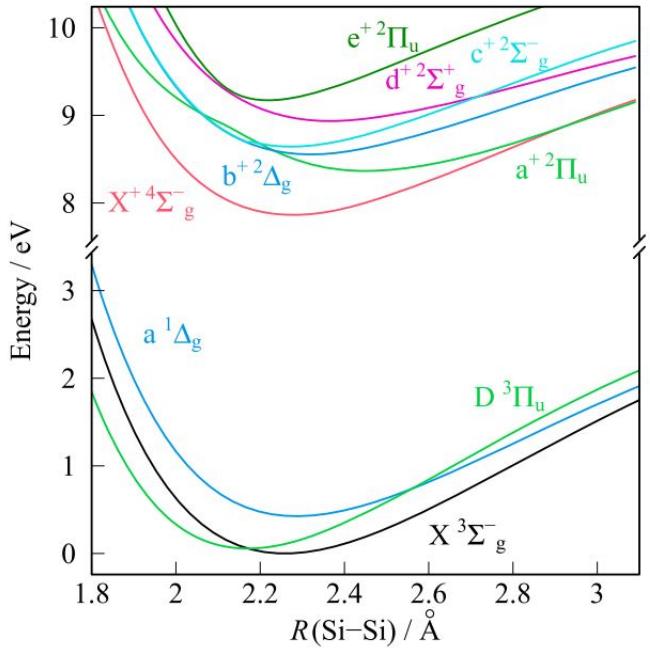

Figure 5.12: Calculated potential energy curves (MRCI/AVQZ method) of the Si_2 and Si_2^+ states from Ref. 27.

The Franck-Condon (FC) calculations were executed with the ezSpectrum software[65] using the *ab initio* Molden output files calculated with the AVQZ basis set for all states and neglecting spin.

5.3.3 Results and discussion

5.3.3.1 Photoelectron spectroscopy

Given the comprehensive visualization of the intricate electronic landscapes encompassing Si_2 and Si_2^+ in proximity to their respective ground electronic states shown in Fig. 5.12 as well as the typical vibronic temperatures spanning a range from a few hundred to a few thousand kelvins in the flow-tube reactor, it becomes conceivable that the photoelectron spectrum of Si_2 in the vicinity of adiabatic ionization potential (*IP*) of Si_2 would exhibit the signature of numerous vibronic transitions involving both neutral and cationic states.

Based on the electronic configurations detailed in Tab. 5.4 and considering the photoionization selection rules applicable to diatomic molecules,[180] it becomes evident that within the energy range of our measurement, a total of 15 photoionization transitions from the three lowest neutral states to the six lowest cationic states are allowed: 4 transitions stem from the $\mathrm{X}\,^3\Sigma_g^-$ state, 6 transitions from the $\mathrm{D}\,^3\Pi_u$ state, and 5 transitions from the metastable $\mathrm{a}\,^1\Delta_g$ state. To assign our experimental photoelectron spectrum, shown in the upper panel of Fig. 5.13, we performed FC simulations for all 15 allowed transitions. The resulting calculated stick spectra, adjusted by the ionization energies computed as tabulated in Tab. 5.5, are displayed in Fig. 5.13, along with their corresponding convolved spectra

Table 5.5: Calculated molecular properties of the electronic states of Si_2 and Si_2^+ from Ref. 27

Species	State	R_e /Å	ω_e / cm^{-1}	$\omega_e x_e$ / cm^{-1}	$\omega_e y_e$ / cm^{-1}	E_e[a] / eV	E_0 / eV
Si_2	$X\ ^3\Sigma_g^-$	2.2568	509.3400	2.01	0.00	0.0000	0.0000
		2.2436[150]	512.75[150]	2.0256[150]	0.0048816[150]		
	$D\ ^3\Pi_u$	2.1678	544.2	2.42	0.00	0.057	0.059
		2.1513[150]	551.62[150]	2.3839[150]	0.048247[150]	0.0894[150]	
	$a\ ^1\Delta_g$	2.2883	480.3	2.07	0.00	0.421	0.419
		2.2752[150]	486.39[150]	1.7896[150]	0.0057418[150]	0.4331[150]	
Si_2^+	$X^+\ ^4\Sigma_g^-$	2.2717	471.3	2.51	0.00	7.883	7.881
		2.2780[106]	467.82[106]	2.5808[106]			7.913[45]
	$a^+\ ^2\Pi_u$	2.4559	393.13	-	-	8.421	8.414
		2.4550[106]	388.48[106]	2.2620[106]		8.3934[106]	8.443[45]
	$b^+\ ^2\Delta_g$	2.3175	429.1	2.77	0.00	8.590	8.585
		2.3215[106]	424.62[106]	2.7988[106]		8.6025[106]	
	$c^+\ ^2\Sigma_g^-$	2.2710	478.3	5.67	0.10	8.653	8.651
		2.2795[106]	464.67[106]	3.0136[106]		8.6624[106]	
	$d^+\ ^2\Sigma_g^+$	2.3650	385.1	2.86	0.00	8.940	8.932
		2.3740[106]	379.38[106]	2.8007[106]		8.9837[106]	
	$e^+\ ^2\Pi_u$	2.2173	615.5	-	-	9.186	9.192
		2.2165[106]	595.54[106]	6.6539[106]		9.2284[106]	

[a] In Ref. 106, the energies with respect to the ground state of Si_2^+ are given. The corresponding ionization energy values reported in the table include our calculated cationic origin (7.883 eV).

generated using a Gaussian-line shape with a FWHM of 25 meV. A vibrational temperature of 1500 K was applied to effectively reproduce the vibrational progressions in the overall transitions, which may not be well defined due to the complexity of the spectrum.

Notably, our investigation revealed an intriguing observation: a distinctive band around 7.48 eV could not be ascribed to any specific allowed transition, except potentially to the nominally spin-forbidden $X^+\ ^4\Sigma_g^- \leftarrow a\ ^1\Delta_g$ transition. Consequently, the FC simulated spectrum corresponding to this forbidden ionization transition is also presented in Fig. 5.13. The observation of this forbidden ionization transition will be discussed in Section 5.3.4.

Moreover, an assessment of the efficiency for each photoionization transition was conducted, based on the assumption of a consistent ionization cross section for each emitted electron as described in the Koizumi model.[96] Taking into account the multi-configuration nature of the electronic states for Si_2 and Si_2^+ (refer to Tab. 5.4), the number of emitted electrons is counted by summing the products of the weights associated with the electronic configurations linked to the Si_2 and Si_2^+ electronic states involved in the specific transition. The corresponding relative ionization efficiencies stemming from this evaluation are documented in Tab. 5.6.

From the calculated spectra, which encompass the predicted ionization energies of the ionizing transitions and associated vibrational progressions, in conjunction with the predicted relative ionization efficiencies, we embarked

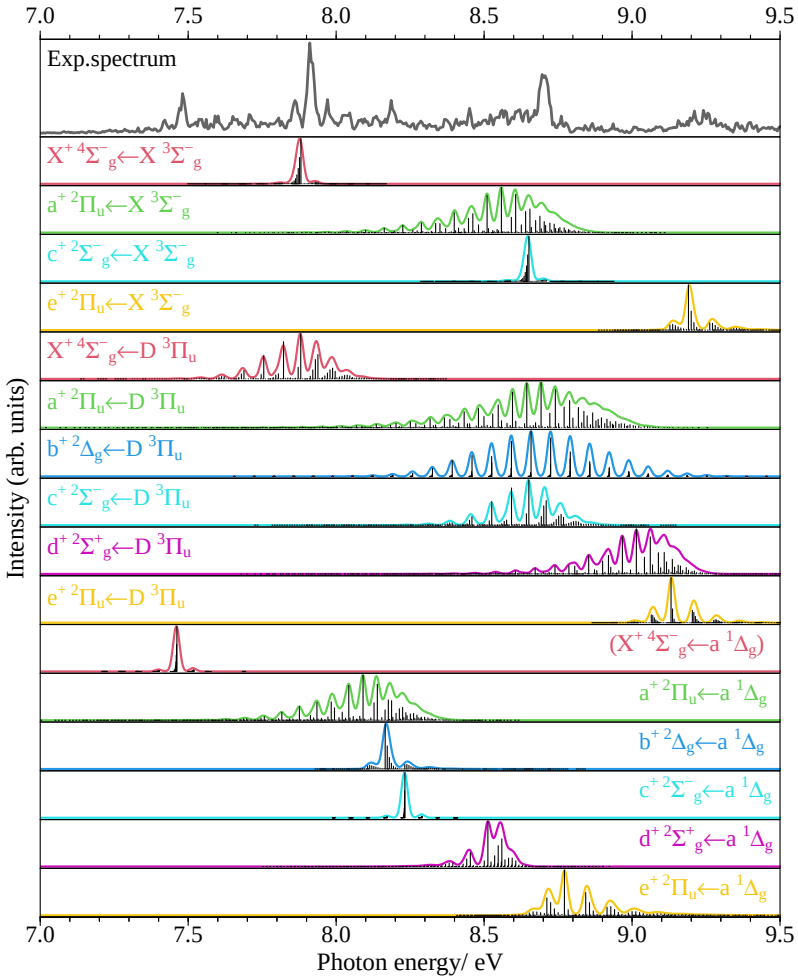

Figure 5.13: Experimental photoelectron spectrum of Si_2 (upper panel) compared with the calculated spectra of 16 vibronic transitions predicted in the energy range from 7.0 eV to 9.5 eV (16 lower panels) from Ref. 27. In the calculated spectra the black sticks correspond to the FCF simulation performed with ezSpectrum software and the curve lines are the spectra obtained after the convolution with a Gaussian line shape of FWHM = 25 meV. The vibrational temperature is 1500 K. The energy positions of the FC simulated spectra for all these vibronic transitions are defined by our calculated adiabatic energies shown in Tab. 5.4.

on an endeavor to attribute the ionization transitions and subsequently reproduce our experimental spectrum. In this purpose, the energies and the relative ionization efficiencies of the transitions were fine-tuned to achieve the best agreement with the experimental spectrum, leading to experimental values documented in Tab. 5.6.

The process of assignment was meticulously conducted in a stepwise manner due to the intricate complexity of the spectral landscape:

1. **Unambiguously Assigned Transitions** Five photoionization transitions involving the three neutral states are unambiguously assigned. The uncertainty on the energy values (as detailed in Tab. 5.6) takes into account factors such as photon energy calibration and energy scaling of the simulation. Calculated relative ionization efficiencies are kept fixed. Note that the transition intensities are modified with manually adjusted factors (1.000, 1.268, 0.750) corresponding to the populations of the three neutral states ($X\ ^3\Sigma_g^-$, $D\ ^3\Pi_u$, $a\ ^1\Delta_g$) at a thermal population of 1500 K.

Table 5.6: Adiabatic ionization energies and relative ionization efficiency (Φ in arbitrary units) of the photoionising transitions of Si_2 from Ref. 27.

Transition	$E_{\mathrm{calc.}}$ /eV	$E_{\mathrm{exp.}}$ /eV	$\Phi_{\mathrm{calc.}}$	$\Phi_{\mathrm{exp.}}$
$\mathrm{X}^{+\,4}\Sigma_{\mathrm{g}}^{-} \leftarrow \mathrm{X}\,^{3}\Sigma_{\mathrm{g}}^{-}$	7.881	7.919(5)	0.83	0.83
	7.913[45]	7.92(5)[97]		
$\mathrm{a}^{+\,2}\Pi_{\mathrm{u}} \leftarrow \mathrm{X}\,^{3}\Sigma_{\mathrm{g}}^{-}$	8.414	8.429(12)	1.59	1.59
	8.443[45]	8.3[97]		
$\mathrm{c}^{+\ 2}\Sigma_{\mathrm{g}}^{-} \leftarrow \mathrm{X}\,^{3}\Sigma_{\mathrm{g}}^{-}$	8.651	8.708(6)	0.55	0.55
$\mathrm{e}^{+\ 2}\Pi_{\mathrm{u}} \leftarrow \mathrm{X}\,^{3}\Sigma_{\mathrm{g}}^{-}$	9.192	9.250(10)	0.66	0.50
$\mathrm{X}^{+\,4}\Sigma_{\mathrm{g}}^{-} \leftarrow \mathrm{D}\,^{3}\Pi_{\mathrm{u}}$	7.822	7.869(5)	1.59	1.59
$\mathrm{a}^{+\,2}\Pi_{\mathrm{u}} \leftarrow \mathrm{D}\,^{3}\Pi_{\mathrm{u}}$	8.355	8.379(16)	0.06	0.06
$\mathrm{b}^{+\ 2}\Delta_{\mathrm{g}} \leftarrow \mathrm{D}\,^{3}\Pi_{\mathrm{u}}$	8.526	8.571(6)	1.54	0.60
$\mathrm{c}^{+\ 2}\Sigma_{\mathrm{g}}^{-} \leftarrow \mathrm{D}\,^{3}\Pi_{\mathrm{u}}$	8.592	8.650(10)	0.27	0.27
$\mathrm{d}^{+\ 2}\Sigma_{\mathrm{g}}^{+} \leftarrow \mathrm{D}\,^{3}\Pi_{\mathrm{u}}$	8.873	-	0.77	-
$\mathrm{e}^{+\ 2}\Pi_{\mathrm{u}} \leftarrow \mathrm{D}\,^{3}\Pi_{\mathrm{u}}$	9.133	9.200(10)	0.84	0.35
$\mathrm{X}^{+\,4}\Sigma_{\mathrm{g}}^{-} \leftarrow \mathrm{a}\,^{1}\Delta_{\mathrm{g}}$	7.462	7.482(5)	-	0.66
$\mathrm{a}^{+\,2}\Pi_{\mathrm{u}} \leftarrow \mathrm{a}\,^{1}\Delta_{\mathrm{g}}$	7.995	1.992(10)	1.55	0.60
$\mathrm{b}^{+\ 2}\Delta_{\mathrm{g}} \leftarrow \mathrm{a}\,^{1}\Delta_{\mathrm{g}}$	8.166	8.185(6)	0.78	0.78
$\mathrm{c}^{+\ 2}\Sigma_{\mathrm{g}}^{-} \leftarrow \mathrm{a}\,^{1}\Delta_{\mathrm{g}}$	8.232	8.271(9)	0.14	0.14
$\mathrm{d}^{+\ 2}\Sigma_{\mathrm{g}}^{+} \leftarrow \mathrm{a}\,^{1}\Delta_{\mathrm{g}}$	8.513	-	0.39	-
$\mathrm{e}^{+\ 2}\Pi_{\mathrm{u}} \leftarrow \mathrm{a}\,^{1}\Delta_{\mathrm{g}}$	8.773	8.813(12)	0.75	0

The factor of $\mathrm{a}\,^{1}\Delta_{\mathrm{g}}$ accounts for its higher value than calculated thermal population (0.069), which is proportional to the spin degeneracy (the ratio of populations on singlet/triplet state = 1:3). This is compatible with the co-production of singlet and triplet states of Si_2 through the Si(^{3}P) + Si(^{3}P) reaction, under the assumption that relaxation from the metastable $\mathrm{a}\,^{1}\Delta_{\mathrm{g}}$ state to the ground state of Si_2 takes longer than the residence time in the flow tube reactor (approximately 1 ms).

- $\mathrm{X}^{+\,4}\Sigma_{\mathrm{g}}^{-} \leftarrow \mathrm{X}\,^{3}\Sigma_{\mathrm{g}}^{-}$
- $\mathrm{c}^{+\ 2}\Sigma_{\mathrm{g}}^{-} \leftarrow \mathrm{X}\,^{3}\Sigma_{\mathrm{g}}^{-}$
- $\mathrm{X}^{+\,4}\Sigma_{\mathrm{g}}^{-} \leftarrow \mathrm{D}\,^{3}\Pi_{\mathrm{u}}$
- $\mathrm{X}^{+\,4}\Sigma_{\mathrm{g}}^{-} \leftarrow \mathrm{a}\,^{1}\Delta_{\mathrm{g}}$
- $\mathrm{b}^{+\ 2}\Delta_{\mathrm{g}} \leftarrow \mathrm{a}\,^{1}\Delta_{\mathrm{g}}$

2. **Partially Assigned Transitions** Several transitions are found to be present, supported by specific spectral features. However, challenges are encountered in accurately determining their positions or intensities due to tran-

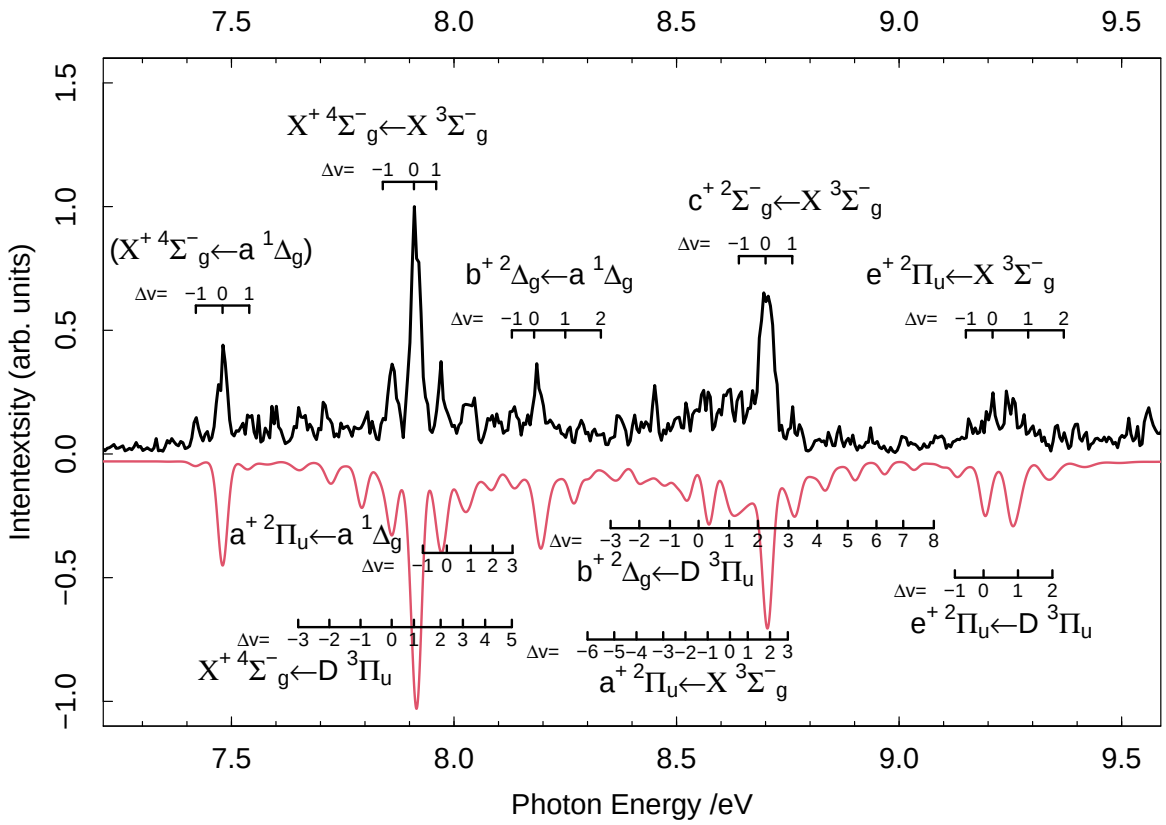

Figure 5.14: Experimental photoelectron spectrum of Si_2 (in black) compared with the complete simulated spectrum (in red) from Ref. 27. The simulated spectrum was obtained by the convolution with Gaussian line shape of FWHM = 25 meV, with the vibrational temperature equal to 1500 K. All the intensities of electronic transitions are normalized by dividing by their curve area.

sition overlap. Larger uncertainties in energies or discrepancies from predicted relative ionization efficiencies are noticeable for these transitions.

- $\mathrm{a}^{+\ 2}\Pi_{\mathrm{u}} \leftarrow \mathrm{X}\ ^{3}\Sigma_{\mathrm{g}}^{-}$
- $\mathrm{b}^{+\ 2}\Delta_{\mathrm{g}} \leftarrow \mathrm{D}\ ^{3}\Pi_{\mathrm{u}}$
- $\mathrm{a}^{+\ 2}\Pi_{\mathrm{u}} \leftarrow \mathrm{a}\ ^{1}\Delta_{\mathrm{g}}$
- $\mathrm{e}^{+\ 2}\Pi_{\mathrm{u}} \leftarrow \mathrm{X}\ ^{3}\Sigma_{\mathrm{g}}^{-}$
- $\mathrm{e}^{+\ 2}\Pi_{\mathrm{u}} \leftarrow \mathrm{D}\ ^{3}\Pi_{\mathrm{u}}$

3. **Tentatively Assigned Transitions** Following the assignment of transitions, the energies of all the involved electronic states have been determined, with the exception of the $\mathrm{d}^{+\ 2}\Sigma_{\mathrm{g}}^{+}$ state. With energies imposed, the following transitions are predicted to contribute minimally to the signals. Therefore their assignments remain tentative due to low signal-to-noise ratios in the spectrum's dense region.

- $\mathrm{a}^{+}\ ^{2}\Pi_{\mathrm{u}} \leftarrow \mathrm{a}\ ^{1}\Delta_{\mathrm{g}}$
- $\mathrm{c}^{+}\ ^{2}\Sigma_{\mathrm{g}}^{-} \leftarrow \mathrm{a}\ ^{1}\Delta_{\mathrm{g}}$
- $\mathrm{e}^{+}\ ^{2}\Pi_{\mathrm{u}} \leftarrow \mathrm{a}\ ^{1}\Delta_{\mathrm{g}}$

4. **Complete Simulation and Verification** A comprehensive simulation incorporating all assigned transitions is presented in Fig. 5.14. The remarkable agreement between the final simulated spectrum and our experimental data seems to indicate that the two transitions involving the $\mathrm{d}^{+}\ ^{2}\Sigma_{\mathrm{g}}^{+}$ state do not contribute significantly to the spectrum. Consequently, no conclusive information regarding the $\mathrm{d}^{+}\ ^{2}\Sigma^{+}g$ state can be inferred from this study.

- $\mathrm{d}^{+}\ ^{2}\Sigma_{\mathrm{g}}^{+} \leftarrow \mathrm{D}\ ^{3}\Pi_{\mathrm{u}}$
- $\mathrm{d}^{+}\ ^{2}\Sigma_{\mathrm{g}}^{+} \leftarrow \mathrm{a}\ ^{1}\Delta_{\mathrm{g}}$

5.3.3.2 Photoion yield

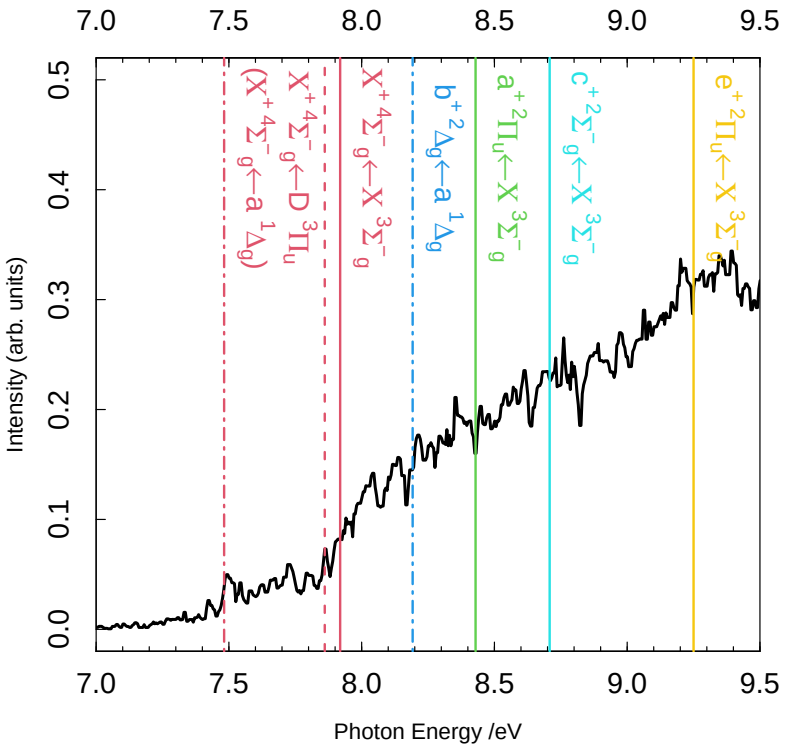

Figure 5.15: Si_2^+ ion yield adapted from Ref. 27. The transition energies acquired from the previous analysis of experimental and simulated spectra for the assigned transitions from the three neutral states $\mathrm{X}\ ^{3}\Sigma_{\mathrm{g}}^{-}$, $\mathrm{D}\ ^{3}\Pi_{\mathrm{u}}$ and $\mathrm{a}\ ^{1}\Delta_{\mathrm{g}}$ are presented as solid, dashed and dot-dashed vertical lines.

The Si_2 ion yield was also measured and reported in Fig. 5.15. The transition energies acquired from the previous analysis of experimental and simulated spectra for the assigned transitions from the three neutral states $\mathrm{X}\ ^{3}\Sigma_{\mathrm{g}}^{-}$,

$\mathrm{D}\ ^3\Pi_\mathrm{u}$ and $\mathrm{a}\ ^1\Delta_\mathrm{g}$ are presented as solid, dashed and dotted vertical lines. Despite the low signal-to-noise ratio we can still see an evident peak assigned to the forbidden transition $\mathrm{X}^+\ ^4\Sigma_\mathrm{g}^- \leftarrow \mathrm{a}\ ^1\Delta_\mathrm{g}$, and its asymmetric shape gives again the clue that the electron correlation is involved giving rise to the photoionization channel.[10] In addition, a small narrow autoionization peak signal is observed at exactly the position (7.87 eV) of $\mathrm{X}^+\ ^4\Sigma_\mathrm{g}^- \leftarrow \mathrm{D}\ ^3\Pi_\mathrm{u}$, which may explain the slightly higher photoelectron signal at $\Delta\nu = 0$ in the experimental spectra than the simulated one in Fig. 5.14. The complex electronic structure of the cation and the quality of the ion yield spectrum make it challenging to extract more detailed information about the Rydberg states responsible for these autoionization signals.

5.3.4 Discussion on the spin-forbidden transition

As mentioned above, a quite strong and distinctive signal observed in SPES can be exclusively attributed to the spin-forbidden photoionization transition $\mathrm{X}^+\ ^4\Sigma_\mathrm{g}^- \leftarrow \mathrm{a}\ ^1\Delta_\mathrm{g}$. This quartet-singlet transition involves not only the emission of an electron but also a change in the electron-spin. Consequently, the conventional selection rules for the photoionization of diatomic molecules, as proposed by Xie *et al.*[180], no longer apply.

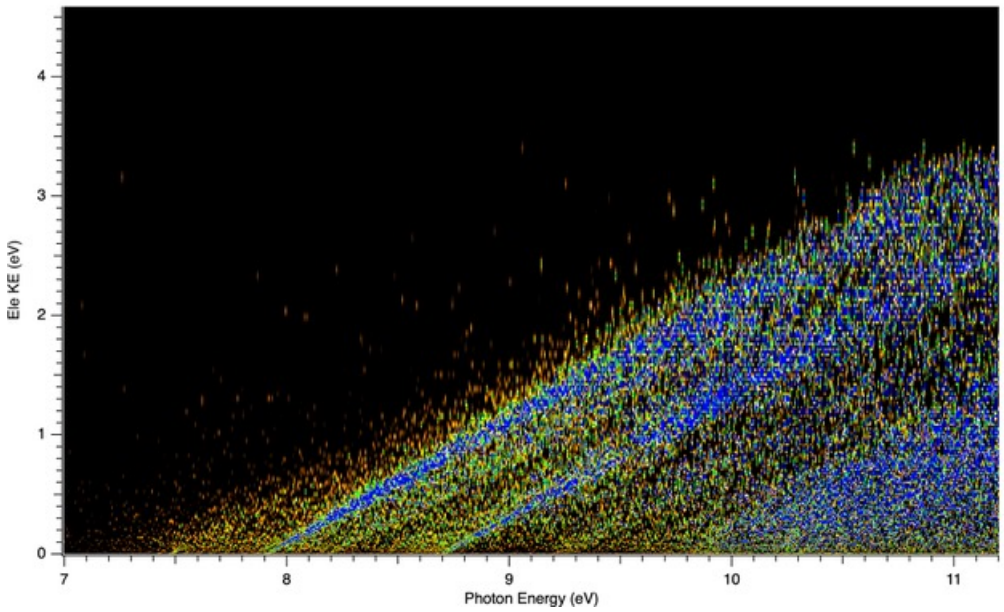

Figure 5.16: Raw photoelectron matrix corresponding to *m/z* = 56 from Ref. 27. The high intensity signals may be saturated in color scale in order to see clearly the low intensity signal at about 7.48 eV.

Furthermore, an intriguing aspect of the observed forbidden transition is its "dynamic" nature, as evident from the analysis of the raw photoelectron matrix (Fig. 5.16), which underlies the SPES presented in the upper panel of Fig. 5.13. In conventional cases, direct photoionizing transitions manifest as diagonal lines in the matrix, reflecting energy conservation, as elucidated in Chapter 1. However, the signal associated with the forbidden transitions exhibits a distinct behavior. The photoelectron signal with zero kinetic energy, which emerges around 7.48 eV, rapidly diminishes with increasing kinetic energy along the diagonal direction. This trend suggests that this signal is influ-

enced by a "dynamic" electron correlation effect, rather than an "intrinsic" one.[10] The latter effect typically arises due to the multiconfigurational nature of both the initial and final ionic states, leading to a photoelectron intensity that remains independent of the incident photon energy above the ionization threshold.[163]

To the best of our knowledge, there are no previous experimental instances of a quartet-singlet photoionization transition in a gas-phase molecular system. Thus, the observation of this unique transition in Si_2 holds significant potential for contributing to the spectroscopic literature. In light of the observed spin-forbidden ionization transition and the dynamic character, we endeavor to discuss several potential mechanisms that could provide an explanation for the authorization of this seemingly forbidden process.

Shake-up process

One potential mechanism that could explain the authorization of the observed forbidden ionization transition is the shake-up process, which can be further categorized into direct shake-up and conjugate shake-up processes. Both of these processes involve two-electron ionization events.[10]

The direct shake-up process involves the relaxation of the molecular system during and after ionization.[10] In this scenario, the ionization event prompts the excitation of an outer electron to an unoccupied orbital, while the nuclear configuration and outer electron shells fail to adapt rapidly to the changes in the screening potential. As a result, the system remains in an unrelaxed state-form, and this phenomenon can be seen as a form of configuration interaction between the unrelaxed and relaxed configurations. For instance, in the diatomic CO molecule, the inner-shell C 1s(2σ) ionization can lead to the excitation of an outer 1π electron to an unoccupied 2π orbital through the direct shake-up process.[10,98]

Conversely, the conjugate shake-up process (also referred to as "internal scattering") occurs when the photoelectron scattering within the ionic potential induces the excitation of another electron in the molecular system, resulting in a two-electron ionization event.[10] A theoretical prediction of the conjugate shake-up process was made for the diatomic C_2 molecule, explaining the authorization of dipole-forbidden ionization transitions $c^{+\,2}\Sigma_g^- \leftarrow X\,^1\Sigma_g^+$ and $d^{+\,2}\Sigma_g^+ \leftarrow X\,^1\Sigma_g^+$.[163] According to Toffoli *et al.*, a photoelectron of character σ_g excited from the $1\pi_u$ orbital of the neutral ground state of C_2 scatters within the ionic potential and excites another $1\pi_u$ electron to the $3\sigma_g$ orbital.[163] However, these predicted transitions were not observed in VUV ionization experiments performed by Harper *et al.*[71]

While shake-up processes are capable of explaining the authorization of some two-electron involved forbidden ionization transitions, they appear to be better suited for dipole-forbidden transitions and may not be applicable to our specific case of a spin-forbidden transition. Additionally, shake-up-induced ionization signals typically exhibit relatively weak intensities, usually amounting to a few percentage points of the dominant one-electron processes.[87] In contrast, the intensity of our observed forbidden transition signal is comparable in magnitude to the allowed transition signals. This leads us to consider other mechanisms to explain the observed spin-forbidden transition in Si_2, as discussed in the following paragraphs.

Spin-orbit coupling

In the article by Chiu *et al.*[31], which discusses spin-forbidden photoionization of diatomic molecules, two examples of spin-forbidden quartet-singlet ionization transitions authorized by spin-orbit coupling in NO and O_2 are mentioned. While we were intrigued by the similarities to our case, we were unable to locate experimental sources specifically for these ionization transitions. However, there are indirect means to confirm the existence of such spin-forbidden transitions.

For instance, let us consider the $\mathrm{X}^+\,^1\Sigma^+ \leftarrow \mathrm{a}\,^4\Pi$ ionization transition in NO. Numerous experimental and theoretical evidences have been put forward to support the spin-orbit coupling of related states. Research has been conducted on the spin-orbit interaction of the first excited $\mathrm{a}\,^4\Pi$ state with various doublet states of neutral NO. This was undertaken to explain the relatively short lifetime of the $\mathrm{a}\,^4\Pi$ state (0.156 s) observed in emission spectra, despite the spin-forbidden nature of its transition to the ground state $\mathrm{X}\,^2\Pi$.[54,102,104,183] Furthermore, a high-resolution gas-phase experiment conducted by Drabbels *et al.*[46] provided additional support for the spin-orbit coupling between $\mathrm{a}\,^4\Pi$ and $\mathrm{B}\,^2\Pi$ states. This finding aligns well with the relatively long lifetime of the $\mathrm{B}\,^2\Pi$ state observed experimentally by Ottinger *et al.*[130] These studies, which confirm the quartet-doublet spin-mixture for $\mathrm{a}\,^4\Pi$ of NO, allow us to infer the authorization of the ionization transition from this neutral state to the ionic singlet state $\mathrm{X}^+\,^1\Sigma^+$.

Despite the discussion above, the presence of spin-orbit coupling alone might not fully explain the observed characteristics of the spin-forbidden transition in the photoelectron matrix of Si_2. The mixing induced by spin-orbit coupling should be an intrinsic property of the state, and therefore the photoelectron signal should not exhibit such a sharp decrease with higher kinetic energy. The theoretical work conducted by Liu *et al.*[106], which calculated the low-lying excited states of Si_2^+ including spin-orbit coupling, is indeed important evidence. The absence of significant mixing of spin-orbit states of $\mathrm{X}^+\,^4\Sigma_g^-$ with other states in their calculations weakens the credibility of spin-orbit coupling as the sole mechanism for authorizing the observed spin-forbidden transition. This reinforces the need to explore alternative mechanisms to explain the observed phenomenon.

Autoionization induced by spin interactions

We propose finally a reasonable mechanism to explain the phenomenon: autoionization induced by spin interactions. This proposed mechanism is rooted in the idea that the spin-forbidden autoionization gains intensity due to weak spin interactions that couple states with different spins. A similar concept was put forth by Pratt *et al.* during their investigation of the photoionization of autoionization levels of atomic oxygen.[137]

In their study, atomic oxygen in the excited $^1\mathrm{D}_2$ state was initially produced and then excited to the $^1\mathrm{P}_1$ and $^1\mathrm{F}_3$ levels. These levels are forbidden to autoionize in the LS coupling scheme to the $\mathrm{O}^+\,^4\mathrm{S}^0_{3/2}$ threshold state. However, experimental observations, including the short lifetimes of these excited states (especially $^1\mathrm{P}_1$) and the photoelectron spectrum indicating the kinetic energy of the emitted electrons, revealed a relatively high rate of autoionization from $^1\mathrm{P}_1$ and $^1\mathrm{F}_3$ to the $\mathrm{O}^+\,^4\mathrm{S}^0_{3/2}$ threshold state. This unexpected behavior is explained by considering spin-orbit and spin-spin interactions. Specifically, the $^1\mathrm{P}_1$ state exhibited the spin-orbit and spin-spin interactions with the $(^4\mathrm{S}^0_{3/2} + \mathrm{e}^-(\mathrm{p}))\ ^3\mathrm{P}_1$ continuum and the $(^4\mathrm{S}^0_{3/2} + \mathrm{e}^-(\mathrm{p}))\ ^5\mathrm{P}_1$ continuum, and the $^1\mathrm{F}_3$ state exhibits the spin-spin interaction with the $(^4\mathrm{S}^0_{3/2} + e\mathrm{p})\ ^5\mathrm{P}_3$ continuum. The selection rules of spin-orbit interaction allow changes in orbital angular momentum ($\Delta L = 0, \pm 1$), total spin ($\Delta S = 0, \pm 1$) and total angular momentum ($\Delta J = 0$) while the spin-spin interaction obeys $\Delta L = 0, \pm 1, \pm 2$, $\Delta S = 0, \pm 1, \pm 2$ and $\Delta J = 0$.

Taking an insight to our case of Si_2, we could presume that the molecule in the $\mathrm{a}\,^1\Delta_\mathrm{g}$ state is excited to an autoionizing $^1\Pi_\mathrm{u}$ Rydberg state. Despite the spin-forbidden nature of the autoionization of the $^1\Pi_\mathrm{u}$ to the $\mathrm{X}^+\,^4\Sigma^-_\mathrm{g}$ threshold, the spin-orbit interaction between the $^1\Pi_\mathrm{u}$ state and the $(\mathrm{X}^+\,^4\Sigma^-_\mathrm{g} + \mathrm{e}^-(\Pi_\mathrm{u}))\ ^3\Pi_\mathrm{u}$ continuum and/or the spin-spin interaction between the $^1\Pi_\mathrm{u}$ state and the $(\mathrm{X}^+\,^4\Sigma^-_\mathrm{g} + \mathrm{e}^-(\Pi_\mathrm{u}))\ ^5\Pi_\mathrm{u}$ continuum could facilitate the process. This mechanism not only addresses the spin-forbidden restriction but also offers an explanation for the kinetic behavior observed. To validate and refine this proposed mechanism, it would indeed be valuable to conduct further theoretical and experimental investigations specifically focused on the ionization processes of Si_2.

5.3.5 Conclusions and perspectives

In this study, we have successfully unraveled the complexities of the experimental photoelectron spectrum of Si_2 by aid of calculations. As a result, we present, for the first time, experimental energy values for the excited states $\mathrm{b}^+\,^2\Delta_\mathrm{g}$, $\mathrm{c}^+\,^2\Sigma^-_\mathrm{g}$, and $\mathrm{e}^+\,^2\Pi_\mathrm{u}$ of Si_2^+. The striking agreement between our simulated and experimental spectra, particularly for the band intensities unaffected by autoionization processes, serves as strong validation for the application of the Koizumi model.[96]

Of significant interest is the observation of a spin-forbidden quartet-singlet transition signal, which has not been previously reported in molecular ionization measurements. We have diligently explored potential mechanisms to explain the authorization of this forbidden transition. While we have discussed various hypothesis, we rationalize it involving an autoionization process induced by spin interactions. This intriguing observation, which represents a

novel occurrence in molecular ionization studies, holds the potential to make a valuable contribution to the existing spectroscopic literature.

5.4 Threshold photoelectron spectrum of SiC

5.4.1 Astrophysical context and spectroscopic background

Silicon carbide (SiC) is the only Si-bearing species under investigation in this chapter that has been detected in space.[22] It is considered as one of the main dust species in the atmospheres of the cool C-rich Asymptotic Giant Branch (AGB) stars, supported by spectroscopic observations of the 11.3 μm characteristic feature in carbon stars such as IRC+10216 and IRC+30219.[22,164] However, in contrast to its widespread presence in AGB stars, it has not been observed in the interstellar medium (ISM). Despite several proposed mechanisms aiming to explain this phenomenon,[30,168] including the oxidative destruction of SiC molecules or clusters,[30] the absence of SiC's spectroscopic signature in the ISM remains an enigma.

One plausible mechanism involves the photoionization of SiC, leading to the formation of more reactive SiC^+ ions or ionized clusters. However, obtaining detailed laboratory information about the SiC^+ cation has been challenging due to the difficulties associated with generating SiC in the gas phase. Notably, only two experimental studies involving SiC^+ were conducted in the 60s, employing hexagonal SiC sublimation coupled with mass spectrometry using electron impact ionization.[47,169] These studies determined the experimental ionization potential of SiC to be approximately 9.2$\pm$0.4 eV[47] and 9.0 eV.[169]. To our knowledge, there is no other spectroscopic information on SiC^+ except a few theoretical calculations.[16,136]

In our work, thanks to the flow-tube reactor coupled to the DELICIOUS 3 spectrometer, we succeeded to produce SiC radicals in the gas phase and performed the first single-photon ionization spectroscopic measurements of the SiC radical between 8.0 and 11.0 eV.

5.4.2 *Ab initio* calculations

The *ab initio* calculations concerning the electronic states of SiC and SiC^+ were carried out by Jacky Liévin from the Free University of Brussels and Philippe Halvick from ISM of Bordeaux. These calculations employed the MRCI + Q method with CASSCF wave-functions, as detailed in Section 5.2.2, using two distinct Active Space (AS). One AS corresponds to the conventional frozen core approximation, which considers solely the correlation among valence electrons denoted as "V" in this text. This calculation employed the aug-cc-pV5Z basis set. The other AS encompasses additional core-core and core-valence correlations, referred to as "CV," and used the aug-cc-pCV6Z basis set. Given that the first two $^2\Pi$ states of SiC^+ undergo significant perturbation due to their avoided crossing, causing their behavior to deviate from simple harmonic oscillator expectations, more intricate calculations were performed. These calculations involved diagonalizing the Hamiltonian matrices to acquire the rovibronic states, factoring in addition the centrifugal potential and interactions such as Scalar Relativity (SR) and spin-orbit (SO) coupling. The obtained Franck-Condon factors were used to perform the spectral simulation. For a comprehensive exploration of the spe-

cific calculation methodologies, please refer to Ref. 57. In this context, my focus is directed towards presenting the outcomes derived from these calculations.

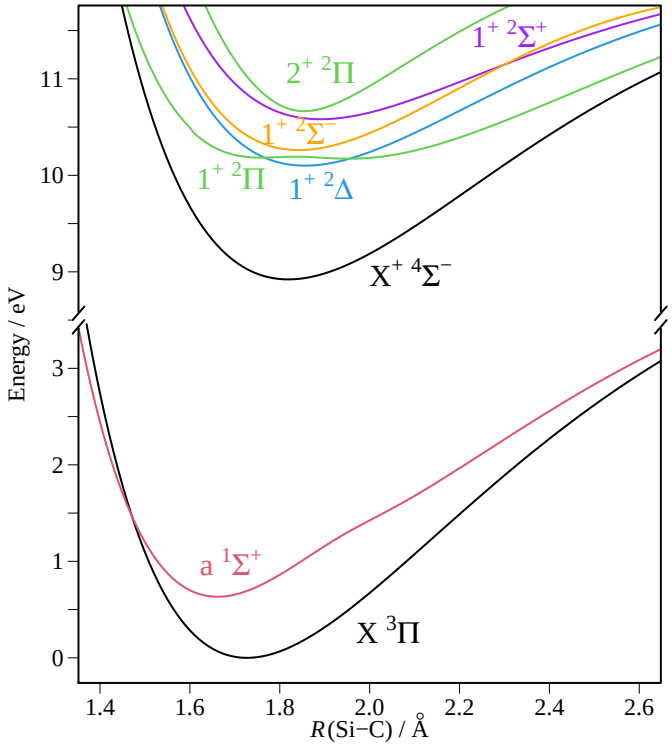

Figure 5.17: Potential energy curves of SiC and SiC^+ computed at the MRCI + Q/AV5Z level of theory. Figure adapted from Ref. 57

The potential energy curves corresponding to the SiC and SiC^+ states are displayed as a function of the Si–C bond length, R(Si-C), in Fig. 5.17. The double-well structure in the curve of the $1^+\,^2\Pi$ state of SiC^+ results from the avoided crossing with the $2^+\,^2\Pi$ state.

Detailed molecular properties calculated for these states are documented in Tab. 5.7 from Ref. 57. A comparison between the results derived from V/AV5Z and CV/ACV6Z computations reveals distinct trends. Specifically, the CV/ACV6Z results exhibit a contraction of the bond distance, an increase in vibrational frequencies, and an increase in the modulus of the dipole moment. These findings align with the anticipated structural contraction due to the inclusion of core-electron correlations. Moreover, significant disparities emerge for states characterized by strong multireference nature and varying core effects on the main configurations. A prime example is shown in the context of the $1^+\,^2\Pi$ state's double-well potential. Here, the relative stability of the two minima undergoes inversion when changing from V/AV5Z to CV/ACV6Z, leading to an approximate 40 meV red shift in $1^+\,^2\Pi$-involved transitions. Nevertheless, this marginal variation does not exert any discernible influence on the assignment process concerning our experimental spectrum.

Tab. 5.8 documents calculated adiabatic ionization energies from Ref. 57.

Table 5.7: Equilibrium spectroscopic properties of the low-lying electronic states of SiC and SiC^+ from *ab initio* calculations. Table extracted from 57

	Ref. [a]	r_e / Å	B_e / cm^{-1}	$10^3\alpha_e$ / cm^{-1}	ω_e / cm^{-1}	$\omega_e x_e$ / cm^{-1}	μ_e / D	ΔE_{SO} [b] / cm^{-1}
SiC								
$X\ ^3\Pi$	AV5Z	1.7269	0.67311	5.608	957.29	5.92	-1.450	74.5 (2, 0^-)
	ACV6Z	1.7176	0.68042	5.584	970.16	5.78	-1.230	
	exp.[19]	1.7182	0.67976	5.38	965.16	5.910		
	calc.[151]	1.7187	0.67963	5.661	965.79	6.04		72.4 (2, 0^+)
	calc.[181]	1.7187	0.6796	5.580	967.21	5.72		
	calc.[135]	1.726			954		-1.62	100 (2, 0^+)
$a\ ^1\Sigma^+$	AV5Z	1.6604	0.72811	7.265	1016.37	10.09	-2.130	
	ACV6Z	1.6483	0.73882	6.959	1043.08	9.28	-2.108	
	calc.[151]	1.6546	0.73311	7.82	1008.45	11.76		
	calc.[184]	1.6551	0.73285	8.296	1006.94	13.05		
	calc.[135]	1.68			975		-2.14	
SiC^+								
$X^+\ ^4\Sigma^-$	AV5Z	1.8190	0.60666	5.203	837.57	5.33	-1.184	0.15 (1/2, 3/2)
	ACV6Z	1.8101	0.61264	5.175	846.75	5.26	-1.037	
	calc.[136]	1.83			817		-1.190	0.0
$1^+\ ^2\Delta$	AV5Z	1.8561	0.58265	6.274	752.12	6.70	-1.008	6.3 (5/2, 3/2)
	ACV6Z	1.8466	0.58870	6.279	760.63	6.65	-0.810	
	calc.[136]	1.88			723		-0.950	87 (5/2, 3/2)
$1^+\ ^2\Pi$ [c]	AV5Z	1.7591/ 1.9430	0.64867/ 0.52383	-	-	-	-1.689/ -1.532	60.5 (3/2, 1/2)/ 30.3 (1/2, 3/2)
	ACV6Z	1.7393/ 1.9283	0.66353/ 0.53983	-	-	-	-1.685/ -1.428	
	calc.[136]	1.99					-	54 (3/2, 1/2)
$1^+\ ^2\Sigma^-$	AV5Z	1.8422	0.59150	6.096	776.13	6.54	-1.527	
	ACV6Z	1.8323	0.59793	6.090	785.56	6.46	-1.421	
	calc.[136]	1.86			759		-1.45	
$1^+\ ^2\Sigma^+$	AV5Z	1.8907	0.56157	7.070	678.29	7.51	-0.818	
	ACV6Z	1.8799	0.56800	6.984	689.67	7.35	-0.689	
	calc.[136]	1.91			651		-0.73	
$2^+\ ^2\Pi$	AV5Z	1.8498	0.58664	-	-	-	-1.656	5.8 (3/2, 1/2)
	ACV6Z	1.8544	0.58375	-	-	-	-1.609	
	calc.[136]	1.87					-	30 (3/2, 1/2)

[a] This work otherwise specified. AV5Z and ACV6Z refer to MRCI+Q/V and CV calculations, respectively.
[b] The Ω value of the lowest and highest SO components, respectively, are given in parentheses.
[c] Properties are listed for both minima of the double-well potential, with those corresponding to the lowest energy underlined.

Table 5.8: Calculated adiabatic ionization energies (in eV) from the ground X $^3\Pi$ electronic state of SiC. Table extracted from 57.

	IE(AV5Z) [a]	IE(ACV6Z) [a]	IE(CBS) [b]	IE(CBS+SR) [c]	IE(CBS+SR+SO) [c]	IE_0(CBS+SR+SO+ZPE) [c]
$X^+ {}^4\Sigma^-$	8.920	8.885	8.896	8.886	8.892	8.884
$1^+ {}^2\Delta$	10.101	10.078	10.098	10.088	10.093	10.080
$1^+ {}^2\Pi$	10.172	10.144	10.162	10.158	10.160	10.132
$1^+ {}^2\Sigma^-$	10.262	10.235	10.253	10.243	10.248	10.237
$1^+ {}^2\Sigma^+$	10.581	10.551	10.570	10.561	10.566	10.549
$2^+ {}^2\Pi$	10.665	10.651	10.671	10.665	10.669	10.678

[a] From V/AV5Z and CV/ACV6Z MRCI+Q geometry optimizations. [b] From CV/ACVnZ CBS limit extrapolations. [c] CBS results with inclusion of SR, SO and ZPE contributions; see text for details.

5.4.3 Results and discussion

Fig. 5.18 depicts the experimental photoelectron spectrum (panel a)) along with the simulated spectra of five potentially involved transitions (panels b) - g)). These simulations used Franck-Condon factors calculated at the MRCI + Q/AV5Z level, and the vibrational origin positions were shifted by the *ab initio IE*(CBS + SR) adiabatic energies (see Tab. 5.8). Given the resolution of our experimental spectrum, spin-orbit (SO) contributions do not need to be considered for the assignment. The photoionization transition involving the ground states of SiC and its cation ($\mathrm{X}^+ {}^4\Sigma^- \leftarrow \mathrm{X}\ {}^3\Pi$) was at first unambiguously identified. The vibrational temperature was set at 2000 K to best reproduce its vibrational progression. Note that this temperature is only indicative and might not be the real temperature. The rotational temperature was assumed to be equal to the beam's translation temperature of 180 K, as determined experimentally from the ion image. The simulated spectra were convolved using a Gaussian line shape featuring a FWHM of 26 meV.

Additionally, the $1^+ {}^2\Pi \leftarrow \mathrm{X}\ {}^3\Pi$ transition can also be assigned due to its distinctive shape, which arises from the double-well structure of the $1^+ {}^2\Pi$ state of SiC^+. Although the other three transitions from the ground neutral state $\mathrm{X}\ {}^3\Pi$ to the $1^+ {}^2\Delta$, $1^+ {}^2\Sigma^-$, and $1^+ {}^2\Sigma^+$ cationic states are believed to contribute to the spectrum, their unambiguous assignment remains challenging. The possibility of the presence of the first excited state $\mathrm{a}\ {}^1\Sigma^+$ of SiC has been explored and excluded due to the absence (or negligible) of an allowed transition to $1^+ {}^2\Pi$. Additionally, potential contributions from allene (H_2CCCH_2) and propyne (CH_3CCH), which are incapable of being mass-resolved in our experiments, have also been deliberated. However, no apparent spectral feature corresponds to either, leading to the conclusion of their absence.

Then, spectra encompassing rotational envelopes for the five involved photoionizing transitions were simulated. To achieve the best agreement with the experimental spectrum (after Stark-shift correction of +7 meV), the simulated $\mathrm{X}^+ {}^4\Sigma^- \leftarrow \mathrm{X}\ {}^3\Pi$ transition, initially positioned according to the *IE*(CBS + SR) value, was additionally shifted by +87 meV. This adjustment yields an experimental adiabatic ionization energy *IE* = 8.973 eV for the origin transition,

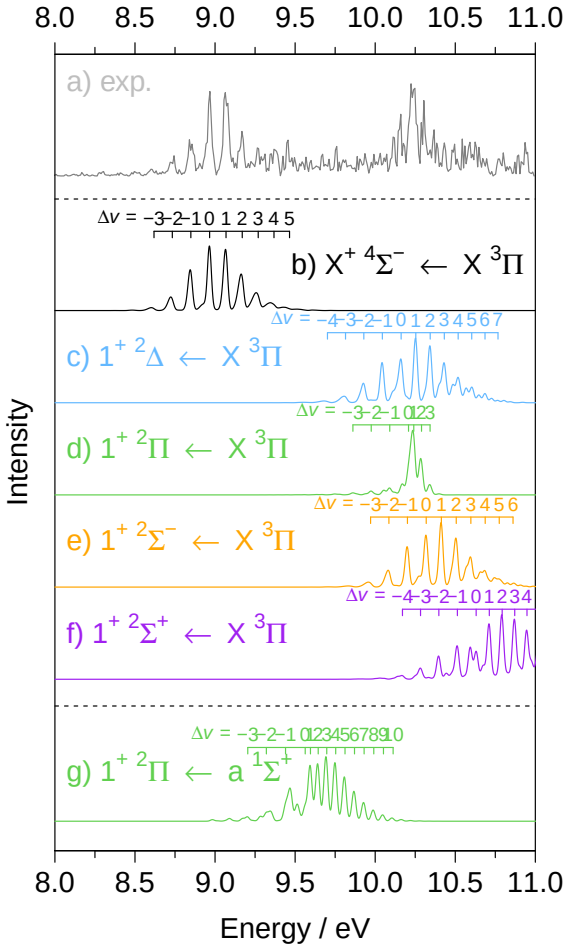

Figure 5.18: Experimental photoelectron spectrum of SiC (upper grey curve, panel (a)) compared with our calculated spectra of five potentially involved transitions (panels b) - g). Figure extracted from Ref. 57.

excluding the incorporation of the spin-orbit effect. For the remaining transitions from the ground neutral state to the four other cationic states, their positions were determined by adding this value (8.973 eV) with the relative *IE*(CBS + SR) values of the cationic state concerning $\mathrm{X}^{+\,4}\Sigma^{-}$. This approach reduces the uncertainty associated with energy values, as we use the term values of cationic states instead of the ionization energy values of neutral ones.[57]

Moreover, employing the Koizumi model-based methodology elaborated in Section 5.3, the relative intensities were estimated to be 1.0/1.0/0.8/0.5/0.5 for the five transitions to the $\mathrm{X}^{+\,4}\Sigma^{-}$, $1^{+\,2}\Delta$, $1^{+\,2}\Pi$, $1^{+\,2}\Sigma^{-}$, and $1^{+\,2}\Sigma^{+}$ electronic states. Consequently, we constructed a complete simulated spectrum, as depicted in Fig. 5.19, exhibiting favorable agreement with the experimental counterpart. The derived semi-experimental values for the transitions to $1^{+\,2}\Delta$, $1^{+\,2}\Pi$, $1^{+\,2}\Sigma^{-}$, and $1^{+\,2}\Sigma^{+}$ offer reasonable estimations of their ionization energies.

At last, the contribution of the spin-orbit effect is brought into consideration. As seen in Tab.1 from Ref. 57, the spin-orbit splitting in the SiC ground state ($\mathrm{X}\,^{3}\Pi$) emerges as notably substantial, resulting in a triplet of doubly degenerate levels characterized by $\Omega = 2$, 1, and 0, separated nearly equidistantly by approximately 37 cm^{-1} (4.6 meV). This rotational structure, while beyond the resolving capacity of our experimental spectrum, contributes to

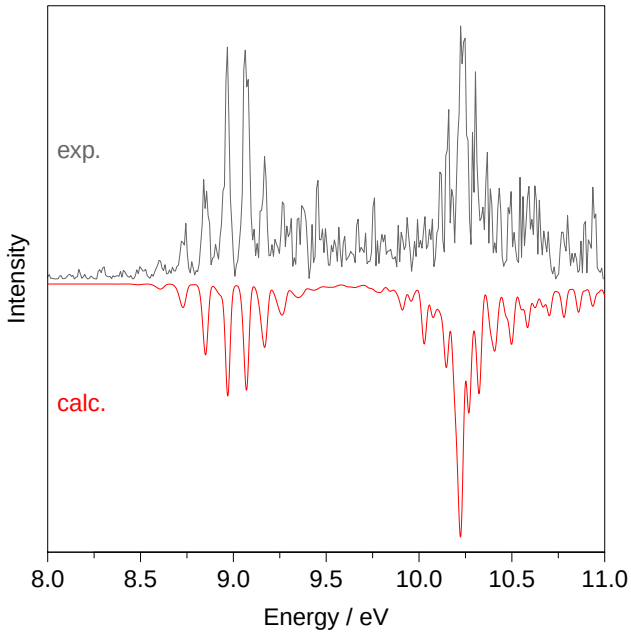

Figure 5.19: Experimental photoelectron spectrum of SiC (in grey) compared with our calculated spectrum (in red). Figure adapted from Ref. 57.

the apparent spectral resolution (26 meV), which surpasses the photoelectron spectral resolution determined by Si atom ionization transitions (22 meV).

Consequently, adjustments are required for the *IE* values, encompassing the inclusion of the spin-orbit component of the neutral state while subtracting that of the cationic state. As an illustrative case, considering the $X^+\,^4\Sigma^-$ $\leftarrow$ $X\,^3\Pi$ transition, the splitting of the $X^+\,^4\Sigma^-$ state (Ω = 3/2 and 1/2) proves negligible (0.15 cm^{-1}), ultimately yielding a conclusive *IE* value of 8.978 eV (8.973 + 0.0046). This value closely aligns with the one from the Active Thermochemical Tables,[2] where it is determined to be 8.930 $\pm$ 0.037 eV. Analogously, the semi-experimental *IE* values for other involved transitions, when accounting for the spin-orbit effect, are determined as 10.173, 10.216, 10.331, and 10.642 eV, corresponding respectively to the photoionizing transitions towards the $1^+\,^2\Delta$, $1^+\,^2\Pi$, $1^+\,^2\Sigma^-$, and $1^+\,^2\Sigma^+$ states.

5.4.4 Conclusions and perspectives

In this study, we have successfully measured the photoelectron spectrum of the SiC radical in the gas phase within the energy range of 8 to 11 eV. This achievement was made possible by employing a flow-tube reactor as a radical source and a double imaging electron/ion spectrometer. The latter allowed us to isolate the weak SiC signal from the complex backdrop of various products. Leveraging high-level *ab initio* calculations played a pivotal role in conducting a thorough analysis of the SiC photoelectron spectrum. Particularly, the calculations concerning the double-well $1^+\,^2\Pi$ state significantly contributed to a comprehensive understanding of the spectral characteristics.

Moreover, we have introduced semi-experimental ionization energy values relevant to the excited states of the cation. While spin-orbit effects remained unresolved in our experimental spectrum, our calculations provided crucial insights into their influence. Incorporating these spin-orbit corrections, we propose refined adiabatic ionization energy values for the $X^{+\,4}\Sigma^{-} \leftarrow X\,^{3}\Pi$ and $1^{+\,2}\Pi \leftarrow X\,^{3}\Pi$ transitions, determined as 8.978(10) eV and 10.216(24) eV, respectively.

5.5 First photoionization spectrum of SiCH

5.5.1 Astrophysical context and spectroscopic background

SiCH, although not yet observed in space, consistently appears in theoretical models concerning silicon chemistry in the ISM.[77,156,179] According to these models, SiCH in interstellar clouds can originate through two possible processes:

1. The reaction involving the transfer of a "carbanionic fragment" to Si^+, such as Si^+ + CH_3NH_2 (which has been detected), resulting in the formation of SiCH + NH_4^+ (suggesting a potential source for organo-silicon compounds in space);

2. The dissociative neutralization of $SiCH_2^+$ through proton detachment or electron capture, followed by hydrogen loss.[77,156,179] This process occurs subsequent to the production of $SiCH_2^+$ by the reaction of SiC^+ with H_2.[167]

Additionally, the $SiCH^+$ cation, as a reactant, may contribute to the formation of the SiC radical (see Section 5.4). Through the study of reactions under electric discharges in SiH_4-CO mixtures, Lim *et al.*[103] proposed that the reaction of $HSiC^+$ ions with any molecule possessing a proton affinity exceeding 424 kJ/mol, such as the abundant H_2 molecule in space, could lead to the formation of SiC radicals in interstellar clouds.

In order to facilitate prospective astronomical observations of SiCH and its cation, and to validate the theoretical models, experimental data are required. Nevertheless, the significant instability associated with SiCH presents substantial obstacles in terms of both its generation and subsequent spectroscopic measurements. Up to this point in time, only a restricted number of experiments and computational investigations have been carried out with respect to SiCH.[17,68,101,140,156]

The existence of SiCH was first confirmed in 1990 through neutralization-reionization mass spectrometry experiments.[156] Additionally, Robbe *et al.*[140] conducted precise calculations on the energy levels of the SiCH ground state ($\mathrm{X}\ ^2\Pi$). This work led to predictions for vibrational frequencies of the ground state, including ω_1 for the Si-C stretching mode ($\nu_1(\sigma)$) at 1011.9 cm^{-1}, ω_2 for the bending mode ($\nu_2(\pi)$) at 469 cm^{-1}, and ω_3 for the Si-H stretching mode ($\nu_3(\sigma)$) at 3260.2 cm^{-1}. Subsequently, the vibrational frequency ω_1 of SiCH was experimentally confirmed at 1010.4 cm^{-1} using Fourier transform infrared (FTIR) spectroscopy in an argon matrix.[68] Moreover, the $\mathrm{A}\ ^2\Sigma^+ \leftarrow \mathrm{X}\ ^2\Pi$ electronic transition of SiCH was studied *via* FTIR investigations, with a comprehensive rotational analysis that considered spin-orbit coupling, spin-rotation coupling, and Fermi resonance.[32,33] Vibrational states of SiCH and SiCD in their ground state ($\mathrm{X}\ ^2\Pi$) were explored by Smith *et al.*,[154,155] using laser-induced fluorescence (LIF) and a pulsed electric discharge radical source.

Furthermore, a few theoretical studies have addressed the isomerization process between SiCH (linear) and its less stable HSiC isomer (bend).[17,101,140] Calculations have consistently shown that the energy difference between SiCH($\mathrm{X}\ ^2\Pi$) and HSiC($\tilde{\mathrm{X}}\ ^2\mathrm{A}'$) is approximately 2.2 eV.[101,140] Regarding the corresponding isomerization barriers for

HSiC($\tilde{\mathrm{X}}\ ^2\mathrm{A}'$) $\rightarrow$ SiCH($\mathrm{X}\ ^2\Pi$), these were determined to be 0.09 eV (equivalent to 2 kcal/mol)[101] and 0.347 eV (equivalent to 2800 cm^{-1}).[140] The existence of such small isomerization barriers, coupled with the relatively high energy difference between the two isomers, suggests that the experimental detection of the less stable HSiC isomer is likely to be a formidable challenge.

To the best of our knowledge, there has been no prior publication of spectroscopic data related to the SiCH^+ cation, with the exception of theoretical calculations conducted by Buenker *et al.*[17] In their theoretical work, they estimated the threshold ionization energy for SiCH to transition to the ground cationic state $\mathrm{X}^+\ ^3\Sigma^-$ as 8.509 eV. Furthermore, they calculated the energies of the four lowest excited states ($\mathrm{a}^+\ ^1\Delta$, $\mathrm{b}^+\ ^1\Sigma^+$, $\mathrm{A}^+\ ^3\Pi$, and $\mathrm{c}^+\ ^1\Pi$) with respect to the ground cationic state and obtained values of 0.967, 1.518, 1.843, and 2.411 eV, respectively. During my PhD, we investigated the photoionization of SiCH, an area that has not been explored experimentally in the past. Detailed descriptions and results of these experiments will be provided in an upcoming publication.[28]

5.5.2 *Ab initio* calculations

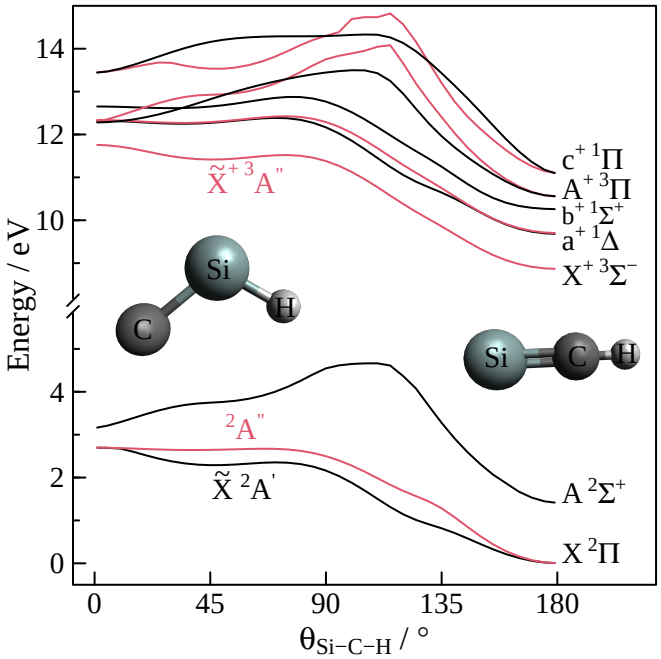

Figure 5.20: Energy diagram calculated using MRCI/AVQZ for the ground state of SiCH and the four lowest states of its cation SiCH^+ (shown on the right), along with their transformation to corresponding states in HSiC and HSiC^+ (depicted on the left) as a function of the Si-C-H angle during the isomerization reaction. The black and red states correspond to A′ and A″ symmetries in the C_s point group, respectively.

The *ab initio* calculations were conducted by Jean-Christophe Loison, using the MRCI + Q method with CASSCF wave-functions, as outlined in Section 5.2.2. Here only the main results of the calculations are reported.

The main configurations of the electronic states calculated in this work, *i.e.* the two lowest states of SiCH and the

four lowest states of $SiCH^+$, respectively, are given below:

$$\mathrm{SiCH}(\mathrm{X}\ ^2\Pi) : [\ldots](7\sigma)^2(2\pi)^3$$
$$\mathrm{SiCH}(\mathrm{A}\ ^2\Sigma^+) : [\ldots](7\sigma)^1(2\pi)^4$$
$$\mathrm{SiCH}^+(\mathrm{X}^+\ ^3\Sigma^-,\mathrm{a}^+\ ^1\Delta,\ \mathrm{b}^+\ ^1\Sigma^+) : [\ldots](7\sigma)^2(2\pi)^2$$
$$\mathrm{SiCH}^+(\mathrm{A}^+\ ^3\Pi, \mathrm{c}^+\ ^1\Pi) : [\ldots](7\sigma)^1(2\pi)^3$$

where [...] stands for $(1\sigma)^2(2\sigma)^2(3\sigma)^2(4\sigma)^2(1\pi)^4(5\sigma)^2(6\sigma)^2$.

In Fig. 5.20, an overview of the lowest electronic states of SiCH (HSiC) and $SiCH^+$ ($HSiC^+$) is depicted along the $\Theta_{\mathrm{Si-C-H}}$ coordinate. The calculated equilibrium properties of both SiCH/HSiC isomers and their cations, including bond lengths, Si-C-H bond angles, vibrational frequencies and energies concerning the neutral ground state, are reported in Tab. 5.9.

5.5.3 Vibronic structure of the photoelectron spectrum

Fig. 5.21, in panel a), presents our experimental photoelectron spectrum of SiCH/HSiC spanning from 8 to 11 eV. In panel b) to i), we conducted spectral simulations for 9 allowed photoionization transitions of SiCH and its HSiC isomer, represented in red and blue, respectively. To create these simulated spectra, we shifted the stick spectra calculated through Franck-Condon calculations to align their origin transitions with our corresponding calculated energies (E_0, refer to Table 5.9). Subsequently, we convolved them with a Gaussian line shape characterized by a FWHM of 25 meV. From the preliminary analysis, we can confidently attribute two distinctive and intense bands, positioned at approximately 9 eV and 10.7 eV, to the $\mathrm{X}^+\ ^3\Sigma^+ \leftarrow \mathrm{X}\ ^2\Pi$ and $\mathrm{A}^+\ ^3\Pi \leftarrow \mathrm{X}\ ^2\Pi$ photoionization transitions of SiCH. Based on this assignment, we fine-tuned the vibrational temperature of our simulation to 700 K to best replicate the observed vibrational progression displayed in these two bands. Note that this temperature is indicative and may not necessarily reflect the actual conditions of our radical source.

Alongside these unambiguous features, we can consider two supplementary transitions originating from the SiCH ground state ($\mathrm{a}^+\ ^1\Delta \leftarrow \mathrm{X}\ ^2\Pi$ and $\mathrm{b}^+\ ^1\Sigma^+ \leftarrow \mathrm{X}\ ^2\Pi$) to account for the remaining observed bands within the energy range of 9.7 to 10.5 eV. However, the density of features in this energy range introduces a level of uncertainty to the assignments, potentially leading to increased uncertainties in the derived ionization energies.

Considering that our radical source can produce species with relatively high internal energy, we conducted an examination to determine whether the first excited electronic state of SiCH, denoted as $\mathrm{A}\ ^2\Sigma^+$, or the ground electronic state of HSiC could potentially influence our experimental spectrum. Regarding the $\mathrm{A}\ ^2\Sigma^+$ electronic state of SiCH, we identified two photoionizing transitions within the energy range of our measurement: the $\mathrm{A}^+\ ^3\Pi \leftarrow \mathrm{A}\ ^2\Sigma^+$ and the $\mathrm{c}^+\ ^1\Pi \leftarrow \mathrm{A}\ ^2\Sigma^+$ transitions. Their corresponding simulations are presented in panel e) and f) of Fig. 5.21.

Table 5.9: Calculated (MRCI/CBS extrapolation) molecular properties of the lowest electronic states of the two isomers SiCH and HSiC as well as their cations.

	State	$R_{\mathrm{Si-C}}$ (Å)	$R^{a}_{\mathrm{x-H}}$ (Å)	θ^{b} (°)	ω_1 (cm^{-1})	ω_2 (cm^{-1})		ω_3 (cm^{-1})	E_{e} (eV)	E_0 (eV)
SiCH	$\mathrm{X}\,^2\Pi$	1.6937	1.0621	180	1024.27	481.82	547.29	3265.18	0.000	0.000
		1.702[140]	1.078[140]		1011.9[140]	469.9[140]		3260.2[140]		
		1.69252(8)[154]	1.0677(4)[154]		1010.4[68]					
	$\mathrm{A}\,^2\Sigma^+$	1.6102	1.0717	180	1182.75	740.33	740.33	3319.05	1.411	1.452
		1.587[140]	1.08[140]		1150.9[101]	848.7[101]		3249.6[101]		1.4589(0)[33,154]
		1.624[101]	0.084[101]							
		1.6118(1)[154]	1.0625(5)[154]		1168[154]	715[154]				
$SiCH^+$	$\mathrm{X}^+\,^3\Sigma^-$	1.7809	1.0833	180	900.66	444.01	444.01	3211.22	8.900	8.881
		1.81[17]	1.11[17]							8.509[17]
	$\mathrm{a}^+\,^1\Delta$	1.7993	1.0841	180	859.90	425.75	425.77	3208.89	9.766	9.741
		1.81[17]	1.09[17]							
	$\mathrm{b}^+\,^1\Sigma^+$	1.8206	1.0863	180	800.76	316.55[c]	316.55[c]	3191.89	10.288	10.246
		1.81[17]	1.09[17]							
	$\mathrm{A}^+\,^3\Pi$	1.6558	1.0806	180	1091.29	636.18	703.16	3238.88	10.579	10.600
		1.67[17]	1.08[17]							
	$\mathrm{c}^+\,^1\Pi$	1.6513	1.0852	180	1104.97	846.55	846.55	3194.85	11.118	11.159
		1.67[17]	1.08[17]							
HSiC	$\mathrm{X}\,^2\mathrm{A}'$	1.7022	1.4871	120	948.05	428.92[d]		2183.79	0.000	0.000
		1.70[140]	2.74[140]	116[140]						
$HSiC^+$	$\mathrm{X}^+\,^3\mathrm{A}''$	1.7823	1.4881	120	807.36	427.00		2174.65	9.158	9.149
	$^1\mathrm{A}''$	1.8359	1.4821	133	712.79	176.50[c]		2209.51	10.005	9.975
	$^1\mathrm{A}'$	1.7892	1.4867	123	809.30	311.27		2185.11	10.106	10.090

[a] X = Si in SiCH, X = C in HSiC.
[b] $\theta_{\mathrm{Si-C-H}}$ in SiCH, $\theta_{\mathrm{H-Si-C}}$ in HSiC.
[c] Calculated value using MRCI/AV5Z. (The calculations do not converge for AV6Z basis.)
[d] Calculated value using MRCI/AV6Z.
[c,d] These values cannot be extrapolated using the CBS method due to non-regular variations of the values depending on the base used.
Values offered by Ref.[10] and [11] are *ab initio* calculated.
Values offered by Ref.[12]-[15] are experimentally obtained.

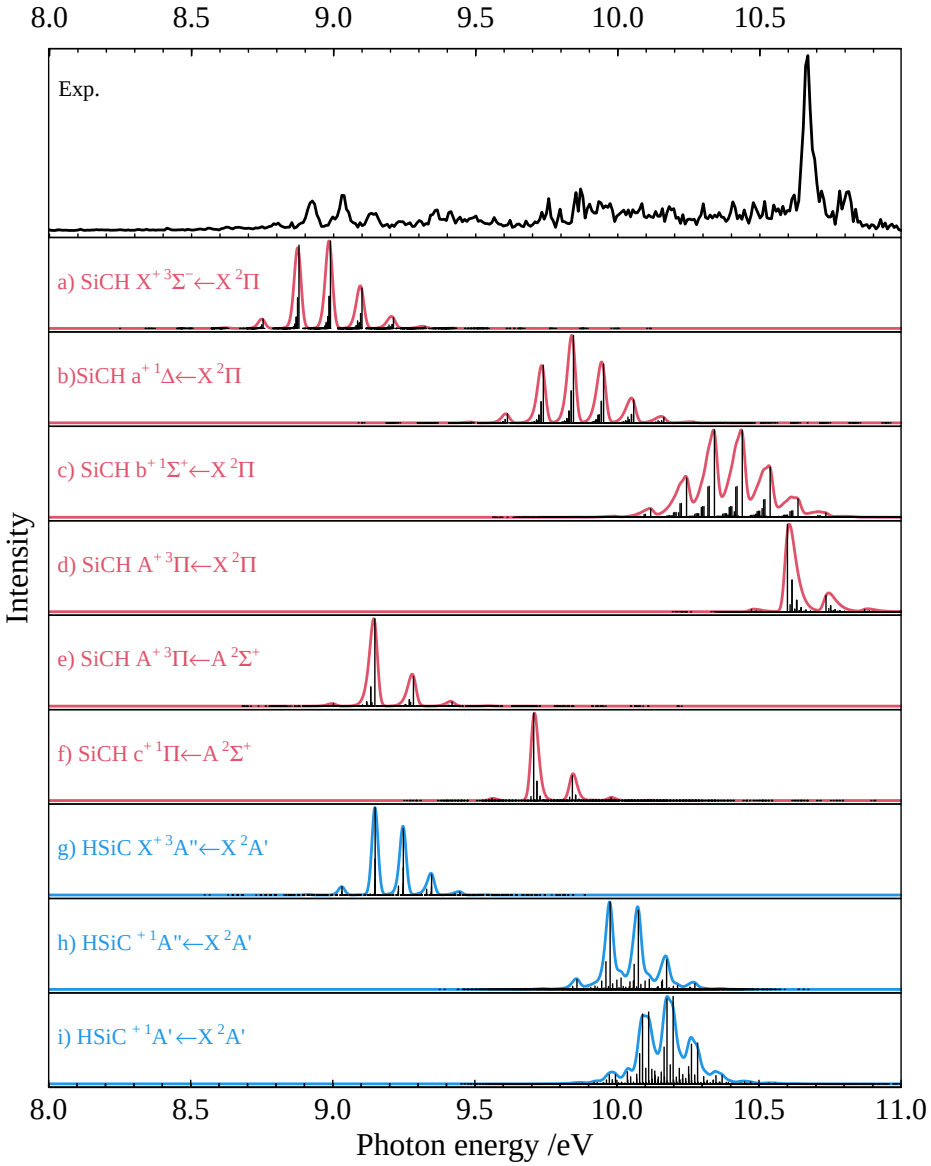

Figure 5.21: Experimental photoelectron spectrum (in black) compared to the calculated spectra of 9 allowed photoionization transitions of SiCH (in red) and its isomer HSiC (in blue) in the energy range from 8 to 11 eV. In the calculated spectra, the black sticks represent the FC simulations at 700 K and the lines are their convolved spectra using a Gaussian line shape with a full width at half maximum (FWHM) of 25 meV. Note that the experimental spectra are not corrected by the 7 meV Stark-shift, which is negligible for the transition attribution here.

Table 5.10: Calculated adiabatic ionization energies (in eV) from the ground $\mathrm{X}\ ^2\Pi$ electronic state of SiCH.

Transition	$E_{\mathrm{calc.}}$ [a]	$E_{\mathrm{calc.}}$+SO[b]	$E_{\mathrm{exp.}}$ [c]	$E_{\mathrm{exp.}}$+SO[d]	$\Phi_{\mathrm{calc.}}$	$\Phi_{\mathrm{exp.}}$
$\mathrm{X}^+\ ^3\Sigma^- \leftarrow \mathrm{X}\ ^2\Pi$	8.881	8.885	8.935(6)	8.939(6)	0.83	0.45
$\mathrm{a}^+\ ^1\Delta \leftarrow \mathrm{X}\ ^2\Pi$	9.741	9.745	9.765(15)	9.769(15)	0.84	0.65
$\mathrm{b}^+\ ^1\Sigma^+ \leftarrow \mathrm{X}\ ^2\Pi$	10.246	10.250	10.207(15)	10.211(15)	0.8	0.8
$\mathrm{A}^+\ ^3\Pi \leftarrow \mathrm{X}\ ^2\Pi$	10.600	10.599	10.664(6)	10.668(6)	1.64	1.64

[a] From CBS limit extrapolation of calculated energies using CASSCF method followed by MRCI+Q approach, corrected by the zero point energy (ZPE).
[b] The final calculated values with inclusion of the spin-orbit splitting of $\mathrm{X}\ ^2\Pi$ of SiCH and that of $\mathrm{A}^+\ ^3\Pi$ of $SiCH^+$ calculated in our work.
[c] The experimental values are obtained by manually fitting our simulation with the experimental spectrum, followed by a correction of the Stark-shift at 0.007 cm^{-1}.
[d] The final experimental values with inclusion of the spin-orbit splitting (71.4 cm^{-1}) of $\mathrm{X}\ ^2\Pi$ of SiCH, the latter is experimentally obtained by Smith *et al.*.[155]

The energy level of the $\mathrm{A}\ ^2\Sigma^+$ state relative to the ground state has been meticulously determined through FTIR experiments[33] and LIF experiments,[154] yielding a value of 1.4589(0) eV. This value closely aligns with our computed result of 1.4523 eV (refer to Table 5.9). The population of this state at our vibrational temperature of 700 K is negligible, which should prevent us from observing transitions originating from this state. This observation is further corroborated by our calculated spectra in Fig. 5.21. Indeed, the experimental spectrum presented in panel a) does not exhibit any detectable signals corresponding to these transitions.

Finally, we undertook an exploration to assess the potential existence of a spectral signature originating from the less stable isomer, HSiC, within our experimental spectrum. Our computational calculations yielded an isomerization energy of 2.1869 eV, a result consistent with prior theoretical findings.[17,101,140] Consequently, we anticipate that the thermal population of the ground state of HSiC would be even lower than that of the first excited electronic state of SiCH. Moreover, the weak isomerization barrier suggests that any produced HSiC would quickly convert into its stable isomer, SiCH, making its detection exceptionally challenging. Ultimately, the absence of any discernible experimental signals corresponding to the HSiC calculated spectra (depicted in blue in Fig. 5.21) leads us to confidently exclude the possibility of HSiC presence in our experiments.

Furthermore, we also examined the potential contribution from the ^{29}SiC radical. The natural ratio of ^{29}Si to ^{28}Si is 4.67% to 92.23%, respectively. By overlapping the measured SiC photoelectron spectrum (see Section 5.4) with the SiCH spectrum, we identified no significant signals aligning with the principal features of SiC. Consequently, we can confidently dismiss the notion of any substantial impact stemming from ^{29}SiC.

Building upon the findings presented above, we have effectively generated a complete simulated spectrum by taking into account the four assigned transitions of SiCH, depicted in red in Fig. 5.22. The simulated spectrum was convolved with a FWHM of 25 meV, which emcompasses the unresolved rotational envelope. To ensure proper alignment with the experimental spectra, the position of each transition was meticulously adjusted. The resulting experimental ionization energy values have been documented alongside their corresponding calculated counter-

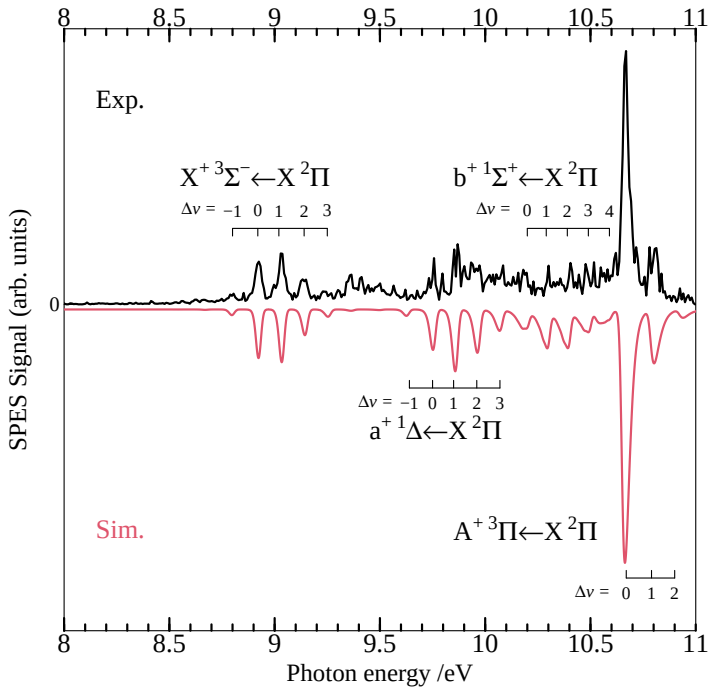

Figure 5.22: Experimental photoelectron spectrum of SiCH (in black) compared with the simulated one (in red) taking account 4 transitions: $\mathrm{X}^{+\,3}\Sigma^{-} \leftarrow \mathrm{X}\,^{2}\Pi$, $\mathrm{a}^{+\,1}\Delta \leftarrow \mathrm{X}\,^{2}\Pi$, $\mathrm{b}^{+\,1}\Sigma^{+} \leftarrow \mathrm{X}\,^{2}\Pi$ and $\mathrm{A}^{+\,3}\Pi \leftarrow \mathrm{X}\,^{2}\Pi$. The simulated spectrum is obtained by summing the FC simulations of the 4 transitions convolved with a Gaussian line shape of FWHM = 25 meV, at vibrational temperature of 700 K. The positions and intensities are manually adjusted to fit the experimental one.

parts in Table 5.10, demonstrating a high degree of agreement between the two sets of data.

In terms of intensity, we employed an evaluation method which has been described in Section 5.3, and yielded calculated relative ionization efficiencies listed in Tab. 5.10. By scaling based on the highest calculated value, we introduced a series of adjusted efficiency values (0.45, 0.65, 0.8, 1.64) corresponding to transitions originating from $\mathrm{X}\,^{2}\Pi$ to $\mathrm{X}^{+\,3}\Sigma^{-}$, $\mathrm{a}^{+\,1}\Delta$, $\mathrm{b}^{+\,1}\Sigma^{+}$, and $\mathrm{A}^{+\,3}\Pi$, respectively, to achieve the best agreement with the experimental spectrum. The overall agreement between our measurement and our simulation is quite good despite an overestimation of the origin transition.

Given our medium spectral resolution, our analysis is constrained to the examination of the vibronic structure of $SiCH^{+}$, with finer details like rotational structure or spin-orbit coupling lying beyond the scope of our investigation. Nonetheless, it has been experimentally established that the ground state $\mathrm{X}\,^{2}\Pi$ of SiCH possesses a substantial spin-orbit coupling constant of 71.9 cm^{-1}.[155] Consequently, making the approximation of equal population between the two spin-orbit components, $\mathrm{X}\,^{2}\Pi_{1/2}$ and $\mathrm{X}\,^{2}\Pi_{3/2}$, we find it necessary to include half of the spin-orbit constant to correct the final ionization energy values. It is important to note that this is a simplified approximation, and a comprehensive rotational analysis (which falls beyond the scope of this work) would be essential for an accurate consideration of the spin-orbit coupling. As shown in Tab. 5.10, for transitions originating from $\mathrm{X}\,^{2}\Pi$ towards $\mathrm{X}^{+\,3}\Sigma^{-}$, $\mathrm{a}^{+\,1}\Delta$, and $\mathrm{b}^{+\,1}\Sigma^{+}$, the calculated and experimental ionization energies are obtained using our calculated spin-orbit splitting value and the experimental value from Ref. 155, respectively. Additionally, it is worth noting that the excited

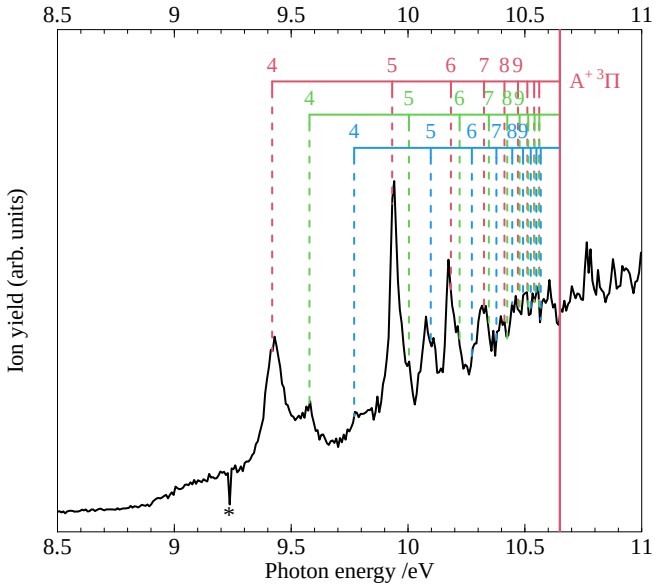

Figure 5.23: Mass-selected ion yield of the SiCH radical. The labels located by combs correspond to the assignments of the Rydberg series of neutral species observed by autoionization.

state $A^+\,^3\Pi$ also exhibits spin-orbit splitting, characterized by a calculated parameter *A* of 37.09 cm^{-1}. This splitting provides a partial compensation for the ground state's splitting. However, in Table 5.10, its subtle influence on the $A^+\,^3\Pi \leftarrow X\,^2\Pi$ transition has only been considered for the calculated value, as its impact has been neglected in the experimental results due to the spectral resolution constraints.

5.5.4 Photoion yield

The complete simulated spectrum in Fig. 5.22 agrees well with the experimental data, faithfully reproducing the majority of spectral features. The exceptions are the distinct bands at approximately 9.4 eV and the weak, scattered peaks distributed within the energy range of 9.7 to 10.5 eV. From our FC simulation, we can exclude any other photoionizing transitions from SiCH or its HSiC isomer (see previous section).

To understand these unassigned features, it is interesting to investigate the ion yield spectrum displayed in Fig. 5.23. This spectrum consists in a slowly rising slope originating from around 8.9 eV, consistent with the first photoionizing transition (see the SPES of Fig. 5.22). This slope extends across the remaining measured photon energy range and is altered by several prominent autoionization peaks signing Rydberg series of neutral SiCH converging to the $A^+\,^3\Pi$ state of $SiCH^+$. In particular, strong peaks at approximately 9.4 eV and 9.9 eV are observed and suggest that the unassigned SPES bands are probably due to "resonant" autoionization processes (ie autoionization producing threshold electrons).

Within Fig. 5.23, three sets of combs are displayed, representing the energies of Rydberg states converging towards the $A^+\,^3\Pi$ cationic state and calculated using the Rydberg formula in Eq. 5.1 where *IE* is the ionization energy of

SiCH towards $\mathrm{A}^{+\,3}\Pi$ (10.668 eV determined by our experiments), R_y the Rydberg constant of SiCH (R_y = 13.60551 eV) and $n^* = n - \delta$ the effective quantum number (n being the main quantum number and δ the quantum defect). Using this formula we were able to fit three distinct series with three different quantum defects (0.68, 0.46, and 0.05) highlighted by the red, green, and blue combs in Fig. 5.23, respectively.

Similar pronounced autoionization features have been previously observed in the spectra of several small radicals, including CH[56], SiH[26] (detailed in Section 5.2.3.2), CF, and SiF.[89] In these instances, the autoionization processes give rise to non-Franck-Condon vibrational progressions in the photoelectron spectra, providing valuable insights into highly excited vibrational levels. This has been exemplified in our recent studies on SiF and CF (not shown in this thesis). However, in the case of SiCH, despite the observation of prominent autoionization structures, their impact on the photoelectron spectrum is comparatively subtle, primarily manifesting as modest signals around 9.4 eV. This can be attributed to the remarkably close agreement between our experimental measurements and simulations, as illustrated in Fig. 5.22. These bands in the photoelectron spectrum can be reasonably ascribed to a non-Franck-Condon vibrational progression associated with the $\mathrm{X}^{+\,3}\Sigma^- \leftarrow \mathrm{X}\,^2\Pi$ photoionizing transition, which is evident through the occurrence of autoionization processes. However, the dense spectral landscape of SiCH makes it challenging to discern specific details about the excited vibrational levels participating in these observed transitions. To delve deeper into this analysis, higher spectral resolution measurements are imperative.

5.5.5 Conclusions

Our pioneering work presents the first experimental insights into the elusive $SiCH^+$ cation through single-photon ionization spectroscopy of gas-phase SiCH. Despite its significance in theoretical models of silicon chemistry within the interstellar medium, SiCH and its cation had remained unobserved in space due to their inherent instability. By generating SiCH radicals in a controlled environment and employing cutting-edge spectroscopic techniques, we successfully acquired mass-selected ion yield and photoelectron spectra. Our measurements revealed information about the adiabatic ionization energies for transitions originating from the SiCH ground electronic state towards the four lowest electronic states of $SiCH^+$. The experimental determination of these ionization energies provides a solid foundation for understanding the electronic structure and properties of $SiCH^+$.

The successful characterization of $SiCH^+$ marks a significant advancement towards facilitating astronomical observations of SiCH and its cation and validating theoretical models of silicon chemistry in the interstellar medium. As our understanding of silicon chemistry continues to evolve, this work lays the groundwork for further investigations into the role of SiCH and its cation in the complex chemical network

5.6 Summary on the properties of silicon-bearing compounds and comparison with their equivalent carbonated species

During my PhD, the VUV photoionization of several silicon-bearing compounds has been investigated, and the complete analysis of SiH, SiC, SiCH and Si_2 has been reported in this manuscript. Let us note that similar studies on the corresponding carbon-bearing radicals have been performed in the group before my PhD, in particular on CH [56] and C_2.[71] In this paragraph, I propose to summarize the main results, to extract general ideas and trends for some of the species, and to discuss comparisons with the equivalent carbon-bearing radical.

5.6.1 Ionization energy and electronic structure

Table 5.11: C-bearing species

	Photoionization transition	Character of photoelectron	IE_{ad}, eV
C	$^2\mathrm{P} \leftarrow {}^3\mathrm{P}$	$(2\mathrm{p})^1 \leftarrow (2\mathrm{p})^2$	11.2603(0) [105]
CH	$\mathrm{X}^+\,{}^1\Sigma^+ \leftarrow \mathrm{X}\,{}^2\Pi$	$(1\pi)^0 \leftarrow (1\pi)^1$	10.640(4) [56]
	$\mathrm{a}^+\,{}^3\Pi \leftarrow \mathrm{X}\,{}^2\Pi$	$(3\sigma)^1 \leftarrow (3\sigma)^2$	11.827(4) [56]
C_2	$\mathrm{X}^+\,{}^4\Sigma_\mathrm{g}^- \leftarrow \mathrm{X}\,{}^1\Sigma_\mathrm{g}^+$	forbidden	11.873(10) [71]
	$\mathrm{X}^+\,{}^4\Sigma_\mathrm{g}^- \leftarrow \mathrm{a}\,{}^3\Pi_\mathrm{u}$	$(1\pi_\mathrm{u})^3 \leftarrow (1\pi_\mathrm{u})^4$	11.795(10) [71]
	$\mathrm{a}^+\,{}^2\Pi_\mathrm{u} \leftarrow \mathrm{X}\,{}^1\Sigma_\mathrm{g}^+$	$(1\pi_\mathrm{u})^2 \leftarrow (1\pi_\mathrm{u})^3$	12.440(10) [71]

Table 5.12: Si-bearing species

	Photoionization transition	Character of photoelectron	IE_{ad}, eV
Si	$^2\mathrm{P} \leftarrow {}^3\mathrm{P}$	$(3\mathrm{p})^1 \leftarrow (3\mathrm{p})^2$	8.1517(0) [105]
SiH	$\mathrm{X}^+\,{}^1\Sigma^+ \leftarrow \mathrm{X}\,{}^2\Pi$	$(2\pi)^0 \leftarrow (2\pi)^1$	7.934(5) [26]
	$\mathrm{a}^+\,{}^3\Pi \leftarrow \mathrm{X}\,{}^2\Pi$	$(5\sigma)^1 \leftarrow (5\sigma)^2$	10.205(5) [26]
Si_2	$\mathrm{X}^+\,{}^4\Sigma_\mathrm{g}^- \leftarrow \mathrm{X}\,{}^3\Sigma_\mathrm{g}^-$	$(5\sigma_\mathrm{g})^1 \leftarrow (5\sigma_\mathrm{g})^2$	7.919(5) [27]
	$\mathrm{X}^+\,{}^4\Sigma_\mathrm{g}^- \leftarrow \mathrm{D}\,{}^3\Pi_\mathrm{u}$	$(2\pi_\mathrm{u})^2 \leftarrow (2\pi_\mathrm{u})^3$	7.869(5) [27]
	$\mathrm{a}^+\,{}^2\Pi_\mathrm{u} \leftarrow \mathrm{X}\,{}^3\Sigma_\mathrm{g}^-$	$(2\pi_\mathrm{u})^1 \leftarrow (2\pi_\mathrm{u})^2$	8.429(12) [27]

Table 5.13: C- and Si-bearing species

	Photoionization transition	Character of photoelectron	IE_{ad}, eV
SiC	$\mathrm{X}^+\,{}^4\Sigma^- \leftarrow \mathrm{X}\,{}^3\Pi$	$(2\pi)^2 \leftarrow (2\pi)^3$	8.978(10) [57]
SiCH	$\mathrm{X}^+\,{}^3\Sigma^- \leftarrow \mathrm{X}\,{}^2\Pi$	$(2\pi)^2 \leftarrow (2\pi)^3$	8.939(6) [28 28]
	$\mathrm{A}^+\,{}^3\Pi \leftarrow \mathrm{X}\,{}^2\Pi$	$(7\sigma)^1 \leftarrow (7\sigma)^2$	10.668(6)

Tab. 5.11 summarizes the lowest photoionization transitions and ionization energies for atomic C, CH and C_2 dimer. Tab. 5.12 gives the same information for atomic Si, SiH and Si_2 dimer. A first simple observation is that CH/C_2 and SiH/Si_2 exhibit ionization energies very close to that of atomic carbon and silicon, respectively. Upon comparing Tab. 5.11 and Tab. 5.12, we observe that the adiabatic ionization energy of silicon compounds is generally lower than that of the corresponding carbon compounds. This is a logical outcome due to the larger size of the silicon atom compared to carbon, resulting in weaker bonding energy for the outer electron. Given the similar electronic configurations of these two elements, their monohydrogenides (CH/SiH) and cations exhibit strikingly similar electronic structures and ionization processes. For instance, both exhibit strong autoionization structures occurring above the first ionization threshold from Rydberg states converging to the excited cationic state $\mathrm{a}^+\,{}^3\Pi$.

This phenomenon extends to SiCH (see Tab. 5.13), which exhibits autoionization from Rydberg series converging to $\mathrm{A}^+\,^3\Pi$. From these observations, one could deduce intriguing insights regarding the autoionization processes involving the $^1\Sigma^+$ or $^3\Sigma^-$ cationic ground state in all these species and the $^3\Pi$ excited state: the ejected electron in both ionization channels, $^1\Sigma^+/^3\Sigma^-$ ground state and the $^3\Pi$ excited state, is a p-like electron (pπ and pσ, respectively). In the Rydberg series of $^3\Pi$, the excited pσ electron leaves a p-like hole, creating a favorable condition for the outer pπ electron to occupy. This highlights a high possibility of interaction/coupling between these two ionization channels.

However, the electronic structures of C_2 and Si_2 exhibit notable distinctions, primarily due to the varying order of energy levels within their electronic states. Both molecules feature closely located low-lying electronic states, particularly the ground and first excited states, which are separated by a mere 0.05 eV. In the case of C_2, the complete occupation of the $1\pi_\mathrm{u}$ orbital (π primarily composed of the 2p orbital of carbon) appears to result in a more energetically stable molecular system. Conversely, Si_2 demonstrates greater energetic stability when its $5\sigma_\mathrm{g}$ orbital (σ mainly composed of the 3p orbital of silicon) is occupied. This fundamental difference in orbital occupancy contributes to their distinct electronic structures and state orderings. As a result, we observe a $\mathrm{X}^+ \leftarrow \mathrm{X}$ forbidden photoionization transition in C_2, while Si_2 exhibits a pronounced $X^+\leftarrow$ X allowed photoionization.

Tab. 5.13 gathers information on mixed Si/C species, *i.e.* SiC and SiCH. We clearly observe that their lowest ionization energy is closer to that of atomic silicon than atomic carbon.

Table 5.14: Singlet-triplet or doublet-quadruplet state energy differences

	singlet-triplet	ΔE, eV		doublet-quadruplet	ΔE, eV
CH^+	$\mathrm{X}^+\,^1\Sigma^+$-$\mathrm{a}^+\,^3\Pi$	1.187(4)[56]	CH	/	/
SiH^+	$\mathrm{X}^+\,^1\Sigma^+$-$\mathrm{a}^+\,^3\Pi$	2.272(5)[26]	SiH	$\mathrm{X}\,^2\Pi$-$\mathrm{a}\,^4\Sigma^-$	1.716*[26]
C_2	$\mathrm{X}\,^1\Sigma_\mathrm{g}^+$-$\mathrm{a}\,^3\Pi_\mathrm{u}$	0.079(10)[71]	C_2^+	$\mathrm{X}^+\,^4\Sigma_\mathrm{g}^-$-$\mathrm{a}^+\,^2\Pi_\mathrm{u}$	0.567(10)[71]
Si_2	$\mathrm{X}\,^3\Sigma_\mathrm{g}^+$-$\mathrm{a}\,^1\Delta_\mathrm{g}$	0.437[27]	Si_2^+	$\mathrm{X}^+\,^4\Sigma_\mathrm{g}^-$-$\mathrm{a}^+\,^2\Pi_\mathrm{u}$	0.51[27]
SiC	$\mathrm{X}\,^3\Pi$-$\mathrm{a}\,^1\Sigma^+$	0.652*[57]	SiC^+	$\mathrm{X}^+\,^4\Sigma^-$-$\mathrm{X}^+\,^2\Delta$	1.195[57]
$SiCH^+$	$\mathrm{X}\,^3\Sigma^-$-$\mathrm{a}\,^1\Delta$	0.83[28]	SiCH	/	/

* Calculated values

Tab. 5.14 summarizes the singlet-triplet and doublet-quadruplet energy differences in the studied C- and Si-radical species obtained in our studies. No obvious trend is observed.

5.6.2 Thermochemical considerations

A possible outcome of our photoionization studies is to derive unprecedented thermochemical data which are important for refining databases such as that of the Active Thermochemical Tables (ATcT) designed and updated by Branko Ruscic (Argonne National Lab).[2] The ATcT provide comprehensive thermochemical data by using the entirety of available experimental measurements alongside state-of-the-art theoretical information. In contrast to conventional sequential thermochemistry, where each result builds upon the previous (A leads to B, which leads to C, and

neutral species X	$\Delta_f H_0^\circ$(X), kJ/mol	$\Delta_f H_0^\circ$(X^+), kJ/mol	$IE_{ad,ATcT}$, eV	IE_{ad}, eV
CH	592.832±0.095	1619.753±0.042	10.643±0.001	10.640(4)[56]
SiH	371.32±0.76	1134.7±1.1	7.912±0.014	7.934(5)[26]
C_2	819.991±0.087	1964.96±0.40	11.867±0.004	11.873(10)[71]
Si_2	587.5±1.6	1349.9±2.7	7.902±0.033	7.919(5)[27]
SiC	740.4±2.4	1602±2.6	8.930±0.0367	8.978(10)[57]
SiCH	/	/	/	8.939(6)[28]

Table 5.15: Enthalpies of formation for the neutral and cationic species of various Si- and C-species studied in our group

so on), ATcT is rooted in the construction, analysis, and resolution of the underlying thermochemical network. Our experimental data can serve various purposes within this framework, including the potential to revise or fine-tune existing data and offer new data for previously unexplored species. Tab. 5.15 documents the enthalpies of formation for the neutral and cationic species examined in this chapter, along with their corresponding ionization energies retrieved from the ATcT website. The ATcT data of ionization energies are calculated from their formation enthalpies. In a broader context, our measured ionization energies establish a means to indirectly provide the enthalpies of formation or dissociation energies associated with the cationic species documented in ATcT.

Tab. 5.16 summarizes the extracted dissociation energies of silicon-bearing cations investigated during my PhD. These D_0 energies are calculated using the following formula:

$$D_0(X^+) = D_0(X) + IE(M) - IE_{ad}(X) \tag{5.2}$$

with M= H, Si, Si in SiH^+, Si_2^+, and SiC^+. We used the following values for calculating the dissociation energies: *IE*(H) = 13.5984(0) eV,[105] *IE*(Si)= 8.15168(3) eV,[105] D_0(SiH)= 2.98(3) eV,[11] D_0(SiC)=4.466(217) eV,[47] D_0(Si_2)=3.252(217) eV;[47]

Cations X^+	ATcT[2], eV	our work, eV
SiH^+	8.745(10)	8.644(30)
Si_2^+	3.496(24)	3.485(217)
SiC^+	3.589(26)	3.640(217)

Table 5.16: Dissociation energies of silicon-bearing cations

To conclude this chapter, let us note that additional studies on SiH_2, SiN and SiNH have been performed during my thesis and are still currently under analysis. Moreover, CF and SiF fluorinated radicals, not discussed in this thesis, have been produced in the flow-tube reactor, giving rise to nicely structured photoelectron spectra.[89] All of these data will be of great interest for the ATcT and should contribute to its completeness.

Chapter 6

Conclusions and perspectives

In this manuscript, I presented my doctoral work which focuses on photoionization spectroscopic measurements of gas-phase radical species of astrophysical interest. These experiments were conducted using two setups: the VULCAIM setup at ISMO and the SAPHIRS setup at the DESIRS beamline of the SOLEIL synchrotron. Both setups allowed for the coupling of a radical source with a photoionization spectrometer, with the goal of investigating the (ro)vibrational structure of cations of radical molecules at high and medium spectral resolution, respectively.

The VULCAIM setup is characterized by its capacity to provide a high-resolution tunable VUV laser through a non-linear 4-wave mixing process. Its pulsed mode enables high-resolution spectroscopic measurements *via* PFI-ZEKE photoelectron spectroscopy or its variant (MATI spectroscopy). During my PhD, an important work has been performed to improve the properties of this setup, and to increase its versatility. This manuscript highlighted 3 main developments performed on this setup within the scope of my thesis:

1. **Introduction of a new tunable laser line based on the OPO laser.**

   Using the tunable laser chain with the Cobra dye laser, the generated VUV laser is characterized by a high spectral resolution of 0.1 cm^{-1} but a relatively reduced tunability range (approximately 1000 cm^{-1}) due to limitations imposed by the dye solution. The newly installed OPO laser line extends the continuous tunability range up to 24000 cm^{-1}, albeit with a medium spectral resolution of 3 cm^{-1}. By switching between these two tunable laser lines, we can now perform initial exploratory scans across a broad energy range, facilitating the investigation of molecules lacking prior energy information, and then conduct high-resolution spectroscopic measurements over a specific energy range.

2. **Exploration of radical sources through pyrolysis and electric discharge.**

   A significant aspect of my doctoral work involved investigating radical molecular sources compatible with the VULCAIM setup for conducting photoionization experiments on free radicals. Given the pulsed nature of ex-

periments on this setup, I explored pyrolysis and electric discharge strategies. Using the pyrolysis device, CH_3 radicals were successfully produced from CH_3NO_2 precursor. Further investigations are planned, including the exploration of slightly larger radicals containing an aromatic ring, such as the benzyl radical (C_7H_7) which may be formed *via* pyrolysis of bibenzyl and is expected to have a partially resolved ZEKE spectrum.[146]

Using high-voltage electric discharge, CH_3 and NH_2 were generated from CH_4 and NH_3, respectively. A new strategy, combining the electric discharge and the reaction with metastable atoms, has also been explored. This approach exhibited the potential to produce small radicals with higher efficiency. However, the spectroscopic work on the generated NH radical was not achieved due to limitations related to the VUV generation in the vicinity of its adiabatic ionization energy (13.480 eV). Nevertheless, further investigations on small radicals are planned using electric discharge or its variant method. Optimizing radical yield will be a focus of future work. For instance, modifying the precursor feeding in the variant discharge device from continuous to pulsed mode may improve radical generation yield. Introducing different precursor species (or even mixtures) is interesting for both methods to explore more radicals, such as SiH, SiC, CN, etc.

Especially for Si-bearing species, based on our medium-resolution studies performed at SOLEIL, high-resolution measurements are intriguing. They will enable us to investigate the fine structure inherent in the discussed ionizing transitions. For instance, concerning the studied SiH, SiC, and SiCH radicals, high-resolution ZEKE spectroscopic measurements can investigate the rotational and spin-orbit structures and provide enhanced precision in determining ionization energies. Regarding the Si_2 radical, a rotationally resolved investigation might help us to examine our proposed mechanism (autoionization induced by spin interactions) to explain the observation of the spin-forbidden quartet-singlet transition signal.

Additionally, to facilitate experiments with the discharge radical source, we are planning to modify the initial spectrometer to a vertical configuration. This will help avoid interference from intense discharge light since the MCP detector will be perpendicular to the beam axis.

3. **Implementation of a reflectron.**

   The installation of a Reflectron mass spectrometer addressed the issue of MCP saturation caused by discharge light from the molecular source. Currently, the mass resolution stands at 1200, which should be enhanced by introducing focus voltages to reach the manufacturer's specification of 1500. In addition, following the successful implementation of MATI spectroscopy on VULCAIM, the reflectron is planned to be coupled to the MATI technique to further enhance mass selectivity and spectral resolution in MATI experiments. For instance, MATI spectra of the C_7H_6 and C_7H_5 transient species could be recorded, using the flash pyrolysis of phthalide.[157] Distinct spectral signatures of these species (and potentially their isomers) would be obtained thanks to the mass-selectivity of the technique.

In addition to the advancements in the setup, this manuscript introduces a novel high-resolution and high signal-

to-noise ratio PRFI-ZEKE Photoelectron Spectroscopy method. Building upon the conventional PFI-ZEKE PES technique, this method incorporates a new data acquisition scheme as well as a data treatment procedure designed to improve the signal-to-noise ratio without degrading the spectral resolution. It also incorporates a series of data treatment procedures with the intention of 'artificially' increasing statistics. Using the VULCAIM setup, we achieved a spectral resolution of approximately 0.25 cm^{-1} during the recording of the NO spectrum. Recently, our method has been employed by Professor Merkt's research group to investigate the photoionization thresholds of metastable rare gases.[78] A groundbreaking achievement for spectral resolution of 0.05 cm^{-1} was realized during their measurements on metastable Argon using an home-made high-resolution UV laser (bandwidth < 0.001 cm^{-1}). We plan to apply this technique to study radical species for which the temporal stability of the radical source is limited and a reduced acquisition time is required.

Apart from these experimental developments, this manuscript highlights a notable achievement in high-resolution photoelectron spectroscopic measurements applied to CH_3 radicals. A key point of this work involved the use of a pyrolysis radical source coupled to the VULCAIM setup, enabling the production of vibrationally hot CH_3 radicals. This experiment allowed for rotationally resolved laboratory measurements *via* PFI-ZEKE photoelectron spectroscopy, focusing on the sequence band transition $\tilde{\mathrm{X}}^{+\,1}\mathrm{A}_1^{'}(\nu_2^+ = 1) \leftarrow \tilde{\mathrm{X}}\,^2\mathrm{A}_2^{''}(\nu_2 = 1)$ of CH_3. The result represents a pioneering contribution by providing essential laboratory data to support the JWST detection of CH_3^+ in space for the first time.

In parallel with the studies performed at ISMO, several beamtime sessions have been conducted at SOLEIL synchrotron facility on the Saclay plateau during my PhD, in collaboration with J.C. Loison (ISM). The SAPHIRS setup, on the VUV beamline DESIRS, coupling a fluorine flow-tube reactor-based radical source with a double-imaging photoelectron/photoion coincidence (i^2PEPICO) spectrometer and the synchrotron radiation, has been used to study a variety of $Si_xC_yH_z$ radicals generated using SiH_4 or SiH_4/CH_4 as precursors. The configuration of the double-imaging spectrometer allowed for simultaneous recording of ion yield and mass-selective photoelectron spectra for these generated radicals, enabling the investigation of the vibronic structure of their cations. In this manuscript, I presented experimental results on SiH, Si_2, SiC, and SiCH radicals. These studies have provided reliable photoionization energy values and information on the vibronic structures of cations and Rydberg states of the neutral species observed *via* autoionization. They mark an important initial step in understanding the silicon chemistry occurring within interstellar clouds and they provide reliable data to refine the thermochemical network of Active Thermochemical Tables.[2]

With this setup at SOLEIL, more projects focused on qualitative and quantitative photoionization spectroscopic experiments involving radicals are in process or forthcoming. For instance, in November 2022, we initiated experiments with the objective of measuring the photoionization cross sections of free radicals such as C_3H_7, C_4H_9, and C_5H_{11}. The resulting data is currently undergoing analysis by Hai Linh LE, a second-year PhD student within our re-

search group. These experimental findings have the potential to help determine whether the ionization cross section value is dependent on the size of the radical within a given family or remains quasi-constant, primarily determined by the radical's nature (possessing a single free electron). Besides, these data hold significance for photochemical models in astrophysics and planetology, as well as for quantitative measurements in combustion involving mass spectrometry. Another project focusing on the photoionization spectroscopic measurements on N-bearing molecules, such as SiN and SiNH, has been performed thanks to the development of a double-discharge radical source. The analysis of the resulting experimental data is under progress. In the near future, we plan to investigate the photoionization of sulfur-bearing radicals, including SiS, C_2S, C_3S, HCCS and its isomer. Indeed, these compounds have been detected in space and their behaviors under VUV irradiation is of significance to account for their photoprocessing. These experiments aim to investigate the vibronic structure of cations of those sulfur-bearing radicals, marking an essential step towards conducting higher-resolution spectroscopic investigations using our VULCAIM setup.

Bibliography

[1] Amsterdam piezo valve website. URL http://www.amsterdampiezovalve.com.

[2] Active thermochemical tables. URL https://atct.anl.gov/.

[3] Jordan TOF products. URL http://www.rmjordan.com/reflectron-tof.html.

[4] SOLEIL website. URL https://www.synchrotron-soleil.fr.

[5] "Cosmic Cliffs" in the Carina Nebula (NIRCam Image), 2022. URL https://webbtelescope.org/contents/media/images/2022/031/01G77PKB8NKR7S8Z6HBXMYATGJ.

[6] Webb's View of the Molecular Cloud Chameleon I. 2023. URL https://www.esa.int/ESA_Multimedia/Images/2023/01/Webb_s_View_of_the_Molecular_Cloud_Chameleon_I.

[7] L. Åsbrink. The photoelectron spectrum of H_2. *Chemical Physics Letters*, 7(5):549–552, 1970. ISSN 0009-2614. doi: https://doi.org/10.1016/0009-2614(70)80169-5. URL https://www.sciencedirect.com/science/article/pii/0009261470801695.

[8] T. Baer, W. Peatman, and E. Schlag. Photoionization resonance studies with a steradiancy analyzer. II. The photoionization of CH_3I. *Chemical Physics Letters*, 4(5):243–247, nov 1969. ISSN 00092614. doi: 10.1016/0009-2614(69)80174-0. URL https://linkinghub.elsevier.com/retrieve/pii/0009261469801740.

[9] F. Baletto and R. Ferrando. Structural properties of nanoclusters: Energetic, thermodynamic, and kinetic effects. *Reviews of Modern Physics*, 77(1):371–423, may 2005. ISSN 0034-6861. doi: 10.1103/RevModPhys.77.371. URL https://link.aps.org/doi/10.1103/RevModPhys.77.371.

[10] U. Becker and D. A. Shirley. Threshold Behaviour and Resonances in the Photoionization of Atoms and Molecules. *Physica Scripta*, T31:56–66, jan 1990. ISSN 0031-8949. doi: 10.1088/0031-8949/1990/T31/008. URL https://iopscience.iop.org/article/10.1088/0031-8949/1990/T31/008.

[11] J. Berkowitz, J. P. Greene, H. Cho, and B. Ruščić. Photoionization mass spectrometric studies of SiH_n (n=1-4). *The Journal of Chemical Physics*, 86(3):1235–1248, feb 1987. ISSN 0021-

9606. doi: 10.1063/1.452213. URL https://pubs.aip.org/jcp/article/86/3/1235/660155/Photoionization-mass-spectrometric-studies-of-SiHn.

[12] O. Berné, M.-A. Martin-Drumel, I. Schroetter, J. R. Goicoechea, U. Jacovella, B. Gans, E. Dartois, L. Coudert, E. Bergin, F. Alarcon, J. Cami, E. Roueff, J. H. Black, O. Asvany, E. Habart, E. Peeters, A. Canin, B. Trahin, C. Joblin, S. Schlemmer, S. Thorwirth, J. Cernicharo, M. Gerin, A. Tielens, M. Zannese, A. Abergel, J. Bernard-Salas, C. Boersma, E. Bron, R. Chown, S. Cuadrado, D. Dicken, M. Elyajouri, A. Fuente, K. D. Gordon, L. Issa, O. Kannavou, B. Khan, O. Lacinbala, D. Languignon, R. Le Gal, A. Maragkoudakis, R. Meshaka, Y. Okada, T. Onaka, S. Pasquini, M. W. Pound, M. Robberto, M. Röllig, B. Schefter, T. Schirmer, A. Sidhu, B. Tabone, D. Van De Putte, S. Vicente, and M. G. Wolfire. Formation of the Methyl Cation by Photochemistry in a Protoplanetary Disk. *Nature*, 2023. ISSN 0028-0836. doi: 10.1038/s41586-023-06307-x. URL https://doi.org/10.1038/s41586-023-06307-x.

[13] J. A. Blush, P. Chen, R. T. Wiedmann, and M. G. White. Rotationally resolved threshold photoelectron spectrum of the methyl radical. *The Journal of Chemical Physics*, 98(4):3557–3559, feb 1993. ISSN 0021-9606. doi: 10.1063/1.464077. URL https://pubs.aip.org/jcp/article/98/4/3557/980265/Rotationally-resolved-threshold-photoelectron.

[14] B. H. Boo and P. B. Armentrout. Reaction of Silicon Ion (^{2}P) with Silane (SiH_4, SiD_4). Heats of Formation of SiH_n, SiH_n^+ (n = 1, 2, 3), and $Si_2H_n^+$(n = 0, 1, 2, 3). Remarkable Isotope Exchange Reaction Involving Four Hydrogen Shifts. *Journal of the American Chemical Society*, 109(12):3549–3559, jun 1987. ISSN 0002-7863. doi: 10.1021/ja00246a010. URL https://pubs.acs.org/doi/abs/10.1021/ja00246a010.

[15] C. M. Brown, S. G. Tilford, R. Tousey, and M. L. Ginter. Absorption spectrum of SiI between 1500 and 1900 Å. *Journal of the Optical Society of America*, 64(12):1665, dec 1974. ISSN 0030-3941. doi: 10.1364/JOSA.64.001665. URL https://opg.optica.org/abstract.cfm?URI=josa-64-12-1665.

[16] P. J. Bruna, C. Petrongolo, R. J. Buenker, and S. D. Peyerimhoff. Theoretical prediction of the potential curves for the lowest-lying states of the CSi^+ and Si_2^+ molecular ions. *The Journal of Chemical Physics*, 74(8):4611–4620, apr 1981. ISSN 0021-9606. doi: 10.1063/1.441650. URL https://pubs.aip.org/jcp/article/74/8/4611/217715/Theoretical-prediction-of-the-potential-curves-for.

[17] R. J. Buenker, P. J. Bruna, and S. D. Peyerimhoff. Ab Initio MRD-CI Calculations for HAB Molecules I. Isomerization Energies for HOS, HNP and HCSi and Their Positive Ions. *Israel Journal of Chemistry*, 19(1-4):309–316, jan 1980. ISSN 0021-2148. doi: 10.1002/ijch.198000038. URL https://onlinelibrary.wiley.com/doi/10.1002/ijch.198000038.

[18] J. B. Burkholder, C. J. Howard, and A. R. W. McKellar. Fourier transform infrared spectrum of the ν_2 band of the NH_2 radical. *Journal of Molecular Spectroscopy*, 127(2):415–424, 1988. ISSN 0022-2852. doi:

https://doi.org/10.1016/0022-2852(88)90131-2. URL https://www.sciencedirect.com/science/article/pii/0022285288901312.

[19] T. J. Butenhoff and E. A. Rohlfing. The C $^3\Pi$–X $^3\Pi$ band system of the SiC radical. *The Journal of Chemical Physics*, 95(6):3939–3943, 1991. ISSN 0021-9606. doi: 10.1063/1.460800. URL https://doi.org/10.1063/1.460800.

[20] T. Carlson, J. Copley, N. Duric, N. Elander, P. Erman, M. Larsson, and M. Lyyra. The oscillator strengths and the dissociation energy of SiH^+ as determined from time resolved precision spectroscopy. *Astronomy and Astrophysics*, 83(1-2):238–244, mar 1980. URL https://ui.adsabs.harvard.edu/abs/1980A&A....83..238C.

[21] P. Caselli and C. Ceccarelli. Our astrochemical heritage. *The Astronomy and Astrophysics Review*, 20(1):56, oct 2012. ISSN 0935-4956. doi: 10.1007/s00159-012-0056-x. URL http://link.springer.com/10.1007/s00159-012-0056-x.

[22] J. Cernicharo, C. A. Gottlieb, M. Guelin, P. Thaddeus, and J. M. Vrtilek. Astonomical and laboratory detection of the SiC radical. *The Astrophysical Journal*, 341:L25, jun 1989. ISSN 0004-637X. doi: 10.1086/185449. URL http://adsabs.harvard.edu/doi/10.1086/185449.

[23] J. Cernicharo, F. Daniel, A. Castro-Carrizo, M. Agundez, N. Marcelino, C. Joblin, J. R. Goicoechea, and M. Guélin. Unveiling the dust nucleation zone of IRC+10216 with ALMA. *The Astrophysical Journal*, 778(2):L25, nov 2013. ISSN 2041-8205. doi: 10.1088/2041-8205/778/2/L25. URL https://iopscience.iop.org/article/10.1088/2041-8205/778/2/L25.

[24] P. B. Changala, N. L. Chen, H. L. Le, B. Gans, K. Steenbakkers, T. Salomon, L. Bonah, I. Schroetter, A. Canin, M.-A. Martin-Drumel, U. Jacovella, E. Dartois, S. Boyé-Péronne, C. Alcaraz, O. Asvany, S. Brünken, S. Thorwirth, S. Schlemmer, J. R. Goicoechea, G. Rouillé, A. Sidhu, R. Chown, D. Van De Putte, B. Trahin, F. Alarcón, O. Berné, E. Habart, and E. Peeters. Astronomical CH_3^+ rovibrational assignments.A combined theoretical and experimental study validating observational findings in the d203-506 UV-irradiated protoplanetary disk. *Astronomy & Astrophysics*, 680:A19, dec 2023. ISSN 0004-6361. doi: 10.1051/0004-6361/202347765. URL https://www.aanda.org/10.1051/0004-6361/202347765.

[25] S. B. Charnley. Sulfuretted Molecules in Hot Cores. *The Astrophysical Journal*, 481(1):396–405, may 1997. ISSN 0004-637X. doi: 10.1086/304011. URL https://dx.doi.org/10.1086/304011.

[26] N. L. Chen, B. Gans, S. Hartweg, G. A. Garcia, S. Boyé-Péronne, and J.-C. Loison. Photoionization spectroscopy of the SiH free radical in the vacuum-ultraviolet range. *The Journal of Chemical Physics*, 157(1):14303, 2022. doi: 10.1063/5.0094863. URL https://doi.org/10.1063/5.0094863.

[27] N. L. Chen, B. Gans, S. Hartweg, G. A. Garcia, S. Boyé-Péronne, and J.-C. Loison. Unravelling the electronic structure of the silicon dimer using threshold photoelectron spectroscopy. *Molecular Physics*, nov 2022. ISSN

0026-8976. doi: 10.1080/00268976.2022.2140721. URL https://www.tandfonline.com/doi/full/10.1080/00268976.2022.2140721.

[28] N. L. Chen, B. Gans, S. Boyé-Péronne, S. Hartweg, G. Garcia, and J.-C. Loison. First experimental characterization of $SiCH^+$ via single-photon ionization of gas-phase SiCH. *Journal of Chemical Physics*, (to be submitted), 2024.

[29] P. Chen, S. D. Colson, W. A. Chupka, and J. A. Berson. Flash pyrolytic production of rotationally cold free radicals in a supersonic jet. Resonant multiphoton spectrum of the $3p^2A_2'' \leftarrow X^2A_2''$ origin band of methyl. *The Journal of Physical Chemistry*, 90(11):2319–2321, may 1986. ISSN 0022-3654. doi: 10.1021/j100402a014. URL https://doi.org/10.1021/j100402a014.

[30] T. Chen, C. Y. Xiao, A. Li, and C. T. Zhou. Where have all the interstellar silicon carbides gone? *Monthly Notices of the Royal Astronomical Society*, 509(4):5231–5236, dec 2021. ISSN 0035-8711. doi: 10.1093/mnras/stab3175. URL https://academic.oup.com/mnras/article/509/4/5231/6415899.

[31] Y.-N. Chiu and L.-Y. C. Chiu. An alternative mechanism for spin-forbidden photo-ionization of diatomic molecules and its rotation–electronic selection rules. *Canadian Journal of Physics*, 68(2):177–183, feb 1990. ISSN 0008-4204. doi: 10.1139/p90-025. URL http://www.nrcresearchpress.com/doi/10.1139/p90-025.

[32] R. Cireasa, D. Cossart, and M. Vervloet. The optical spectrum of HCSi. *The European Physical Journal D*, 2(3): 199–201, jul 1998. ISSN 1434-6060. doi: 10.1007/PL00021570. URL http://link.springer.com/10.1007/PL00021570.

[33] R. Cireasa, D. Cossart, M. Vervloet, and J. M. Robbe. Fourier transform emission spectrum of the HCSi radical, $\tilde{A}_2\Sigma^+ - \tilde{X}\,^2\Pi_i$ transition. *The Journal of Chemical Physics*, 112(24):10806–10810, jun 2000. ISSN 0021-9606. doi: 10.1063/1.481724. URL https://pubs.aip.org/jcp/article/112/24/10806/530472/Fourier-transform-emission-spectrum-of-the-HCSi.

[34] D. E. Couch, D. D. Hickstein, D. G. Winters, S. J. Backus, M. S. Kirchner, S. R. Domingue, J. J. Ramirez, C. G. Durfee, M. M. Murnane, and H. C. Kapteyn. Ultrafast 1 MHz vacuum-ultraviolet source via highly cascaded harmonic generation in negative-curvature hollow-core fibers. *Optica*, 7(7):832, jul 2020. ISSN 2334-2536. doi: 10.1364/OPTICA.395688. URL https://opg.optica.org/abstract.cfm?URI=optica-7-7-832.

[35] L. H. Coudert, B. Gans, F. Holzmeier, J.-C. Loison, G. A. Garcia, C. Alcaraz, A. Lopes, and A. Röder. Experimental and theoretical threshold photoelectron spectra of methylene. *The Journal of Chemical Physics*, 149(22), dec 2018. ISSN 0021-9606. doi: 10.1063/1.5062834. URL https://pubs.aip.org/jcp/article/149/22/224304/196664/Experimental-and-theoretical-threshold.

[36] A. Crapsi, P. Caselli, C. M. Walmsley, P. C. Myers, M. Tafalla, C. W. Lee, and T. L. Bourke. Probing the Evolutionary Status of Starless Cores through N_2H^+ and N_2D^+ Observations. *The Astrophysical Journal*, 619(1):379–406, jan 2005. ISSN 0004-637X. doi: $10.1086/426472$. URL https://iopscience.iop.org/article/10.1086/426472.

[37] M. W. Crofton, M.-F. Jagod, B. D. Rehfuss, W. A. Kreiner, and T. Oka. Infrared spectroscopy of carbo-ions. III. ν_3 band of methyl cation CH_3^+. *The Journal of Chemical Physics*, 88(2):666–678, jan 1988. ISSN 0021-9606. doi: $10.1063/1.454194$. URL https://pubs.aip.org/jcp/article/88/2/666/223119/Infrared-spectroscopy-of-carbo-ions-III-3-band-of.

[38] E. Cromwell, T. Trickl, Y. T. Lee, and A. H. Kung. Ultranarrow bandwidth VUV-XUV laser system. *Review of Scientific Instruments*, 60(9):2888–2892, sep 1989. ISSN 0034-6748. doi: $10.1063/1.1140623$. URL https://pubs.aip.org/rsi/article/60/9/2888/324407/Ultranarrow-bandwidth-VUV-XUV-laser-systemVUV-XUV.

[39] B. K. Cunha de Miranda. *Études de la photoionisation de radicaux et de réactions ion-molécule d'intérêt planétaire avec du rayonnement VUV synchrotron et laser*. PhD thesis, Université Paris-Sud 11 (Orsay) and Universidade Federal Fluminense (Niterói), 2011. URL https://theses.hal.science/tel-00619442.

[40] B. K. Cunha de Miranda, C. Alcaraz, M. Elhanine, B. Noller, P. Hemberger, I. Fischer, G. A. Garcia, H. Soldi-Lose, B. Gans, L. A. Vieira Mendes, S. Boyé-Péronne, S. Douin, J. Zabka, and P. Botschwina. Threshold photoelectron spectroscopy of the methyl radical isotopomers, CH_3, CH_2D, CHD_2 and CD_3: Synergy between VUV synchrotron radiation experiments and explicitly correlated coupled cluster calculations. *The Journal of Physical Chemistry A*, 114(14):4818–4830, apr 2010. ISSN 1089-5639. doi: $10.1021/jp909422q$. URL https://pubs.acs.org/doi/10.1021/jp909422q.

[41] A. A. de Almeida and P. D. Singh. Predictions on finding the SiH^+ and SiH in interstellar space. *Astrophysics and Space Science*, 56(2):415–419, jul 1978. ISSN 0004-640X. doi: $10.1007/BF01879572$. URL http://link.springer.com/10.1007/BF01879572.

[42] N. de Oliveira, M. Roudjane, D. Joyeux, D. Phalippou, J.-C. Rodier, and L. Nahon. High-resolution broad-bandwidth Fourier-transform absorption spectroscopy in the VUV range down to 40 nm. *Nature Photonics*, 5(3):149–153, mar 2011. ISSN 1749-4885. doi: $10.1038/nphoton.2010.314$. URL https://www.nature.com/articles/nphoton.2010.314.

[43] C. E. Dessent, S. R. Haines, and K. Müller-Dethlefs. A new detection scheme for synchronous, high resolution ZEKE and MATI spectroscopy demonstrated on the Phenol·Ar complex. *Chemical Physics Letters*, 315(1-2):103–108, dec 1999. ISSN 00092614. doi: $10.1016/S0009-2614(99)01193-8$. URL https://linkinghub.elsevier.com/retrieve/pii/S0009261499011938.

[44] C. E. H. Dessent and K. Müller-Dethlefs. Hydrogen-Bonding and van der Waals Complexes Studied by ZEKE and REMPI Spectroscopy. *Chemical Reviews*, 100(11):3999–4022, 2000. doi: $10.1021/\mathrm{cr990060r}$. URL https://doi.org/10.1021/cr990060r.

[45] D. A. Dixon, D. Feller, K. A. Peterson, and J. L. Gole. The Molecular Structure and Ionization Potential of Si_2 : The Role of the Excited States in the Photoionization of Si_2. *The Journal of Physical Chemistry A*, 104(11):2326–2332, mar 2000. ISSN 1089-5639. doi: $10.1021/\mathrm{jp992078b}$. URL https://pubs.acs.org/doi/10.1021/jp992078b.

[46] M. Drabbels, C. G. Morgan, and A. M. Wodtke. The spin-forbidden a $^4\Pi(\nu$=13-15) and b $^4\Sigma^-(\nu$=3)$\leftarrow$X $^2\Pi(\nu$=0) bands of nitric oxide: A new scheme for quantum state-specific high-resolution kinetic energy measurements. *The Journal of Chemical Physics*, 103(18):7700–7707, nov 1995. ISSN 0021-9606. doi: $10.1063/1.470292$. URL https://pubs.aip.org/jcp/article/103/18/7700/480428/The-spin-forbidden-a-4-13-15-and-b-4-3-X-2-0-bands.

[47] J. Drowart, G. De Maria, and M. G. Inghram. Thermodynamic study of SiC utilizing a mass spectrometer. *The Journal of Chemical Physics*, 29(5):1015–1021, 1958. ISSN 00219606. doi: $10.1063/1.1744646$. URL https://doi.org/10.1063/1.1744646.

[48] J. Dyke, N. Jonathan, E. Lee, and A. Morris. Vacuum ultraviolet photoelectron spectroscopy of transient species. Part 7.—The methyl radical. *J. Chem. Soc., Faraday Trans. 2*, 72(0):1385–1396, 1976. doi: $10.1039/\mathrm{F29767201385}$. URL http://dx.doi.org/10.1039/F29767201385.

[49] J. Dyke, M. Ghosh, M. Goubet, E. Lee, G. Levita, K. Miqueu, and D. Shallcross. A study of the atmospherically relevant reaction between molecular chlorine and dimethylsulfide (DMS): Establishing the reaction intermediate and measurement of absolute photoionization cross-sections. *Chemical Physics*, 324(1):85–95, may 2006. ISSN 03010104. doi: $10.1016/\mathrm{j.chemphys.2005.11.045}$. URL https://linkinghub.elsevier.com/retrieve/pii/S0301010405006270.

[50] K. S. E. Eikema, W. Ubachs, W. Vassen, and W. Hogervorst. Lamb shift measurement in the 1 ^{1}S ground state of helium. *Physical Review A*, 55(3):1866–1884, mar 1997. ISSN 1050-2947. doi: $10.1103/\mathrm{PhysRevA.55.1866}$. URL https://link.aps.org/doi/10.1103/PhysRevA.55.1866.

[51] A. T. J. B. Eppink and D. H. Parker. Velocity map imaging of ions and electrons using electrostatic lenses: Application in photoelectron and photofragment ion imaging of molecular oxygen. *Review of Scientific Instruments*, 68(9):3477–3484, sep 1997. ISSN 0034-6748. doi: $10.1063/1.1148310$. URL https://pubs.aip.org/rsi/article/68/9/3477/322674/Velocity-map-imaging-of-ions-and-electrons-using.

[52] B. Fell, I. V. Rivas, and D. L. McFadden. Kinetic study of electronically metastable nitrogen atoms, N(2 $^2\mathrm{D_J}$), by

electron spin resonance absorption. *The Journal of Physical Chemistry*, 85(3):224–228, feb 1981. ISSN 0022-3654. doi: 10.1021/j150603a003. URL https://pubs.acs.org/doi/abs/10.1021/j150603a003.

[53] I. Fischer, R. Lindner, and K. Müller-Dethlefs. State-to-state photoionisation dynamics probed by zero kinetic energy (ZEKE) photoelectron spectroscopy. *J. Chem. Soc., Faraday Trans.*, 90(17):2425–2442, 1994. ISSN 0956-5000. doi: 10.1039/FT9949002425. URL http://xlink.rsc.org/?DOI=FT9949002425.

[54] R. P. Frosch and G. W. Robinson. Emission Spectrum of NO in Solid Rare Gases: The lifetime of the $a^4\Pi$ state and the spectrum of the $a^4\Pi \rightarrow X^2\Pi$ and $B^2\Pi \rightarrow X\ ^2\Pi$ Transitions. *The Journal of Chemical Physics*, 41(2):367–374, jul 1964. ISSN 0021-9606. doi: 10.1063/1.1725876. URL https://pubs.aip.org/jcp/article/41/2/367/209014/Emission-Spectrum-of-NO-in-Solid-Rare-Gases-The.

[55] B. Gans, L. A. V. Mendes, S. Boyé-Péronne, S. Douin, G. Garcia, H. Soldi-Lose, B. K. C. de Miranda, C. Alcaraz, N. Carrasco, P. Pernot, and D. Gauyacq. Determination of the absolute photoionization cross sections of CH_3 and I produced from a pyrolysis source, by combined synchrotron and vacuum ultraviolet laser studies. *The Journal of Physical Chemistry A*, 114(9):3237–3246, mar 2010. ISSN 1089-5639. doi: 10.1021/jp909414d. URL https://pubs.acs.org/doi/10.1021/jp909414d.

[56] B. Gans, F. Holzmeier, J. Krüger, C. Falvo, A. Röder, A. Lopes, G. A. Garcia, C. Fittschen, J.-C. Loison, and C. Alcaraz. Synchrotron-based valence shell photoionization of CH radical. *The Journal of Chemical Physics*, 144(20):204307, may 2016. ISSN 0021-9606. doi: 10.1063/1.4950880. URL https://pubs.aip.org/jcp/article/144/20/204307/913102/Synchrotron-based-valence-shell-photoionization-of.

[57] B. Gans, J. Liévin, P. Halvick, N. L. Chen, S. Boyé-Péronne, S. Hartweg, G. A. Garcia, and J.-C. Loison. Single-photon ionization of SiC in the gas phase: experimental and ab initio characterizations of SiC^+. *Physical Chemistry Chemical Physics*, 25(35):23568–23578, 2023. ISSN 1463-9076. doi: 10.1039/D3CP02775A. URL http://dx.doi.org/10.1039/D3CP02775Ahttp://xlink.rsc.org/?DOI=D3CP02775A.

[58] E. Garand, T. I. Yacovitch, and D. M. Neumark. Slow photoelectron velocity-map imaging spectroscopy of C_2N^-, C_4N^-, and C_6N^-. *The Journal of Chemical Physics*, 130(6):0643, feb 2009. ISSN 0021-9606. doi: 10.1063/1.3076320. URL https://pubs.aip.org/jcp/article/130/6/064304/565121/Slow-photoelectron-velocity-map-imaging.

[59] G. A. Garcia, L. Nahon, and I. Powis. Two-dimensional charged particle image inversion using a polar basis function expansion. *Review of Scientific Instruments*, 75(11):4989–4996, nov 2004. ISSN 0034-6748. doi: 10.1063/1.1807578. URL https://pubs.aip.org/rsi/article/75/11/4989/351229/Two-dimensional-charged-particle-image-inversion.

[60] G. A. Garcia, H. Soldi-Lose, and L. Nahon. A versatile electron-ion coincidence spectrometer for photoelectron momentum imaging and threshold spectroscopy on mass selected ions using synchrotron radiation. *Review of Scientific Instruments*, 80(2):23102, feb 2009. ISSN 0034-6748. doi: 10.1063/1.3079331. URL https://doi.org/10.1063/1.3079331https://pubs.aip.org/rsi/article/80/2/023102/1017841/A-versatile-electron-ion-coincidence-spectrometer.

[61] G. A. Garcia, B. K. Cunha De Miranda, M. Tia, S. Daly, and L. Nahon. DELICIOUS III: A multipurpose double imaging particle coincidence spectrometer for gas phase vacuum ultraviolet photodynamics studies. *Review of Scientific Instruments*, 84(5):053112, 2013. ISSN 00346748. doi: http://dx.doi.org/10.1063/1.4807751. URL http://scitation.aip.org/content/aip/journal/rsi/84/5/10.1063/1.4807751.

[62] G. A. Garcia, B. Gans, X. Tang, M. Ward, S. Batut, L. Nahon, C. Fittschen, and J. C. Loison. Threshold photoelectron spectroscopy of the imidogen radical. *Journal of Electron Spectroscopy and Related Phenomena*, 203:25–30, 2015. ISSN 03682048. doi: 10.1016/j.elspec.2015.05.010. URL http://dx.doi.org/10.1016/j.elspec.2015.05.010.

[63] G. A. Garcia, X. Tang, J.-F. Gil, L. Nahon, M. Ward, S. Batut, C. Fittschen, C. A. Taatjes, D. L. Osborn, and J.-C. Loison. Synchrotron-based double imaging photoelectron/photoion coincidence spectroscopy of radicals produced in a flow tube: OH and OD. *The Journal of Chemical Physics*, 142(16):164201, apr 2015. ISSN 0021-9606. doi: 10.1063/1.4918634. URL https://pubs.aip.org/jcp/article/142/16/164201/397829/Synchrotron-based-double-imaging-photoelectron.

[64] S. T. Gibson, J. P. Greene, and J. Berkowitz. Photoionization of the amidogen radical. *The Journal of Chemical Physics*, 83(9):4319–4328, nov 1985. ISSN 0021-9606. doi: 10.1063/1.449045. URL https://pubs.aip.org/jcp/article/83/9/4319/782579/Photoionization-of-the-amidogen.

[65] S. Gozem and A. I. Krylov. The ezSpectra suite: An easy-to-use toolkit for spectroscopy modeling. *WIREs Computational Molecular Science*, 12(2):e1546, 2022. doi: https://doi.org/10.1002/wcms.1546. URL https://wires.onlinelibrary.wiley.com/doi/abs/10.1002/wcms.1546.

[66] A. M. Green, F. Liu, and M. I. Lester. UV + VUV double-resonance studies of autoionizing Rydberg states of the hydroxyl radical. *Journal of Chemical Physics*, 144(18), 2016. ISSN 00219606. doi: 10.1063/1.4948640. URL http://dx.doi.org/10.1063/1.4948640.

[67] S. Hamano, H. Kawakita, N. Kobayashi, K. Takenaka, Y. Ikeda, N. Matsunaga, S. Kondo, H. Sameshima, K. Fukue, C. Yasui, M. Mizumoto, S. Otsubo, A. Watase, T. Yoshikawa, and H. Kobayashi. First Detection of A–X (0,0) Bands of Interstellar C_2 and CN. *The Astrophysical Journal*, 881(2):143, aug 2019. doi: 10.3847/1538-4357/ab2e0f. URL https://doi.org/10.3847%2F1538-4357%2Fab2e0f.

[68] D. S. Han, C. M. L. Rittby, and W. R. M. Graham. Fourier transform infrared observation of the $\nu 1(\sigma)$ mode of linear SiCH in Ar at 10 K. *The Journal of Chemical Physics*, 108(9):3504–3508, 1998. ISSN 0021-9606. doi: $10.1063/1.475748$. URL https://doi.org/10.1063/1.475748.

[69] O. J. Harper. *VUV photoionisation of astrophysical molecules: fundamental and quantitative aspects*. PhD thesis, Université Paris-Saclay, 2020. URL https://theses.hal.science/tel-02926158.

[70] O. J. Harper, M. Hassenfratz, J.-C. Loison, G. A. Garcia, N. de Oliveira, H. Hrodmarsson, S. T. Pratt, S. Boyé-Péronne, and B. Gans. Quantifying the photoionization cross section of the hydroxyl radical. *The Journal of Chemical Physics*, 150(14), apr 2019. ISSN 0021-9606. doi: $10.1063/1.5091966$. URL https://pubs.aip.org/jcp/article/150/14/141103/198647/Quantifying-the-photoionization-cross-section-of.

[71] O. J. Harper, S. Boyé-Péronne, G. A. Garcia, H. R. Hrodmarsson, J. C. Loison, and B. Gans. To see C_2: Single-photon ionization of the dicarbon molecule. *Journal of Chemical Physics*, 152(4):41105, 2020. ISSN 00219606. doi: $10.1063/1.5139309$. URL https://doi.org/10.1063/1.5139309.

[72] O. J. Harper, B. Gans, J.-C. Loison, G. A. Garcia, H. R. Hrodmarsson, and S. Boyé-Péronne. Photoionization Cross Section of the NH_2 Free Radical in the 11.1-15.7 eV Energy Range. *The Journal of Physical Chemistry A*, 125(13): 2764–2769, apr 2021. ISSN 1089-5639. doi: $10.1021/\mathrm{acs.jpca.1c01876}$. URL https://pubs.acs.org/doi/10.1021/acs.jpca.1c01876.

[73] O. J. Harper, N. L. Chen, S. Boyé-Péronne, and B. Gans. Pulsed-ramped-field-ionization zero-kinetic-energy photoelectron spectroscopy: a methodological advance. *Phys. Chem. Chem. Phys.*, 24(5):2777–2784, 2022. doi: $10.1039/\mathrm{D1CP04569E}$. URL http://dx.doi.org/10.1039/D1CP04569E.

[74] A. Heays. NO absorption Spectrum with VUV FTS on the DESIRS beamline. *Private communication*.

[75] A. N. Heays, N. de Oliveira, B. Gans, K. Ito, S. Boyé-Péronne, S. Douin, K. M. Hickson, L. Nahon, and J. C. Loison. High-resolution one-photon absorption spectroscopy of the D $^2\Sigma^- \leftarrow$ X $^2\Pi$ system of radical OH and OD. *Journal of Quantitative Spectroscopy and Radiative Transfer*, 204:12–22, 2018. ISSN 00224073. doi: $10.1016/\mathrm{j.jqsrt.2017.08.021}$. URL http://dx.doi.org/10.1016/j.jqsrt.2017.08.021.

[76] E. Herbst. Unusual Chemical Processes in Interstellar Chemistry: Past and Present. *Frontiers in Astronomy and Space Sciences*, 8(December):1–18, dec 2021. ISSN 2296-987X. doi: $10.3389/\mathrm{fspas.2021.776942}$. URL https://www.frontiersin.org/articles/10.3389/fspas.2021.776942/full.

[77] E. Herbst, T. Millar, S. Wlodek, and D. Bohme. The Chemistry of Silicon in Dense Interstellar Clouds. *Astronomy & Astrophysics*, 222:205–210, 1989. URL https://ui.adsabs.harvard.edu/abs/1989A&A...222..205H.

[78] H. Herburger, V. Wirth, U. Hollenstein, and F. Merkt. Pulsed-ramped-field-ionisation zero-kinetic-energy photoelectron spectroscopy of the metastable rare-gas atoms Ar, Kr and Xe. *Phys. Chem. Chem. Phys.*, 25:22437–22454, 2023. doi: 10.1039/D3CP02881J. URL http://dx.doi.org/10.1039/D3CP02881J.

[79] G. Herzberg. *Molecular Spectra and Molecular Structure: Spectra of diatomic molecules*. Molecular Spectra and Molecular Structure. Van Nostrand, 1950. ISBN 9780442033866. URL https://books.google.fr/books?id=tSVRAAAAMAAJ.

[80] R. Hilbig, G. Hilber, A. Lago, B. Wolff, and R. Wallenstein. Tunable Coherent VUV Radiation Generated by Nonlinear Optical Frequency Conversion in Gases. In P. Yeh, editor, *Nonlinear Optics and Applications*, volume 0613, pages 48–57. International Society for Optics and Photonics, SPIE, 1986. doi: 10.1117/12.960383. URL https://doi.org/10.1117/12.960383.

[81] D. M. Hirst. Ab initio potential energy curves for the X $^1\Sigma^+$, A $^1\Pi$, a $^3\Pi$ and $^3\Sigma^+$ states of SiH$^+$. *Chemical Physics Letters*, 128(5):504–506, 1986. ISSN 0009-2614. doi: https://doi.org/10.1016/0009-2614(86)80662-5. URL https://www.sciencedirect.com/science/article/pii/0009261486806625.

[82] U. Hollenstein, H. Palm, and F. Merkt. A broadly tunable extreme ultraviolet laser source with a 0.008 cm^{-1} bandwidth. *Review of Scientific Instruments*, 71(11):4023–4028, 2000. ISSN 00346748. doi: 10.1063/1.1310344. URL http://link.aip.org/link/?RSI/71/4023/1.

[83] U. Hollenstein, R. Seiler, H. Schmutz, M. Andrist, and F. Merkt. Selective field ionization of high Rydberg states: Application to zero-kinetic-energy photoelectron spectroscopy. *The Journal of Chemical Physics*, 115(12):5461–5469, sep 2001. ISSN 0021-9606. doi: 10.1063/1.1396856. URL https://pubs.aip.org/jcp/article/115/12/5461/457882/Selective-field-ionization-of-high-Rydberg-states.

[84] H. R. Hrodmarsson, G. A. Garcia, L. Nahon, J.-C. Loison, and B. Gans. High resolution threshold photoelectron spectrum and autoionization processes of S_2 up to 15.0 eV. *Journal of Molecular Spectroscopy*, 381:111533, 2021. ISSN 0022-2852. doi: https://doi.org/10.1016/j.jms.2021.111533. URL https://www.sciencedirect.com/science/article/pii/S0022285221001132.

[85] K. P. Huber and G. Herzberg. *Molecular Spectra and Molecular Structure*. Springer US, Boston, MA, 1979. ISBN 978-1-4757-0963-6. doi: 10.1007/978-1-4757-0961-2. URL http://link.springer.com/10.1007/978-1-4757-0961-2.

[86] C. J. Humphreys and E. Paul. Interferometric Wavelength Determinations in the First Spectrum of ^{136}Xe. *J. Opt. Soc. Am.*, 60(10):1302–1310, oct 1970. doi: 10.1364/JOSA.60.001302. URL https://opg.optica.org/abstract.cfm?URI=josa-60-10-1302.

[87] M. Ilchen, T. Mazza, E. T. Karamatskos, D. Markellos, S. Bakhtiarzadeh, A. J. Rafipoor, T. J. Kelly, N. Walsh, J. T. Costello, P. O'Keeffe, N. Gerken, M. Martins, P. Lambropoulos, and M. Meyer. Two-electron processes in multiple ionization under strong soft-x-ray radiation. *Physical Review A*, 94(1):013413, jul 2016. ISSN 2469-9926. doi: $10.1103/\mathrm{PhysRevA}.94.013413$. URL `https://link.aps.org/doi/10.1103/PhysRevA.94.013413`.

[88] U. Jacovella, B. Gans, and F. Merkt. On the adiabatic ionization energy of the propargyl radical. *The Journal of Chemical Physics*, 139(8):84308, 2013. ISSN 0021-9606. doi: $10.1063/1.4818982$. URL `https://doi.org/10.1063/1.4818982`.

[89] U. Jacovella, B. Ruscic, N. L. Chen, H.-L. Le, S. Boyé-Péronne, S. Hartweg, M. R. Chowdhury, G. A. Garcia, J.-C. Loison, and B. Gans. Refining the thermochemical properties of CF, SiF, and their cations by combining photoelectron spectroscopy, quantum chemical calculations, and the Active Thermochemical Tables approach. *Physical Chemistry Chemical Physics*, 25(45):30838–30847, 2023. ISSN 1463-9076. doi: $10.1039/\mathrm{D3CP04244H}$. URL `http://xlink.rsc.org/?DOI=D3CP04244H`.

[90] T. C. James and R. J. Thibault. Spin—Orbit Coupling Constant of Nitric Oxide. Determination from Fundamental and Satellite Band Origins. *The Journal of Chemical Physics*, 41(9):2806–2813, nov 1964. ISSN 0021-9606. doi: $10.1063/1.1726356$. URL `https://pubs.aip.org/jcp/article/41/9/2806/209362/Spin-Orbit-Coupling-Constant-of-Nitric-Oxide`.

[91] G. K. Jarvis, M. Evans, C. Y. Ng, and K. Mitsuke. Rotational-resolved pulsed field ionization photoelectron study of NO^+($X\ ^1\Sigma^+, \nu^+ = 0 - 32$) in the energy range of 9.24–16.80 eV. *The Journal of Chemical Physics*, 111(7):3058–3069, aug 1999. ISSN 0021-9606. doi: $10.1063/1.479586$. URL `https://pubs.aip.org/jcp/article/111/7/3058/294393/Rotational-resolved-pulsed-field-ionization`.

[92] E. B. Jenkins. A unified representation of gas-phase element depletions in the interstellar medium. *The Astrophysical Journal*, 700(2):1299–1348, aug 2009. ISSN 0004-637X. doi: $10.1088/0004\text{-}637\mathrm{X}/700/2/1299$. URL `https://iopscience.iop.org/article/10.1088/0004-637X/700/2/1299`.

[93] E. W. Kaiser and T. J. Wallington. Kinetics of the reactions of chlorine atoms with C_2H_4 (k_1) and C_2H_2 (k_2): A determination of $\Delta H_{\mathrm{f},298}$ for C_2H_3. *The Journal of Physical Chemistry*, 100(10):4111–4119, 1996. doi: $10.1021/\mathrm{jp}953178\mathrm{u}$. URL `https://doi.org/10.1021/jp953178u`.

[94] T. N. Kitsopoulos, C. J. Chick, Y. Zhao, and D. M. Neumark. Study of the low-lying electronic states of Si_2 and Si_2^- using negative ion photodetachment techniques. *The Journal of Chemical Physics*, 95(3):1441–1448, aug 1991. ISSN 0021-9606. doi: $10.1063/1.461057$. URL `https://pubs.aip.org/jcp/article/95/3/1441/959722/Study-of-the-low-lying-electronic-states-of-Si2`.

[95] D. W. Kohn, H. Clauberg, and P. Chen. Flash pyrolysis nozzle for generation of radicals in a supersonic jet expansion. *Review of Scientific Instruments*, 63(8):4003–4005, aug 1992. ISSN 0034-6748. doi: $10.1063/1.1143254$. URL https://pubs.aip.org/rsi/article/63/8/4003/328069/Flash-pyrolysis-nozzle-for-generation-of-radicals.

[96] H. Koizumi. Predominant decay channel for superexcited organic molecules. *The Journal of Chemical Physics*, 95(8):5846–5852, 1991. doi: $10.1063/1.461605$. URL https://doi.org/10.1063/1.461605.

[97] O. Kostko, S. R. Leone, M. A. Duncan, and M. Ahmed. Determination of Ionization Energies of Small Silicon Clusters with Vacuum Ultraviolet Radiation. *The Journal of Physical Chemistry A*, 114(9):3176–3181, mar 2010. ISSN 1089-5639. doi: $10.1021/\mathrm{jp9091688}$. URL https://pubs.acs.org/doi/10.1021/jp9091688.

[98] Y. S. Krivosenko and A. A. Pavlychev. The influence of valence excitations on spectral distribution of vibrational excitations associated with C 1s photoionization in the CO molecule. *Chemical Physics Letters*, 500(1-3):14–17, 2010. ISSN 00092614. doi: $10.1016/\mathrm{j.cplett.2010.09.083}$. URL http://dx.doi.org/10.1016/j.cplett.2010.09.083.

[99] N. Lamarre, B. Gans, C. Alcaraz, B. C. de Miranda, J.-C. Guillemin, M. Broquier, J. Liévin, and S. Boyé-Péronne. Vibronic structure of the $^2\Pi_u$ ground electronic state of dicyanoacetylene cation revisited by PFI-ZEKE photoelectron spectroscopy and ab initio calculations. *Molecular Physics*, 113(24):3946–3954, dec 2015. ISSN 0026-8976. doi: $10.1080/00268976.2015.1075074$. URL http://www.tandfonline.com/doi/full/10.1080/00268976.2015.1075074.

[100] F. Laruelle, S. Boyé-Péronne, D. Gauyacq, and J. Liévin. Revisiting Mulliken's Concepts about Rydberg States and Rydberg-Valence Interactions from Large-Scale Ab Initio Calculations on the Acetylene Molecule. *The Journal of Physical Chemistry A*, 113(47):13210–13220, nov 2009. ISSN 1089-5639. doi: $10.1021/\mathrm{jp903948k}$. URL https://pubs.acs.org/doi/10.1021/jp903948k.

[101] H. Lavendy, J. M. Robbe, D. Duflot, and J. P. Flament. MCSCF-CI study of the isomerization reaction HCSi $\rightarrow$ HSiC. In *AIP Conference Proceedings*, volume 312, pages 343–347. AIP, 1994. doi: $10.1063/1.46617$. URL https://pubs.aip.org/aip/acp/article/312/1/343-347/614198.

[102] H. Lefebvre-Brion and F. Guerin. Calculation of the Radiative Lifetime of the a $^4\Pi$ State of NO. *The Journal of Chemical Physics*, 49(3):1446–1447, aug 1968. ISSN 0021-9606. doi: $10.1063/1.1670258$. URL https://pubs.aip.org/jcp/article/49/3/1446/446335/Calculation-of-the-Radiative-Lifetime-of-the-a4.

[103] K. Lim and F. Lampe. Ion/molecule reactions in silane—carbon monoxide mixtures: possible synthesis of the SiC radical in the electric discharge chemistry. *International Journal of Mass Spectrometry and Ion Processes*, 101(2-3):245–256, dec 1990. ISSN 01681176. doi: $10.1016/0168\text{-}1176(90)87014\text{-}8$.

URL https://www.sciencedirect.com/science/article/pii/0168117690870148https://linkinghub.elsevier.com/retrieve/pii/0168117690870148.

[104] S. H. Lin. Calculation of the lifetime of the a $^4\Pi$ state of NO. *The Journal of Chemical Physics*, 46(1):279–282, jan 1967. ISSN 0021-9606. doi: $10.1063/1.1840383$. URL https://pubs.aip.org/jcp/article/46/1/279/83414/Calculation-of-the-Lifetime-of-the-a-4-State-of-NO.

[105] P. J. Linstrom and W. G. Mallard. NIST Chemistry WebBook , NIST Standard Reference Database Number 69. URL http://webbook.nist.gov.

[106] Y. Liu, H. Zhai, X. Zhang, and Y. Liu. Ab initio calculation on the low-lying excited states of Si_2^+ cation including spin–orbit coupling. *Chemical Physics*, 425:156–161, nov 2013. ISSN 03010104. doi: $10.1016/\mathrm{j.chemphys.2013.09.002}$. URL http://dx.doi.org/10.1016/j.chemphys.2013.09.002.

[107] K. Lodders. Solar System Abundances and Condensation Temperatures of the Elements. *The Astrophysical Journal*, 591(2):1220–1247, jul 2003. ISSN 0004-637X. doi: $10.1086/375492$. URL https://iopscience.iop.org/article/10.1086/375492.

[108] I.-C. Lu, W.-J. Huang, C. Chaudhuri, W.-K. Chen, and S.-H. Lee. Development of a stable source of atomic oxygen with a pulsed high-voltage discharge and its application to crossed-beam reactions. *Review of Scientific Instruments*, 78(8), aug 2007. ISSN 0034-6748. doi: $10.1063/1.2772090$. URL https://pubs.aip.org/rsi/article/78/8/083103/911674/Development-of-a-stable-source-of-atomic-oxygen.

[109] R. Lucas and H. Liszt. SiO in diffuse, translucent and 'spiral-arm' clouds. *Astronomy and Astrophysics*, 355: 327–332, mar 2000. URL https://ui.adsabs.harvard.edu/abs/2000A&A...355..327L.

[110] R. Macdonald and J. J. Sloan. The microscopic reaction dynamics and branching ratio in the F + HCOOH and F + H_2CO reactions. *Chemical Physics*, 31(2):165–176, 1978. ISSN 0301-0104. doi: $\mathrm{https://doi.org/10.1016/0301\text{-}0104(78)87033\text{-}5}$. URL https://www.sciencedirect.com/science/article/pii/0301010478870335.

[111] A. Marijnissen and J. ter Meulen. Determination of the adiabatic ionization potentials of Si_2 and SiCl by photoionization efficiency spectroscopy. *Chemical Physics Letters*, 263(6):803–810, dec 1996. ISSN 00092614. doi: $10.1016/\mathrm{S0009\text{-}2614(96)01284\text{-}5}$. URL https://linkinghub.elsevier.com/retrieve/pii/S0009261496012845.

[112] B. A. McGuire. 2021 Census of Interstellar, Circumstellar, Extragalactic, Protoplanetary Disk, and Exoplanetary Molecules. *The Astrophysical Journal Supplement Series*, 259(2):30, 2022. ISSN 0067-0049. doi: $10.3847/\mathrm{1538\text{-}4365/ac2a48}$. URL http://dx.doi.org/10.3847/1538-4365/ac2a48.

[113] A. McKellar. Evidence for the molecular origin of some hitherto unidentified interstellar lines. *Publications of the Astronomical Society of the Pacific*, 52(307):187, 1940. doi: 10.1086/125159. URL https://dx.doi.org/10.1086/125159.

[114] Q. Meng, K. M. Hickson, K. Shao, J. C. Loison, and D. H. Zhang. Theoretical and experimental investigations of rate coefficients of O(^{1}D) + CH_4 at low temperature. *Physical Chemistry Chemical Physics*, 18(42):29286–29292, 2016. ISSN 14639076. doi: 10.1039/c6cp05517f. URL http://dx.doi.org/10.1039/C6CP05517F.

[115] A. J. Merer, D. N. Malm, R. W. Martin, M. Horani, and J. Rostas. The Ultraviolet Emission Spectra of OH^+ and OD^+. Rotational Structure and Perturbations in the $A^3\Pi_i$–$X^3\Sigma^-$ Transition. *Canadian Journal of Physics*, 53(3): 251–283, 1975. doi: 10.1139/p75-037. URL https://doi.org/10.1139/p75-037.

[116] F. Merkt. Molecules in high Rydberg states. *Annual Review of Physical Chemistry*, 48(1):675–709, oct 1997. ISSN 0066-426X. doi: 10.1146/annurev.physchem.48.1.675. URL https://www.annualreviews.org/doi/10.1146/annurev.physchem.48.1.675.

[117] F. Merkt, A. Osterwalder, R. Seiler, R. Signorell, H. Palm, H. Schmutz, and R. Gunzinger. High Rydberg states of argon: Stark effect and field-ionization properties. *Journal of Physics B: Atomic, Molecular and Optical Physics*, 31(8):1705–1724, apr 1998. ISSN 0953-4075. doi: 10.1088/0953-4075/31/8/020. URL https://iopscience.iop.org/article/10.1088/0953-4075/31/8/020.

[118] F. Merkt, S. Willitsch, and U. Hollenstein. High-resolution Photoelectron Spectroscopy. In *Handbook of High-resolution Spectroscopy*, number 3, pages 1617–1654. Wiley, sep 2011. ISBN 9780470066539. doi: 10.1002/9780470749593.hrs071. URL https://onlinelibrary.wiley.com/doi/10.1002/9780470749593.hrs071.

[119] P. W. Merrill. Stationary Lines in the Spectrum of the Binary Star Boss 6142. *The Astrophysical Journal*, 83 (59):126, mar 1936. ISSN 0004-637X. doi: 10.1086/143707. URL http://adsabs.harvard.edu/doi/10.1086/143707.

[120] T. J. Millar. Silicon chemistry in dense clouds. *Astrophysics and Space Science*, 72(2):509–517, oct 1980. ISSN 0004-640X. doi: 10.1007/BF00639153. URL http://link.springer.com/10.1007/BF00639153.

[121] S. Mohamed, M. C. McCarthy, A. L. Cooksy, C. Hinton, and P. Thaddeus. Rotational spectra of the carbon-chain radicals HC_5O, HC_6O, and HC_7O. *The Journal of Chemical Physics*, 123(23):234301, 2005. ISSN 0021-9606. doi: 10.1063/1.2126970. URL https://doi.org/10.1063/1.2126970.

[122] K. Müller-Dethlefs, M. Sander, and E. W. Schlag. Two-colour photoionization resonance spectroscopy of NO: Complete separation of rotational levels of NO^+ at the ionization threshold. *Chemical Physics Letters*, 112(4): 291–294, dec 1984. ISSN 00092614. doi: 10.1016/0009-2614(84)85743-7. URL https://linkinghub.elsevier.com/retrieve/pii/0009261484857437.

[123] K. Müller-Dethlefs, E. W. Schlag, K. Müller-Dethlefs, and E. W. Schlag. High-resolution Zero Kinetic Energy (ZEKE) photoelectron spectroscopy of molecular systems. *Annual Review of Physical Chemistry*, 42(1):109–136, 1991. ISSN 0066426X. doi: 10.1146/annurev.pc.42.100191.000545. URL https://doi.org/10.1146/annurev.pc.42.100191.000545.

[124] L. Nahon, N. de Oliveira, G. A. Garcia, J.-F. Gil, B. Pilette, O. Marcouillé, B. Lagarde, and F. Polack. DESIRS: a state-of-the-art VUV beamline featuring high resolution and variable polarization for spectroscopy and dichroism at SOLEIL. *Journal of Synchrotron Radiation*, 19(4):508–520, jul 2012. ISSN 0909-0495. doi: 10.1107/S0909049512010588. URL https://scripts.iucr.org/cgi-bin/paper?S0909049512010588.

[125] M. R. Nimlos, L. B. Harding, and G. B. Ellison. The electronic states of Si_2 and Si_2^- as revealed by photoelectron spectroscopy. *The Journal of Chemical Physics*, 87(9):5116–5124, nov 1987. ISSN 0021-9606. doi: 10.1063/1.453679. URL https://pubs.aip.org/jcp/article/87/9/5116/92191/The-electronic-states-of-Si2-and-Si-2-as-revealed.

[126] D. Nuñez-Reyes and K. M. Hickson. Rate Constants and H-Atom Product Yields for the Reactions of O(^{1}D) Atoms with Ethane and Acetylene from 50 to 296 K. *The Journal of Physical Chemistry A*, 122(20):4696–4703, may 2018. ISSN 1089-5639. doi: 10.1021/acs.jpca.8b02267. URL https://pubs.acs.org/doi/10.1021/acs.jpca.8b02267.

[127] D. Nuñez-Reyes, J. C. Loison, K. M. Hickson, and M. Dobrijevic. A low temperature investigation of the N(^{2}D) + CH_4, C_2H_6 and C_3H_8 reactions. *Physical Chemistry Chemical Physics*, 21(12):6574–6581, 2019. ISSN 14639076. doi: 10.1039/c9cp00798a. URL http://dx.doi.org/10.1039/C9CP00798A.

[128] Y. Ono, S. H. Linn, H. F. Prest, C. Y. Ng, and E. Miescher. Higher resolution photoionization study of NO near the threshold. *The Journal of Chemical Physics*, 73(10):4855–4861, nov 1980. ISSN 0021-9606. doi: 10.1063/1.440013. URL https://pubs.aip.org/jcp/article/73/10/4855/794242/Higher-resolution-photoionization-study-of-NO-near.

[129] D. L. Osborn, P. Zou, H. Johnsen, C. C. Hayden, C. A. Taatjes, V. D. Knyazev, S. W. North, D. S. Peterka, M. Ahmed, and S. R. Leone. The multiplexed chemical kinetic photoionization mass spectrometer: A new approach to isomer-resolved chemical kinetics. *Review of Scientific Instruments*, 79(10), oct 2008. ISSN 0034-6748. doi: 10.1063/1.3000004. URL https://pubs.aip.org/rsi/article/79/10/104103/1029809/The-multiplexed-chemical-kinetic-photoionization.

[130] C. Ottinger and A. F. Vilesov. Lifetime measurements on perturbed levels of NO(B $^2\Pi$) and precise term energy of the NO(a $^4\Pi$) state. *The Journal of Chemical Physics*, 100(3):1815–1822, feb 1994. ISSN 0021-9606. doi: 10.1063/1.466534. URL https://pubs.aip.org/jcp/article/100/3/1815/474014/Lifetime-measurements-on-perturbed-levels-of-NO-B.

[131] W. Peatman, T. Borne, and E. Schlag. Photoionization resonance spectra I. nitric oxide and benzene. *Chemical Physics Letters*, 3(7):492–497, aug 1969. ISSN 00092614. doi: 10.1016/0009-2614(69)85042-6. URL https://linkinghub.elsevier.com/retrieve/pii/0009261469850426.

[132] L. Podio, C. Codella, B. Lefloch, N. Balucani, C. Ceccarelli, R. Bachiller, M. Benedettini, J. Cernicharo, N. Faginas-Lago, F. Fontani, A. Gusdorf, and M. Rosi. Silicon-bearing molecules in the shock L1157-B1: first detection of SiS around a Sun-like protostar. *Monthly Notices of the Royal Astronomical Society: Letters*, 470(1):L16–L20, sep 2017. ISSN 1745-3925. doi: 10.1093/mnrasl/slx068. URL https://academic.oup.com/mnrasl/article-lookup/doi/10.1093/mnrasl/slx068.

[133] J. A. Pople and L. A. Curtiss. Theoretical thermochemistry. 3. A modified procedure for ionization energies of AH_n species. *The Journal of Physical Chemistry*, 91(13):3637–3639, jun 1987. ISSN 0022-3654. doi: 10.1021/j100297a034. URL https://pubs.acs.org/doi/abs/10.1021/j100297a034.

[134] J. C. Poully, J. P. Schermann, N. Nieuwjaer, F. Lecomte, G. Grégoire, C. Desfrançois, G. A. Garcia, L. Nahon, D. Nandi, L. Poisson, and M. Hochlaf. Photoionization of 2-pyridone and 2-hydroxypyridine. *Physical Chemistry Chemical Physics*, 12(14):3566, 2010. ISSN 1463-9076. doi: 10.1039/b923630a. URL http://xlink.rsc.org/?DOI=b923630a.

[135] A. Pramanik and K. K. Das. The electronic spectrum of the SiC radical: A theoretical study. *Journal of Molecular Spectroscopy*, 244(1):13–23, 2007. ISSN 0022-2852. doi: https://doi.org/10.1016/j.jms.2007.05.007. URL https://www.sciencedirect.com/science/article/pii/S0022285207001312.

[136] A. Pramanik, S. Chakrabarti, and K. K. Das. Theoretical studies of the electronic spectrum of SiC^+. *Chemical Physics Letters*, 450(4-6):221–227, jan 2008. ISSN 00092614. doi: 10.1016/j.cplett.2007.11.020. URL https://linkinghub.elsevier.com/retrieve/pii/S0009261407015321.

[137] S. T. Pratt, P. M. Dehmer, and J. L. Dehmer. Photoionization of an autoionizing level of atomic oxygen. *Physical Review A*, 43(1):282–286, jan 1991. ISSN 1050-2947. doi: 10.1103/PhysRevA.43.282. URL https://link.aps.org/doi/10.1103/PhysRevA.43.282.

[138] G. Reiser, W. Habenicht, K. Müller-Dethlefs, and E. W. Schlag. The ionization energy of nitric oxide. *Chemical Physics Letters*, 152(2-3):119–123, nov 1988. ISSN 00092614. doi: 10.1016/0009-2614(88)87340-8. URL https://linkinghub.elsevier.com/retrieve/pii/0009261488873408.

[139] M. Richard-Viard, A. Delboulbé, and M. Vervloet. Experimental study of the dissociation of selected internal energy ions produced in low quantities: Application to N_2O^+ ions in the Franck-Condon gap and to small ionic water clusters. *Chemical Physics*, 209(2-3):159–167, sep 1996. ISSN 03010104. doi: 10.1016/0301-0104(96)00164-4. URL https://linkinghub.elsevier.com/retrieve/pii/0301010496001644.

[140] J. Robbe, H. Lavendy, J. Flament, and G. Chambaud. Ro-vibronic spectrum of the HCSi radical. *Chemical Physics Letters*, 267(1-2):91–97, mar 1997. ISSN 00092614. doi: 10.1016/S0009-2614(97)00086-9. URL https://linkinghub.elsevier.com/retrieve/pii/S0009261497000869.

[141] P. Rosmus and W. Meyer. PNO–CI and CEPA studies of electron correlation effects. IV. Ionization energies of the first and second row diatomic hydrides and the spectroscopic constants of their ions. *The Journal of Chemical Physics*, 66(1):13–19, jan 1977. ISSN 0021-9606. doi: 10.1063/1.433661. URL https://pubs.aip.org/jcp/article/66/1/13/454844/PNO-CI-and-CEPA-studies-of-electron-correlation.

[142] E. Roueff and F. Lique. Molecular Excitation in the Interstellar Medium: Recent Advances in Collisional, Radiative, and Chemical Processes. *Chemical Reviews*, 113(12):8906–8938, dec 2013. ISSN 0009-2665. doi: 10.1021/cr400145a. URL https://pubs.acs.org/doi/10.1021/cr400145a.

[143] P. Rupper and F. Merkt. Intense narrow-bandwidth extreme ultraviolet laser system tunable up to 20 eV. *Review of Scientific Instruments*, 75(3):613–622, mar 2004. ISSN 0034-6748. doi: 10.1063/1.1646744. URL https://pubs.aip.org/rsi/article/75/3/613/460503/Intense-narrow-bandwidth-extreme-ultraviolet-laser.

[144] A. B. Sannigrahi, R. J. Buenker, G. Hirsch, and J.-p. Gu. Ab initio configuration interaction study of the electronic spectrum of SiH^+. *Chemical Physics Letters*, 237(3-4):204–211, may 1995. ISSN 00092614. doi: 10.1016/0009-2614(95)00307-P. URL https://linkinghub.elsevier.com/retrieve/pii/000926149500307P.

[145] B. D. Savage and K. R. Sembach. Interstellar Abundances from Absorption-Line Observations with the Hubble Space Telescope. *Annual Review of Astronomy and Astrophysics*, 34(1):279–329, sep 1996. ISSN 0066-4146. doi: 10.1146/annurev.astro.34.1.279. URL https://www.annualreviews.org/doi/10.1146/annurev.astro.34.1.279.

[146] J. D. Savee, J. Zádor, P. Hemberger, B. Sztáray, A. Bodi, and D. L. Osborn. Threshold photoelectron spectrum of the benzyl radical. *Molecular Physics*, 113(15-16):2217–2227, aug 2015. ISSN 0026-8976. doi: 10.1080/00268976.2015.1021398. URL http://www.tandfonline.com/doi/full/10.1080/00268976.2015.1021398.

[147] P. Schilke, D. J. Benford, T. R. Hunter, D. C. Lis, and T. G. Phillips. A Line Survey of Orion-KL from 607 to 725 GHz. *The Astrophysical Journal Supplement Series*, 132(2):281–364, feb 2001. doi: 10.1086/318951. URL https://doi.org/10.1086/318951.

[148] P. Schilke, S. Leurini, K. M. Menten, and J. Alcolea. Interstellar SiN. *Astronomy & Astrophysics*, 412(2):L15–L18, dec 2003. ISSN 0004-6361. doi: 10.1051/0004-6361:20031649. URL http://www.aanda.org/10.1051/0004-6361:20031649.

[149] A. M. Schulenburg, C. Alcaraz, G. Grassi, and F. Merkt. Rovibrational photoionization dynamics of methyl and its isotopomers studied by high-resolution photoionization and photoelectron spectroscopy. *The Journal of Chemical Physics*, 125(10), sep 2006. ISSN 0021-9606. doi: $10.1063/1.2348875$. URL https://pubs.aip.org/jcp/article/125/10/104310/186634/Rovibrational-photoionization-dynamics-of-methyl.

[150] D. H. Shi, H. Liu, J. F. Sun, Z. L. Zhu, and Y. F. Liu. Spectroscopic and molecular properties of 14 selected electronic states of Si_2 molecule. *Journal of Quantitative Spectroscopy and Radiative Transfer*, 112(16):2567–2583, 2011. ISSN 00224073. doi: $10.1016/j.jqsrt.2011.07.007$. URL http://dx.doi.org/10.1016/j.jqsrt.2011.07.007.

[151] D. H. Shi, W. Xing, J. F. Sun, and Z. L. Zhu. Theoretical studies on the SiC radical: electronic structure, spectroscopy and spin-orbit couplings. *The European Physical Journal D*, 66(10):262, 2012. ISSN 1434-6079. doi: $10.1140/epjd/e2012-30313-0$. URL https://doi.org/10.1140/epjd/e2012-30313-0.

[152] R. Signorell and F. Merkt. General symmetry selection rules for the photoionization of polyatomic molecules. *Molecular Physics*, 92(5):793–804, dec 1997. ISSN 0026-8976. doi: $10.1080/002689797169745$. URL http://www.tandfonline.com/doi/abs/10.1080/002689797169745.

[153] D. Smith. The ion chemistry of interstellar clouds. *Chemical Reviews*, 92(7):1473–1485, nov 1992. ISSN 0009-2665. doi: $10.1021/cr00015a001$. URL https://pubs.acs.org/doi/abs/10.1021/cr00015a001.

[154] T. C. Smith, H. Li, D. J. Clouthier, C. T. Kingston, and A. J. Merer. The electronic spectrum of silicon methylidyne (SiCH), a molecule with a silicon–carbon triple bond in the excited state. *The Journal of Chemical Physics*, 112 (8):3662–3670, feb 2000. ISSN 0021-9606. doi: $10.1063/1.480518$. URL https://pubs.aip.org/jcp/article/112/8/3662/473142/The-electronic-spectrum-of-silicon-methylidyne.

[155] T. C. Smith, H. Li, D. A. Hostutler, D. J. Clouthier, and A. J. Merer. Orbital angular momentum (Renner-Teller) effects in the $^2\Pi_i$ ground state of silicon methylidyne (SiCH). *The Journal of Chemical Physics*, 114(2):725–734, jan 2001. ISSN 0021-9606. doi: $10.1063/1.1331316$. URL https://pubs.aip.org/jcp/article/114/2/725/184117/Orbital-angular-momentum-Renner-Teller-effects-in.

[156] R. Srinivas, D. Suelzle, and H. Schwarz. Experimental Evidence for the Existence of $SiCH_x$ (x = 1–3) Molecules in the Gas Phase. *Journal of the American Chemical Society*, 113(1):52–54, jan 1991. ISSN 0002-7863. doi: $10.1021/ja00001a010$. URL https://pubs.acs.org/doi/abs/10.1021/ja00001a010.

[157] M. Steinbauer, P. Hemberger, I. Fischer, and A. Bodi. Photoionization of C_7H_6 and C_7H_5: Observation of the Fulvenallenyl Radical. *ChemPhysChem*, 12(10):1795–1797, jul 2011. ISSN 1439-4235. doi: $10.1002/cphc.201000892$. URL https://chemistry-europe.onlinelibrary.wiley.com/doi/10.1002/cphc.201000892.

[158] T. Studemund, K. Pollow, S. Verhoeven, E. Mickein, O. Dopfer, and M. Förstel. The Electronic Spectrum of Si_2^+. *The Journal of Physical Chemistry Letters*, 13(33):7624–7628, 2022. doi: 10.1021/acs.jpclett.2c02200. URL https://doi.org/10.1021/acs.jpclett.2c02200.

[159] J. Sugar and A. Musgrove. Energy Levels of Krypton, Kr I through Kr XXXVI. *Journal of Physical and Chemical Reference Data*, 20(5):859–915, sep 1991. ISSN 0047-2689. doi: 10.1063/1.555896. URL https://pubs.aip.org/jpr/article/20/5/859/241552/Energy-Levels-of-Krypton-Kr-I-through-Kr.

[160] P. Swings and L. Rosenfeld. Considerations Regarding Interstellar Molecules. *The Astrophysical Journal*, 86:483, nov 1937. ISSN 0004-637X. doi: 10.1086/143880. URL http://adsabs.harvard.edu/doi/10.1086/143880.

[161] X. Tang, G. A. Garcia, J.-F. F. Gil, and L. Nahon. Vacuum upgrade and enhanced performances of the double imaging electron/ion coincidence end-station at the vacuum ultraviolet beamline DESIRS. *Review of Scientific Instruments*, 86(12):123108, 2015. ISSN 10897623. doi: 10.1063/1.4937624. URL https://doi.org/10.1063/1.4937624.

[162] A. G. G. M. Tielens. Chemical processes. In *The Physics and Chemistry of the Interstellar Medium*, pages 85–116. Cambridge University Press, aug 2005. doi: 10.1017/CBO9780511819056.005. URL https://www.cambridge.org/core/product/identifier/CBO9780511819056A038/type/book_part.

[163] D. Toffoli and R. R. Lucchese. Near threshold photoionization of the ground and first excited states of C_2. *The Journal of Chemical Physics*, 120(13):6010–6018, apr 2004. ISSN 0021-9606. doi: 10.1063/1.1651477. URL https://pubs.aip.org/jcp/article/120/13/6010/186410/Near-threshold-photoionization-of-the-ground-and.

[164] R. Treffers and M. Cohen. High-resolution spectra of cool stars in the 10- and 20-micron regions. *The Astrophysical Journal*, 188:545, mar 1974. ISSN 0004-637X. doi: 10.1086/152746. URL http://adsabs.harvard.edu/doi/10.1086/152746.

[165] D. J. Trevor, D. M. Cox, K. C. Reichmann, R. O. Brickman, and A. Kaldor. Ionizing laser intensity dependence of the silicon cluster photoionization mass spectrum. *The Journal of Physical Chemistry*, 91(10):2598–2601, may 1987. ISSN 0022-3654. doi: 10.1021/j100294a030. URL https://pubs.acs.org/doi/abs/10.1021/j100294a030.

[166] B. E. Turner. The Physics and Chemistry of Small Translucent Molecular Clouds. X. SiO. *The Astrophysical Journal*, 495(2):804–820, mar 1998. ISSN 0004-637X. doi: 10.1086/305319. URL https://iopscience.iop.org/article/10.1086/305319.

[167] J. L. Turner and A. Dalgarno. The chemistry of silicon in interstellar clouds. *The Astrophysical Journal*, 213(1):386, apr 1977. ISSN 0004-637X. doi: 10.1086/155167. URL http://adsabs.harvard.edu/doi/10.1086/155167.

[168] L. Velilla-Prieto, J. Cernicharo, M. Agúndez, J. P. Fonfría, A. Castro-Carrizo, G. Quintana-Lacaci, N. Marcelino, M. C. McCarthy, C. A. Gottlieb, C. Sánchez Contreras, K. H. Young, N. A. Patel, C. Joblin, and J. A. Martín-Gago. Circumstellar chemistry of Si-C bearing molecules in the C-rich AGB star IRC+10216. *Proceedings of the International Astronomical Union*, 14(S343):535–537, aug 2018. ISSN 1743-9213. doi: 10.1017/S1743921318005410. URL https://www.cambridge.org/core/product/identifier/S1743921318005410/type/journal_article.

[169] G. Verhaegen, F. E. Stafford, J. Deowart, J. Drowart, and J. Deowart. Mass spectrometric study of the systems boron-carbon and boron-carbon-silicon. *The Journal of Chemical Physics*, 40(6):1622–1628, 1964. ISSN 00219606. doi: 10.1063/1.1725370. URL https://doi.org/10.1063/1.1725370.

[170] K.-S. Wang, Y.-J. Kuan, S.-Y. Liu, H.-C. Huang, and S. B. Charnley. Organic Molecules in the Orion KL Hot Molecular Core. *Bioastronomy 2007: Molecules, Microbes and Extraterrestrial Life*, 420:49, 2009. ISSN 1050-3390. URL http://esoads.eso.org/abs/2009ASPC..420...49W.

[171] C. M. Western. PGOPHER: A program for simulating rotational, vibrational and electronic spectra. *Journal of Quantitative Spectroscopy and Radiative Transfer*, 186:221–242, 2017. ISSN 0022-4073. doi: https://doi.org/10.1016/j.jqsrt.2016.04.010. URL http://www.sciencedirect.com/science/article/pii/S0022407316300437.

[172] J. C. Whitehead. Molecular beam studies of free-radical processes: photodissociation, inelastic and reactive collisions. *Reports on Progress in Physics*, 59(8):993–1040, aug 1996. ISSN 0034-4885. doi: 10.1088/0034-4885/59/8/002. URL https://iopscience.iop.org/article/10.1088/0034-4885/59/8/002.

[173] A. Wicaksana and T. Rachman. Models of interstellar clouds. I. The Zeta Ophiuchi cloud. *Astrophysical Journal*, 3(1):10–27, 1977. URL https://medium.com/@arifwicaksanaa/pengertian-use-case-a7e576e1b6bf.

[174] M. Wickramaaratchi, D. Setser, H. Hildebrandt, B. Kōrbitzer, and H. Heydtmann. Evaluation of HF product distributions deduced from infrared chemiluminiscence. II. F atom reactions. *Chemical Physics*, 94(1-2):109–129, mar 1985. ISSN 03010104. doi: 10.1016/0301-0104(85)85070-9. URL https://linkinghub.elsevier.com/retrieve/pii/0301010485850709.

[175] R. T. Wiedmann, M. G. White, K. Wang, and V. McKoy. Rotationally resolved photoionization of polyatomic hydrides: CH_3, H_2O, H_2S, H_2CO. *The Journal of Chemical Physics*, 100(7):4738–4746, apr 1994. ISSN 0021-9606. doi: 10.1063/1.466264. URL https://pubs.aip.org/jcp/article/100/7/4738/482962/Rotationally-resolved-photoionization-of.

[176] W. C. Wiley and I. H. McLaren. Time-of-Flight Mass Spectrometer with Improved Resolution. *Review of Scientific Instruments*, 26(12):1150–1157, dec 1955. ISSN 0034-6748. doi: 10.1063/1.1715212. URL https://pubs.aip.org/rsi/article/26/12/1150/298880/Time-of-Flight-Mass-Spectrometer-with-Improved.

[177] H. Winick. Fourth generation light sources. *Proceedings of the IEEE Particle Accelerator Conference*, 1:37–41, 1998. URL https://ui.adsabs.harvard.edu/abs/1997APS..PAC.FBC03W.

[178] C. Winstead, S. Paukstis, and J. Gole. What is the ionization potential of silicon dimer? *Chemical Physics Letters*, 237(1-2):81–85, may 1995. ISSN 00092614. doi: $10.1016/0009\text{-}2614(95)00266\text{-}7$. URL https://linkinghub.elsevier.com/retrieve/pii/0009261495002667.

[179] S. Wlodek and D. K. Bohme. Gas-phase reactions of silicon ion (Si^+ with ammonia and the amines $(CH_3)_xNH_{3-x}$ (x = 1-3): possible ion-molecule reaction pathways toward SiH, SiCH, SiNH, $SiCH_3$, $SiNCH_3$, and H_2SiNH. *Journal of the American Chemical Society*, 110(8):2396–2399, apr 1988. ISSN 0002-7863. doi: $10.1021/ja00216a010$. URL https://pubs.acs.org/doi/abs/10.1021/ja00216a010.

[180] J. Xie and R. N. Zare. Selection rules for the photoionization of diatomic molecules. *The Journal of Chemical Physics*, 93(5):3033–3038, sep 1990. ISSN 0021-9606. doi: $10.1063/1.458837$. URL https://pubs.aip.org/jcp/article/93/5/3033/971811/Selection-rules-for-the-photoionization-of.

[181] W. Xing, D. Shi, and J. Sun. Transition probabilities between the $X^3\Pi$, $A^3\Sigma^-$, $B^3\Sigma^+$, $C^3\Pi$, $D^3\Delta$, and $E^3\Pi$ states of SiC molecules. *Journal of Quantitative Spectroscopy and Radiative Transfer*, 227:86–93, 2019. ISSN 0022-4073. doi: $\text{https://doi.org/}10.1016/\text{j.jqsrt.}2019.02.003$. URL https://www.sciencedirect.com/science/article/pii/S0022407319300093.

[182] C. Yamada, E. Hirota, and K. Kawaguchi. Diode laser study of the ν_2 band of the methyl radical. *The Journal of Chemical Physics*, 75(11):5256–5264, dec 1981. ISSN 0021-9606. doi: $10.1063/1.441991$. URL https://pubs.aip.org/jcp/article/75/11/5256/217069/Diode-laser-study-of-the-2-band-of-the-methyl.

[183] G. L. Zarur and Y.-N. Chiu. Cooperative optical phenomena. II. Spin-forbidden lifetime of the a $^4\Pi$ state of nitric oxide. *The Journal of Chemical Physics*, 59(1):82–88, jul 1973. ISSN 0021-9606. doi: $10.1063/1.1679861$. URL https://pubs.aip.org/jcp/article/59/1/82/769075/Cooperative-optical-phenomena-II-Spin-forbidden.

[184] M. Zhang and K. Wang. Vibronic emissions between the $a^1\Sigma^+$, $b^1\Pi$, $c^1\Delta$, $d^1\Sigma^+$, $e^1\Sigma^-$, and $f^1\Pi$ states of the diatomic silicon carbide SiC. *Journal of Quantitative Spectroscopy and Radiative Transfer*, 233:13–20, 2019. ISSN 0022-4073. doi: $\text{https://doi.org/}10.1016/\text{j.jqsrt.}2019.05.005$. URL https://www.sciencedirect.com/science/article/pii/S002240731930233X.

[185] Y. G. Zhang, G. Dou, J. X. Qi, and J. Cui. Ab inito study on the electronic structure and laser cooling of SiH. *Computational and Theoretical Chemistry*, 1134(April):8–14, 2018. ISSN 2210271X. doi: $10.1016/\text{j.comptc.}2018.04.014$. URL https://doi.org/10.1016/j.comptc.2018.04.014.

[186] L. Zhu and P. Johnson. Mass analyzed threshold ionization spectroscopy. *The Journal of Chemical Physics*, 94 (8):5769–5771, apr 1991. ISSN 0021-9606. doi: $10.1063/1.460460$. URL https://pubs.aip.org/jcp/article/94/8/5769/441880/Mass-analyzed-threshold-ionization.

[187] L. M. Ziurys, R. J. Saykally, M. Colvin, H. F. Schaefer, and D. P. Clemens. A search for interstellar silicon nitride. *The Astrophysical Journal*, 281:219, jun 1984. ISSN 0004-637X. doi: $10.1086/162091$. URL http://adsabs.harvard.edu/doi/10.1086/162091.

[188] L. M. Ziurys, P. Friberg, and W. M. Irvine. Interstellar SiO as a tracer of high-temperature chemistry. *The Astrophysical Journal*, 343:201, aug 1989. ISSN 0004-637X. doi: $10.1086/167696$. URL http://adsabs.harvard.edu/doi/10.1086/167696.